Remote Sensing of Water Temperature using Raman Spectroscopy

Christopher Peter Artlett

BTech (Optoelectronics), MSc.

This thesis is submitted to Macquarie University
for the degree of Doctor of Philosophy.

Department of Physics and Astronomy

February 2015

MACQUARIE
University

Declaration

This thesis is submitted in fulfilment of the requirements of the degree of Doctor of Philosophy at Macquarie University and has not been submitted for a higher degree at any other university or institution. I certify that to the best of my knowledge, all sources used and assistance received in the preparation of this thesis have been acknowledged.

_____

Christopher Artlett

February 2015

Acknowledgments

I would never have been able to complete this thesis without the tireless encouragement, support and optimism of my principal supervisor Helen Pask. I owe her a great deal, and I look forward to continuing our work together this year.

Thanks also to my associate supervisor David Spence for helpful discussions, good advice and high–speed reviewing at short notice!

Many thanks are owed to my friends and colleagues at Macquarie University for their support, valuable discussion and kindness offered during the course of my studies. In particular Josh, Aaron, Andrew, Doug, Ondrej, Tristan and Robbie have assisted me greatly, both in terms of advice and providing (at times) much needed distractions from work.

Thanks go to my best mates, Tom, Andy, Corina, Sarsha and Hua for their support, many good meals and adventurous bike rides.

The international crew of Varun, Annie, Tristan, Barbara, Ondrej and Katya etc. provided me with a vague semblance of a social life, with great barbeques, parties and games nights, thanks guys.

Thank you also to the morning tea regulars for interesting discussions and humorous conversations which definitely helped me to reduce stress levels.

Lastly, many thanks to my family for much support and many phone calls. Now when you ask me “Is it finished?” I will have something to say besides “Nearly!”

Abstract

The measurement of water temperature, both at and below the surface in bodies of water, is of great importance for research fields including climate change, marine biology, hydrologic modelling and marine engineering. While sea surface temperature can be obtained with passive satellite sensing, sub–surface measurements are limited to suspended arrays of detectors, expendable probes and autonomous vehicles. None of these methods are compatible with rapid systematic mapping of sub–surface water temperature.

The aim of the research presented in this thesis is to develop methods for rapid, depth–resolved remote sensing of water temperature using Raman spectroscopy, and to explore the potential to incorporate measurement of salinity. An optical, depth–resolved temperature sensing solution would provide a capability for rapid, three–dimensional sub–surface measurement (tens of metres) within bodies of water from airborne, surface or sub–surface platforms. Raman scattered light from vibrational transitions of water have temperature dependent properties which may be exploited for temperature determination.

In order to achieve these goals, a detailed laboratory study of the polarised and unpolarised Raman spectra of water was conducted. This identified spectral features and measurement parameters which gave the greatest temperature determination accuracy.

Multiple linear regression was employed to combine these parameters in models for determination of water temperature. An assessment was made of the temperature accuracy which might be expected for practical sensing using these parameters. Raman spectra of samples from natural water sources were analysed to assess the effect of water constitution on temperature determination accuracy and the application of baseline correction to improve this. The effect of changing both temperature and salinity on Raman spectra was examined using multivariate analysis, and the potential measurement accuracy of both quantities was determined. Configurations for simple multi–channel sensing instruments were designed based on the Raman temperature and salinity determination methods investigated, and these will be evaluated in future field studies.

Table of Contents

Declaration iii
Acknowledgments v
Abstract vii
Table of Contents ix
List of Acronyms/Abbreviations xiii
1 Introduction 1
1.1 Physical and Optical Properties of Water 2
1.1.1 Physical Properties 3
1.1.2 Refractive Index 4
1.1.3 Optical Absorption 4
1.1.4 Fluorescence 5
1.1.5 Elastic Scattering 6
1.1.6 Inelastic Scattering 7
1.2 Raman Spectroscopy 10
1.3 Raman Spectra of Water 13
1.4 Temperature Determination from Raman Spectra 16
1.4.1 "Two-Colour" Method 16
1.4.2 Depolarisation Ratio Method 18
1.5 Past Research 19
1.5.1 Raman determination of ocean water temperature 19
1.5.2 Raman measurement of water temperature for other applications 23
1.6 Thesis Context and Outline 24
2 Experimental and Analysis Methods 29
2.1 Spectrometers and Spectrophotometers 29
2.2 Water Sample Cells 32
2.3 Water Samples 33
2.4 Temperature and Salinity Measurement 35
2.5 Pre–processing of Raman Spectra 36
2.5.1 Smoothing 36
2.5.2 Baseline Correction 36
2.5.3 Normalisation 37
2.5.4 Derivatives 38

2.6 Multivariate Analysis Techniques 38
2.6.1 Multiple Linear Regression (MLR) 39
2.6.2 Principal Component Analysis (PCA) 39
2.6.3 Principal Component Regression (PCR) 41
2.6.4 Partial Least Squares Regression (PLS–R) 42
2.7 Multivariate Analysis with The Unscrambler 43
2.8 Numerical Analysis with Matlab 43

3 Raman Spectroscopy of Laboratory Water 45

3.1 Experimental Approach 46
3.2 Temperature dependence of Raman spectra for RO water samples 47
3.2.1 Temperature Dependence of Unpolarised Raman Spectra 47
3.2.2 Temperature dependence of polarised Raman spectra 50
3.3 Determining temperature from Raman spectra 52
3.3.1 "Two–colour" Method with unpolarised Raman spectra 52
3.3.2 Two–colour ratio with parallel polarised spectra 58
3.3.3 Depolarisation Ratio Method 59
3.4 Predictive models for determining water temperature from Raman spectra 61
3.4.1 Two–colour ratio 62
3.4.2 Depolarisation ratio 65
3.4.3 Linear combination of spectral parameters 67
3.5 Proposed designs for multi–channel spectrometers 69
3.6 Discussion and Summary 73

4 Raman Spectra of Natural Water Samples 75

4.1 Sample Collection and Analysis Methods 75
4.2 Raman spectra and numerical analysis for natural water samples 76
4.3 Origins and implications of baseline variation 98
4.3.1 Fluorescence 98
4.3.2 Broad fluorescence and elastic scattering 100
4.3.3 Implications of baseline for temperature determination 101
4.4 Assessment of temperature determination accuracy 102
4.4.1 Baseline Correction 102
4.4.2 Two–Colour Method 103
4.4.3 Depolarisation Ratio 105
4.4.4 Combination of parameters with multiple linear regression 107
4.5 Site specificity of predictive models 107
4.6 Proposed design for multi–channel sensing system 108
4.7 Discussion and summary 109

5 Temperature–Salinity Analysis 113

5.1 Experimental Methods 114
5.2 Examination of Raman Spectra 116
5.2.1 Unpolarised Raman Spectra 116
5.2.2 Parallel Polarised Spectra 117
5.2.3 Perpendicular Polarised Spectra 119
5.2.4 Depolarisation Ratio 120
5.3 Multivariate Analysis of Raman spectra 121
5.3.1 Multivariate Analysis – Unpolarised Spectra 121
5.3.2 Multivariate Analysis – Parallel polarised spectra 127
5.3.3 Multivariate Analysis – Perpendicular polarised spectra 129
5.3.4 Multivariate Analysis – Depolarisation Ratio 130
5.4 Effect of parameter variation on measurement accuracy 131
5.5 Proposed design of multi–channel sensing system 134
5.6 Discussion and Summary 135

6 Conclusions and Future Outlook 137

6.1 Research Outcomes 138
6.2 Future Outlook 140

Bibliography 143

Appendices 153

Appendix A 154
Appendix B 177
Appendix C 178
Appendix D 190
Appendix E 198
Appendix F 205

List of Acronyms/Abbreviations

CW – Continuous–Wave

CCD – Charge–Coupled Device

FWHM – Full Width Half Maximum

LIDAR – Light Detection and Ranging

MLR – Multiple Linear Regression

Nd:YAG – Neodymium doped Yttrium Aluminium Garnet (laser gain material)

PCA – Principal Component Analysis

PCR – Principal Component Regression

PLS–R – Partial Least Squares – Regression

PMT – Photo–Multiplier Tube

PSU – Practical Salinity Unit

RMSE – Root Mean Square Error

TEC – Thermo–Electric Cooling

IMOS – Integrated Marine Observing System

HOD – Chemical formula for deuterated water (Hydrogen Oxygen Deuterium)

1 Introduction

Water is perhaps the most important substance on Earth for the existence of plant and animal life. The Earth's climate and weather patterns are largely regulated by the oceans, which retain the heat required to maintain the planet's surface at liveable temperatures.

The measurement of water temperature, both at and below the surface in bodies of water, is of great importance in fields including various branches of oceanography (such as ocean chemistry, marine biology), hydrologic modelling, atmospheric science, marine engineering and climate change research. While sea surface temperature can be readily obtained by satellite sensing methods, subsurface measurements are currently limited to suspended cables carrying either thermocouple arrays or optical fibre sensors, or expendable probes dropped from surface vessels. Sensor networks of drifting or fixed buoys such as Argo or IMOS (Integrated Marine Observing System) provide substantial data [1, 2], but provide no ability to quickly profile temperature over a specific area for the upper regions of the water column (tens of metres range).

Very few remote sensing methods exist which can conceivably fill this niche. Water is effectively opaque to the vast majority of the electromagnetic spectrum. The visible region of the spectrum has a high transmission window in water, which offers a means of propagating signals through useful water depths. An optical, depth resolved temperature sensing solution would provide a capability for rapid, three dimensional sub–surface measurement (with depths of metres to tens of metres) within bodies of water from a surface vessel, aircraft or fixed monitoring station. Optical techniques which may be suitable for this purpose include active remote sensing of Brillouin scattered or Raman scattered radiation. The Raman spectrum

of liquid water has been demonstrated to have significant temperature dependence, and it is this behaviour which we investigate here for potential in remote sensing of water temperature.

Substantial challenges exist which must be overcome if such a remote sensing system is to be realised. Natural water is inherently variable, in its composition, optical properties and background irradiance, and this variability can interfere with Raman–based remote sensing. Raman scattering in water is relatively weak, and can be impacted by ambient light or laser induced fluorescence, particularly in the yellow/red wavelength region of the spectrum.

The aim of the research presented in this thesis, and additional research to explore the practicality of implementing the key findings, is to develop methods leading to rapid, depth–resolved remote sensing of water temperature using Raman spectroscopy and LIDAR (LIght Detection And Ranging) techniques, and to explore the potential to incorporate measurement of salinity. A few studies have been conducted in this area, though only rarely was any attempt made to acquire temperature at multiple depths. This thesis covers the laboratory studies of fresh and salt water conducted towards these goals, and an assessment of the potential measurement capability of temperature and salinity which might be achieved.

This chapter briefly reviews the optical properties of water, Raman spectroscopy and previous research which aimed to determine water temperature using Raman spectroscopy. The thesis work is then placed in the context of previous work, and an outline of the thesis is provided.

1.1 Physical and Optical Properties of Water

Water is the most abundant substance on the Earth's surface. It is fundamental to the existence and survival of living organisms, and it is heavily involved in virtually all natural phenomena, from weather conditions to the structure and composition of natural terrain. Liquid water exists in the form of many dynamically changing, hydrogen–bonded clusters of H_2O molecules. Bonds are continuously created and destroyed, existing in an equilibrium affected by temperature, pressure and other conditions [3]. Substantial research has gone into explaining the behaviour of water, though with limited success in contributing new

knowledge on the subject. A quote from science writer Phillip Ball states "no one really understands water" [4], and this continues to be the case.

The optical properties of artificially pure and natural water (both fresh and seawater) have been widely studied. Measuring and understanding these properties has been a significant and active field of research, both generally and with a view to practical applications [5, 6]. Optical properties of interest include refractive index, absorption, fluorescence and scattering.

1.1.1 Physical Properties

Table 1.1 contrasts values for physical properties of pure water and sea water at standard ambient temperature and pressure (25 °C and 100 kPa).

	Pure water	Sea water
Specific electrical conductivity (S/m)	~5.5×10^{-6}	5.32
Density (kgm^{-3})	997.0	1023.3
Specific heat capacity ($J\ kg^{-1}\ K^{-1}$)	4186	3998
Freezing point (°C)	0.0 (under normal conditions)	-1.91
Boiling point (°C)	99.98	100.56

Table 1.1 – Physical properties of pure water (25 °C, 100 kPa) and sea water (35 ppt, 25 °C, 100 kPa) [7-9].

The various salts found in sea water produce substantially greater electrical conductivity compared with pure water (approximately six orders of magnitude). Density is slightly higher for seawater, while the specific heat capacity is lower. The freezing point of sea water is well below 0 °C, while the boiling point is slightly higher than that of pure water.

Many properties of water are anomalous in comparison with other compounds at temperatures and pressures which occur naturally on Earth. The maximum density of pure water occurs at approximately 4 °C [10], as opposed to being at or below the freezing point. This is due to the rearrangement of water bonding at low temperatures leading to phase transition to ice. The structure of ice is intrinsically less dense than closely packed clusters or chains of water molecules. The specific heat capacity of water is extremely high due to the storage of energy in the vibrational states of hydrogen bonds [11].

1.1.2 Refractive Index

The refractive index of a medium describes the relationship between the speed of light travelling in a vacuum and the speed observed when travelling within the medium. It is dependent upon frequency and polarisation, as well as physical properties including material structure, temperature and pressure.

Hale et al. reviewed and collated extensive published data for the refractive index of water [12]. More recently, Daimon and Masumura made careful measurements of the absolute refractive index of water. The data they obtained showed good agreement with the dispersion formula of Harvey et al. in the visible wavelength region [13, 14]. The refractive index of pure water is 1.334 at 25 °C and atmospheric pressure for 532 nm radiation. Ocean water, with a salinity of 35 ppt (the approximate average of the world's oceans) has a slightly higher refractive index value of 1.34 [15].

Refractive index values for water vary slightly with wavelength through the visible spectrum. At ~400-420 nm at the same temperature and pressure conditions as above the value is 1.34, while it remains effectively constant at 1.33 from 420-700 nm for the purposes of calculation. The refractive index of water is reduced by increasing temperature and increases with increasing pressure.

1.1.3 Optical Absorption

The optical absorption spectrum of pure water has a strong transmission band from the UV to near–infrared wavelengths (~0.2-1.3 μm). Studies of absorption in pure water are difficult in the blue–green spectral region (~400-550 nm) where absorption is extremely low. Many groups have made such measurements, and values can vary substantially [15-21].

The loss in intensity experienced by light propagating in natural water consists of both absorption and scattering effects and this total loss is commonly termed attenuation. In ocean water, attenuation is often dominated by scattering (predominantly elastic scattering, which is described in Section 1.1.5). Light attenuation can be described by the diffuse attenuation coefficient which has the same units as absorption (m^{-1}). Thus it is similar to, or slightly higher than the corresponding absorption coefficient for very clear ocean water. A correlated parameter is often used, the attenuation length, which is the inverse of the diffuse attenuation coefficient and represents the distance light must travel through water

for the intensity to be reduced to 1/*e* of its initial intensity. The attenuation length can be considered somewhat representative of water quality.

Figure 1.1 shows the absorption coefficient data for pure water and diffuse attenuation coefficient data for clear ocean water over the visible region of the spectrum. The figure was generated from data published by Pope et al. and Smith et al. [17, 21]. Minimum absorption occurs at approximately 420 nm (4.5×10^{-3} m^{-1}), with values below 0.1 m^{-1} observed at wavelengths from 380 to 580 nm [19, 21]. Clean ocean water has marginally higher absorption and scattering in contrast with pure fresh water due to very low level organic matter and particulate content.

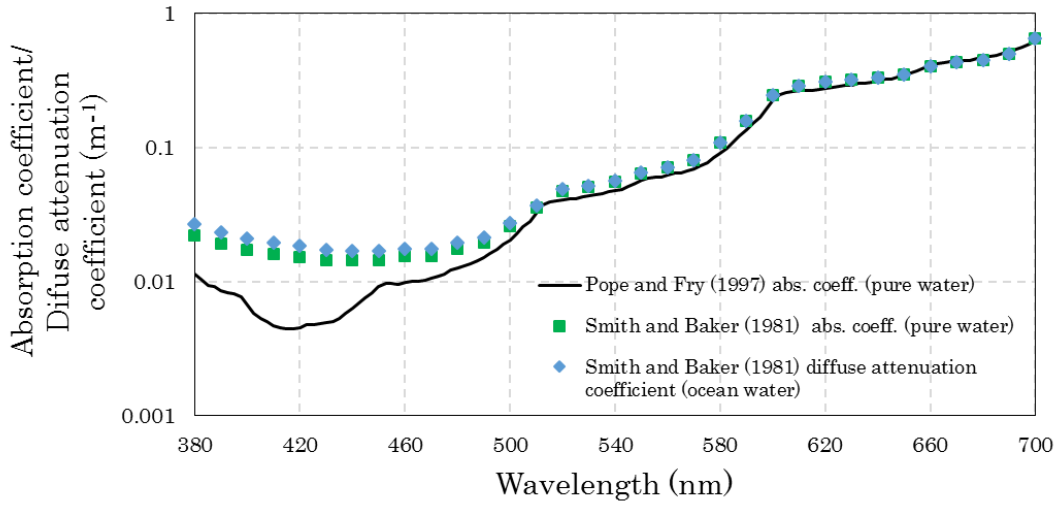

Figure 1.1 – Absorption and attenuation coefficients of pure water and clean ocean water [17, 21].

The constituents of natural waters include dissolved organic matter, organisms and particulates, and these can have a significant impact on the value of the diffuse attenuation coefficient. The optical properties of natural water also vary substantially with depth, location, currents and tides. This variability of fundamental properties is one of the fundamental issues which restrict the development of optical techniques to remotely sense ocean properties. The quality of ocean water is often divided into categories based on measurements of diffuse attenuation coefficient; these are known as Jerlov water types [5, 6].

1.1.4 Fluorescence

Fluorescence is a consequence of the absorption of light by a molecule transferring an electron to a higher energy “excited” state. The excited state can

decay by some radiative or non–radiative process or a combination of both, depending on the molecular structure. The product of such radiative decay is termed fluorescence and generally has lower energy than the excitation photon. Ultraviolet (UV) sources are conventionally used in applications such as fluorescence spectroscopy for this reason. The time taken for the population of the excited state to decay (to 1/e of initial value) is referred to as the "lifetime" of the interaction. This time is unique for every fluorescence process and is often used to identify specific substances.

Liquid water itself has no significant fluorescence response in the visible portion of the spectrum [19]. Organic constituents in natural water are responsible for the majority of fluorescence observed. Chlorophyll contained within phytoplankton (such as algae) in both and fresh and salt water produce substantial fluorescence in the visible wavelength range, particularly red wavelengths (approximately 600-720 nm) [22]. Dissolved organic matter (DOM) is responsible for a broad fluorescence peak in the yellow region (~550 nm). Remote sensing systems involving detection of visible light require careful consideration of fluorescence effects. For example, the Raman scattered return for 532 nm excitation is centred at ~650 nm, and thus may be impacted by fluorescence from organic matter.

1.1.5 Elastic Scattering

Light can be elastically scattered both by water molecules directly, or by the various constituents found in natural water.

Elastic scattering by water itself consists of what is commonly described as Rayleigh scattering, but is also termed Einstein–Smoluchowski scattering or "fluctuation" scattering [23]. Rayleigh scattering is the scattering of a photon incident upon a molecule or a small particle (scatterer diameter $<< \lambda$) without a net change in energy [24]. This can be interpreted as direct interaction with molecules or scattering from local density fluctuations, with either interpretation producing very similar results. A photon transfers its energy to the molecule in question, raising the molecule from its ground energy state to a virtual energy level. The molecule can then relax back to the original energy state, emitting a photon with the same energy (frequency) as the initial photon. Equation 1.1 describes Rayleigh scattered intensity of unpolarised light with incident intensity I_0 and wavelength λ from a group of scattering particles or molecules:

$$I = I_0 \frac{8\pi^4 N\alpha^2}{\lambda^4 r^2}(1 + \cos^2\theta) \quad 1.1$$

where N is the number of scatterers, r is the distance from the molecule to the measurement location, α is the molecular polarisability and θ is the angle between incident and scattered light. Elastic water scattering is of particular concern in systems involving detection of Raman signals. It is a stronger effect compared with spontaneous Raman scattering (by roughly an order of magnitude in water), and can saturate sensitive detectors, overwhelming the weaker Raman signal. It is therefore important to reject elastically scattered light from any Raman system. This is generally done with optical filters, usually with a combination of two or more to ensure maximum rejection of elastic scattering while efficiently transmitting the Raman signal.

Scattering interactions with larger particles are generally described with the Mie theory (and is sometimes referred to as Mie scattering). This is most often applied to particles having diameters similar to or greater than the incident photon wavelength. This type of scattering is strongly directional, with the majority of scattered radiation continuing in the direction of incident light propagation [24].

1.1.6 Inelastic Scattering

Inelastic optical scattering involves a net change in energy between incident and scattered photons. The two main inelastic scattering processes are Brillouin and Raman scattering [25, 26].

Brillouin scattering involves the scattering of photons from local fluctuations in the dielectric constant of media (i.e. acoustic phonons). This process results in Doppler shifting of a small proportion of scattered photons. Frequency shifts for Brillouin scattered radiation in water are generally very small, ranging from 4-10 GHz over the visible region. Spontaneous Brillouin scattering has been investigated as a means for remote measurement of the velocity of sound and temperature in water [27-29].

Raman scattering involves the interaction of a photon with an optical phonon, with a net transfer of energy to or from vibrational, rotational or electronic energy states of a molecule or lattice structure. It is a relatively weak phenomenon, first observed experimentally by Raman and Krishnan in 1928 [30]. The description which follows is restricted to vibrational Raman scattering.

In a Raman scattering event, an incident photon with energy ν_0 interacts with a molecular dipole, and a photon is scattered with frequency $\nu_0 \pm \nu_m$, where ν_m is the frequency of a vibrational mode of the molecule. When the scattered photon has a lower frequency than the incident photon $(\nu_0 - \nu_m)$ this is referred to as a Stokes Raman shift. When the emitted photon is of higher energy $(\nu_0 + \nu_m)$ this is termed an anti–Stokes Raman shift. All Raman scattering processes referred to in the results chapters of this thesis are Stokes shifted. The energy transitions of Rayleigh and vibrational Raman scattering events are illustrated in Figure 1.2.

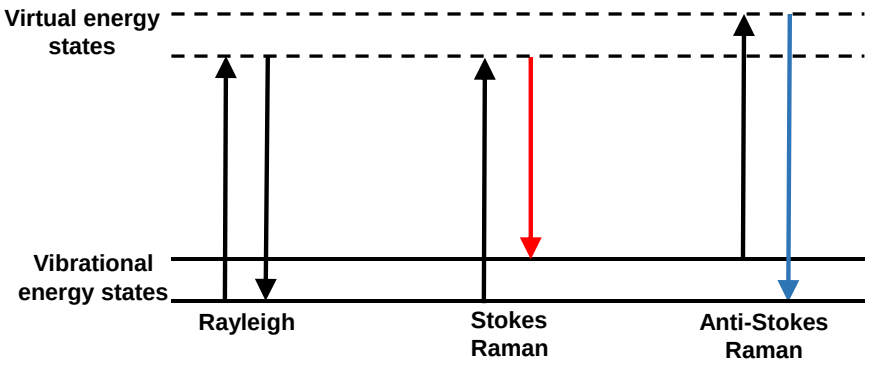

Figure 1.2 – Energy transitions involved in Rayleigh and Raman scattering events.

The Raman shift (the difference in energy between incident and Raman scattered photons) is constant for specific vibrational modes. The difference in photon energy is defined by the allowed vibrational energy levels of the molecule (and hence its physical structure) and so is identical for a specific molecule, regardless of the properties of the excitation source. Consequently, the observed Raman spectrum is unique to the molecule in question. Raman spectroscopy is widely employed as a chemical identification technique for this reason. Raman spectra are generally displayed in units of inverse centimetres (cm^{-1}) which refer to the observed Raman shifts of the species under analysis and are independent of the excitation wavelength.

In order for a vibrational mode of the molecule in question to be Raman–active, i.e. to produce Raman scattered radiation, it must have a net change in polarisability during a vibration [31]. In the case of the water molecule, the three vibrational modes are Raman–active. Figure 1.3 shows the fundamental vibrational modes of a free water molecule.

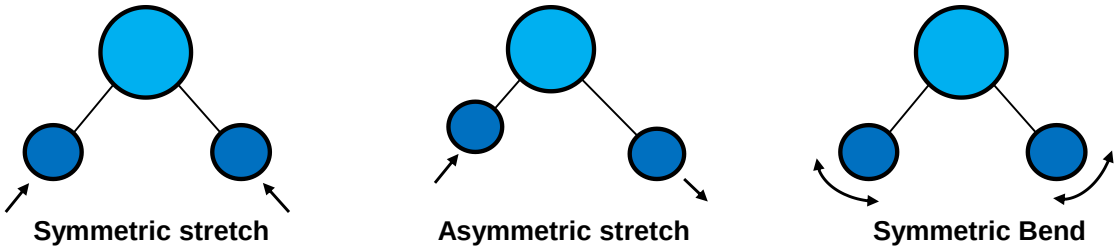

Figure 1.3 - Vibrational modes of a free H_2O molecule.

Raman scattering of a single molecule can be described in terms of an empirically–determined Raman cross–section (σ), which is expressed in units of $cm^2 molecule^{-1}$. This parameter relates the probability of Raman scattering occurring from the interaction of an incident photon with a particular molecular energy state [32]. The Raman scattered intensity for a laser–excited vibrational mode can be written as:

$$I = I_0 \sigma N_D dz \qquad 1.2$$

where I_0 is the laser intensity, N_D is the number density of molecules per unit volume and dz is the interaction length (path length in the sample or spectrometer depth of field) [32]. The Raman cross–section includes scattering over the full solid angle of 4π steradians from the water volume in question. A more practically useful parameter is the differential Raman cross–section $d\sigma/d\Omega$, ($cm^2 sr^{-1} molecule^{-1}$) which includes only the solid angle component over which scattering will be detected.

The Raman scattering equations presented thus far are scalar expressions. In reality, polarisation and other properties of light play a role and must be taken into account using vector analysis. The intensity of Raman emissions can then be calculated in terms of incident and scattered polarisation states [33]. This allows calculation of theoretical depolarisation ratios for Raman transitions.

The intensity of Stokes–shifted Raman emission polarised in direction ρ and excited by a laser polarised in direction φ [34, 35] can be expressed as:

$$I_R(\rho) = I_0(\varphi) \frac{2\pi^2 (\nu_0 - \nu_m)^4 h N_e}{\mu c^4 \nu_m [1 - e^{(-h\nu_m/KT)}]} \frac{\partial \alpha_{\varphi\rho}}{\partial q_m} \qquad 1.3$$

where N_e is the effective number of illuminated molecules, $\alpha_{\varphi\rho}$ is the averaged φρ component of the molecular polarisability tensor and q_m is the normal vibrational coordinate of the molecule at equilibrium.

Raman emission lines can be strongly polarised for molecule vibrational modes which are totally symmetric and the incident light is polarised. The

symmetric stretching vibration of the water molecule in Figure 1.3 produces highly polarised emissions under laser excitation.

The differential Raman cross–section for pure water has been theoretically calculated and experimentally measured by multiple research groups. The majority of studies obtained values which were defined for 488 nm excitation and a 90° detection geometry (relative to the incident light). Values obtained in some studies ranged as high as 20×10^{-30} to 45×10^{-30} $cm^2sr^{-1}molecule^{-1}$ [36, 37], although the majority of values were between 8.1×10^{-30} and 9.0×10^{-30} $cm^2sr^{-1}molecule^{-1}$ [38-40].

An absolute Raman scattering coefficient for water, b_r may also be obtained which has units of reciprocal length (m^{-1}). This parameter provides the number of scattered photons per unit length travelled through the scattering medium by incident light. It is related to the Raman cross–sections described above in the form:

$$b_r = N_D \int_{4\pi} \left(\frac{d\sigma}{d\Omega}\right) d\Omega = N_D \sigma \qquad 1.4$$

The commonly accepted value of b_r for pure water with 488 nm excitation is 2.6×10^{-4} m^{-1} from measurements by Marshall and Smith [40]. This has been verified by other groups as empirically correct within experimental error for both pure water and very clear ocean water [38, 41]. By contrast, the absolute elastic scattering coefficient for pure seawater at 488 nm is ~$2.5 \times 10^{-3} m^{-1}$, approximately an order of magnitude greater [42].

1.2 Raman Spectroscopy

Spectroscopy is the study of interactions between light and matter, including reflection, scattering, absorption and luminescence. By analysing these phenomena, information concerning the physical or optical properties of a sample can be determined. The field of Raman spectroscopy deals specifically with the measurement and analysis of Raman scattered radiation from a sample of interest. This tends to involve UV and visible excitation, as Raman scattering exhibits a λ^{-4} wavelength dependence (shown in Equation 1.1), and thus occurs more frequently at shorter excitation wavelengths. In addition, this means the required detection bandwidth for anti–Stokes and Stokes Raman scattering with visible excitation will generally fall within the UV and visible wavelength regions respectively.

Early use of Raman spectroscopic methods involved the use of lamps (typically mercury) for excitation and photographic plates for detection, allowing only limited observation of broad spectral features. The development of technologies including cascading photodetectors (such as photomultipliers), holographic gratings and lasers enabled the resolution of narrow rotational, vibrational and electronic transitions, leading to the modern instruments now in use. Today, Raman spectroscopy is widely employed in fields including drug and explosive detection, pharmaceuticals, geology, semiconductor development and medicine. The major reason for this widespread use is the reliability with which chemical species can be identified. Mixtures of compounds can be analysed to determine composition and the relative concentration of Raman–active species.

Conventional Raman spectroscopy is based on detection of spontaneous Stokes Raman scattering. Similar information can be obtained from anti–Stokes emission lines, though signals are substantially weaker. Other methods exist which employ different aspects of Raman scattering to make measurements of samples. Common examples include CARS (Coherent Anti–Stokes Raman Spectroscopy), SERS (Surface Enhanced Raman Spectroscopy), RRS (Resonance Raman Spectroscopy) and TRRS (Time–Resolved Raman Spectroscopy) [43-46] amongst many others.

A dispersive Raman spectrometer consists of an excitation source (generally a laser), focusing and collection optics, a detector and a means of wavelength selectivity (generally a scanning monochromator). Strong rejection of light at the laser wavelength is important to ensure detection of weak Raman features. A generic example of this type of spectrometer is shown in Figure 1.4.

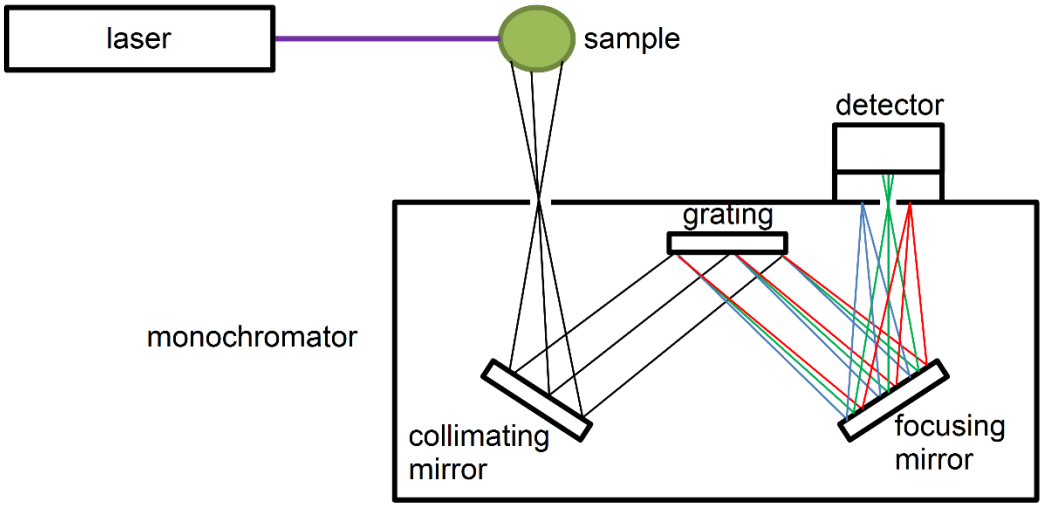

Figure 1.4 – Schematic of a simple dispersive Raman spectrometer with a single stage monochromator.

The grating in Figure 1.4 is either rotated in order to scan light of varying wavelength over the detector aperture for PMT detection, or it is fixed and the entire spectrum dispersed over a cooled CCD, the usual scheme in modern instruments. The width of the monochromator entrance and exit apertures define the wavelength resolution, wavelength range and signal intensity of the spectrometer. A long pass filter and a second monochromator stage are common additions to improve signal to noise ratio. Modern dispersive instruments are most often designed for collinear operation (180° backscattering) and integrated with an optical microscope, with both excitation light and the Raman signal propagating through the microscope optical train. This allows for accurate selection of a target location on a sample (~1 μm accuracy), or alignment with and measurement of small samples. The signal to noise ratio of a dispersive Raman spectrometer can be improved by increasing the excitation intensity, increasing the exposure time (the time over which the grating scans the full spectral range), or by reducing the noise floor of the detector.

Fourier Transform Raman (FT–Raman) is an alternative option to dispersive spectrometers for certain applications. It is based around a Michelson interferometer configuration, with a varying path difference to produce a coherence profile at the detector. The detected time varying signal is then Fourier transformed to generate a frequency spectrum.

FT–Raman has different advantages and disadvantages compared with dispersive devices. Advantages of FT–Raman instruments include superior spectral resolution and freedom from fluorescence interference (fluorescence is incoherent). On the other hand, excitation is limited to longer wavelength laser sources (1064 nm

is a common excitation wavelength), spatial resolution is limited due to the interferometric nature of the method, and instruments cannot be miniaturised for the same reason. The use of near infrared excitation also has the effect of significantly reducing the incidence of Raman scattering relative to UV or visible excitation. At present FT–Raman is primarily used for routine measurements in industry. Dispersive spectrometers are far more widely used in research, particularly where UV or visible wavelength excitation is required.

The key requirements of a Raman spectrometer are: high sensitivity, appropriate wavelength range and adequate resolution to sufficiently resolve those spectral features which are of interest. Depending upon the application, the cut–off frequency of laser/Rayleigh scattering rejection for the instrument may be of importance. Crystalline solids and glasses in particular exhibit features at very low Raman shifts. High–end spectrometers may allow resolution of features within a few wavenumbers of the laser line, though most commercial instruments provide a cut–off frequency in the range 30-250 cm^{-1}.

1.3 Raman Spectra of Water

The Raman scattered spectrum of liquid water has a complex structure comprising intermolecular vibrations, intermolecular librations, molecular vibrational bending and stretching modes, as well as various overtones and frequency mixing terms. Figure 1.5 shows a 180° backscattered, unpolarised Raman spectrum of liquid water at 25 °C collected by the author.

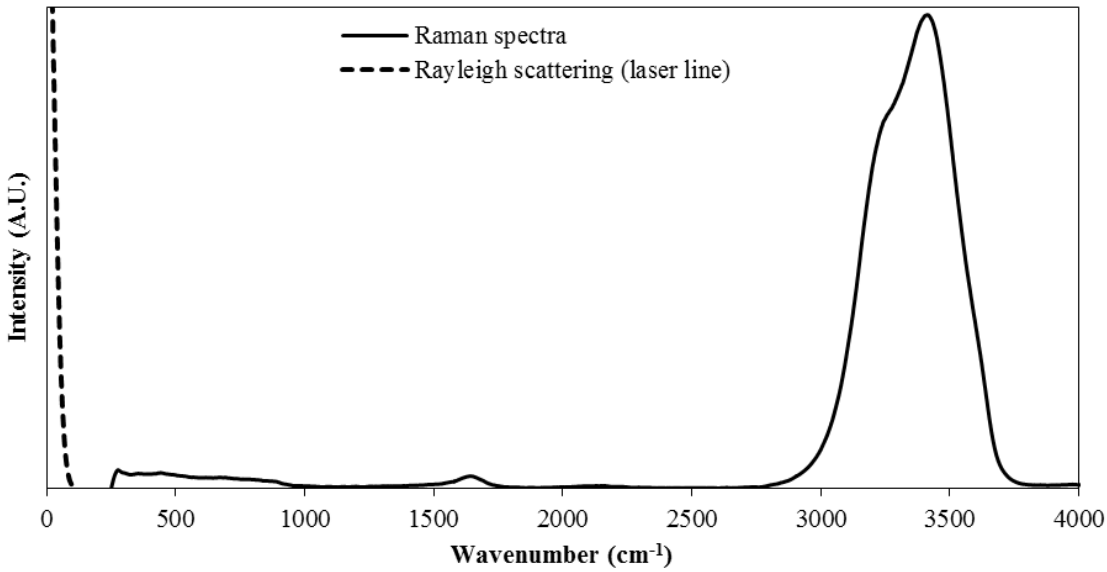

Figure 1.5 – Unpolarised Raman spectra of near-pure liquid water. The spectrum edge at 250 cm^{-1} represents the cut–off frequency of the spectrometer.

The components of the water Raman spectrum are shown in Table 1.2.

Emission range	Description
0-1000 cm^{-1}	Intermolecular vibrations and librations
1600-1700 cm^{-1}	H_2O bending mode (centred at 1650 cm^{-1})
2000-2300 cm^{-1}	Overtones/combinations of intermolecular vibrations.
2800-3800 cm^{-1}	OH stretching peak comprising multiple overlapping bands.
3900-4200 cm^{-1}	Overtones/combinations of intermolecular vibrations.

Table 1.2 – Band assignments for unpolarised water Raman emission [3, 47, 48].

The OH stretching emission peak (2800-3800 cm^{-1}) consists of up to 5 vibrational modes (depending on environmental conditions) which show similar vibrational frequencies to the theoretical predictions for an isolated water molecule [31], but arise from OH bonds within clusters or chains of hydrogen–bonded water molecules. It is noteworthy that the interpretation of Raman spectra in relation to the molecular structure of water remains contentious [49, 50].

Analysis of water Raman spectra has been the focus of substantial research, both for the purpose of understanding its structure and bonding, and interpreting waters unusual physical properties [48, 51-58]. The behaviour of the Raman spectrum in response to a variety of physical and chemical changes has also been heavily studied, [47, 59-65]. These studies included temperature, pressure, salinity and a variety of other solutes. The OH stretching band has been frequently studied as part of investigations into water bonding behaviour, often also examining heavy

water (D_20) and HOD (Hydrogen Oxygen Deuterium), which have different characteristics [66, 67].

The Raman spectra of liquid water exhibit temperature–dependent behaviour. This behaviour has been documented by multiple research groups [3, 49, 55, 56, 60]. Water Raman spectra also vary in response to changes in salinity, pressure and other parameters [61, 68-70]. The basis for this behaviour is not well understood, but may be due to changes in the relative energy of hydrogen bonds as temperature changes. The effects are observed with salinity variation, are at least partially caused by the bonding of various salt ions into the water structure, thereby altering vibrational frequencies.

This temperature dependence is primarily observed in the OH stretching band. Figure 1.6 displays backscattered polarised and unpolarised Raman spectra of laboratory water (RO filtered) acquired using CW polarised excitation at 532 nm. The Raman spectra are shown in terms of emission wavelength (nm) as opposed to the Raman shift frequency (cm^{-1}) in order to illustrate the red wavelength range of the stretching band with 532 nm excitation (the excitation wavelength employed in the majority of experimental work described in this thesis). The unpolarised spectra are the sum of the parallel and perpendicular polarised spectra (with losses due to polarising filters).

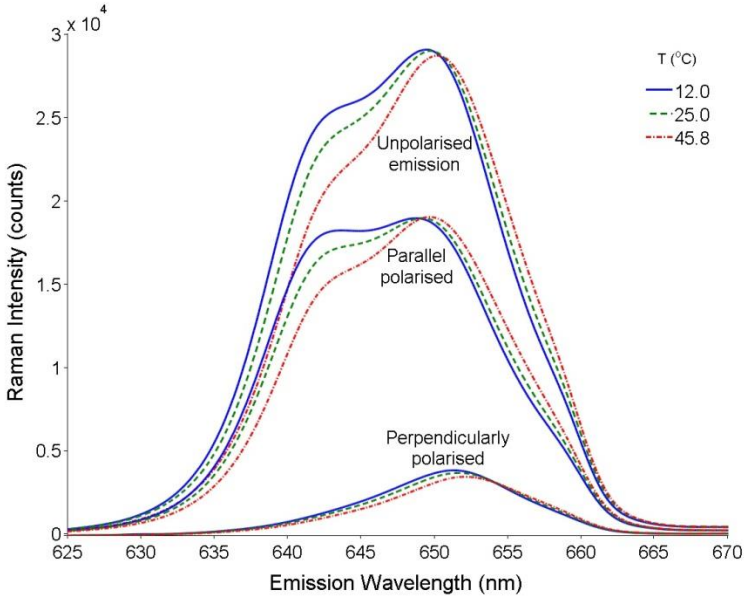

Figure 1.6 – Linearly polarised and unpolarised Raman OH band spectra of laboratory water for several temperatures with 532 nm excitation.

An isosbestic point (point of equal absorption or scattering) occurs near 650.5 nm (3425 cm^{-1}) for the backscattering configuration used here [63, 71]. As temperature

increases, regions below the isosbestic point decrease in intensity, while regions above the isosbestic point increase in intensity. Thus there is a net shift in the centre position of the entire stretching band towards longer Raman shifts (and wavelengths). A subtle transition is evident at ~658 nm (3650 cm^{-1}) which appears in all of the spectra is caused by stretching of free OH groups and is completely unpolarised.

The linearly polarised spectral components differ significantly from each other. The parallel polarised component (relative to polarisation of the excitation laser) shows similar behaviour to the unpolarised spectra, with a reduction in intensity at longer shifts. This reduction is due to the asymmetric stretching vibration mode (see Figure 1.3) which emits light in both polarisations (a depolarised mode). The remaining vibrational modes are symmetric and maintain the polarisation of the excitation light. The perpendicularly polarised spectra consist of the asymmetric stretching mode and free OH emission.

Past research which has examined the OH stretching band has tended to have one of two motivations. The first seeks to understand the molecular and bonding structure of water, while the second makes use of the response of the OH band to physical parameters to extract information about the state of a system. For the purposes of this research we can take advantage of the behaviour of water Raman spectra without understanding its precise origin.

1.4 Temperature Determination from Raman Spectra

Several spectral parameters evident within Raman spectra of water are dependent on temperature, and so may be used to extract temperature information from the Raman signal. A variety of techniques have been developed by different groups which produce empirical relationships between spectral parameters and water temperature.

1.4.1 "Two-Colour" Method

This simple technique involves comparing the relative intensity of backscattered light at two wavelengths, generally on either side of the isosbestic point in the OH stretching band of the water molecule. The intensities of these two

points change in opposite directions as water temperature changes. By taking a ratio of these intensity values, a parameter which varies linearly with temperature can be obtained.

The two–colour method has been most widely implemented using spectral decomposition (sometimes termed Gaussian deconvolution in literature) [69, 72-80]. The OH stretching band can be fitted with a sum of Gaussian, (or other distribution) components. It should be noted that there is no scientific basis for the use of Gaussian line shapes in fitting liquid phase Raman spectra. The combination of Raman emission with collisional broadening in liquids produces lines with a Voigt profile [81, 82]. The fitted components can be used to provide ratios for temperature calibration and measurement. The components do not necessarily correspond directly with Raman modes, but rather represent an empirical observation of the structure of the water stretching band. A near-infinite number of possible peak combinations can be found which fit the stretching band when larger numbers of fitted peaks are included (more than three). The set of peaks arrived at by fitting algorithms is heavily dependent on the starting parameters used, and thus appropriate selection of these parameters is essential to arrive at a set of peaks appropriate to build a spectral parameter with substantial temperature dependence. Figure 1.7 shows an example of decomposition of the OH stretching band into Gaussian peaks by Furić et al. [69, 83].

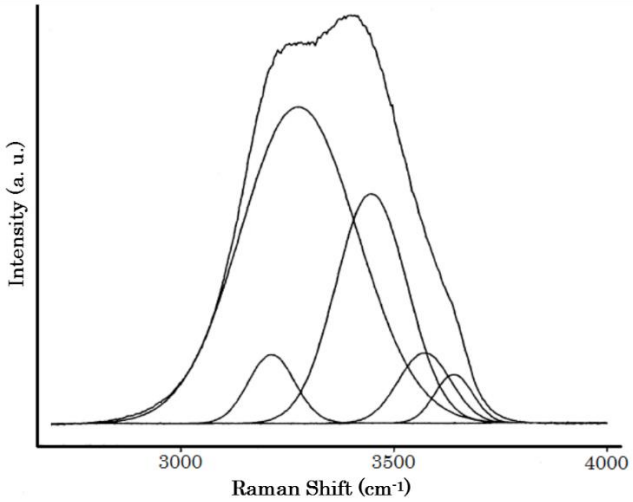

Figure 1.7 – Raman spectrum of the OH stretching band with decomposition into five Gaussian peaks [69].

The stretching band is commonly fitted with two to five components. A ratio is taken between the areas of two components which exhibit temperature dependence. Ratios of other spectral decomposition parameters such as peak

amplitudes, peak widths and centre positions, or combinations of these parameters, have also been used [72].

Challenging issues relating to the two–colour method have been highlighted by various authors. Chang et al. claimed that the spectral transmission of coastal water shows considerable spatial and temporal variability which severely limits the accuracy of this method for practical implementation [84]. Differential absorption between the wavelength channels has previously been noted as a shortcoming of the two–colour method. Absorption and fluorescence from organic matter can strongly impact on the performance of two–colour measurements, particularly where an absorption or fluorescence peak overlaps with the Raman band. James et al. examined the use of multiple excitation wavelengths to minimise this problem [85]. Spectra obtained with excitation wavelengths ranging from 510-570 nm were averaged point by point, disregarding the regions in each which were influenced by the Raman signal. This produced a reasonably consistent background signal which could be subtracted from spectra to produce near–background–free Raman spectra.

1.4.2 Depolarisation Ratio Method

Temperature dependent behaviour is also found in the depolarisation ratio of the water OH stretching band [63, 66]. The depolarisation ratio is the ratio of intensities between the perpendicularly polarised component and the parallel polarised component of Raman scattered light at a specific Raman shift or wavelength. The depolarisation ratio of the stretching band, measured at an appropriate wavelength, varies approximately linearly with changing temperature, offering another method for determining water temperature.

The depolarisation ratio method can be used with linear, circular or elliptical polarised excitation and detection. In the circularly polarised case for example, if RHCP (Right Hand Circularly Polarised) light were used for excitation, then the LHCP and RHCP Raman intensity at some wavelength may be measured and the LHCP/RHCP ratio calculated to find the depolarisation ratio. Improved temperature resolution and a larger depolarisation ratio value have been reported with circular polarisation when compared with linear polarisation measurements [84]. The depolarisation ratio method was also suggested to be better suited for practical implementation when compared with the two–colour method because it is not affected by differential attenuation effects [84, 86].

1.5 Past Research

Investigations have been conducted by numerous groups over several decades to explore the potential of Raman spectroscopy as a means to determine water temperature in laboratory and remote sensing applications. This section provides details of those studies which are most relevant to the work in this thesis.

1.5.1 Raman determination of ocean water temperature

The first suggestion and experiments indicating that Raman spectroscopy might be employed for remote water temperature determination was by Schwiesow in 1971 [87], which inspired comprehensive investigations by other groups.

Chang and Young conducted research and published technical reports concerning Raman–based water temperature determination in the early to mid–1970s. They carried out laboratory–based experiments investigating both two–colour intensity ratios and circular depolarisation ratios for temperature calibration [84, 86]. A 460 nm dye laser pumped with a pulsed nitrogen laser was used for excitation. The sensitivity of temperature dependence for the two–colour ratio parameter used was found to be approximately 1 % per °C, although no reference temperature for the calculation of this value was provided. Salinity was also examined for Raman–based remote sensing, and it was found that it could be separated from temperature in terms of spectral parameters using depolarisation ratio methods, with a sensitivity of 1 % per 3 ppt (parts per thousand) change in concentration. The investigators estimated performance capabilities for practical airborne remote sensing systems. They favoured the depolarisation method, predicting that the two–colour spectral decomposition would be too dependent upon water attenuation to be practical for coastal waters greater than 1 to 2 metres in depth [84].

Studies by Leonard et al. in the late 1970s investigated practical considerations involved in Raman–based remote sensing of ocean temperature [74, 75]. Interference and noise sources were discussed including surface waves, transmission effects (differential attenuation and depolarisation), and optical effects (laser induced fluorescence and background ambient light). Both two–colour and depolarisation ratio methods were discussed. The depolarisation ratio method was stated to be the superior option, and it was indicated that the polarisation state of

light travelling in water was mostly maintained (>80 %) over long distances (~20 attenuation lengths).

Leonard et al. also conducted ship–based field experiments with a 337.1 nm pulsed nitrogen laser and a liquid absorption cell for laser line filtering, using the two–colour method to determine temperature. They retrieved Raman spectra from several depths down to 30 metres, and made remote temperature measurements at several depths down to ~3 metres. RMS temperature error of ±1.2 °C was calculated between Raman measurements and reference temperature [74]. Each measurement was made with individual laser pulses, using adjustable detection gating to manually select a single depth at which measurements were collected. Chang, Young and Leonard also collaborated in the design of a temperature sensing system based on depolarisation ratio measurement [88]. They concluded that deep (10-100 m) Raman temperature measurement should be possible with appropriate laser wavelength selection and system design.

Collins et al. published a review in 1984 of the state of research into optical scattering methods for ocean temperature and salinity measurement [89]. This included an overview of the theoretical models for Raman scattering in water and assessment of several methods of temperature measurement including two–colour methods, linear depolarisation and circular depolarisation. The authors noted considerable systematic differences between spectral data sets produced by Leonard et al., Chang et al. and Scherer et al. [67], observing that this error would be eliminated by working with a calibrated experimental setup.

Liu et al. built a Raman LIDAR system for ocean temperature measurement in 1992 using a 532 nm laser as an excitation source [83]. Temperature calibration was performed with spectral decomposition of the OH stretching band into two Gaussians as described by Leonard et al., and temperature accuracy in laboratory experiments was ±0.4 °C. Ocean experimentation gave temperature accuracy of ±0.5 °C with measurements taken at depths of 2 to 3 metres.

Breschi et al. and Cecchi et al. conducted both laboratory and field Raman temperature experiments in the early to mid–1990s, using 514 nm excitation and employing the two–colour method with spectral decomposition [73, 77, 79]. Field experimentation used a pre–existing fluorescence LIDAR system (308 nm excitation) which had no capability for temporal resolution of spectral measurement. This meant that the Raman spectra collected, and hence the calculated temperature

values, were averaged over the accessible portion of the water column. The average temperature deviation from reference values was ±0.5 ºC.

James et al. simulated laser induced fluorescence and Raman emissions in turbid water to test background signal removal techniques and temperature extraction algorithms [85]. Visible fluorescence spectra were recorded for a range of excitation wavelengths from 510 to 570 nm. These spectra were point–by–point averaged to obtain the background fluorescence spectra with the Raman stretching band removed. This process allowed effective extraction of the Raman signal from the raw spectra. Simulated temperature measurement was then analysed with the spectral decomposition method. This method was applied by Lin in a preliminary coastal temperature measurement study, which showed substantial inaccuracies in temperature values (standard deviation >5 ºC) [90, 91]. Lin stated that residual fluorescence after the correction method is applied is an issue, and that multiple laser wavelengths are needed for coastal water measurements.

Becucci et al. investigated the accuracy of Raman–based temperature sensing in laboratory experiments [72, 92]. Spectral decomposition of the OH peak was employed for temperature calibration, and the behaviour of pulsed vs. CW (continuous wave) laser excitation at 514.5 nm for measurement of temperature and salinity was studied. Differences between pulsed and CW sources were attributed to stimulated Raman scattering from high peak power laser pulses.

Researchers at Moscow State University measured both temperature and salinity using three spectral channels from the water OH stretching band, which were used to produce several two–colour ratios [93-97]. Laboratory experiments yielded temperature and salinity average errors of ±0.7 ºC and ±1 ppt respectively. Field experiments with the method produced deviations of ±1.1 ºC and ±1.4 ppt. An expanded form of the same concept was also tested in the laboratory, which used a larger number of spectral channels, and produced errors of ±0.5 ºC and ±0.7 ppt [96]. In later studies by the group analysis of a larger range of water Raman spectra (800-4000 cm^{-1}) was performed using artificial neural network techniques for temperature and salinity extraction in artificial seawater solutions with varying amounts of dissolved organic matter (DOM) added [95]. The calculated temperature and salinity deviations were ±0.8 ºC and ±1.1 ppt. None of these studies involved depth–resolved or long–range measurement.

In 2012, Bunkin et al. developed a Raman LIDAR system (527 nm excitation) for remote sensing of various parameters in seawater, including temperature and

chlorophyll concentration [98, 99]. Signals were detected with a spectrograph and a gated intensified CCD. The group monitored the central position of a single Gaussian fit of the OH stretching band as a temperature dependent parameter. Laboratory studies produced temperature measurement accuracy of ±0.5 °C, and field experimentation gave accuracy of ±1 °C, with approximate depth resolution of 0.85 m. A variable delay between laser pulse emission and gating was used to set detection depth, and the maximum depth at which temperature could be measured was 3 metres.

Table 1.3 shows a summary of the temperature studies described here, outlining the best performance produced in both laboratory and field studies, as well as the methods of temperature determination and the laser sources used. The minimum temperature error observed in field experiments was ± 0.5 °C, which is consistent with the proposed theoretical minimum error of Chang and Young [38], while other groups observed values of ±1 °C or higher.

First Author	Year	Techniques used	Laser Source	Laboratory Temp. Error (°C)	Field Temp. Error (°C)
Chang [84, 86, 88]	1972,1975	Depol. ratio (circular)	Dye laser 460 nm	–	±0.5 (theoretical)
Leonard [74, 75]	1977,1979	Two–colour	Nitrogen 337.1 nm	±1	±1.2
Leonard [100]	1983	Depol. ratio	Dye laser 470 nm	±0.5	–
Liu [83]	1992	Two–colour w/ decomp.	Nd:YAG 532 nm	±0.4	±0.5
Breschi [77]	1992	Two–colour w/ decomp.	Argon–ion 514.5 nm	±0.5	–
Cecchi / Raimondi [73, 79]	1995,1999	Two–colour w/ decomp.	Lab: Argon–ion, 514.5 nm Field: excimer 308 nm	–	–
Becucci	1999	Two–colour w/ decomp.	Argon–ion 514.5 nm	–	–
Dolenko/Burikov/ Patsayeva [93, 94, 96]	2000,2004,2011	Two–colour	Argon–ion 514.5 nm	±0.5-0.8	±1.1
Bunkin [98]	2012	Whole band shift	Nd:YVO_4 527 nm	±0.5	±1

Table 1.3 – Summary of past research aimed at sensing of ocean temperature.

1.5.2 Raman measurement of water temperature for other applications

Pan et al. in 1984 demonstrated simple laboratory-based Raman temperature determination in pure water over a temperature range of 15 to 65 °C [101]. This was intended as a non–contact means to ascertain water temperature for general laboratory use. Calibration was performed using a two–colour intensity method. The temperature uncertainty was ±2 °C (estimated standard deviation).

Davis et al. employed Raman techniques for spatially resolved measurement of water temperature in electrophoresis capillaries [102]. The parallel polarised (relative to the laser polarisation) component of the OH stretching band was divided at the isosbestic point into "hydrogen bonded" and "non–hydrogen bonded" regions [63] and the two regions were integrated and the ratio of these values taken, effectively a variant of the two–colour method. The measured temperature accuracy was ±1 °C, with acquisition times of 2-5 minutes. Similar micro–Raman thermometry work to that of Davis et al. has been undertaken by multiple groups, with similar accuracy achieved (~±1 °C) in most cases [103-106].

Furić and Risović studied Raman measurement of temperature and salinity, and conducted laboratory experiments comparing variants of the two–colour method with spectral decomposition and Raman difference spectroscopy for calibration [69, 80]. The accuracy and linearity of measured temperature for each method were assessed. Raman difference spectroscopy involves compares entire Raman spectra (or a reasonable subset) by subtracting all spectra from a reference set of spectral data, thus employing the overall increase in the Raman shift of the OH stretching band with temperature as the measurement parameter [44]. By subtracting spectral intensity data measured at different temperatures from a reference spectrum, a temperature dependent parameter can be generated. This is similar in effect to directly taking the first derivative of the Raman spectra and produces similar features. Pure water was investigated at a temperature range from -7.5 °C (supercooled) to 32.5 °C. The two spectral decomposition techniques involved fitted Gaussian peak area ratios, and the ratio of the height–width ratios for the same Gaussian components. Temperature standard deviations from true temperature for these methods were ±1.9 °C and ±0.7 °C respectively. Raman Difference Spectroscopy was found to produce a more linear relationship between measured and reference temperature. The standard deviation of measured temperature was ±0.4 °C. The Raman difference spectroscopy method was effective, but required a large amount of

spectral information. While this technique has excellent sensitivity to temperature change, it would be impractical to implement in a ranged scenario with depth resolution due to spectral bandwidth detection requirements.

Bauer et al. examined the feasibility of Raman spectroscopy for *in vivo* remote temperature measurement in ocular tissues [107]. The group measured temperature within the aqueous humour of rabbit eyes, both *in vivo* and *ex vivo*, and found temperature accuracy ranging from 0.2 – 0.7 °C with 250 mJ of laser energy at 514.5 nm.

Pikov and Siegel used Raman microscopy to monitor temperature within water, water–based biological culture media and human cell cultures while exposed to millimetre–wave radiation (60 GHz) [108]. Two–colour spectral decomposition of the OH stretching band was used to obtain accuracy of ±1 °C.

Beier et al. used coherent anti–stokes Raman spectroscopy (CARS) to measure spatially–resolved temperature within water samples [109]. This technique was developed for laboratory study of biological samples. Temperature measurement accuracy was ±0.5 °C with diffraction–limited spatial resolution.

Table 1.4 briefly summarises the studies described above.

First Author	Year	Calibration method	Laser source	Temp. Error (°C)
Pan [101]	1984	Two–colour	Argon–ion 488nm	±2
Davis [102]	1993	Two–colour	Nd:YAG 532 nm	±1
Furić/Risović [69, 80]	2000,2005	Whole band shift	Argon–ion 514.5 nm	±0.4
Kim [105]	2006	Two–colour	Argon–ion 488 nm	±1
Pikov [108]	2010	Two–colour, Spectral decomposition	Diode 671 nm	±1
Beier [109]	2012	CARS	Ti:sapphire 780 nm	±0.5
Ewinger [103]	2013	Two–colour	Argon–ion 488 nm	±1.2
Kuriyama [104, 106]	2013	Two–colour	Nd:YAG 532 nm	±1

Table 1.4 – Summary of past research aimed at other applications.

1.6 Thesis Context and Outline

The potential for using Raman spectroscopy to determine water temperature has been established by past research. Two publications in 1984 and 2001 from

government laboratories in the USA [89] and Australia [110] reviewed the scope for practical temperature measurement, however further development towards practical remote sensing of temperature in the field has occurred only at a low level. Limited use of the general technique has been made for laboratory–based temperature sensing in specific applications.

Much of the past research in this area was constrained by the laser sources, detectors and data acquisition hardware available at the time. With the benefit of hindsight we can now identify shortcomings and considerable potential for improvement with regards to previous studies.

Laser sources used in past research were not always optimal for the experimental work undertaken. For example, several studies have used laser wavelengths which were not well suited to remote sensing of ocean water. Leonard et al. used a pulsed nitrogen laser operating at 337.1 nm for field experimentation, a wavelength with stronger absorption in water and increased scattering from particulates compared with blue–green wavelengths [33]. Laboratory studies have tended to use argon–ion lasers operating at either 488 nm or 514.5 nm. More recent field research has used frequency–doubled Neodymium laser sources with wavelengths of 527-532 nm. These wavelengths are widely employed in ocean measurements (e.g. bathymetry) as they experience near–minimum attenuation (see Figure 1.1) [74].

Pulsed laser sources at 532 nm are widely available today, and are commonly used in Raman LIDAR systems. Such sources are well suited to produce sufficiently intense Raman scattering from long path lengths in water, in addition to providing for time–of–flight ranging and hence depth resolution.

The way in which temperature measurement accuracy is specified has been somewhat inconsistent between previous studies. The use of root mean square temperature error dates back to the work of Leonard et al., and Chang and Young [74, 86]. Later research has generally supplied error values without any definition of calculation method. It is presumed that most of these are based on the maximum differences observed between predicted and reference temperature, however this gives no sense of relative temperature accuracy over multiple acquisitions. The research in this thesis employs the RMS temperature error definition as a sensible means of describing an inherently variable parameter.

Improvements in detector and data acquisition technology have been made since the earliest field research [75, 86]. Leonard et al. and Chang et al. amongst

others, used commercial photomultipliers requiring high bias voltages (several kV), to obtain maximum gain of ~10^6 and rise times of several microseconds. Today high–speed photomultipliers are readily available, which are compact and require low power inputs (tens of milliWatts), feature sub–nanosecond rise times and have internal electronics to produce the required bias voltage for amplification. PC–based or self–contained oscilloscopes were used for data acquisition, digitisation and data storage. The capability of these instruments has come a long way in the last few decades, with sample rates of multiple gigasamples per second readily available, and high bandwidths far in excess of the requirements for fast photodetectors.

Complementary techniques and technologies exist which could conceivably be employed in parallel with Raman temperature sensing. Airborne laser bathymetry is in active use world–wide for depth sounding in coastal waters. The systems involved require similar laser characteristics to those used for Raman sensing (532 nm pulsed laser source for bottom reflectance measurement) and they could conceivably be implemented simultaneously. Measurement of other parameters could also be implemented as extensions to a Raman sensing system, including salinity, phytoplankton and/or dissolved organic matter concentration and the presence of oil (and oil layer thickness) or other pollutants.

This thesis addresses the key aspects of sensing water temperature (primary goal) and salinity (secondary goal). Specifically, it contains experimental investigations and numerical analysis of laser–induced Raman scattering in water focused on our eventual goal of implementing rapid, depth–resolved measurement of water temperature and salinity in natural waters.

Chapter 2 outlines the equipment and the experimental and numerical methods employed in the course of this research. Chapter 3 contains a comprehensive analysis of Raman scattering in laboratory water samples, the response to changes in water temperature and how that response may be best exploited for quantification of temperature from Raman spectra. Chapter 4 exhibits the Raman spectra of a variety of natural water samples, both fresh and seawater, and explores how these samples differ from laboratory water (reverse osmosis filtered). Baseline correction is used to compensate for fluorescent background signals, and the accuracy of temperature determination is assessed. In Chapter 5, the potential for simultaneous measurement of water temperature and salinity is explored. Multivariate analysis methods are applied to interpret the changes in Raman spectra in response to changing temperature and salinity, and to develop a

suitable scheme for collection of both temperature and salinity from Raman spectra. The extent to which salinity variations in water might adversely impact the accuracy of temperature determination is also analysed. Chapter 6 presents the conclusions drawn from this research, and describes further work which is planned towards our goal of practical remote sensing of water temperature. Appendices are then presented which include publications of work related to this research, full specifications of key equipment, tabulated experimental data and examples of Matlab code written to analyse spectral data. Appendix D provides brief descriptions of remote sensing experiments conducted in parallel with the work presented in this thesis. These include laboratory studies for ranged acquisition of Raman signals, analytic and numerical modelling of remote sensing retrieval of Raman scattered light, and preliminary field experimentation with prototype sensing system configurations which have been conducted.

2 Experimental and Analysis Methods

A wide variety of experimental techniques, equipment and materials were employed in the course of the experimentation undertaken in this research. This chapter provides general information concerning these topics, leaving details specific to particular experiments to appropriate later chapters. Topics covered here include: Raman spectroscopy, water sample selection and collection, the capabilities of both commercial and custom–built equipment used, and analysis and simulation techniques.

2.1 Spectrometers and Spectrophotometers

In this research, the Raman spectra of liquid water samples were examined for subtle changes in response to changes in temperature and/or salinity over a large spectral range. Raman scattering in water is relatively weak (compared with Rayleigh scattering or Raman scattering from other Raman–active molecules), and hence good sensitivity (and high SNR) were required. Few useful spectral features are observed at low Raman shifts, meaning the cut–off frequency is not of great importance, but important Raman features are observed out to ~4000 cm^{-1}, necessitating a relatively large wavelength coverage (For 532 nm excitation, a Raman shift of 4000 cm^{-1} requires detection out to ~675 nm in order to be completely observed). The water Raman stretching band is broad (>40 nm) with no narrow

spectral features, and thus high spectral resolution is not required. A Raman spectrometer was selected with these criteria in mind.

The study of subtle changes in water Raman spectra requires accurate detection of spectra with low noise and high sensitivity. Water Raman spectra for temperature and salinity analysis were acquired using several commercial Raman spectrometers, in addition to the multi–channel Raman sensing instruments developed in the course of this research. The majority of experimentation was conducted using a mid–range dispersive Raman spectrometer which provides measurement of polarised spectra with low noise floor and polarisation selectivity (Enwave EZRaman–I series). The instrument is shown in Figure 2.1a. A schematic of a fibre–coupled Raman sensing probe similar to that used with the Enwave Raman spectrometer is shown in Figure 2.1b.

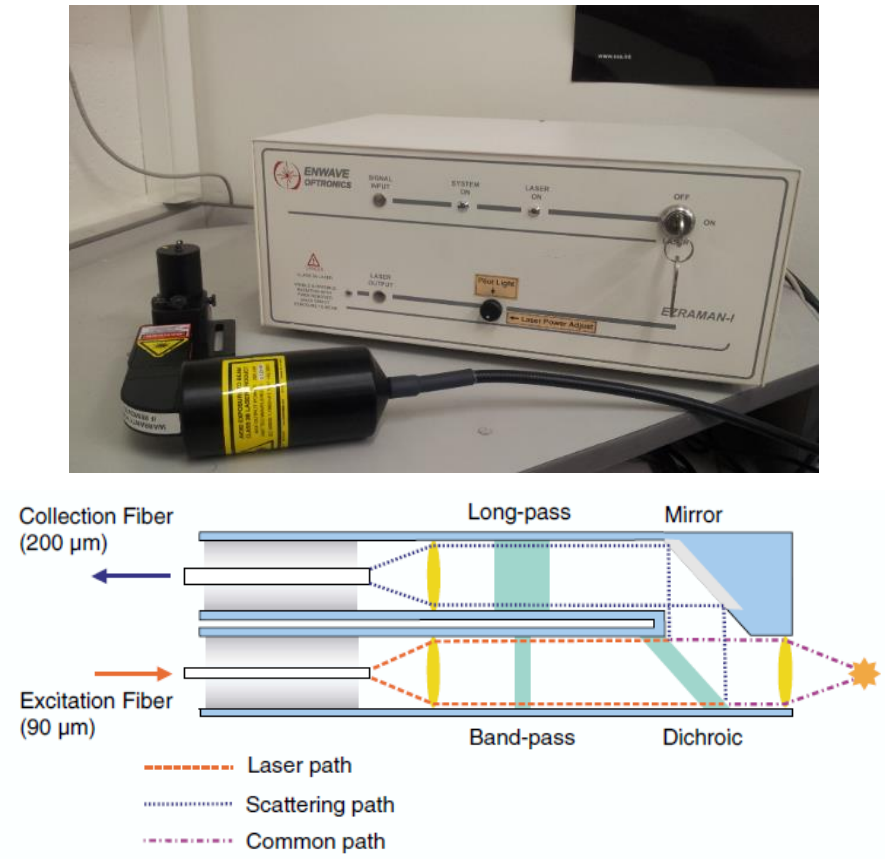

Figure 2.1 – (a) Enwave Raman spectrometer. (b) Schematic of a similar Raman probe [111].

This spectrometer was customised for larger wavelength coverage at the cost of spectral resolution. The increased spectral range was required to enable acquisition of the entire water Raman emission band which extends out to ~680 nm with 532 nm excitation. Key specifications of the instrument are shown in Table 2.1.

Excitation Laser	**532 nm CW Nd:YAG**
Laser Power	30 mW
Spectral Range	250 – 4400 cm^{-1}
Spectral Resolution	~8 cm^{-1}
Detector Type	TEC CCD (-50 °C)
Rayleigh rejection	OD > 8 @ 532 nm

Table 2.1 – Specifications of Enwave EZRaman–I spectrometer.

This spectrometer can be either coupled to a sample cuvette–held sample, or connected to an optical microscope for focusing on small samples. Polarised detection is achieved with a pair of linear polarising filters (Thorlabs LPVISB050) which are inserted in the return signal path. These filters are aligned to produce parallel or perpendicularly polarised signals relative to the laser polarisation.

Wavelength calibration of the spectrometer was conducted before beginning each new experiment using a reference sample of acetonitrile (CH_3CN), a chemical with a well–known Raman emission peak structure which extends over a substantial portion of the range covered by the spectrometer. The position of five acetonitrile peaks (in terms of CCD pixels) was correlated with reference wavenumber values and this data was used to produce a set of calibration coefficients. These were employed within the spectrometer software to calculate an accurate wavenumber scale to match system performance.

Additional measurements and comparison studies were made with an alternative system, an Ocean Optics QE65000 Raman spectrometer. This unit incorporated a grating covering the visible spectrum, but without built–in Rayleigh filtering. Instead it was used in conjunction with several sets of external interference filters. This allowed the spectrometer to be used for Raman measurements with a variety of laser wavelengths and acquisition ranges.

Optical filter transmission and water absorption measurements were made with a commercial spectrophotometer (Agilent Cary 5000 UV–Vis–NIR). This instrument has a spectral range of 175 – 3300 nm and variable resolution down to 0.01 nm.

2.2 Water Sample Cells

In order to make Raman spectral measurements of water samples at varying temperatures a suitable method for containing, heating and cooling samples was required, which included a window for light transmission. An aluminium water cell was constructed for low–volume (~1 ml) water samples. A chamber was milled out of a solid block of aluminium, with a broadband anti–reflection coated window adhered to the exterior. The cell was designed to maintain a near–uniform temperature around the water sample, and hence achieve as near as possible to uniform water temperature. The cell is shown in Figure 2.2.

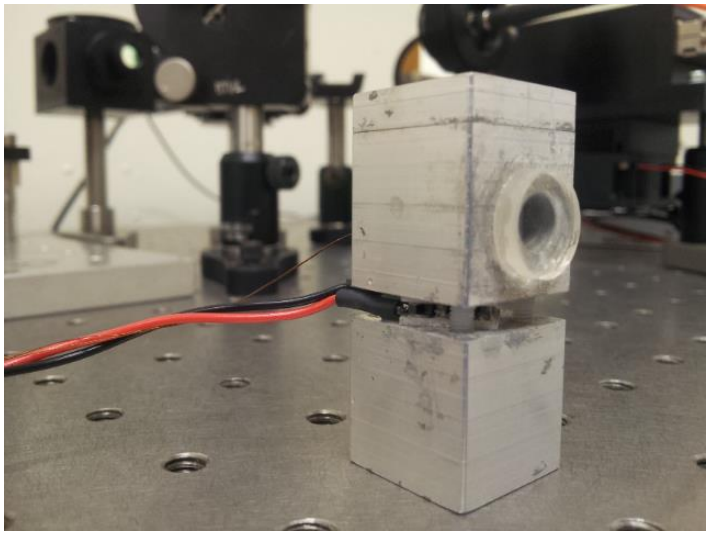

Figure 2.2 – Low volume temperature–controlled water cell.

The cell incorporates a single–stage TEC for temperature control, with a 10 kΩ NTC thermistor with accuracy of ±0.2 °C for feedback. The TEC and thermistor were connected to a TEC controller (Newport 350B). The thermistor was calibrated using the handheld temperature probe (Digitron) in Section 2.4. This water cell was used for the spectroscopic analysis of laboratory water Raman spectra in Chapter 3.

To reduce the time taken for measurements and slightly improve reference temperature accuracy, a high–accuracy temperature controlled cuvette holder (Quantum Northwest QPod 2e) was acquired for later temperature experimentation, including analysis of natural water samples and simultaneous temperature–salinity analysis (Chapters 4 and 5). Figure 2.3 shows the QPod 2e cuvette holder.

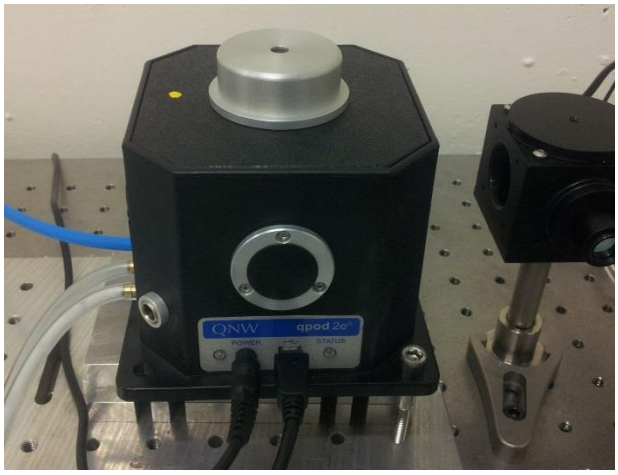

Figure 2.3 – QNW QPod 2e temperature–controlled cuvette–holder.

Optical ports in the four walls of the device provided access to samples for excitation and detection. An integrated TEC with a water cooled heatsink provides temperature accuracy of ±0.05 °C, and computer control allows for automation of temperature ramping. Magnetic stirring with speeds up to 1000 rpm is also incorporated. Water samples were placed in fused silica cuvettes for analysis in this device (Starna). These cuvettes were selected to maximise signal transmission while eliminating fluorescence associated with standard polymer or low quality glass cuvettes.

2.3 Water Samples

In order to assess temperature determination with Raman spectra in natural waters, samples were collected from both natural and filtered water sources. These water samples were analysed both in terms of general spectral properties (fluorescence, background variation etc.) and for Raman emission behaviour in response to temperature change.

The majority of natural samples were taken from various locations around Sydney Harbour and its estuaries. Collection of the water samples was undertaken at a variety of times and tidal conditions, leading to variation in organic and sediment content. All water samples were analysed within 24 hours of collection, with the majority being examined within several hours. Samples were collected and stored in clean polyethylene or laboratory glass bottles. These containers were well

rinsed with water from the source before sample collection. The main water source locations are displayed in Table 2.2.

Sample Sources	Type
Laboratory water (RO filtered)	Fresh
Mains supply	
Millipore (deionised)	
Manly Dam	
Macquarie University Lake	
MQ Seawater Facility (filtered)	Saline
Sugarloaf Bay	
North Head	
Blaxland Rd, Rhodes	
Wharf Rd, West Ryde	
Clontarf	
Roseville Bridge	
Coogee Beach	
Manly Beach	
Shoalhaven Heads	

Table 2.2 – Water sample sources and locations.

System testing, calibration and baseline measurements were conducted with filtered water samples. Mains supply water was also used as a point of comparison. Reverse osmosis filtered water samples were obtained from a commercial reverse–osmosis filtration system (Boss Watermax RO). This was the primary water source used for early studies.

High purity deionised water was used for dilution purposes to produce samples with varying salinity as required for simultaneous temperature and salinity analysis experiments. This was taken from a laboratory water filtration unit, producing water with a resistivity of 18.2 MΩ (Millipore Direct–Q 3).

Filtered seawater from the Macquarie University Seawater Storage Facility was used as a basis for comparison with directly collected natural seawater samples, and as a sample for dilution in temperature–salinity studies. The water in this facility was collected from Rose Bay in Sydney Harbour after a minimum of 10 days without rainfall.

2.4 Temperature and Salinity Measurement

The accurate measurement of temperature can be a complex problem. While a wide variety of thermometry equipment exists, the vast majority are limited to an accuracy of approximately ±1 °C. Achieving reliable measurement below this level requires careful calibration and system design.

Direct temperature measurements were made with a hand–held digital thermometer and probe (Digitron 2024T & P0234D). This device uses a PT100 sensor and has a display resolution of 0.1 °C, with a reading accuracy of ±0.2 %. All temperature sensors used for feedback were either PT100 type platinum resistance thermometers (PRT), or 10 kΩ NTC thermistors with a measurement accuracy of ±0.1 °C.

Figure 2.4 – (left) Digitron temperature probe. (right) Extech salinity probe.

Conductivity and salinity measurements were conducted with a waterproof conductivity probe (Extech EC600). This unit is capable of measuring conductivity, total dissolved solids, salinity, resistivity, pH and temperature. Automatic temperature compensation was used to compensate conductivity measurements for varying sample temperature, though raw conductivity data was also collected. Calibration of the probe was conducted with a potassium chloride (KCl) solution with a conductivity of 1413 µS/cm at 25 °C. The measurement accuracy of the instrument was 2 % F.S. (full scale reading).

2.5 Pre–processing of Raman Spectra

A variety of methods for processing Raman spectra prior to analysis were explored in an effort to improve temperature determination accuracy. These included smoothing, baseline correction and normalisation procedures.

2.5.1 Smoothing

Smoothing of Raman spectral data was performed to minimise undesired variations in signal acquisition. Several smoothing methods were trialled initially, with the Savitsky–Golay smoothing algorithm being selected for general use [112]. This method was chosen for the ability to reduce the effect of high frequency noise without compromising important spectral features. This algorithm applies a moving window to a data set and performs a linear least squares fit to a low–degree polynomial. The centre point of the window is adjusted to fit this polynomial. All analysis was conducted using a second order polynomial applied to a 25 point window. This corresponds to a 50 cm^{-1} spectral range, which is broad enough to correct small signal fluctuations, but narrow enough to avoid significantly altering the desired water Raman stretching band.

2.5.2 Baseline Correction

The baseline of water Raman spectra is strongly dependent upon water quality. Particulates (both organic and inorganic) in water samples alter the baseline across the detected spectrum via scattering and fluorescence. This has also been seen to vary slightly with temperature, which is attributed to convection within the water sample carrying particles through the laser focal volume.

Organic matter within samples can fluoresce under laser illumination. In particular chlorophyll from plant matter or phytoplankton can emit strongly in the visible wavelength range. Such fluorescent emissions can alter the background signal level and tilt the stretching band, altering the signal and affecting the determination of temperature. The origin and implications of such baselines are considered in Chapter 4. Standard methods for baseline correction are as follows.

Horizontal linear subtraction

The simplest possible baseline correction method is a subtraction of a single value from the entire spectrum. This is done by selecting a region of the spectrum with no Raman emission and minimal fluorescence, and subtracting the intensity of this region from the entire data set. This method is trivial to implement, but may provide little improvement in signal quality.

Tilted linear subtraction

In this case two points which are separated in the spectrum, but with minimal signal intensity are located. A line is fitted between the points, and the values at each point on the line are subtracted from the spectrum. This method can significantly decrease the impact of fluorescence tilting the Raman water emission band. This is the method applied in Chapter 4 for correction of spectra from natural water samples.

Fitted subtraction

This covers many techniques which aim to fit and subtract undesirable components from a spectrum. These include Gaussian deconvolution, polynomial fitting and asymmetric least squares fitting methods [113]. The usefulness of these techniques varies depending on the signal, the type of interference to be removed and noise levels. Some also require pre–knowledge or some intuition about the sources of background noise/interference. While this method might ultimately produce nearly background–free Raman spectrum, it requires knowledge of the background structure, and would be difficult to implement in field experiments.

2.5.3 Normalisation

Variation in CW laser intensity over time can change the relative Raman signal intensity between spectrometer acquisitions. In the case of pulsed laser sources, the pulse energy can vary substantially from shot to shot, and hence influence the corresponding Raman response to each pulse. Total signal variations like this are easily corrected by normalising Raman spectra. This is done either by normalising all spectra to a specific intensity value, or by area (integrated over the full stretching band). Alternatively retrieved signals can be averaged over multiple acquisitions to improve consistency. Normalisation was experimented with initially,

but it has no impact on the value of two–colour ratio, or the depolarisation ratio parameters if the spectra are acquired simultaneously. Thus it was determined that normalisation of spectra was not necessary and was not performed on the spectra presented in this thesis.

2.5.4 Derivatives

Reduction in background interference and baseline effects can be achieved by taking the derivative of spectral data. Commonly the 1st or 2nd derivatives may be taken, which alter the appearance of the spectra but maintain the information content while removing baseline offsets between spectra. This is a commonly used pre-processing technique in the multivariate data analysis methods described in Section 2.6.

2.6 Multivariate Analysis Techniques

Analysis and visualisation of large data sets consisting of multiple variables can be challenging. Conventional plotting and regression methods can work for up to three variables, but rapidly fall off in usefulness as data becomes more complex. Data with multiple dependent and independent parameters can't be interpreted for interactions between variables without more sophisticated analysis methods.

The various mathematical techniques which fall under the heading of multivariate analysis enable complex data sets to be visualised and interpreted. Multiple linear regression (MLR) provides a means to incorporate the effect of multiple variables into linear regression fitting. Principal Component Analysis (PCA) provides a means to visualise the interactions and behaviour of variables in data. Regression methods including principal component regression (PCR) and partial least squares regression (PLS–R) can then be applied to develop predictive models based on multiple parameters. This type of analysis has uses in a wide range of fields and disciplines, including many branches of spectroscopy. In particular PCR and PLS–R deal well with highly correlated independent variables such as spectral data and are well suited to use in analysing Raman spectra. In the course of this research, all of the methods discussed below were investigated for several different purposes. In Chapter 3, the linear combination of multiple spectral parameters was

conducted with multiple linear regression (MLR). In Chapter 5, PCA was used for initial observation of the relationship between temperature and salinity effects on Raman spectra, and PLS-R was employed to estimate uncertainty in quantifying temperature and salinity values.

The following sections present brief summaries of the basic functionality of these multivariate methods. More detailed description and mathematical procedures can be found in appropriate reference texts [114-116].

2.6.1 Multiple Linear Regression (MLR)

Multiple linear regression is the simplest multivariate regression technique, and is directly comparable to conventional univariate, linear least squares fitting methods. It attempts to model a linear relationship between two or more explanatory variables (X) and a response variable (Y). Equation 2.1 shows the relationship between the variables:

$$y = \beta_0 + \beta_1 x_1 + \beta_2 x_2 + \cdots \beta_n x_n + \varepsilon \qquad 2.1$$

Where y is the dependent variable (temperature, salinity etc.), x_1-x_n are the independent variables (spectral parameters), β_0–β_n are the fit coefficients and ε represents the residual error (deviation from the fit). For two independent variables, this equation represents a 2D plane expressed in three dimensions.

This method is used in this research to link multiple spectral parameters and produce models for determination of water temperature. It was chosen as this data relationship is simple enough to produce virtually identical results with MLR, PCR and PLS-R, and MLR requires significantly simpler calculations.

2.6.2 Principal Component Analysis (PCA)

Principal component analysis is perhaps the most used analysis technique for interpretation of multivariate data. It allows the analysis of a data set with large numbers of variables in order to observe the relationships between them [114]. In general PCA is performed on only the independent variables. PCA is generally the first step in the analysis of a data set before moving on to more advanced analysis methods.

In essence this technique involves generating a new coordinate system based on the variance in the data set. The new coordinates are linear combinations of the original parameters, known as “principal components”. Successive components are

orthogonal to each other, and are oriented for maximum alignment with the remaining variance not explained by the previous components. The principal components can represent properties (or combinations of properties) which have a significant impact on the data. The data are mean–centred prior to analysis, and thus the origin of the set of principal coordinates is located at the mean position of the data set. The data can then be described in terms of these principal components.

Several methods can be used to calculate principal components and their corresponding data representation. The X data are mean–centred to place the origin of the principal components in the centre of the data set (some data may also require scaling if variables have significantly different ranges). The covariance matrix for this data is calculated and decomposed into eigenvectors, known as the loadings and eigenvalues which are known as scores). Equation 2.2 represents the relationship between the mean–centred data and the scores and loadings matrices:

$$X = TP^T + E \qquad 2.2$$

where X is the mean–centred data matrix, T is the scores matrix and P is the loadings matrix. E is the residual variance in the data which is not be explained by the principal components used in the model.

The loading vectors represent the correlation between the original coordinates and each principal component. Each element of a loadings vector is the cosine of the angle between an original coordinate vector and the principal component corresponding to that loading vector. The score values represent the position of a sample with respect to the principal components.

Figure 2.5 shows the first principle component PC1 along the direction of greatest variance of the data set (blue points), with the PC1 score (t) marked for a sample, and the angle (theta) between original axis X_1 and PC1 displayed.

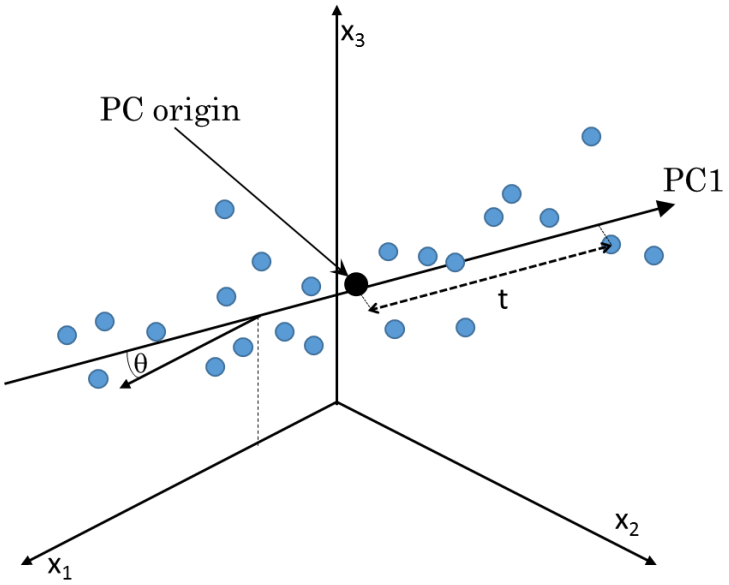

Figure 2.5 – Example of a principal component PC1 for a set of data. The score (t) for a sample and the angle (θ) between an original axis X_1 and PC1 are marked.

The number of components can vary up to the number of variables in the original data. Selecting the appropriate number of components to use is essential; enough components must be included to accurately represent relevant variance in the data, but not so many as to include residual noise.

Plotting the scores and loadings with principal components as axes allows trends in data to be examined and interpreted. Correct interpretation of these plots requires detailed understanding and insight into the system being investigated. Without this knowledge the reduced data presented by PCA and related multivariate methods can often be interpreted incorrectly, particularly where higher numbers of components are used. The same holds true for the following methods as well.

2.6.3 Principal Component Regression (PCR)

Principal component analysis provides a means to interpret complex data set, but no capability for estimation of dependent variables. By regressing dependent variables (Y data) against principal components defined from spectra, a model can be generated which can be used to estimate the equivalent values for other data sets. This is known as principal component regression. Care is required in the use of this technique, as the regression looks for maximum variance in the X data and correlates this with the Y data, regardless of the source of the variance.

2.6.4 Partial Least Squares Regression (PLS–R)

Partial Least Squares Regression is somewhat analogous to Principal Component Regression, though with important differences in the way data is correlated. The PLS–R algorithm finds the variance in the dependent (X) variables which explains the maximum variance in the independent (Y) variables. This can be advantageous in terms of minimising the impact of undesirable variances in the X data which are poorly correlated with the Y data.

To perform a partial least squares regression, decomposition is performed for both the X and Y data, producing scores for each based on covariance with the other, X with Y to produce X scores, then Y with the X scores to produce Y scores. The X scores are then regressed against the Y scores, producing a model which can be used to predict the Y data. The components are referred to as factors in PLS and they refer to the interaction between the X and Y data rather than the variation in X alone. Many iterative algorithms exist for PLS–R calculation, some more efficient than others depending on the dimensions of the data and the number of factors used.

Similar caveats hold for PLS–R as in the other eigenvector decomposition analysis methods described above. The number of factors used in the generated model is critical to model the data appropriately without including residual noise not representative of spectral features. Validation of multivariate models is also essential. Cross–validation was used in all PCA and PLS–R models to assess model robustness and the appropriate number of components/factors.

A measurement of how well predicted values match the data is required for comparison of models and data sets. Root mean square error (RMSE) is a measure of the difference between a set of values predicted by a model (generally a regression such as PLS–R output), and the set of true or reference values. It represents the standard deviation of these differences (residuals). Equation 2.3 shows the calculation for RMSE:

$$RMSE = \sqrt{\frac{\sum_{i=1}^{N}(y_i - \hat{y}_i)^2}{N}} \qquad 2.3$$

where y is the set of reference values, ŷ is the set of predicted values and N is the number of values in these sets. The use of RMSE in the context of this thesis is primarily to assess the relative performance of Raman spectra temperature models, and to provide an estimate of the best–case temperature measurement performance which might be expected in practical Raman sensing of water temperature.

2.7 Multivariate Analysis with The Unscrambler

The majority of multivariate analysis of Raman spectra in this thesis was conducted with software package "The Unscrambler" v10.3 (CAMO Software). The Unscrambler is specifically designed for processing and analysis of multivariate data sets. By using The Unscrambler, a large number of multivariate analysis techniques and processing methods can be tested rapidly on a data set. Once a preferred method was selected, optimised models and predictions could be generated, or the method could be implemented in Matlab for incorporation into existing code if repeated use with multiple data sets was required.

The Unscrambler was used to test combinations of multiple spectral parameters for temperature determination in Chapters 3 and 4, with a variety of regression methods before MLR was finally selected. Several PCA models and a large number of PLS–R models were built for simultaneous analysis of temperature and salinity.

2.8 Numerical Analysis with Matlab

Data manipulation and analysis for the experimental work in this thesis was conducted using Matlab (R2012a, The MathWorks). Matlab is a high–level programming language and development environment designed for numerical computation and data visualisation. It enables more rapid and flexible analysis of data compared with spreadsheets and conventional programming languages used for similar tasks (C, Java, etc.). Toolboxes are available which provide functions for common mathematical operations and data analysis techniques, including multivariate methods. Matlab has been used extensively throughout this project. Code used for work in this thesis may be found in Appendix C.

3 Raman Spectroscopy of Laboratory Water

This chapter describes a thorough experimental study of the Raman emission spectra of liquid water, specifically using a supply of laboratory–grade reverse osmosis filtered water (see Section 2.3). The intent as to examine the response of Raman spectra to changes in water temperature, with the end goal of developing practical methods by which water temperature could be deduced from Raman–spectra using depth–resolved remote sensing techniques.

The Raman spectral response of water to temperature change was investigated in terms of variation in unpolarised and polarised signal intensity, Raman stretching band area, two–colour ratios from polarised and unpolarised spectra, and depolarisation ratios. These properties were characterised to determine how this behaviour may be employed for accurate temperature determination. Linear regression models were developed which correlate reference water temperature with various spectral parameters. Analytical procedures were developed to identify spectral features that were most sensitivity to changes in temperature and which gave the highest accuracy in determining water temperature.

3.1 Experimental Approach

Unpolarised and linearly polarised Raman spectra were recorded for reverse osmosis filtered water samples at temperatures ranging from 10 to 50 °C. Reverse osmosis filtered water was used rather than deionised water to minimise sample variability over the minutes to hours taken for acquisition of spectra. Spectra were collected using the Enwave Raman spectrometer described in section 2.1 and the temperature–controlled aluminium water cell described in Section 2.2. Various integration times and averaging schemes were experimented with to produce consistent spectra in a reasonable timeframe. The acquisition time used in this experiment was 30 seconds and three scans were averaged for consistency. The experimental setup used is shown in Figure 3.1.

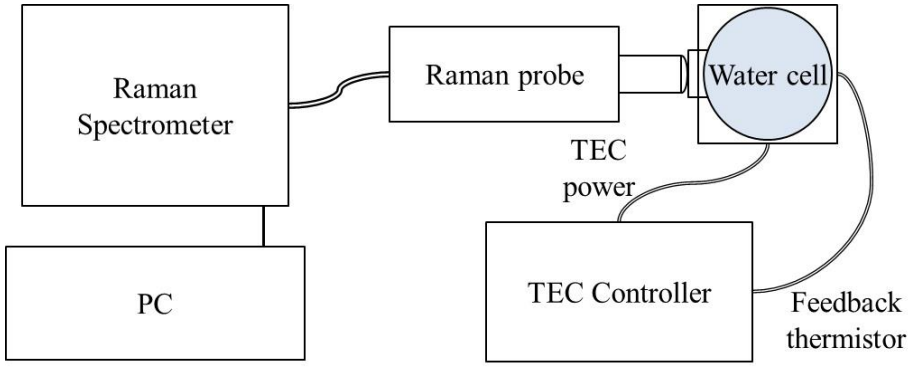

Figure 3.1 – Experimental setup for collection of water Raman spectra.

The signal detection path was collinear with excitation, i.e. the 180° backscattered Raman signal was collected, and polarisers were introduced into the Raman signal beam path to obtain polarised spectra where needed, i.e. the parallel or orthogonal polarisation states relative to the polarisation of the excitation laser. The vertical axes of plotted spectra are given in terms of signal counts, both for completeness and to enable comparisons between polarised spectra. Data were corrected for the spectral response of the spectrometer optics and smoothed with a Savitsky–Golay algorithm to reduce noise (The effect of smoothing on spectra is shown in Appendix F).

3.2 Temperature dependence of Raman spectra for RO water samples

3.2.1 Temperature Dependence of Unpolarised Raman Spectra

Unpolarised Raman spectra of water exhibit subtle changes with temperature, as described in Section 1.3. Figure 3.2 shows complete Raman spectra of laboratory water with varying temperature.

Figure 3.2 – Unpolarised Raman spectra for a laboratory water sample with varying temperature.

The majority of the spectrum, where very weak Raman emissions are observed, shows no temperature dependent behaviour. Some slight temperature dependence is seen in the low wavenumber region (250-500 cm^{-1}) where inter–molecular vibration and libration modes produce relatively weak Raman emissions [60]. The strongest temperature dependence is found in the OH stretching vibration band at 2800-3800 cm^{-1}. Details of the band assignments are found in Section 1.3. A significant linear baseline offset was observed which scales consistently with spectrometer integration time. This did not adversely impact on the temperature behaviour under investigation.

Figure 3.3 shows the OH stretching band in more detail. The behaviour of the stretching band is clearly defined in response to temperature change. A temperature insensitive isosbestic point (point of equal scattering) was observed at ~3422 cm^{-1} in unpolarised spectra, which is consistent with the published value of 3425 cm^{-1} found in several studies [63, 71]. The temperature isosbestic point has been found to be relatively insensitive to the angle between excitation and scattering axes [71].

For Raman shifts below the isosbestic point signal intensity decreases with increasing temperature, while above this point signal intensity increases with increasing temperature. These changes in intensity exhibit a linear relationship with temperature.

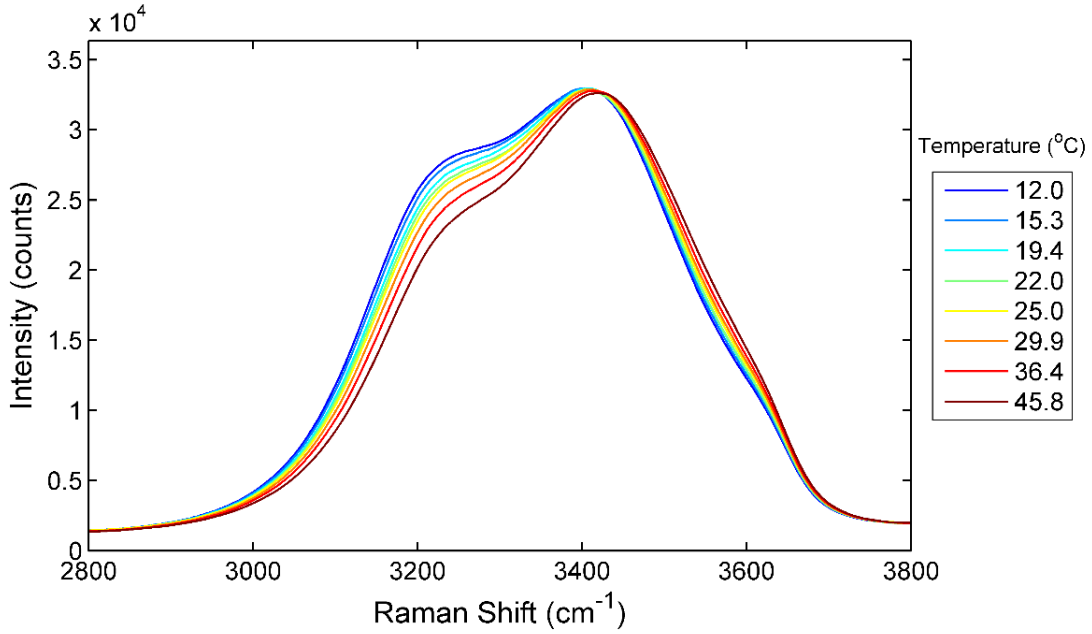

Figure 3.3 – Unpolarised Raman spectra of RO filtered water with varying temperature.

The rate of change of Raman intensity variation with water temperature is shown in Figure 3.4, where it can be seen that the points of greatest temperature response are observed at 3182 cm^{-1} and 3542 cm^{-1}.

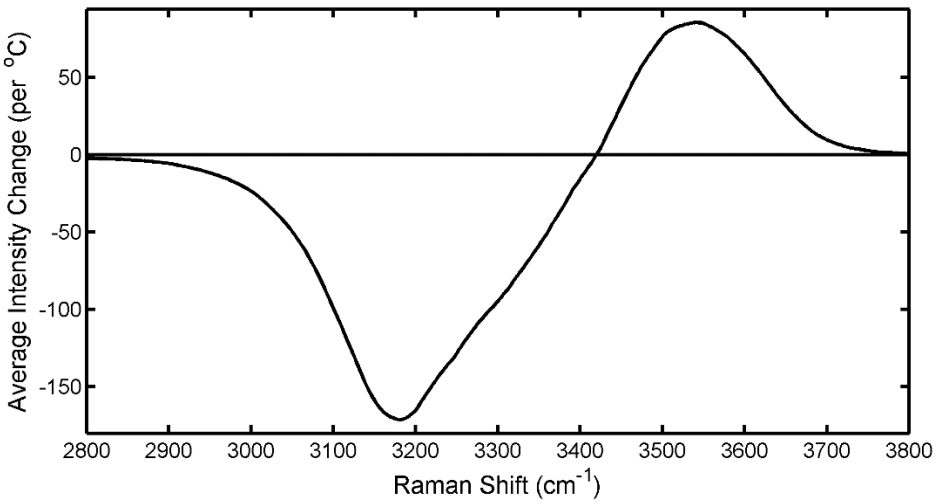

Figure 3.4 – Variation in unpolarised Raman signal intensity in response to temperature change.

These changes have the net effect of translating the band centre to higher Raman shifts with increasing temperature. This property has been previously exploited by Bunkin et al. as a means to quantify water temperature [98].

The integrated OH band intensity (i.e. the area under the Raman stretching band) was found to decline with increasing temperature as seen in Figure 3.5 below.

All spectra were linearly baseline corrected across the OH stretching band between 2800 cm^{-1} and 3800 cm^{-1}.

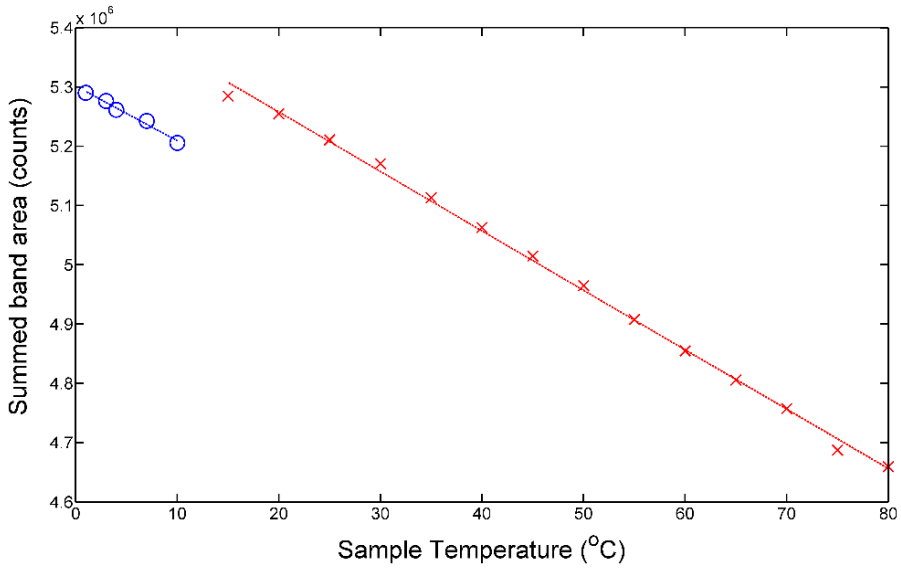

Figure 3.5 – Total intensity of OH stretching band with varying water temperature. The blue and red data were obtained from two separate experiments using different samples. Data were obtained using linear baseline correction.

The average reduction was found to be approximately 0.2 %/°C, with a linear trend in the temperature region studied (15-80 °C). This trend has been noted by other researchers in the past, although no physical explanation was proposed [96]. We hypothesised that this behaviour may be due to the temperature dependence of water density, which affects the number of water molecules within the laser focal volume. By this means, higher temperatures (lower density) could be expected to contribute to lower Raman intensity. The effect of density on Raman scattering can be seen in Equation 3.1:

$$\Delta p = \frac{d\sigma}{d\Omega}(\Delta\Omega).\rho.L \qquad 3.1$$

where Δp is the probability of Raman scattering of a vibrational transition, $\frac{d\sigma}{d\Omega}$ is the Raman scattering cross–section, $\Delta\Omega$ is the solid angle, ρ is the number density of water molecules per unit volume and L is the propagation length.

To investigate this behaviour further, a study of low temperature spectra (1 - 10 °C) was conducted to explore the temperature region around 4 °C where water reaches maximum density [10]. Nitrogen was flowed around the water cell to avoid condensation. These data are shown as blue circles in Figure 3.5. The two data sets are discontinuous because they were collected is at different times, using different water samples, possibly slight condensation on cuvettes, and slightly different

detection efficiency and excitation laser intensity. No evidence of a relationship with density was observed, with the linear trend in band area continuing at temperatures below 4 °C, and the physical origin of the temperature dependence of the OH stretching band area remains unresolved.

3.2.2 Temperature dependence of polarised Raman spectra

Linearly polarised Raman spectra, i.e. polarised parallel and perpendicular to the excitation laser polarisation, are shown in Figure 3.6. The same laser intensity, integration time, averaging and smoothing were employed as for the acquisition of the unpolarised spectra.

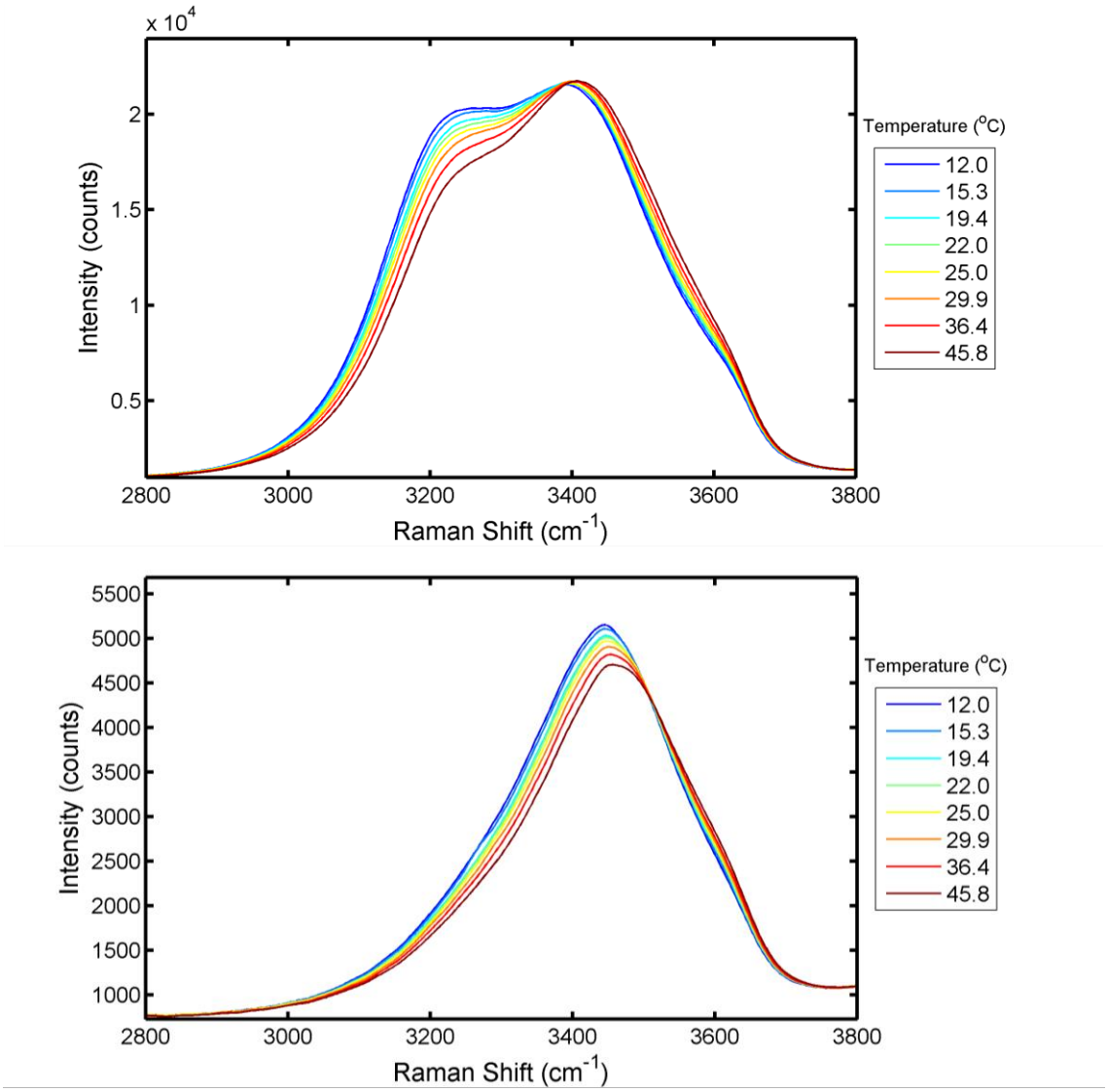

Figure 3.6 – (a) Parallel and (b) perpendicular polarised Raman spectra with varying water temperature.

The form and temperature dependence of the parallel polarised spectra (Figure 3.6a) were similar to the unpolarised spectra, with a change in the isosbestic

point to a shorter Raman shift of 3390 ± 4 cm^{-1}, which is similar to literature values of 3403 cm^{-1} [102]. A higher rate of intensity change was seen to the left of the isosbestic point compared with the unpolarised spectra. The points of intensity change with temperature were found at ~3180 cm^{-1} and ~3516 cm^{-1} respectively.

The perpendicular polarised signal (Figure 3.6b) was substantially weaker than the parallel polarised spectra (approximately 20% relative peak intensity). An isosbestic point was evident at ~3500 cm^{-1}. The points of maximum negative and positive change with temperature occurred at 3390 cm^{-1} and 3588 cm^{-1} respectively. The rates of change in Raman signal with temperature as a function of wavelength are shown in Figure 3.7.

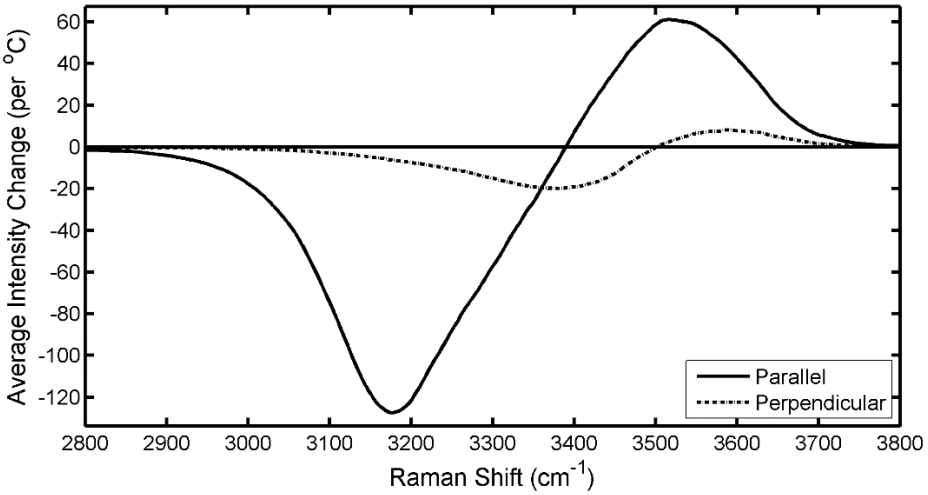

Figure 3.7 – Temperature dependence of polarised Raman spectra.

The sum of the linearly polarised spectral components acquired with the Enwave Raman spectrometer was approximately 30 % weaker than the unpolarised signal, a greater loss than anticipated based on transmission spectra for the polarising filters (~19 % average loss over the wavelength range 630-660 nm).

Table 3.1 summarises the main findings in this section, including isosbestic points, Raman shifts corresponding to regions most sensitive to temperature, and the rates of change in intensity at these shifts expressed in both counts per °C and percentage change per °C relative to the average intensity over all temperatures at the corresponding Raman shift position.

	Unpolarised spectra	Parallel polarised	Perpendicularly polarised
Isosbestic point	3422	3390	3500
Raman shift position for max. positive temp. change (cm^{-1})	3542	3516	3588
Max. positive intensity change (counts/°C and % change / °C)	85 (0.43 %)	61 (0.42 %)	8 (0.28 %)
Raman shift position for max. negative temp. change (cm^{-1})	3182	3180	3390
Maximum negative intensity change (counts/°C and % change / °C)	-171 (-0.81 %)	-127 (-0.83 %)	-20 (-0.47 %)

Table 3.1 – Temperature–dependent properties of unpolarised and polarised Raman spectra.

3.3 Determining temperature from Raman spectra

Based on the observations above, there are multiple means by which temperature may be quantitatively deduced from the Raman spectra of water. The simplest possible scheme would be a measurement of intensity at a single point, or over some wavelength range, with a regression relating Raman intensity to reference temperature values. However in terms of practical usefulness this would have serious failings. Since spontaneous Raman scattering in water is relatively weak, ambient light, scattering from suspended particulates and fluorescence from organic matter would all significantly impact on the accuracy of temperature measurement. As detailed in Section 1.4, previous studies have identified several methods by which information about water temperature can be extracted from Raman spectra. Typically these involve some sort of ratio of quantities in order to overcome these issues. The two main approaches we have adopted are called the "two–colour" method and the depolarisation ratio.

3.3.1 "Two–colour" Method with unpolarised Raman spectra

This method involves a ratio of Raman signals corresponding to Raman shifts on either side of the isosbestic point. Values from the high shift side of the isosbestic point are divided by low side values, leading to a ratio which increases with

increasing water temperature. It can be applied to unpolarised or parallel polarised Raman spectra, but it is not suited to the relatively weak perpendicularly polarised component. It is well suited to our long–term goal of near–real–time remote sensing of water temperature because a ratio of integrated spectral channels can be readily acquired with the high–speed photodetectors required for ranged measurements. In relation to this, the application of the two–colour technique presented here is distinctly different from past studies, which typically involved the fitting of Gaussian peaks to the Raman OH stretching band. The corresponding temperature–dependent parameter was taken to be a ratio of the area of two of these Gaussian curves. No such spectral decomposition is required for the approach taken here.

To optimise the two–colour ratio parameter it is necessary to consider which pairs of wavelengths (or Raman shifts) exhibit the greatest sensitivity to water temperature. The sensitivity was explored both in terms of signal intensity change, and change in the two–colour ratio expressed in % change per ^{o}C. The unpolarised spectra shown in Figure 3.8 were analysed to identify these positions of greatest sensitivity in the spectra. All possible wavelength pairs from Raman spectral ranges of 3000 to 3400 cm^{-1} and 3400 to 3800 cm^{-1} (with steps of 2 cm^{-1}) were used to calculate spectral intensity gradients and two–colour ratio gradients with respect to temperature over the full range of temperature values.

The intensity gradient with respect to temperature of the unpolarised spectra is shown in Figure 3.4. Raman shift pairs corresponding to maximum positive and negative temperature response are indicated by the pair of vertical lines labelled “A” in Figure 3.8. These were found to be approximately 3182 cm^{-1} and 3542 cm^{-1} for negative and positive intensity change (relative to increasing temperature) respectively.

The pair of wavelengths for which the two–colour ratio exhibited the greatest variance with temperature, were found to be 3120 cm^{-1} and 3586 cm^{-1} and these are indicated by the pair of vertical lines labelled ‘B’ in Figure 3.8. The pairs of lines labelled ‘C’ and ‘D’ were arbitrarily selected to provide points of comparison which have dissimilar signal intensities.

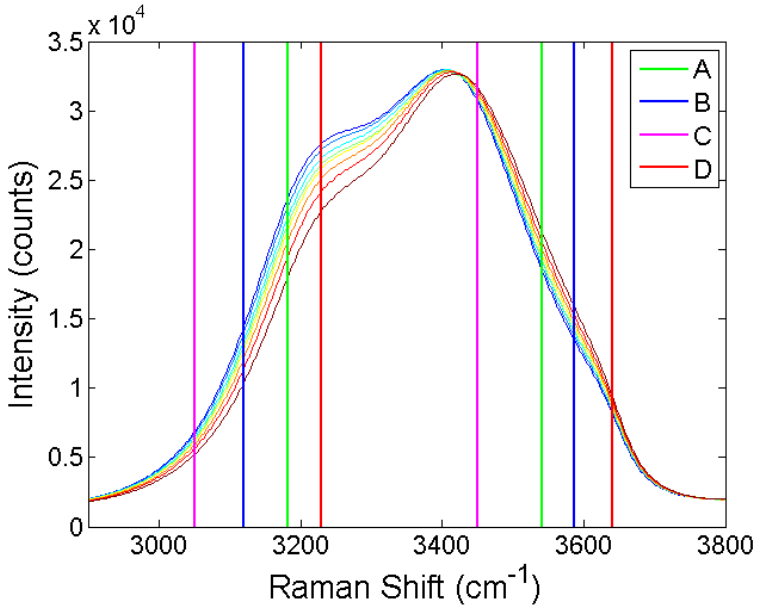

Figure 3.8 – Unpolarised water Raman spectra with changing temperature. Vertical lines represent the two–colour ratio combinations marked in Figure 3.9 and Figure 3.10.

Intuitively the spectral regions exhibiting maximum intensity variation with temperature might be expected to produce the two–colour ratio with the maximum variation. However, it is necessary to consider that low intensity values in the denominator of the ratio will result in larger ratio values, and vice versa for the numerator. To account for this, the two–colour ratio values were scaled by the mean two–colour ratio value over the range of temperatures investigated. The gradient of these scaled ratios with changing temperature gives the "**mean–scaled two–colour ratio temperature sensitivity**", a quantity which will be referred to frequently in this chapter. It is defined as shown in Equation 3.2 below:

$$\text{Mean–scaled two–colour ratio temp. sensitivity} = \frac{dR}{dT}\frac{1}{\text{Mean}(R)} \qquad 3.2$$

where R represents the set of two–colour ratio values, and T is the set of corresponding temperature values.

The mean–scaled two–colour ratios for pairs of wavelengths 'A–D' are plotted in Figure 3.9 as a function of temperature. It can be seen that the highest temperature sensitivity occurs for the 'B' wavelength pair and is 1.50 % per °C, slightly higher than the temperature sensitivities of 1.26, 1.05 and 0.87 % per °C found for wavelength pairs 'A', 'D' and 'C' respectively.

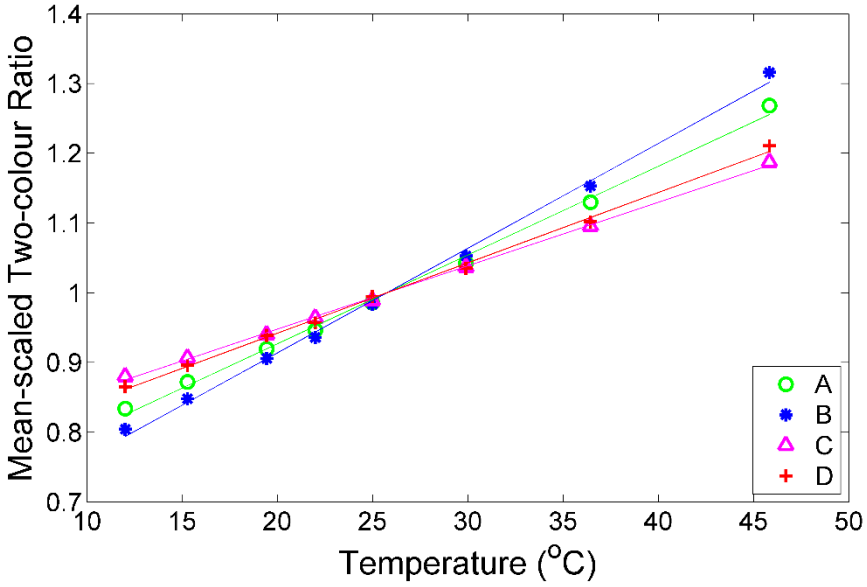

Figure 3.9 – Mean–scaled two–colour ratio values with different spectral positions as a function of sample temperature.

To determine the optimal wavenumber shifts which yield the highest mean–scaled two–colour ratio, the mean–scaled two–colour ratio was calculated for all wavenumber combinations from 3000 to 3800 cm^{-1}, with points drawn from either side of 3400 cm^{-1} (near the isosbestic point). This involved computation of the mean–scaled two–colour ratio for all possible pairs of wavenumbers using Matlab.

Mean–scaled two–colour ratio temperature sensitivity was subsequently calculated for all wavenumber pairs and is mapped in Figure 3.10 as a function of Raman shift on the "high" and "low" sides of 3400 cm^{-1}. The sensitivity scales with colour as shown by the colour–bar on the right–hand side. The wavelength pairs 'A' and 'B' shown in Figure 3.8 and Figure 3.9 are labelled on the map. As described previously, the maximum two–colour ratio sensitivity is found at 'B', while 'A' corresponds to maximum spectral temperature gradient.

While the analysis presented above enables temperature sensitivity to be visualised, it is also necessary to take the relative signal intensity into account in selecting the optimal bands for determining temperature. In other words, there will be a trade–off between maximum temperature sensitivity and signal intensity, depending on the signal to noise ratio in a practical system.

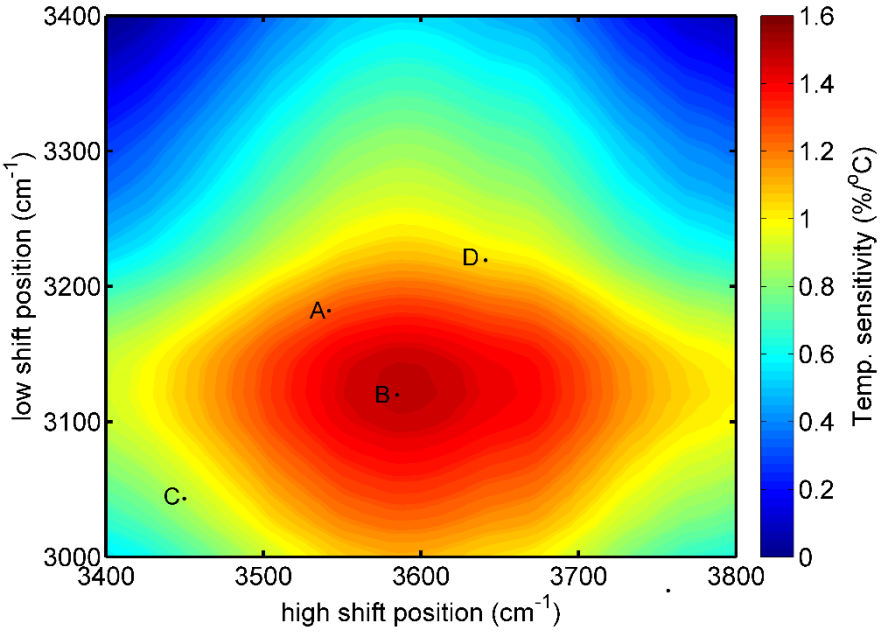

Figure 3.10 – Temperature sensitivity of the mean–scaled two–colour ratio for unpolarised Raman spectra with varying shift positions. The wavenumber pairs A, B, C and D from Figure 3.8 are marked.

Up to this point, Raman intensity values from spectra have been used for calculation of the two–colour ratio. In reality rapid remote sensing of weak signals requires the acquisition of integrated spectral channels with wavelength–insensitive photodetectors. To simulate realistic signal collection, we now transition to the use of channels consisting of summed intensities over a range of Raman shifts from experimental spectral data.

The effect of varying channel width on temperature sensitivity and signal intensity, was examined, producing results shown in Figure 3.11. These two quantities were calculated for a range of channel widths centred on the 'B' wavenumber pairs, and stepping in increments of 10 cm^{-1} from a point intensity value (2 cm^{-1}) up to 500 cm^{-1}. The Raman spectra were integrated over these successively larger channel widths, and the integrated intensity for each channel and the mean–scaled ratio temperature sensitivity ratio were calculated. The integrated signal intensity plot is normalised to the larger of the two signals at maximum channel width.

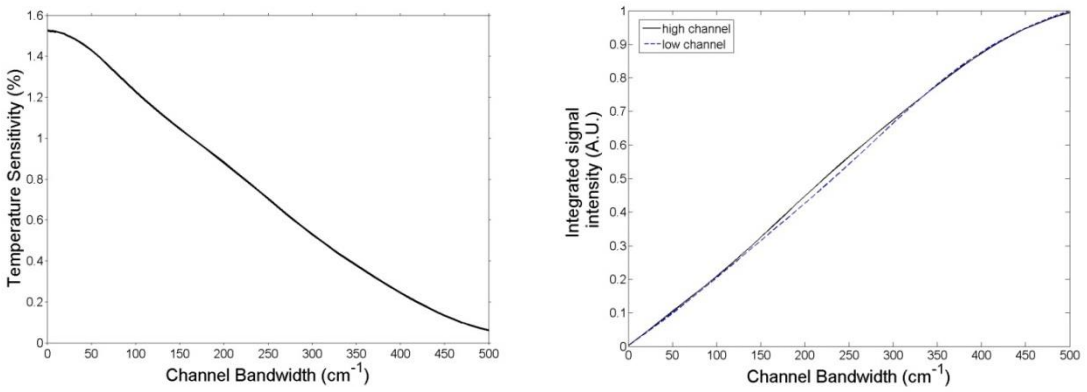

Figure 3.11 – Effect of varying channel width on: (a) Temperature sensitivity of the "B" two–colour ratio. (b) Integrated channel intensity at 25 °C for the "B" two–colour ratio.

Increasing the channel width reduces temperature sensitivity, while the integrated signal intensity increases rapidly. Both channels required for the two–colour ratio parameter exhibit similar signal strength and channel width trends. In practice, the optimal channel width will be a compromise between temperature sensitivity and signal strength, and selection will depend on factors including laser source, receiver and detector characteristics. Optimal channel widths for practical sensing will lie within the range examined here, since 500 cm^{-1} per channel covers the entire OH stretching band.

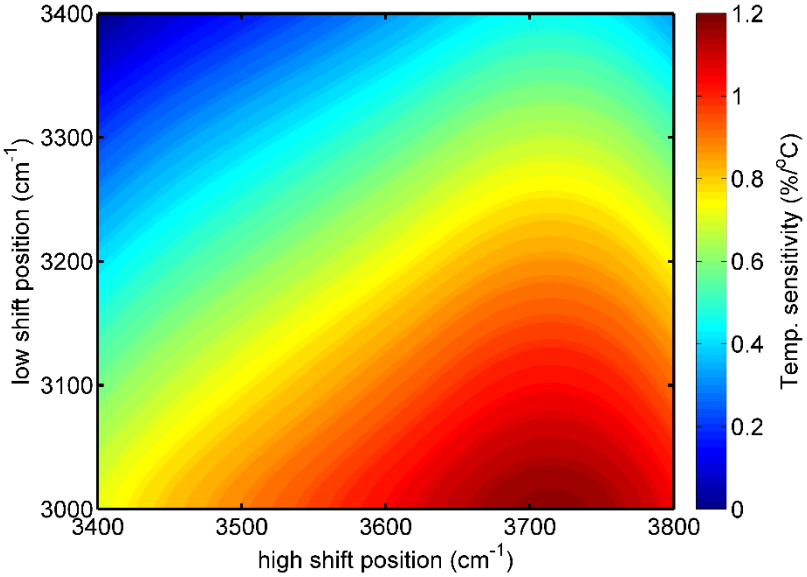

Figure 3.12 – Temperature sensitivity of the mean–scaled two–colour ratio with varying band centre positions (200 cm^{-1} channel widths).

A map of mean–scaled temperature sensitivity with 200 cm^{-1} (~8 nm) channel widths is shown in Figure 3.12. This channel width was selected to represent realistic channels which might be employed in a practical temperature sensing

system, and is roughly similar to the bandwidth of commercially available optical band–pass filters.

The peak sensitivity has shifted compared with the single intensity map, with the ratio centre locations shifting further away from the isosbestic point. The maximum sensitivity value occurs near 3000 cm^{-1} on the low (left) side of the isosbestic point, while on the high (right) side it occurs at ~3720 cm^{-1}. The maximum sensitivity was ~1.18 %/°C, compared with 1.50 %/°C for the single–point intensity ratio map in Figure 3.10. During this analysis it was noted that as channel widths are increased, the precise location of channel centres has progressively less impact on values for the two–colour ratio.

3.3.2 Two–colour ratio with parallel polarised spectra

The two–colour ratio method was applied to parallel polarised spectra as it was to unpolarised spectra previously. Similar performance characteristics were obtained, which is to be expected considering the similarity of the spectra. A map of mean–scaled temperature sensitivity with point intensities is shown in Figure 3.13.

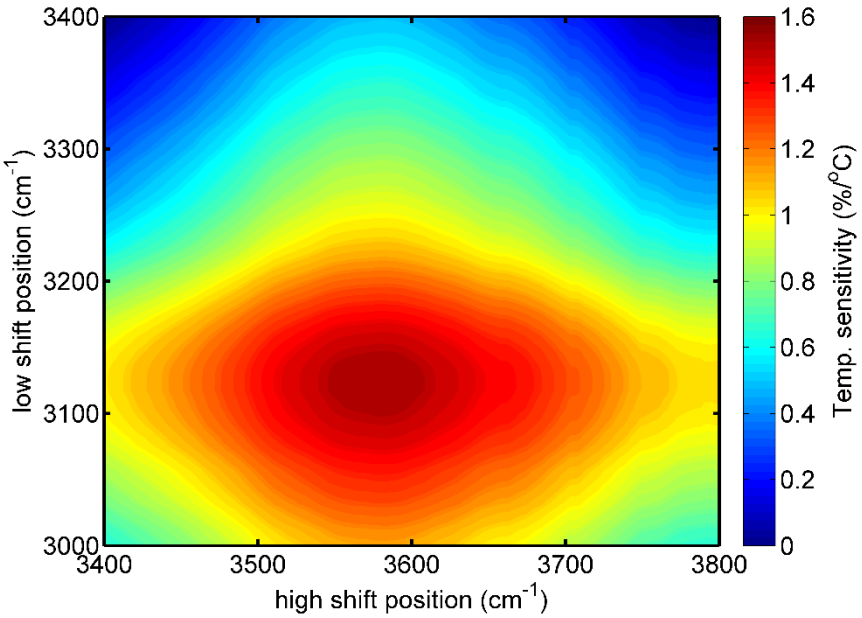

Figure 3.13 – Temperature sensitivity of the mean–scaled two–colour ratio for parallel polarised spectra with varying shift positions and single–point intensity values.

The greatest mean–scaled temperature sensitivity for parallel polarised spectra was approximately 1.52 %/°C, which was observed with the two–colour ratio from 3124 cm^{-1} and 3576 cm^{-1}. This maximum sensitivity was very close to the values

for unpolarised spectra. When 200 cm^{-1} channels were considered, the maximum temperature sensitivity was 1.28 %/°C.

The lower intensity of the parallel polarised stretching band component relative to the unpolarised signal may mean that a parallel polarised two–colour ratio is very slightly less effective, while also being susceptible to polarisation dependent loss mechanisms. What it does provide is a parameter which can be efficiently collected in concert with other temperature dependent polarised parameters, such as the depolarisation ratio described below.

3.3.3 Depolarisation Ratio Method

As described in section 1.4.2, the depolarisation ratio of a Raman emission line is the ratio of signal intensities at a single wavelength, which have linear polarisation states perpendicular and parallel to that of the excitation laser. This ratio exhibits temperature dependence and presents a second approach to determining temperature from Raman spectra.

The depolarisation ratio has advantages and disadvantages as a temperature determination parameter when compared with the two-colour ratio. It relies on signals acquired from a single wavelength (or wavelength channel), effectively avoiding the potential impact of differential attenuation due to water absorption, fluorescence from organic matter and particulate scattering, which could be problematic when using the two colour method to remotely sense water temperature at depth. On the other hand, the depolarisation ratio may be more adversely affected by other light fields due to the relatively weak perpendicular polarised Raman component. In terms of the ultimate goal of remote sensing, the two polarisation signals could be affected differently by the angle of incidence with the water surface, which is highly dependent on sea surface state (or the body of water in question). Further depolarisation of the signal may also be induced by bubbles and particulate matter.

The polarised Raman spectra shown in Figure 3.6 were used to calculate depolarisation ratios for the entire OH stretching band for all temperatures studied. These values were analysed to identify spectral regions of maximum temperature sensitivity. The depolarisation ratio data is shown in Figure 3.14 and the temperature dependence is plotted in Figure 3.15.

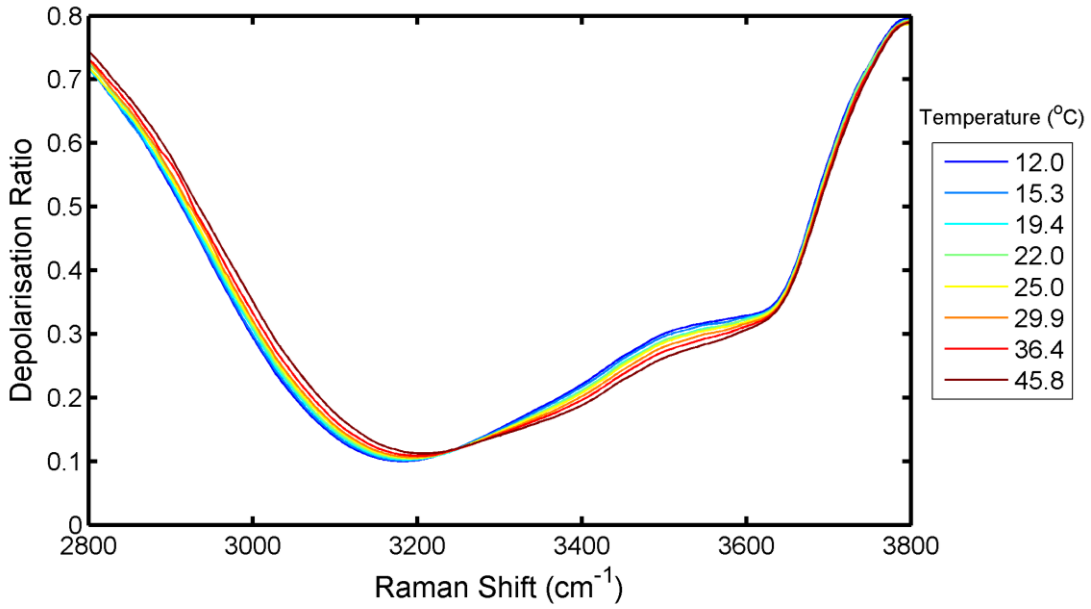

Figure 3.14 – Depolarisation ratio as a function of Raman shift with varying water temperature.

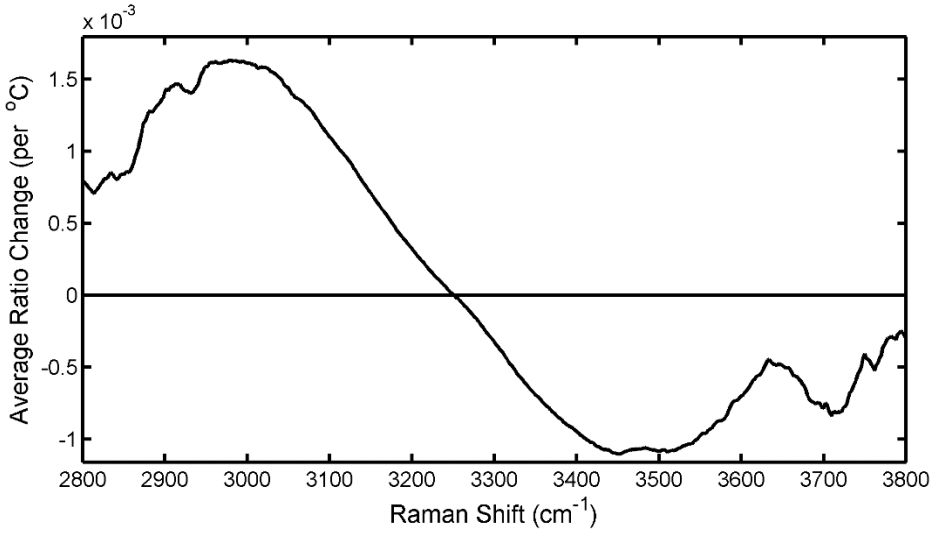

Figure 3.15 – Temperature sensitivity of the depolarisation ratio as a function of Raman shift.

A point in the ratio plot analogous to an isosbestic point was found at ~3250 cm^{-1}. Maximum temperature sensitivity was observed at Raman shifts of 2980 cm^{-1} and 3450 cm^{-1}. While the 2980 cm^{-1} point exhibited greater temperature sensitivity, it is not suitable for a temperature measurement parameter because the intensity of both parallel and perpendicular polarised Raman spectra is extremely weak in this region.

The higher Raman shift point (3450 cm^{-1}) is near the maximum signal for both polarisations, making it the clear choice for investigation. The depolarisation

ratio (0.48 %/°C mean–scaled temperature sensitivity) is substantially less sensitive to temperature change relative to the two–colour ratio (1.50 %/°C).

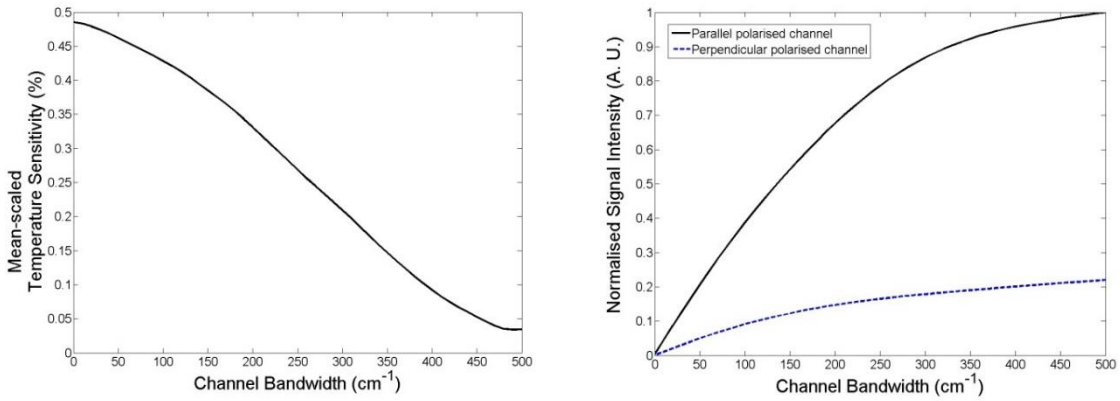

Figure 3.16 – (a) Effect of channel width on the temperature sensitivity of the depolarisation ratio. (b) Integrated channel intensity vs. channel width at 25 °C.

The impact of channel width on temperature sensitivity is examined in Figure 3.16 for a channel centre position of 3450 cm^{-1}. The depolarisation ratio exhibits broadly similar channel width behaviour to the two–colour ratio. The weak intensity of the perpendicular signal is evident in Figure 3.16b, which is normalised to the parallel signal intensity with 500 cm^{-1} channel width. The integrated perpendicular Raman intensity is less than 25 % of the integrated parallel Raman intensity for the OH stretching band.

3.4 Predictive models for determining water temperature from Raman spectra

The temperature–dependent parameters analysed above were applied to the laboratory water Raman spectra and used to estimate water temperature and assess the potential best–case measurement accuracy. Temperature–dependent parameters, namely the two–colour ratio and the depolarisation ratio, were calibrated against the water cell reference temperature recorded during spectra collection, producing a linear relationship with coefficients which can then be applied to estimate the temperature of other water samples. By applying these coefficients to the original calibration data, an estimate of the best–case temperature uncertainty may be obtained. The reference temperature was measured using a 10 kΩ thermistor with an accuracy of ±0.1 °C.

3.4.1 Two–colour ratio

The two–colour ratio was calculated using unpolarised spectra for all possible combinations of spectral data (2 cm^{-1} steps) on the low and high shift sides of 3400 cm^{-1} (over the range 3000 cm^{-1} to 3800 cm^{-1} as described previously) and at each temperature level. A least squares regression was performed for ratio values against reference temperature for each wavenumber pair. This produced sets of coefficients for simple linear expressions:

$$two - colour\ ratio = aT + b \qquad 3.3$$

where T is the temperature and (a,b) are regression coefficients. By rearranging these expressions to predict temperature in terms of the two–colour ratio and coefficients, a predictive model was produced for each wavenumber pair. The ratio values were then used with these models to predict temperature for each combination. The RMS temperature error for each model was calculated, which compares the predicted temperature set with measured reference temperature values. This set of 40,000 RMSE values was calculated with Matlab. The map in Figure 3.17 shows the RMS temperature error values obtained by this method. The colour bar shows RMS temperature error in degrees Celsius. Dark blue regions exhibit relatively low error, while red regions correspond to higher error. The isosbestic point falls in the red region in the upper left corner.

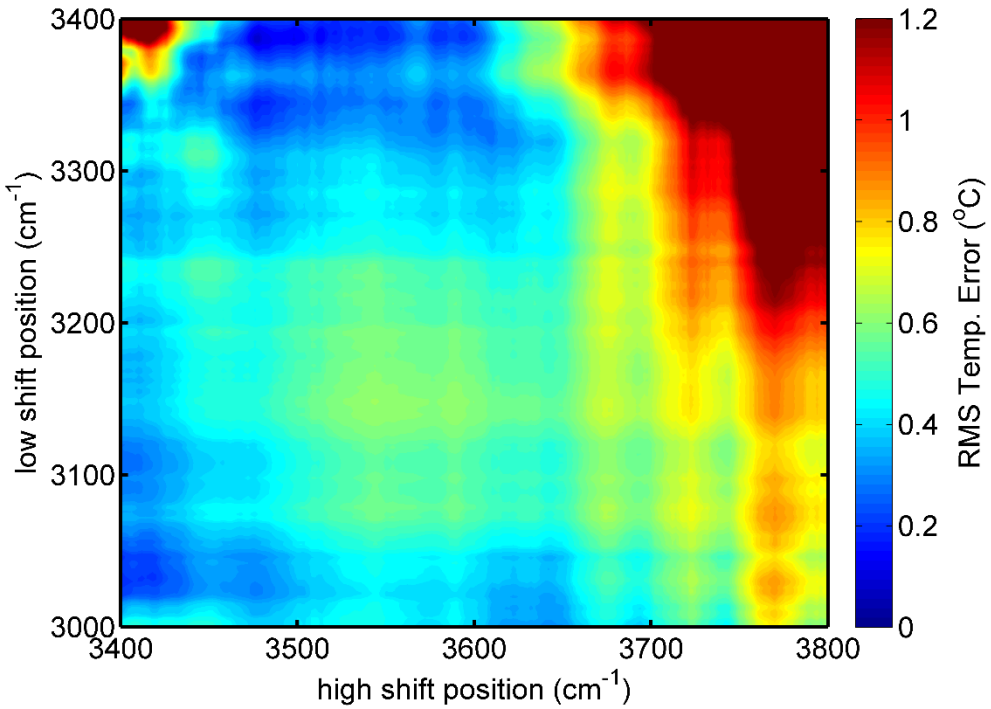

Figure 3.17 – Two–colour ratio RMSE map with varying Raman shift positions for single–point intensity values.

The temperature error is quite variable over the range covered by the map. This is to be expected considering single–point intensity values are used to generate the two–colour ratio. The lowest temperature error did not align with the region of highest temperature sensitivity (as seen in Figure 3.10). In terms of the high shift side of the isosbestic point, lower error values were generally observed for Raman shifts below ~3650 cm^{-1}. For the low shift side of the isosbestic point, lower error was observed near ~3000 cm^{-1} and between 3320 cm^{-1} and 3400 cm^{-1}. The minimum RMS temperature error was ±0.1 °C at 3386 cm^{-1} and 3478 cm^{-1}. The regions of lower RMS error were found close to the isosbestic point. This may possibly be due to these regions lying near the peak of the OH stretching band (and hence where the Raman intensity is greatest). The A and B wavenumber pairs each exhibited similar RMS error values to the other (±0.6 °C).

Next the temperature accuracy was computed for broader channels which were more consistent with practical sensing requirements. Figure 3.18 shows the same spectral data used above recalculated with 200 cm^{-1} channel widths.

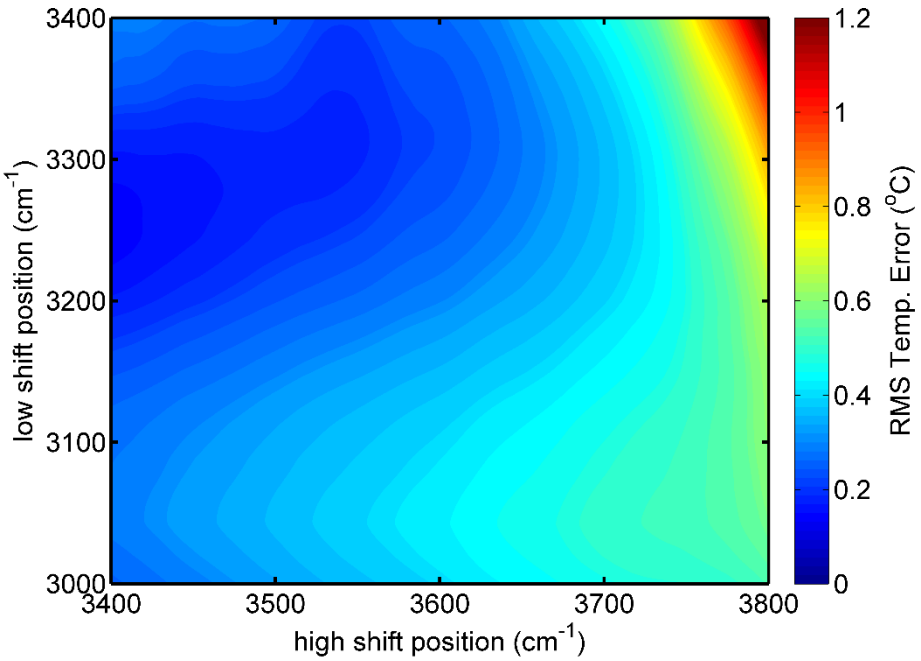

Figure 3.18 – RMS temperature error map for the unpolarised two–colour ratio with varying channel centre positions (200 cm^{-1} channel widths).

The 200 cm^{-1} channel width map shows more consistent and smoother behaviour than the single–point intensity map in Figure 3.17. The minimum RMS temperature error was approximately ±0.1 °C, which occurred with channels centred at approximately 3240 cm^{-1} and 3400 cm^{-1}. The higher channel centre is very close to the isosbestic point, and actually sits on the low shift side, though the large channel

width means the band covers a significant range on both sides. The two channels overlap by ~50 cm^{-1}. While this is somewhat counter–intuitive in terms of temperature sensitivity, this does not preclude such an arrangement providing better temperature accuracy in ideal conditions. RMS temperature error of ±0.2 °C is found with high side channel centre positions up to ~3450 cm^{-1}, where no overlap occurs between the two channels. The 'A' wavenumber pair produced an RMS temperature error of ±0.3 °C, while the 'B' wavenumber pair RMS temperature error was ±0.4 °C.

Larger channel widths have the effect of compensating for intensity fluctuations (noise) in the Raman spectra. These variations are small in comparison with the integrated spectral channels, and are reduced in their impact as channel widths are increased. Hence increased channel width should provide for more consistent temperature prediction, assuming the loss in temperature sensitivity can be coped with.

Figure 3.19 shows regression plots of the temperature predicted from Raman spectra versus physically measured reference temperature values with 200 cm^{-1} channel widths.

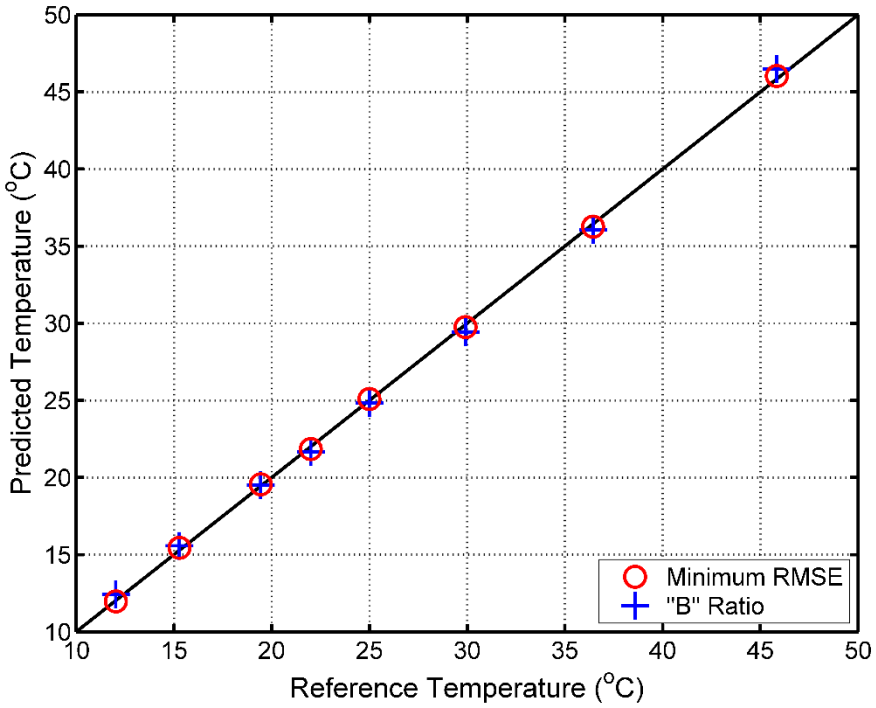

Figure 3.19 – Reference vs. predicted temperature for the unpolarised two–colour ratio with 200 cm^{-1} channel widths (Minimum RMSE: ±0.1 °C, B Ratio RMSE: ±0.4 °C).

The two data series in Figure 3.19 correspond to 200 cm^{-1} channel width two–colour ratios for the minimum temperature error observed (±0.1 °C with centres of 3240 cm^{-1} & 3400 cm^{-1}), and the 'B' wavenumber pair (±0.4 °C with centres of 3120 cm^{-1} & 3586 cm^{-1}) for maximum ratio temperature sensitivity. The black line represents the ideal relationship. In general the unpolarised ratio parameter produced very consistent results with minimal processing applied to spectra (Savitsky–Golay smoothing only).

The same analysis of temperature accuracy described here was also applied to parallel polarised Raman spectra. The results were very similar to those presented for unpolarised spectra and therefore are not presented in detail. The minimum RMS temperature error was found to be ±0.1 °C for single–point intensity values and ±0.2 °C for 200 cm^{-1} channel widths.

3.4.2 Depolarisation ratio

The depolarisation ratio was used to produce temperature–dependent regression models for each wavenumber position over the entire OH stretching band. Estimates of temperature error were made based on reference temperatures as in the two–colour ratio case. Figure 3.20 shows the depolarisation ratio RMSE based on single–point intensities.

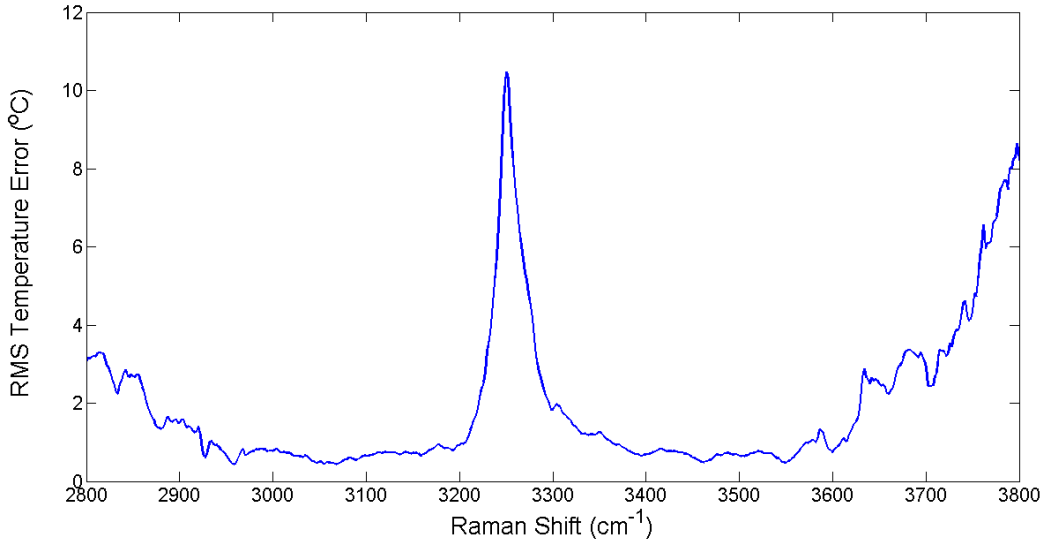

Figure 3.20 – RMS temperature error for the depolarisation ratio over the OH stretching band for single–point intensity values.

The peak at ~3250 cm^{-1} with corresponds to the point of minimum temperature dependence (analogous to an isosbestic point) in the depolarisation

ratio data. The minimum RMSE in the high intensity region (to the right of the peak) was found to be ±0.5 °C at 3550 cm^{-1}. At the point of maximum ratio temperature sensitivity (3450 cm^{-1}), RMS temperature error was ±0.6 °C. Extending to larger channel widths reduced the channel centre position dependence, but increased the magnitude of error values. With a channel width of 200 cm^{-1}, the minimum RMS temperature error was ±0.8 °C at 3428 cm^{-1}. Figure 3.21 shows the correlation between reference temperature and predicted temperature values using the depolarisation ratio with 200 cm^{-1} channel widths centred at 3428 cm^{-1}.

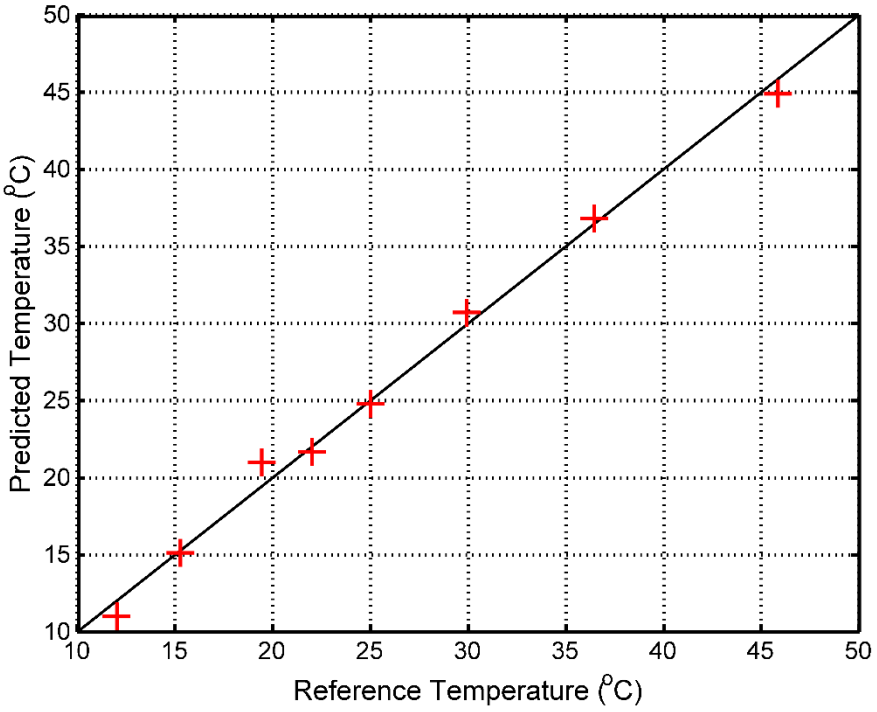

Figure 3.21 – Reference vs. predicted temperature estimated with the depolarisation ratio and 200 cm^{-1} channel widths (RMSE: ±0.8 °C).

Temperature measurement based on the depolarisation ratio exhibits somewhat greater variability, with higher temperature error values observed compared with the two–colour ratio. The weaker temperature dependence of the depolarisation ratio compared with the two–colour ratio may be partially responsible for this. However the variability most likely stems from the inability of the Raman spectrometer to record orthogonal linearly polarised spectra simultaneously. Each polarised spectrum was recorded from a separate spectrometer scan, with appropriately aligned polarising filters inserted in the detection path to select the desired polarisation. By comparison the two–colour ratio was always calculated from a single spectrum. The depolarisation ratio variability was verified by repeated

acquisitions of spectra over time and alternating between the polarising filters. This shortcoming is important to bear in mind when considering the implications of this study for practical remote sensing because it is a direct consequence of instrumentation that could be avoided in a practical field implementation.

3.4.3 Linear combination of spectral parameters

The use of a single temperature–dependent parameter will always be at least somewhat vulnerable to external influence such as fluorescence, ambient light, sea state, etc. A viable and potentially more robust alternative to using a single parameter involves producing a linear combination of multiple parameters, thereby reducing the impact of isolated or non–linear changes in individual parameters on the calibration model. A variety of methods were explored, but multiple linear regression (MLR) was selected for application to Raman temperature analysis.

The two–colour and depolarisation ratio temperature relations developed above were used to produce a linear regression combination of these two parameters with MLR. The individual parameter equations have the standard linear form:

$$\boldsymbol{T = b_1 TwoColourRatio + b_0}$$

$$\boldsymbol{T = c_1 DepolRatio + c_0}$$

while the combined equation takes the form:

$$\boldsymbol{T = a_2 DepolRatio + a_1 TwoColourRatio + a_0}$$

where a_0, a_1 and a_2 are the coefficients generated by the MLR procedure. The relative performance of this combined approach was compared with the two–colour and depolarisation ratio parameters. Figure 3.22 shows the temperature correlation of the MLR model, and the two–colour and depolarisation ratio temperature predictions for minimum RMSE with 200 cm^{-1} channel widths.

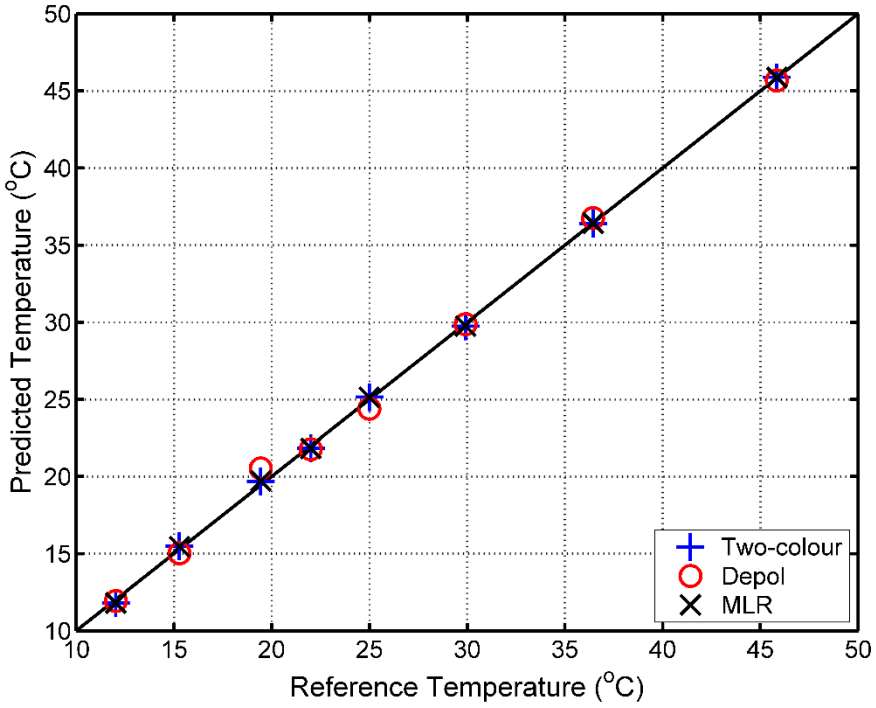

Figure 3.22 – Raman vs. reference temperature calibration for the two–colour ratio, depolarisation ratio and MLR combination with single–point intensities (RMSE: ±0.1 °C, ±0.5 °C, ±0.1 °C respectively).

The linear (MLR) combination data (shown in black) matches well with the two–colour ratio (blue), and hence with the ideal match line. The depolarisation ratio points (red) which vary from the expected linear relationship have minimal to no impact on the corresponding linear combination points. This behaviour was commonly observed with the depolarisation ratio because of the variability previously discussed. MLR models tend to produce similar measurement error behaviour to the unpolarised ratio data. Effectively data which deviates from the expected linear behaviour is down–weighted in its contribution to the regression model.

Figure 3.23 shows an equivalent MLR model for the same parameters calculated for 200 cm^{-1} channel widths and the channel centre positions which gave the minimum RMSE error used in Figure 3.22.

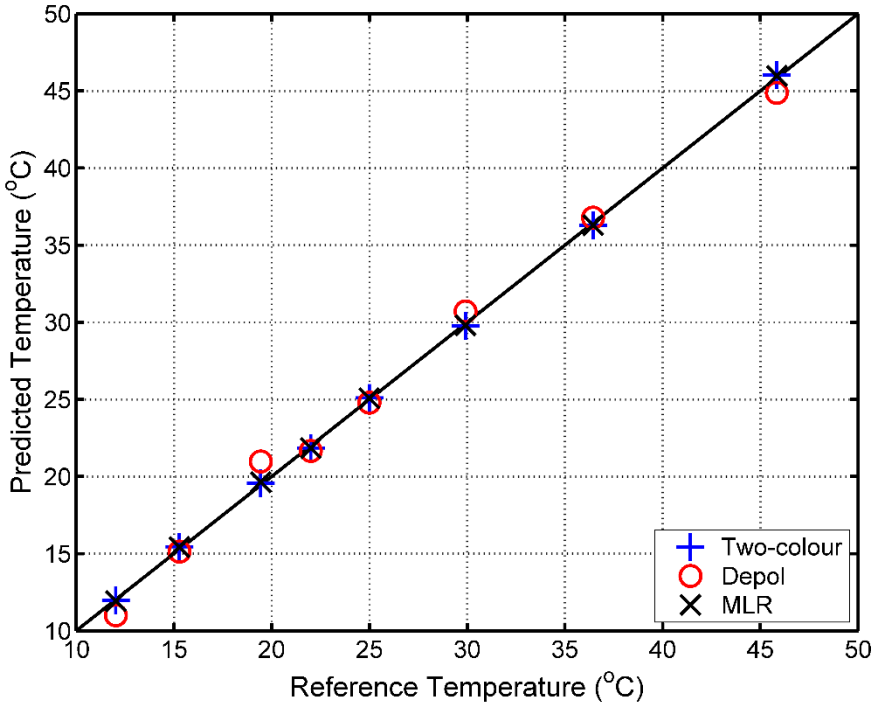

Figure 3.23 – Raman vs. reference temperature calibration for the two–colour ratio, depolarisation ratio and MLR combination with 200 cm^{-1} channel widths (RMSE: 0.1 °C, 0.8 °C 0.1 °C respectively).

The increased error associated with the depolarisation ratio with 200 cm^{-1} channel widths is clearly evident, while the linear combination again tracks closely with the two–colour ratio. It was unfortunate that the relatively large error associated with the depolarisation ratio prevented the benefits of this linear combination approach from being fully realised.

3.5 Proposed designs for multi–channel spectrometers

The detailed analysis of Raman spectra presented in this chapter was used to inform the design of simple multi–channel instruments for determination of water temperature. Three instrument configurations are depicted in Figure 3.24, based on the two–colour ratio, depolarisation ratio and linear combination approaches respectively.

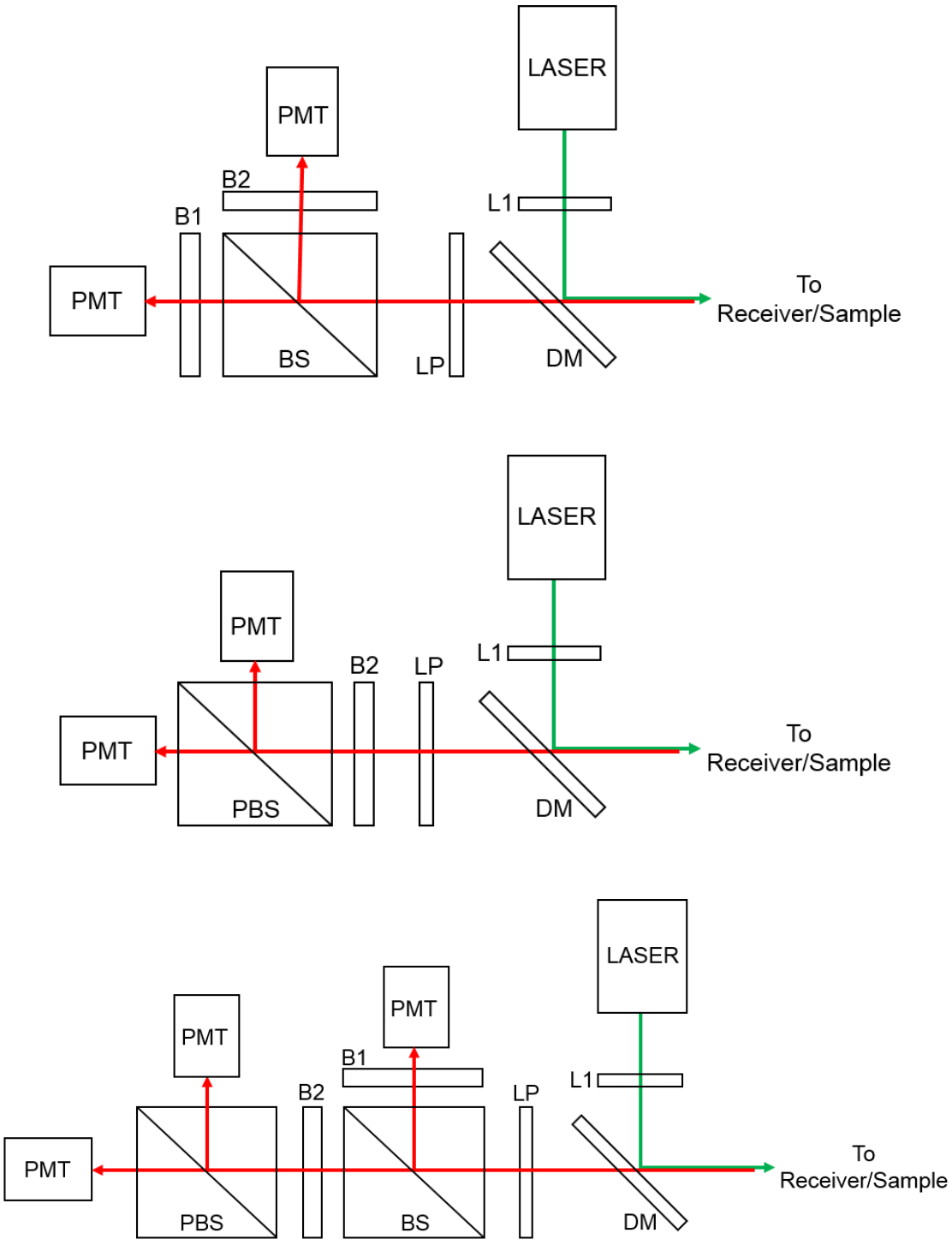

Figure 3.24 – Optical system configurations for multi–channel Raman sensing. (a) two–colour ratio, (b) depolarisation ratio, (c) both two-colour and depolarisation ratios.

The coaxial laser/signal geometry shown in each of the three cases is one possible option, though a variety of alternatives exist depending on the intended purpose. A laser line filter (L1) is used to ensure single wavelength excitation, a dichroic mirror (DM) reflects the laser wavelength to the water sample or a suitable

receiver, while passing returning longer wavelengths. A long–pass filter (LP) with an appropriate edge wavelength is used to improve laser light rejection.

The two–colour ratio design in Figure 3.24(a) uses a 50:50 polarisation–insensitive beamsplitter (BS) to split the return signal to two band–pass filters (B1/B2), followed by detection with photomultipliers (PMT). This is the simplest configuration, and was used for preliminary field experiments in the last stages of these studies.

The depolarisation ratio configuration in Figure 3.24(b) uses a single band–pass filter (B2) corresponding to the optimal channel specifications. A polarising beam–splitter (PBS) divides the signal into linear polarised components for detection with photomultipliers. Polarised spectra are acquired simultaneously in this scheme, which may alleviate the variability issues with the depolarisation ratio described in Section 3.4.2, making it a more effective and accurate means of temperature determination.

The linear combination design in Figure 3.24(c) collects both the two–colour and depolarisation ratios. A 50:50 beamsplitter (BS) passes the signal to a band–pass filter (B1) for the low shift channel of the two–colour ratio and detected with a photomultiplier, and through a band–pass filter (B2), which corresponds to both the high shift channel of the two–colour ratio and an appropriate channel for the depolarisation ratio. A polarising beamsplitter (PBS) is used to divide the signal, with photomultipliers detecting the polarised components. A two–colour ratio is calculated by summing these polarised components to give a high shift channel signal, and the ratio calculated with the low side channel. In this way both the depolarisation ratio and two–colour ratio may be calculated for the MLR combination with minimal signal loss and three detection channels.

These sensing configurations were designed to be compatible with pulsed laser excitation so that time–of–flight ranged measurement can be implemented with fast photomultipliers (e.g. Hamamatsu H10721 PMT modules with ~0.6 ns rise time). The optical components required for these systems are shown in Table 3.2, including examples of suitable commercially available components. Further remote sensing equipment specifications may be found in Appendix E.

Descriptor	Element	Specification	Example
L1	Laser line filter	HT@532 nm	Semrock LL01-532
DM	Dichroic mirror	HR@532nm HT>538nm	Semrock FF538-FDi01
LP	Long–pass filter	HT>537nm	Semrock BLP01-532R
B1 B2	Band–pass filter	HT@637-647nm HT@654-667nm	Semrock FF01-642/10 Semrock FF01-660/13
BS	50:50 beamsplitting cube	HT@400-700nm	Thorlabs BS013
PBS	Polarising beamsplitting cube	HT@400-700nm	Thorlabs PBS251

Table 3.2 –Optical components appropriate for the three multi–channel configurations shown in Figure 3.24 for 532 nm excitation.

Band–pass filters and other optical elements were identified which broadly correspond to the optimal specifications determined previously. The band–pass filters in particular were as close as could be found to the optimal channel specifications for 532 nm excitation, but a limited variety of appropriate commercial filters exist, and are generally designed to complement specific fluorophores. Custom designed filters would be superior, though substantially increasing the cost of such a system.

The sensing configurations described above represent viable options for testing of the temperature determination methods described above. The sensing experimentation which has been conducted in parallel with the research presented in this thesis has employed the first configuration shown in Figure 3.24 as a starting point for laboratory detection of Raman signals including characterisation of photomultiplier and filter performance, ranged sensing of Raman scattering, initial temperature–dependent measurements and field sensing of Raman return from coastal waters. Figure 3.25 shows the system used for remote sensing experiments.

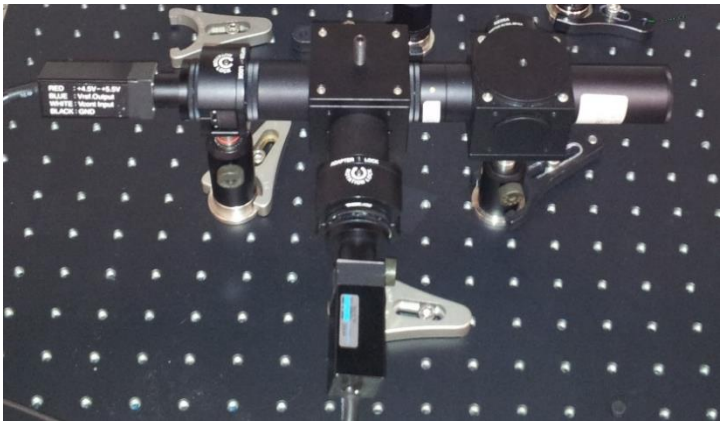

Figure 3.25 – Sensing system designed for temperature sensing with the two–colour method (as shown in Figure 3.24a).

The sensing setup is completely enclosed in a light–tight cage system except for the input port with laser line filter and the receiver aperture. A range of receiver designs are possible. PC–based or hardware oscilloscopes were used for triggering and PMT signal acquisition. Figure 3.26 shows a two–colour configuration used in preliminary field experiments.

Figure 3.26 – Two–colour sensing system (as shown in in Figure 3.24a with an added excitation wavelength detection channel) mounted on a telescope receiver for field sensing experiments.

For these experiments, 532 nm laser pulses were delivered by a turning mirror independent of the receiver and sensing setup. A photomultiplier was added in place of the laser in Figure 3.24a to monitor Rayleigh scattered return. Raman signals were detected from depths down to ~5 metres without using receiver optics (simple 50 mm diameter turning mirror), and were substantially more intense than ambient background illumination, even in full sunlight.

3.6 Discussion and Summary

This chapter covered the analysis of Raman scattering behaviour in water in response to temperature variation, and the development of methods to translate this into water temperature measurement. The effect of temperature change on backscattered Raman spectra of pure water has been described in detail, including analysis of both unpolarised spectra and linearly polarised spectral components. The reduction in stretching band area of unpolarised spectra was noted and experiments

were conducted to observe this behaviour over a larger temperature range. Points of maximum temperature sensitivity were identified.

Temperature–dependent parameters based on point intensity values or integrated channels from Raman spectra were analysed for potential in a remote sensing application. The polarised two–colour ratio and depolarisation ratio were identified as suitable temperature measurement parameters. An analytical method of determining optimum channel centre locations for two–colour ratio parameters was devised. The impact of spectral channel width and channel centre locations on temperature measurement uncertainty was assessed for both parameters studied. Finally these parameters were combined using multiple linear regression to increase the robustness and reliability of temperature measurements.

The analytical tools and procedures presented in this chapter go far beyond the scope of previous studies, and for the case of the two–colour method indicate the potential to determine water temperature from Raman spectra with a high degree of accuracy (RMSE of ±0.1 °C). It was unfortunate that the inability of conventional Raman spectrometers to simultaneously acquire polarised Raman spectra precluded the potential of the depolarisation ratio method and consequently the linear combination method from being quantified.

I have applied the tools and procedures developed here to design and analyse (from a numerical modelling perspective) three multi–channel Raman spectroscopic instruments based on the two–colour ratio, depolarisation ratio and linear combinations methods respectively. In the late stages of my PhD work I constructed one of these systems (two–colour) and showed that, when coupled with a 20 μJ pulsed, 532 nm excitation laser, it was effective in retrieving Raman signals in two channels from depths of 5 metres without additional receiver optics.

Chapter 4 will build on the findings of this chapter by applying these methods to natural fresh and salt water samples, and assessing the potential accuracy of temperature measurement which may be achieved.

4 Raman Spectra of Natural Water Samples

This chapter concerns the analysis of Raman spectra acquired from natural water sources. Raman spectra for ten water samples are presented together with analysis based on the findings of Chapter 3. The variations between spectra from different source locations are discussed, particularly with regard to the baseline present in many spectra. Methods are proposed and evaluated for improving the accuracy with which temperature can be determined, and the prospects for practical field determination of temperature in natural waters is discussed.

4.1 Sample Collection and Analysis Methods

Fresh and saline water samples were acquired from multiple locations around Sydney. The majority of seawater samples were obtained from Sydney Harbour, its estuaries and surrounding coastal waters. Fresh water samples were acquired from several local reservoirs and lakes, with a mains supply sample included for comparison. Each sample was analysed within a few hours of collection from the site. Raman spectra were collected using the method described in Section 3.1, though samples acquired later in the course of this research were analysed using the QPod 2e cuvette holder for temperature control, with the samples placed in fused silica cuvettes for acquisition of spectra. Spectra for the Rhodes, Sugarloaf Bay, Woolwich and Macquarie University lake samples were acquired with the

aluminium cell used in Chapter 3. The reference temperature values, spectrometer integration times and averaging also varied slightly for these earlier analysed water samples. Savitsky–Golay smoothing was applied to all spectra using the same parameters as applied in Chapter 3 (25 point window with 2nd order polynomial).

4.2 Raman spectra and numerical analysis for natural water samples

Figure 4.1 shows a map of Sydney with sample collection sites marked.

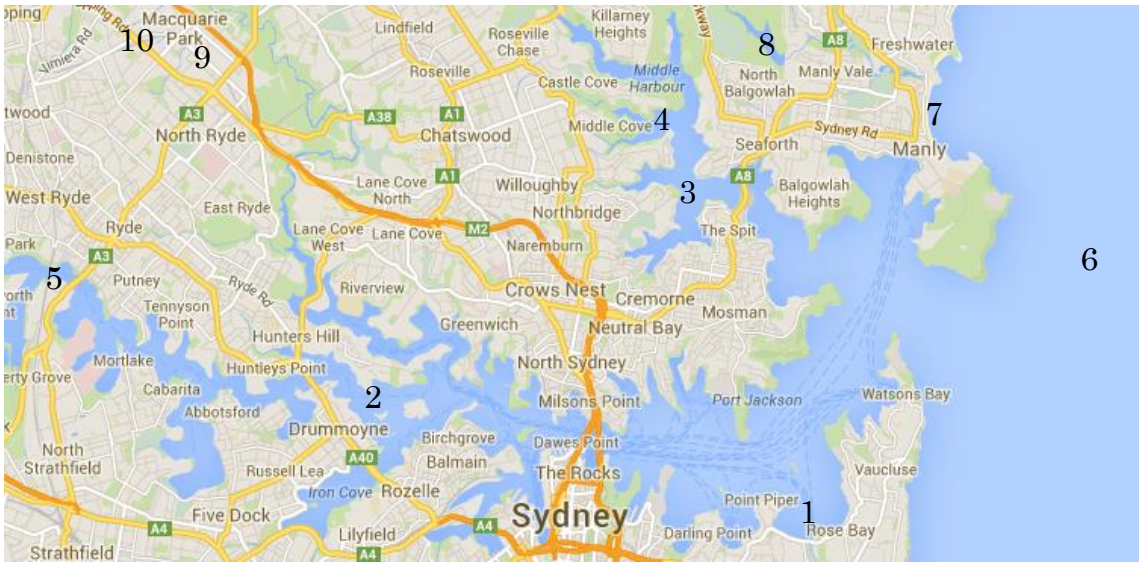

Figure 4.1 – Water sample collection locations. (1) Rose Bay, (2) Woolwich, (3) Clontarf, (4) Sugarloaf Bay, (5) Rhodes, (6) 2 km off North Head, (7) Manly Beach, (8) Manly Dam(fresh), (9) Mains supply(fresh), (10) Macquarie University Lake(fresh). Map: © Google.

Figure 4.2 to Figure 4.11 present temperature dependent Raman spectra and associated analysis plots for water samples collected from the locations shown in Figure 4.1. The figures for each sample are displayed across two pages and arranged as follows:

Left page		Right page	
a)	Unpolarised Raman spectra as a function of temperature.	**d)**	Temperature sensitivity of the mean–scaled two–colour ratio with 200 cm^{-1} channel widths and varying channel centre positions.
b)	Parallel polarised Raman spectra as a function of temperature.	**e)**	Two–colour method RMS temperature error with 200 cm^{-1} channel widths and varying channel centre positions.
		f)	Depolarisation ratio with changing temperature.
c)	Perpendicularly polarised Raman spectra as a function of temperature.	**g)**	Two–colour method predicted vs. reference temperature with 200 cm^{-1} channel widths and centre positions of (3120 cm^{-1} and 3586 cm^{-1}).

The water sample spectra shown in Figure 4.2 to Figure 4.11 exhibit variety in their baseline behaviour and their observed relationship with temperature. Spectra for some samples, such as Rose Bay, have minimal baseline variance and clear isosbestic points, while Rhodes has a moderate baseline offset and no isosbestic point and Clontarf shows severe baseline effects.

The analysis plots in Figure 4.2 to Figure 4.11 were produced using the same methods developed in Chapter 3 for laboratory water. The maps of RMS temperature error for the two–colour ratio in particular, show strong correlations with the quality of sample spectra (assessed on baseline behaviour and spectra consistency). The plots of predicted vs. reference temperature (Figure 4.2g–Figure 4.11g) show reasonable agreement for the majority of water samples, though the samples again show some correlation between RMSE values and perceived water quality (based on the appearance of spectra). The RMSE values were relatively high (> ±1 °C) for Rhodes, Clontarf and Macquarie University Lake in particular. As will be seen in following sections, understanding the origin of baseline effects and applying appropriate correction can lead to substantial improvement in temperature measurement accuracy.

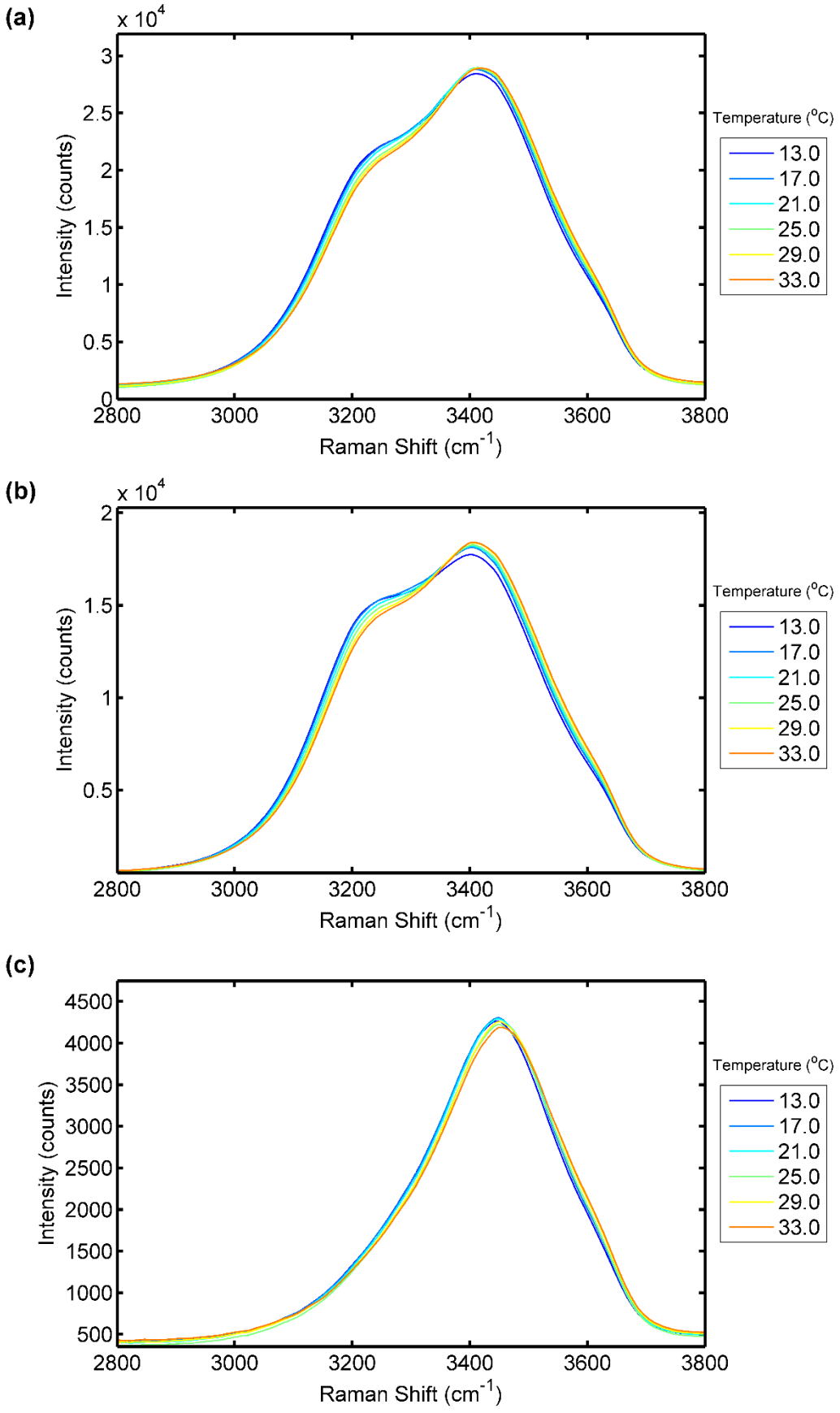

Figure 4.2 – Raman spectra and numerical analysis of the **Rose Bay** water sample: (a) Unpolarised spectra. (b) Parallel polarised spectra. (c) Perpendicularly polarised spectra.

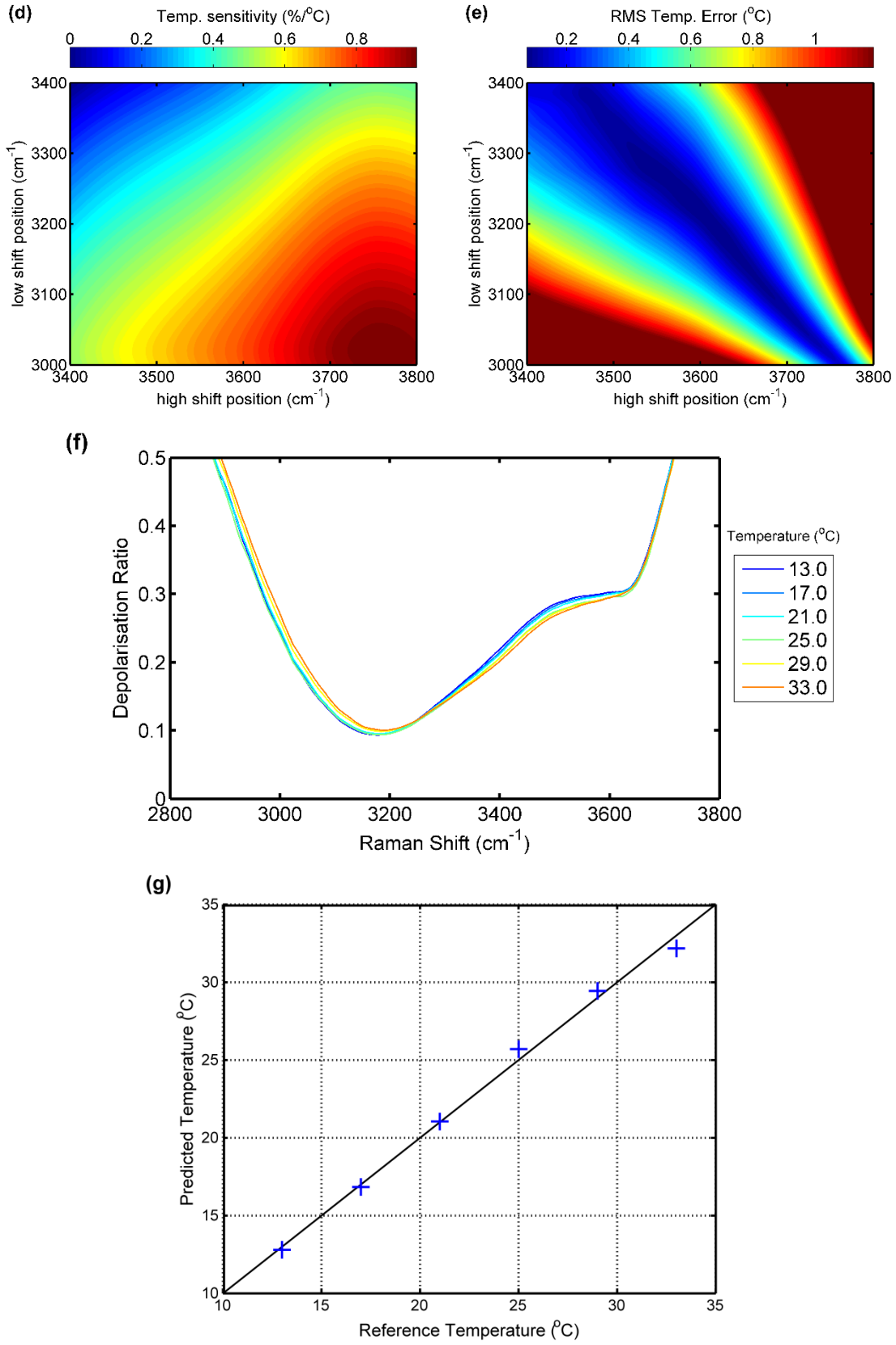

Figure 4.2 – Raman spectral analysis of the **Rose Bay** water sample: (d) Temperature sensitivity for the two–colour ratio. (e) RMS temperature error for the two–colour ratio. (f) Depolarisation ratio. (g) Predicted vs. reference temperature for the two–colour method (RMSE: ±0.5 °C).

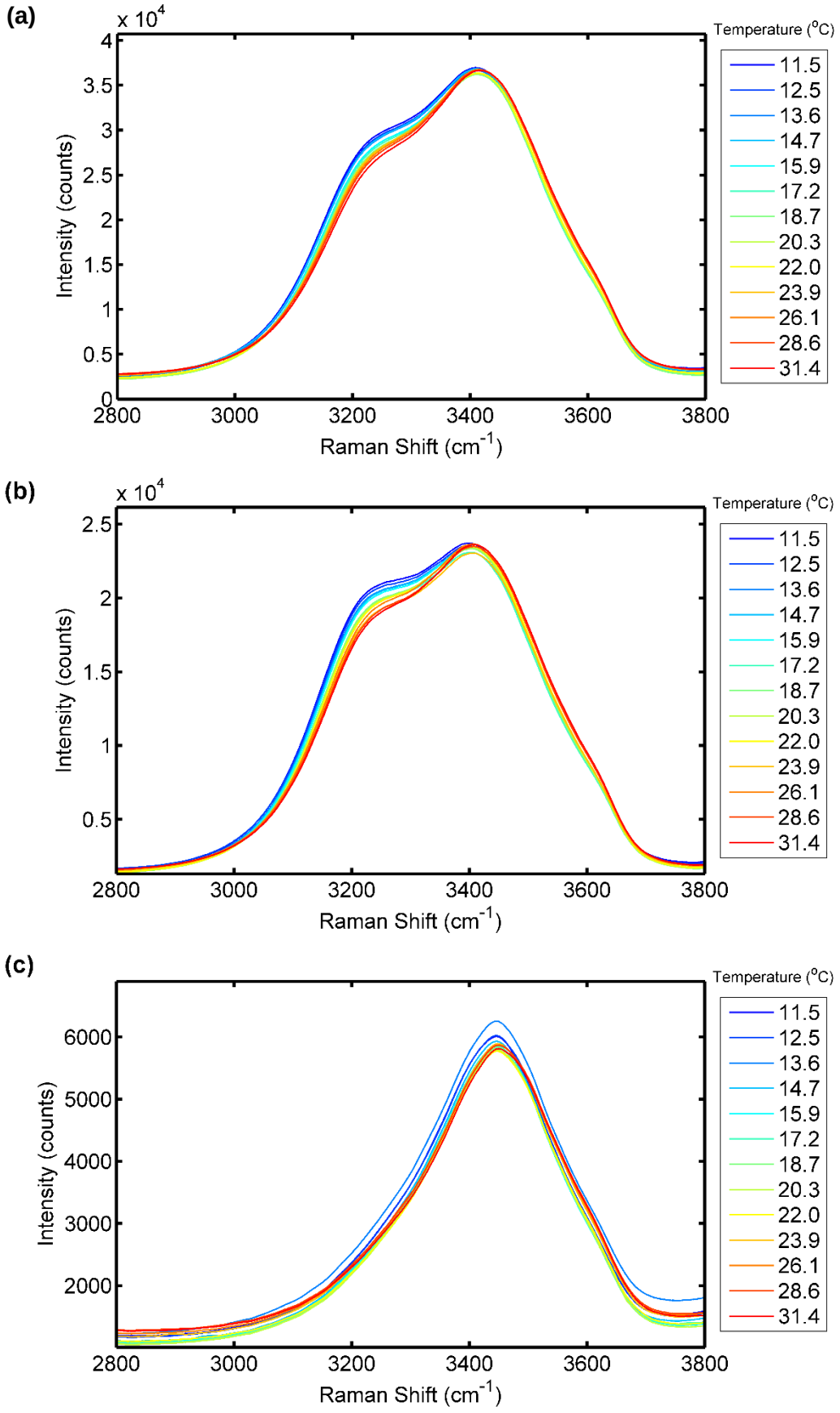

Figure 4.3 – Raman spectra and numerical analysis of the **Woolwich** water sample: (a) Unpolarised spectra. (b) Parallel polarised spectra. (c) Perpendicularly polarised spectra.

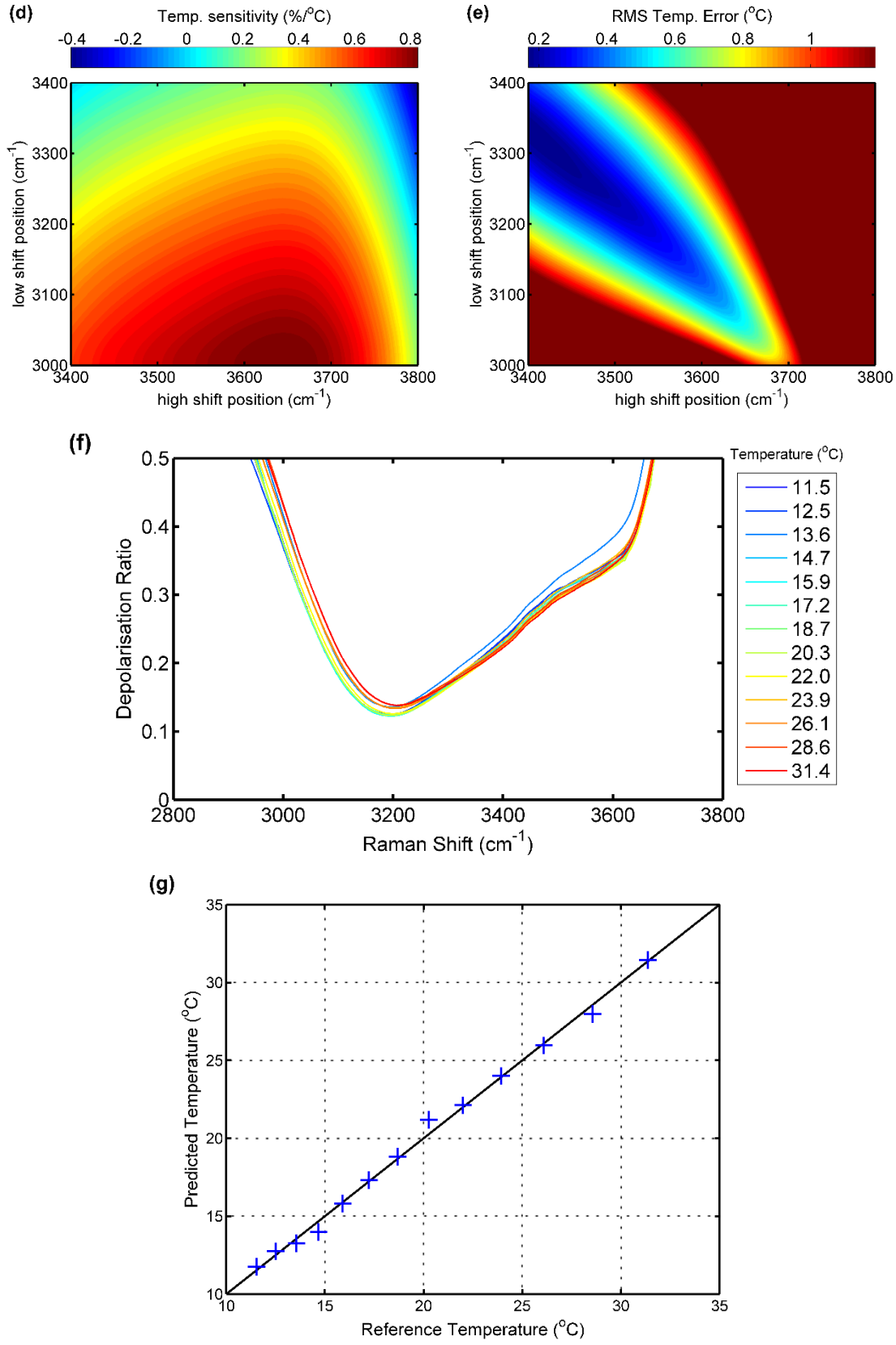

Figure 4.3 – Raman spectral analysis of the **Woolwich** water sample: (d) Temperature sensitivity for the two–colour ratio. (e) RMS temperature error for the two–colour ratio. (f) Depolarisation ratio. (g) Predicted vs. reference temperature for the two–colour method (RMSE: ±0.4 °C).

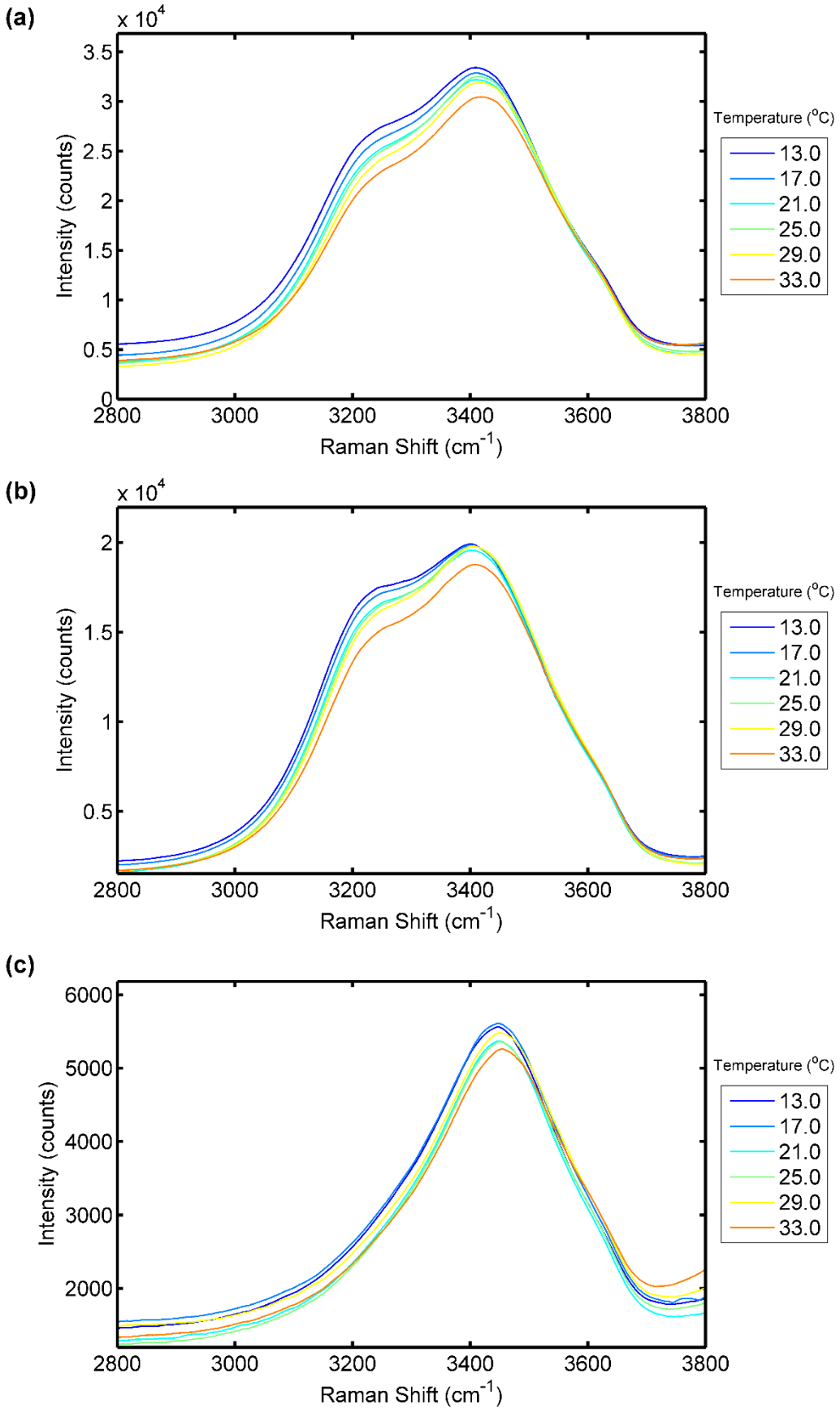

Figure 4.4 – Raman spectra and numerical analysis of the **Clontarf** water sample: (a) Unpolarised spectra. (b) Parallel polarised spectra. (c) Perpendicularly polarised spectra.

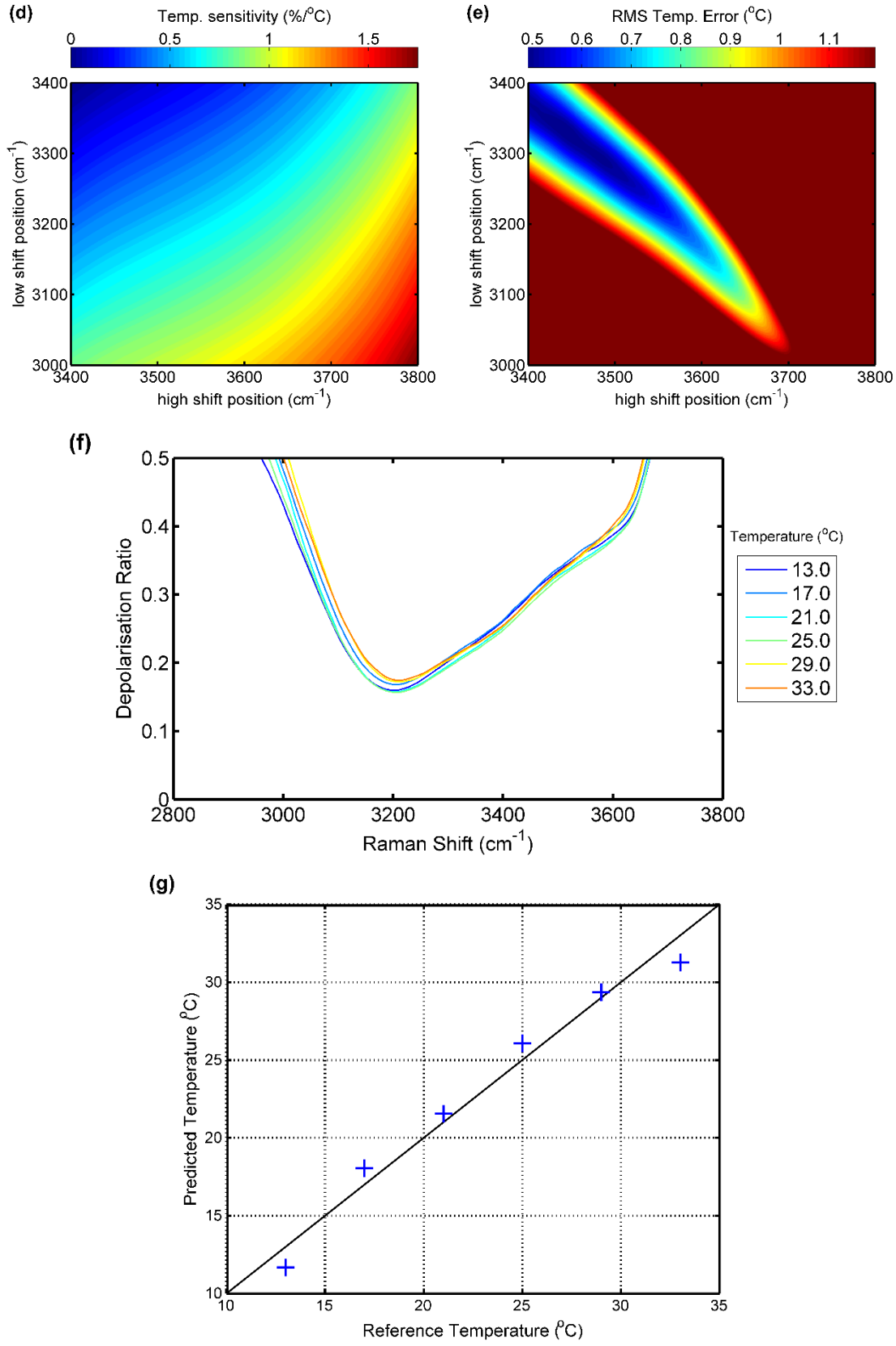

Figure 4.4 – Raman spectral analysis of the **Clontarf** water sample: (d) Temperature sensitivity for the two–colour ratio. (e) RMS temperature error for the two–colour ratio. (f) Depolarisation ratio. (g) Predicted vs. reference temperature for the two–colour method (RMSE: ±1.1 °C).

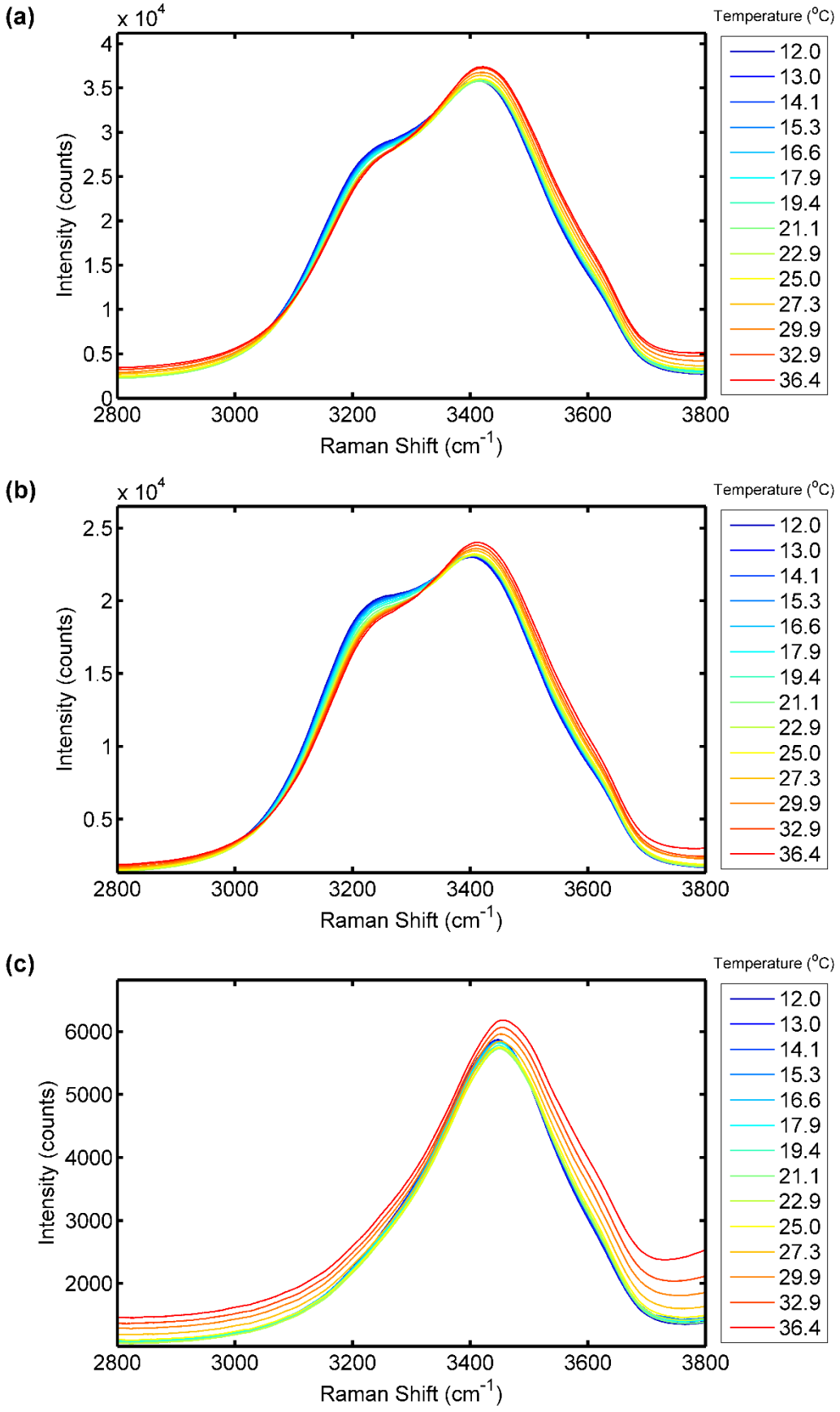

Figure 4.5 – Raman spectra and numerical analysis of the **Sugarloaf Bay** water sample: (a) Unpolarised spectra. (b) Parallel polarised spectra. (c) Perpendicularly polarised spectra.

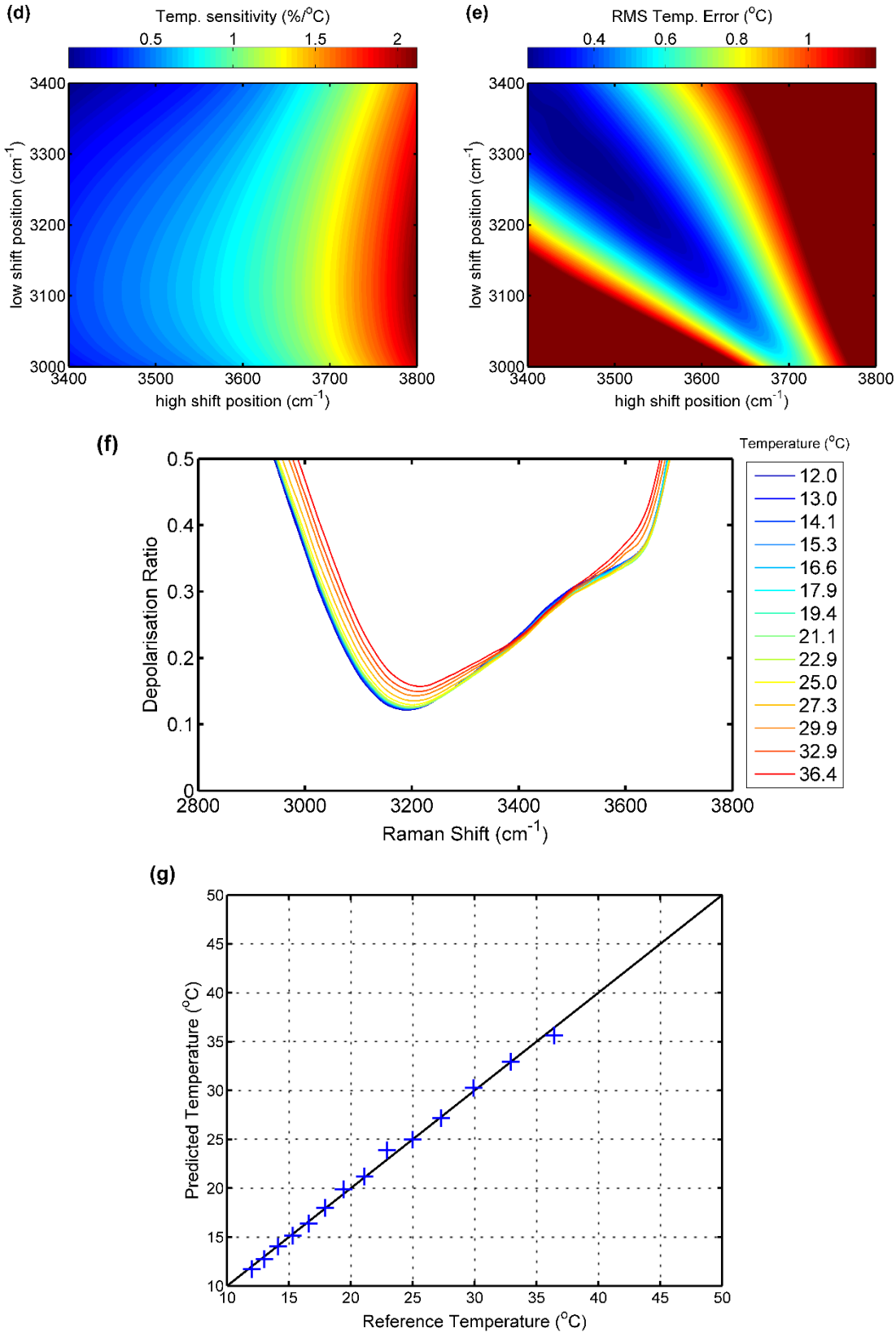

Figure 4.5 – Raman spectral analysis of the **Sugarloaf Bay** water sample: (d) Temperature sensitivity for the two–colour ratio. (e) RMS temperature error for the two–colour ratio. (f) Depolarisation ratio. (g) Predicted vs. reference temperature for the two–colour method (RMSE: ±0.4 °C).

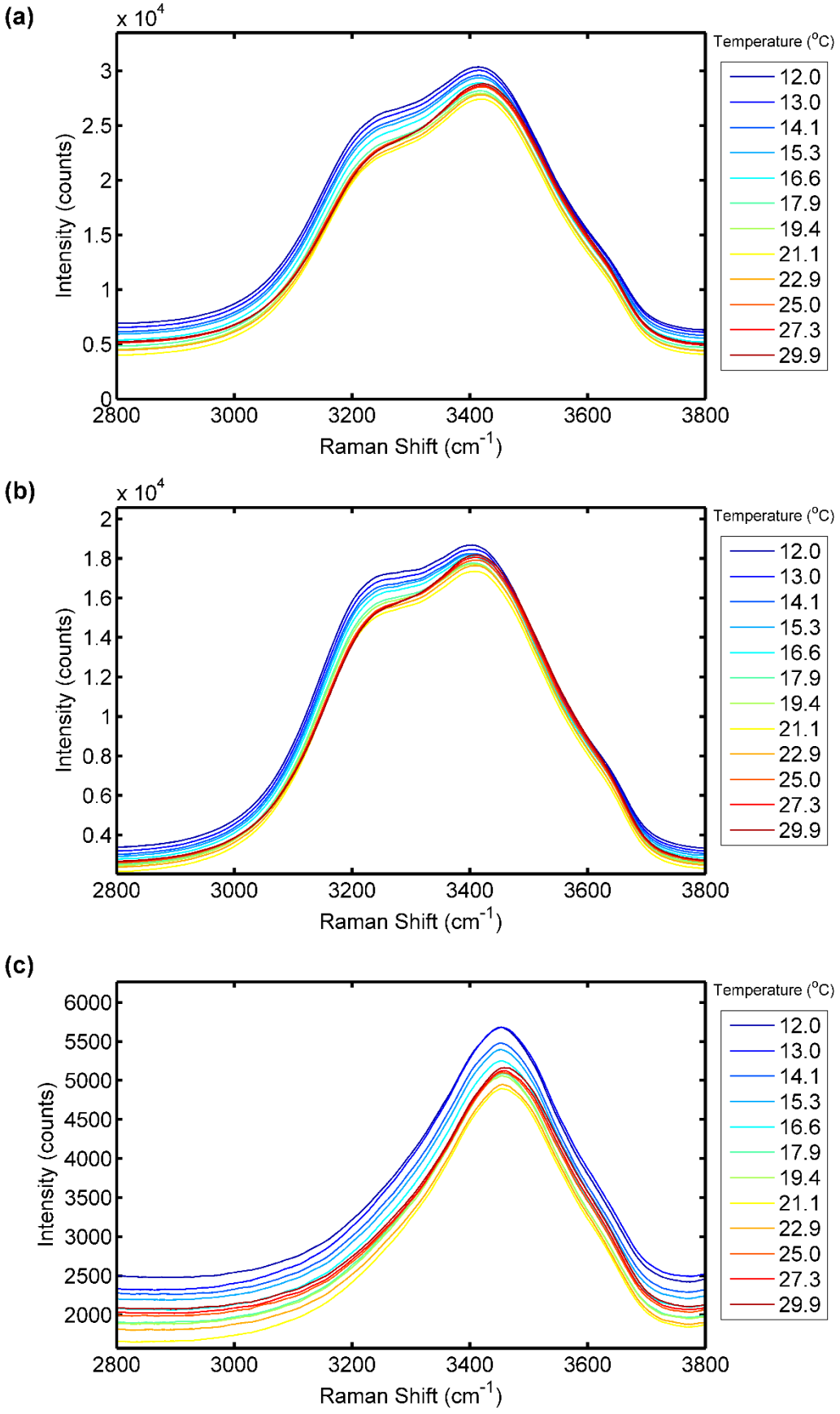

Figure 4.6 – Raman spectra and numerical analysis of the **Rhodes** water sample: (a) Unpolarised spectra. (b) Parallel polarised spectra. (c) Perpendicularly polarised spectra.

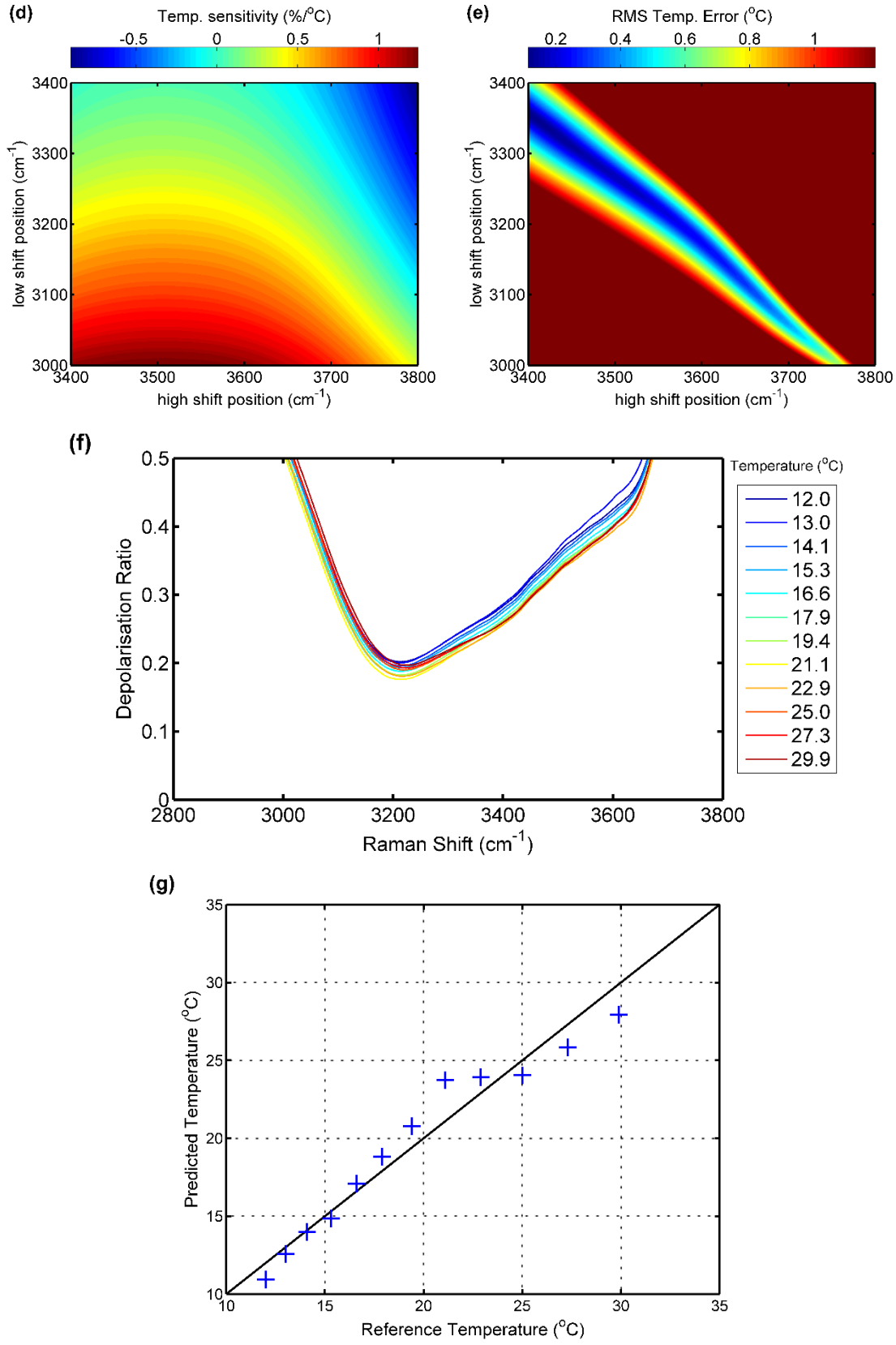

Figure 4.6 – Raman spectral analysis of the **Rhodes** water sample: (d) Temperature sensitivity for the two–colour ratio. (e) RMS temperature error for the two–colour ratio. (f) Depolarisation ratio. (g) Predicted vs. reference temperature for the two–colour method (RMSE: ±1.3 °C).

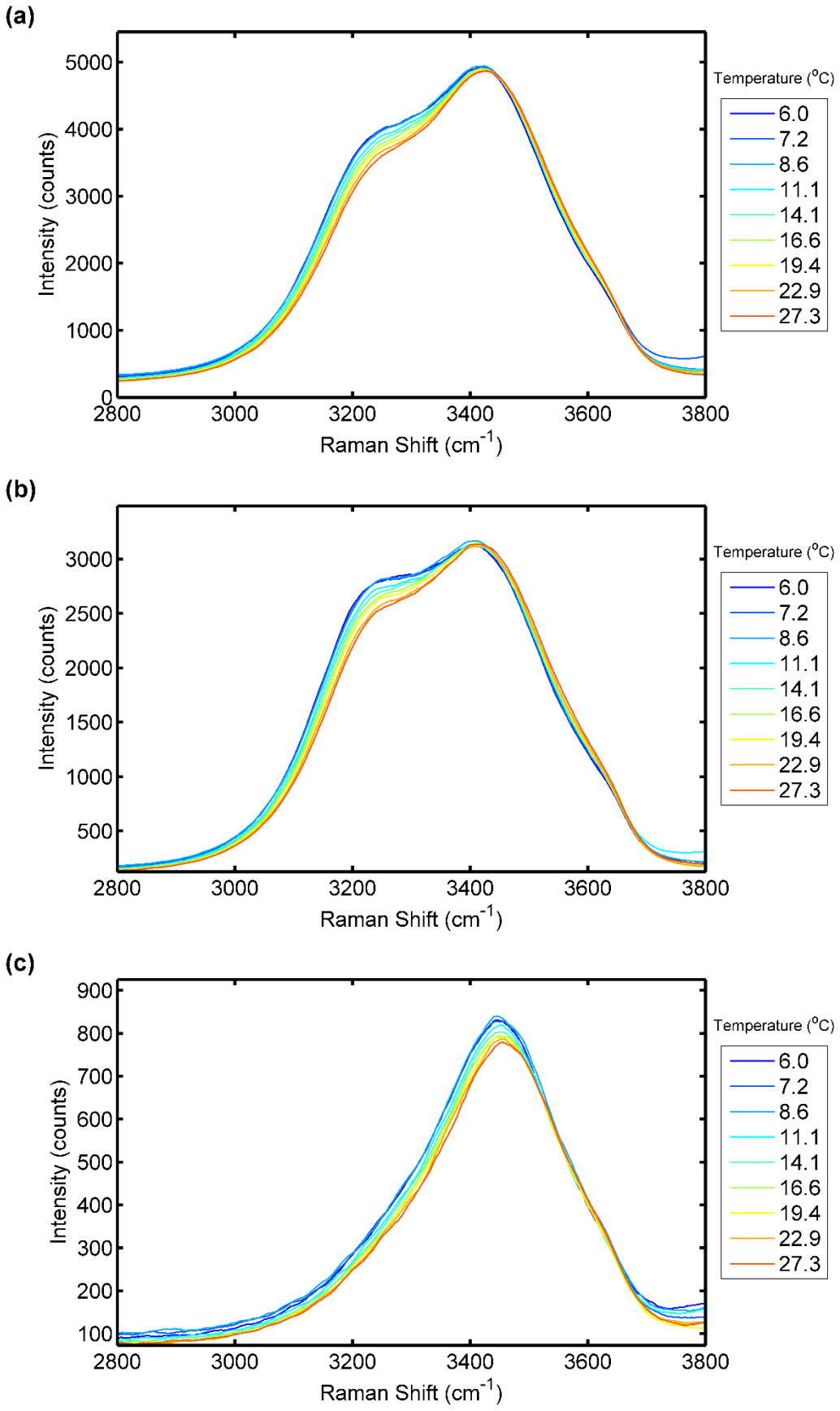

Figure 4.7 – Raman spectra and numerical analysis of the **North Head** water sample: (a) Unpolarised spectra. (b) Parallel polarised spectra. (c) Perpendicularly polarised spectra.

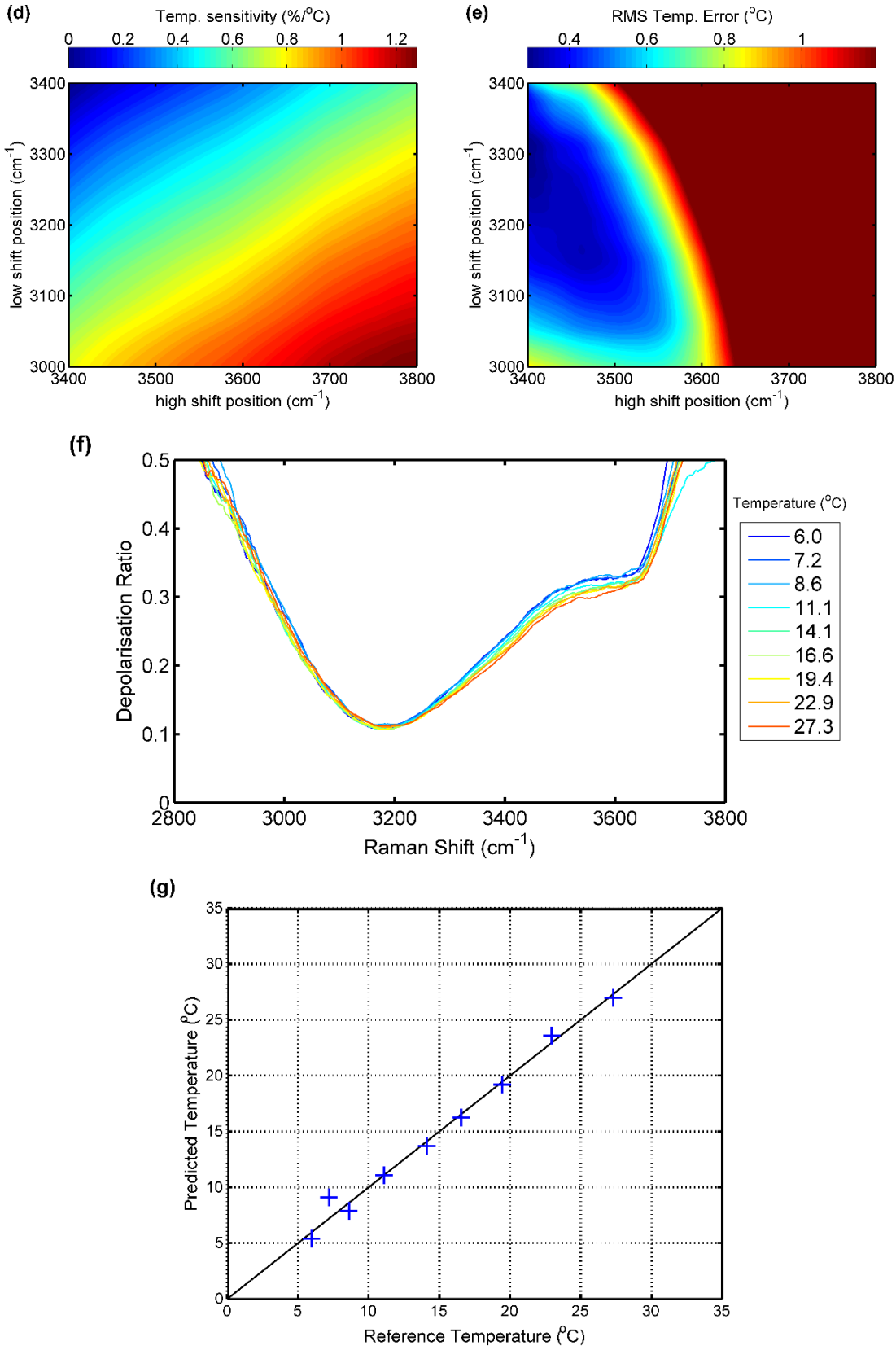

Figure 4.7 – Raman spectral analysis of the **North Head** water sample: (d) Temperature sensitivity for the two–colour ratio. (e) RMS temperature error for the two–colour ratio. (f) Depolarisation ratio. (g) Predicted vs. reference temperature for the two–colour method (RMSE: ±0.8 °C).

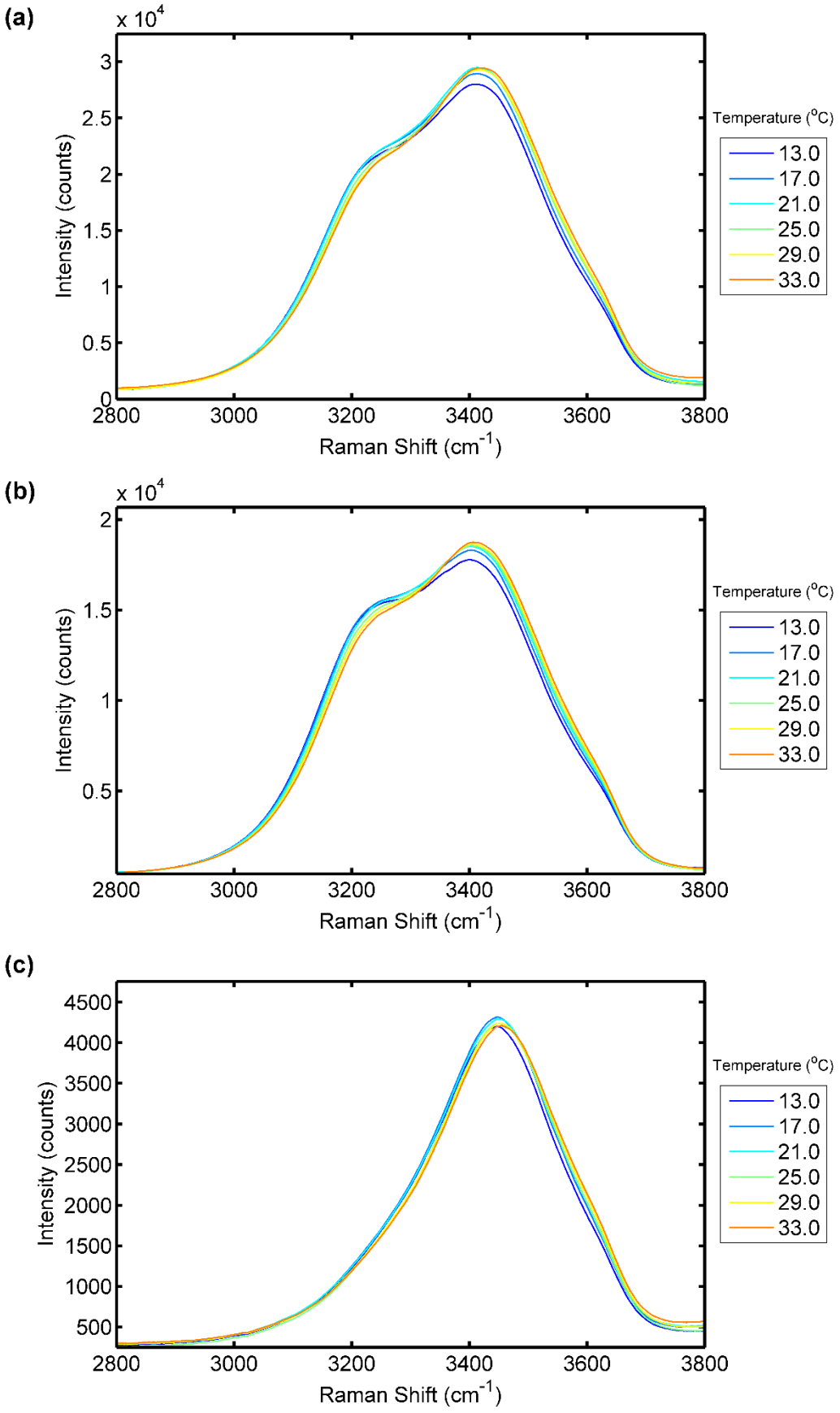

Figure 4.8 – Raman spectra and numerical analysis of the **Manly Beach** water sample: (a) Unpolarised spectra. (b) Parallel polarised spectra. (c) Perpendicularly polarised spectra.

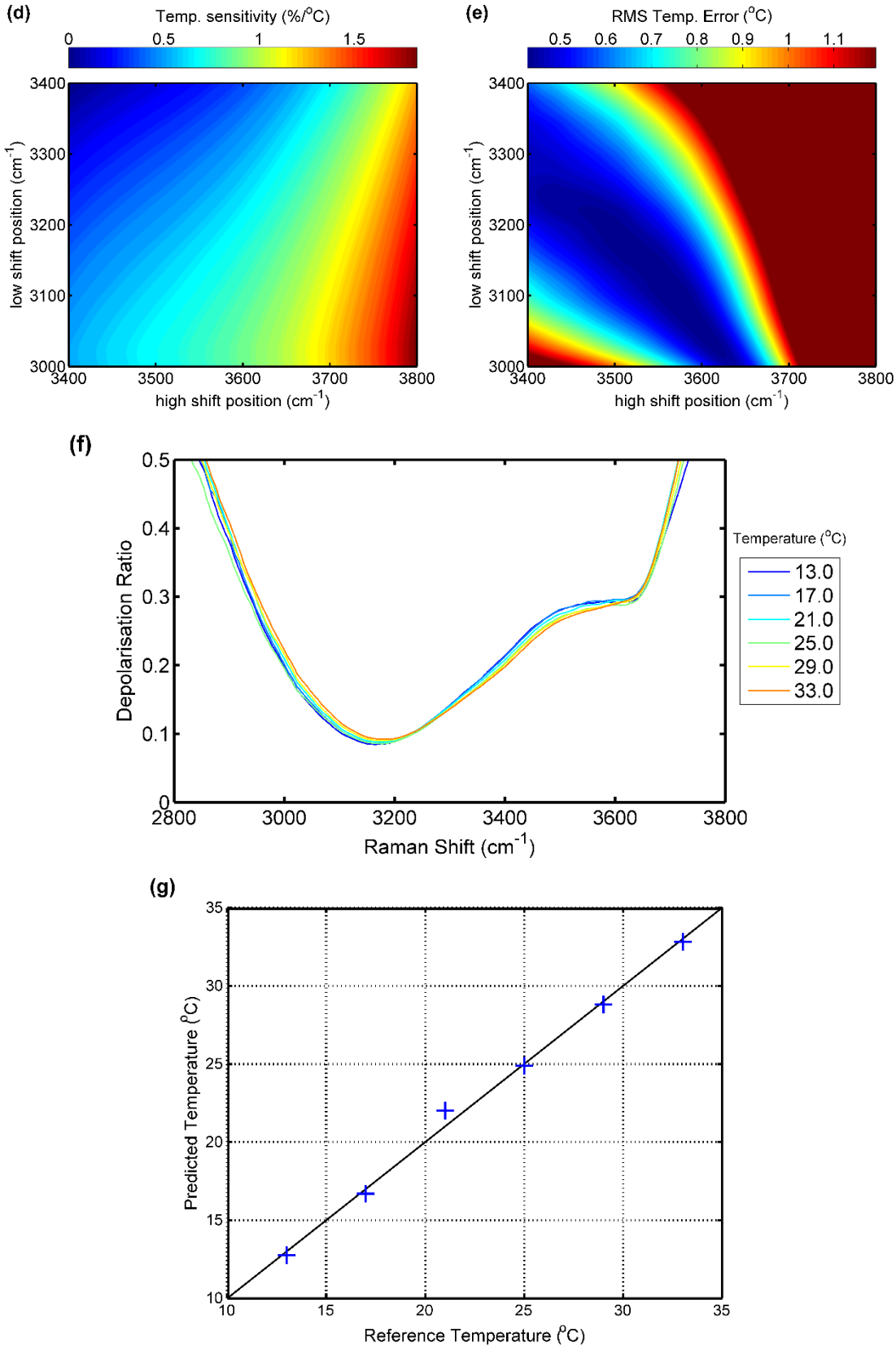

Figure 4.8 – Raman spectral analysis of the **Manly Beach** water sample: (d) Temperature sensitivity for the two–colour ratio. (e) RMS temperature error for the two–colour ratio. (f) Depolarisation ratio. (g) Predicted vs. reference temperature for the two–colour method (RMSE: ±0.5 °C).

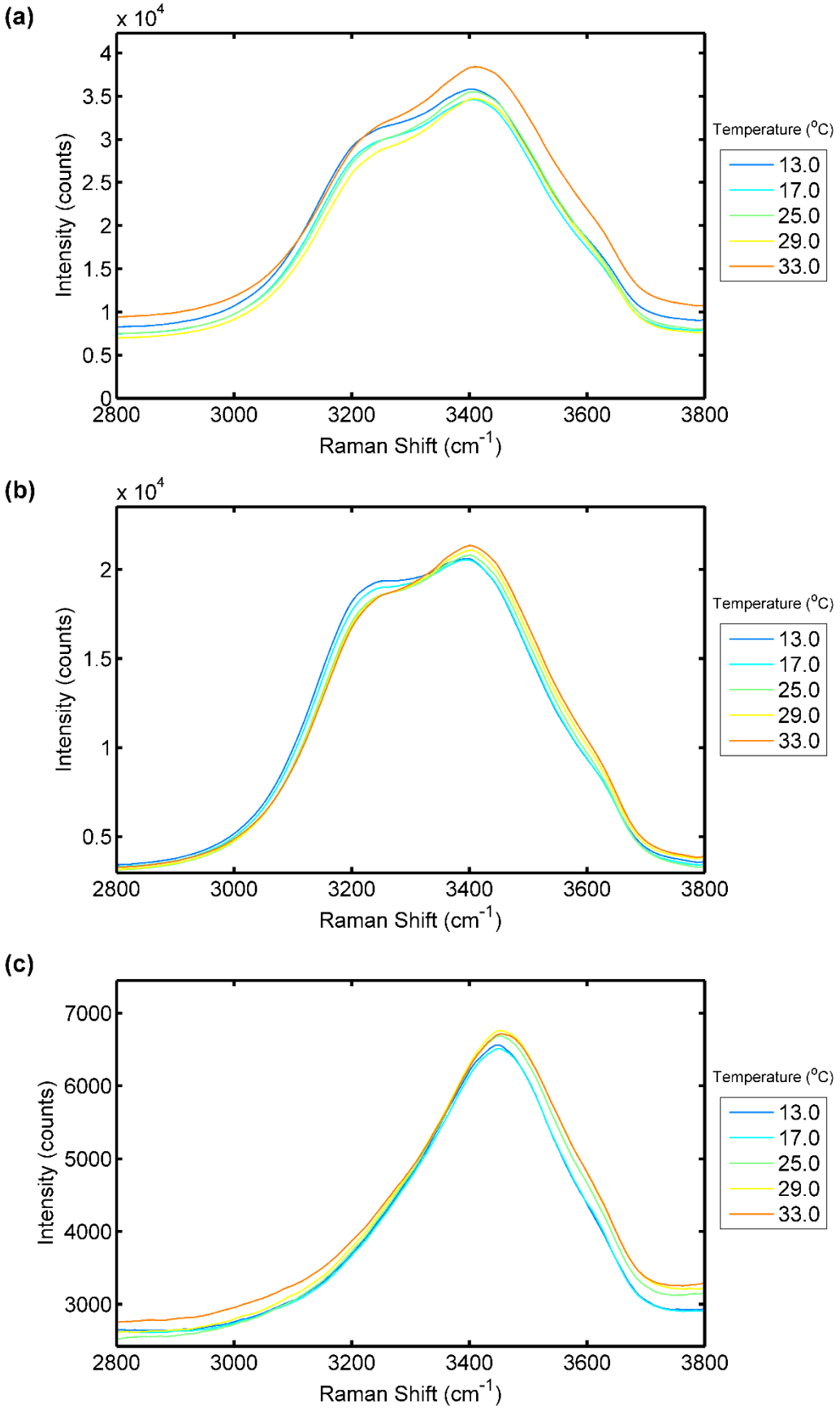

Figure 4.9 – Raman spectra and numerical analysis of the **Manly Dam** water sample: (a) Unpolarised spectra. (b) Parallel polarised spectra. (c) Perpendicularly polarised spectra.

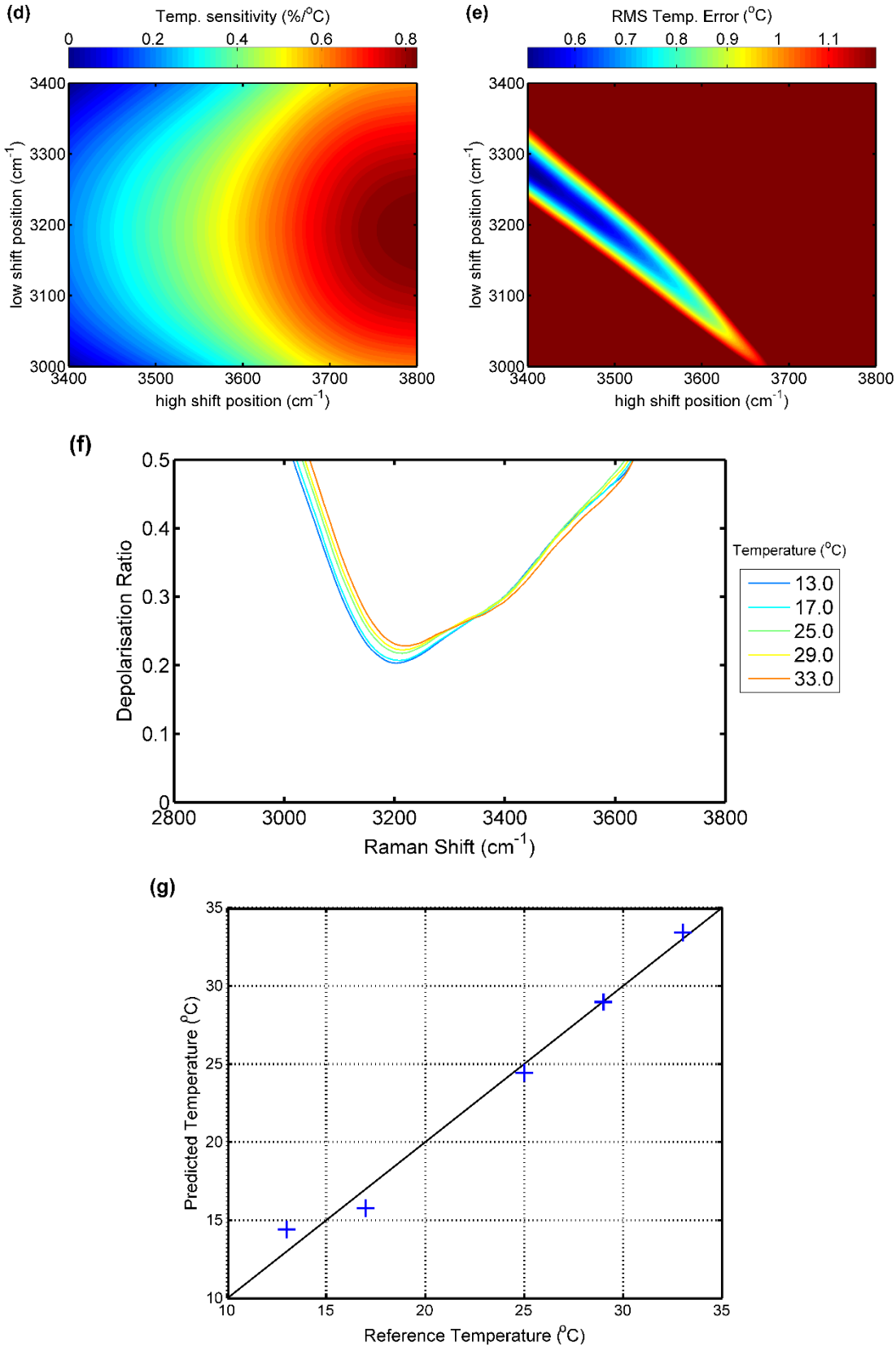

Figure 4.9 – Raman spectral analysis of the **Manly Dam** water sample: (d) Temperature sensitivity for the two–colour ratio. (e) RMS temperature error for the two–colour ratio. (f) Depolarisation ratio. (g) Predicted vs. reference temperature for the two–colour method (RMSE: ±0.9 °C).

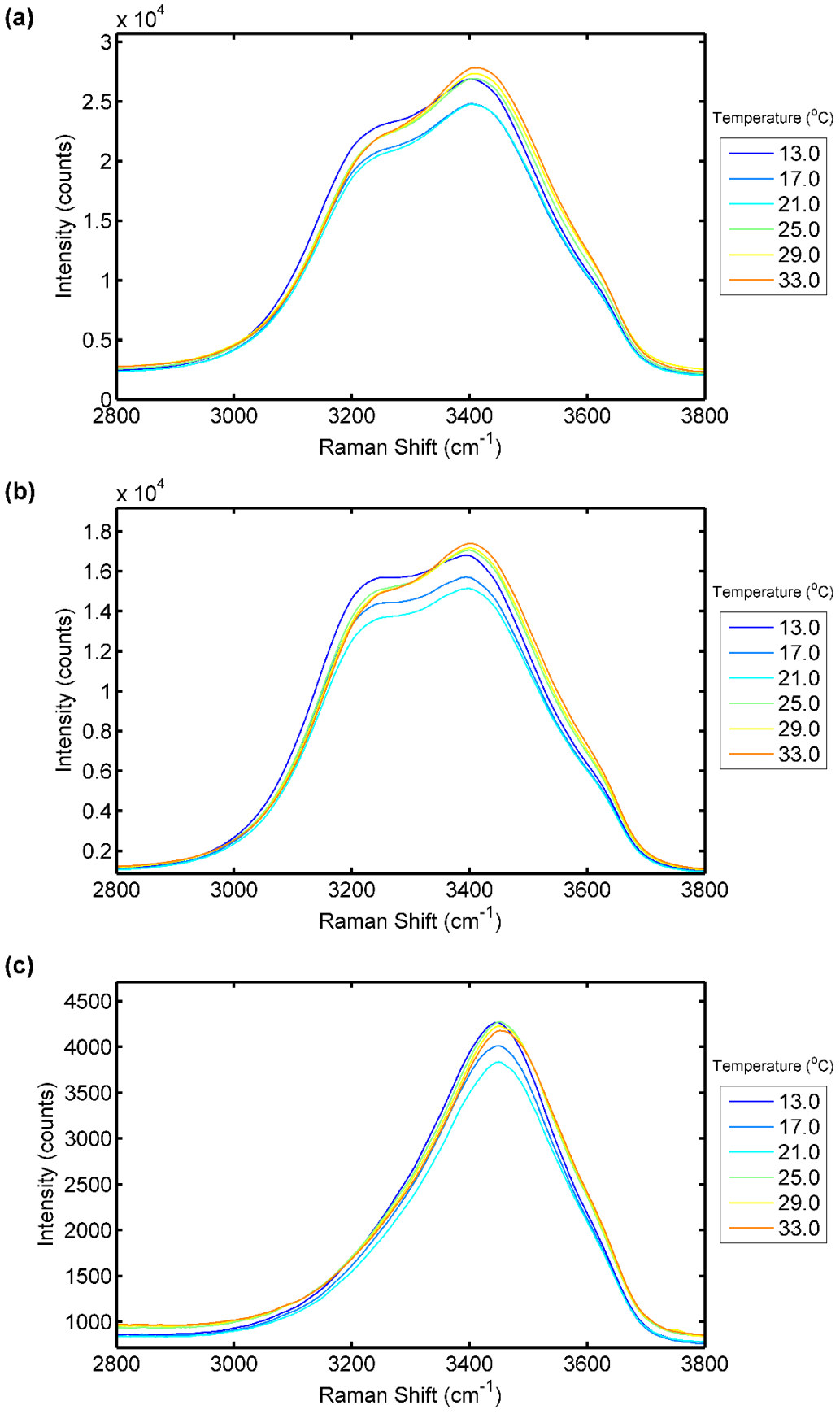

Figure 4.10 – Raman spectra and numerical analysis of the **Mains supply** water sample: (a) Unpolarised spectra. (b) Parallel polarised spectra. (c) Perpendicularly polarised spectra.

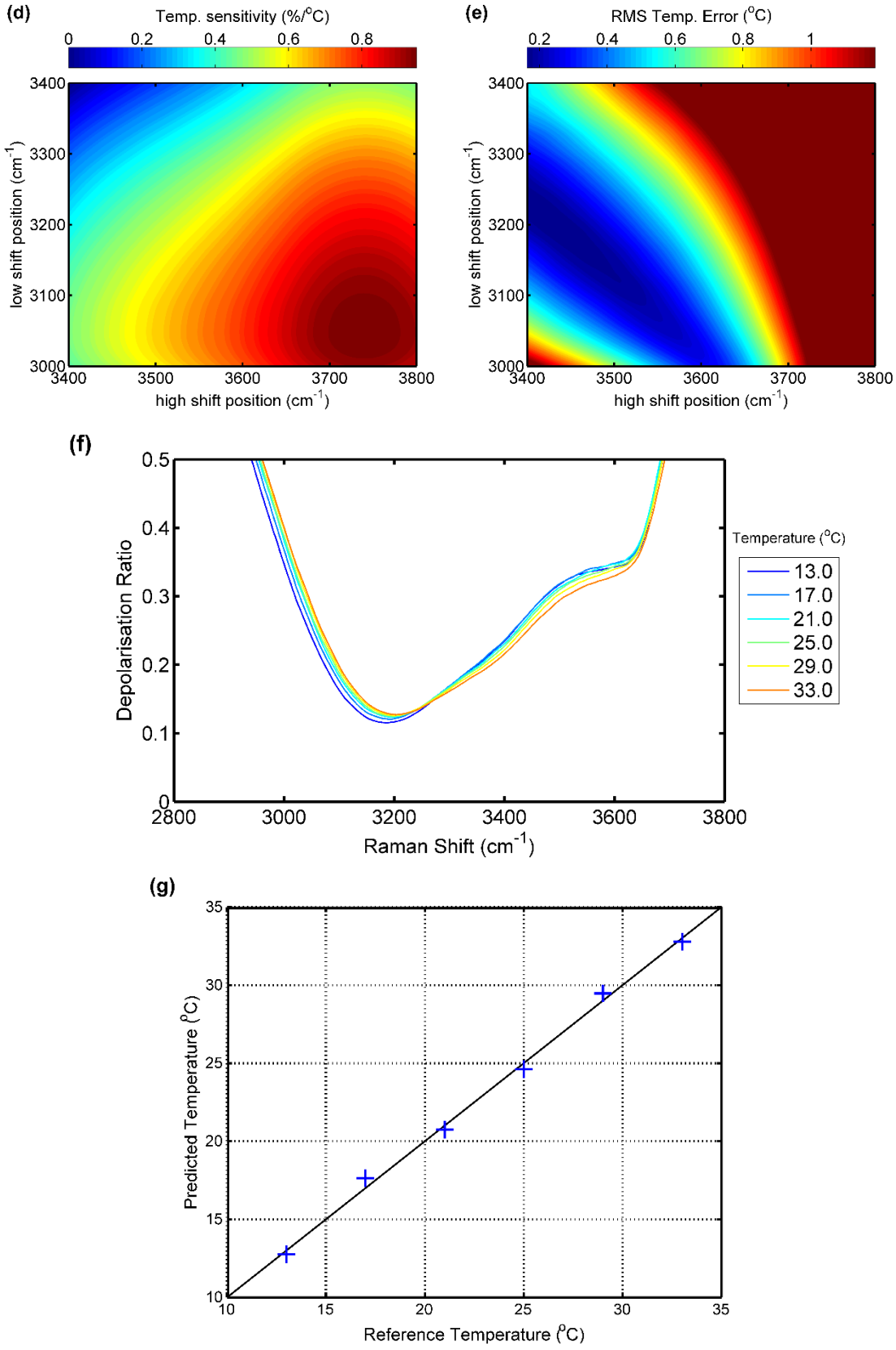

Figure 4.10 – Raman spectral analysis of the **Mains supply** water sample: (d) Temperature sensitivity for the two–colour ratio. (e) RMS temperature error for the two–colour ratio. (f) Depolarisation ratio. (g) Predicted vs. reference temperature for the two–colour method (RMSE: ±0.4 °C).

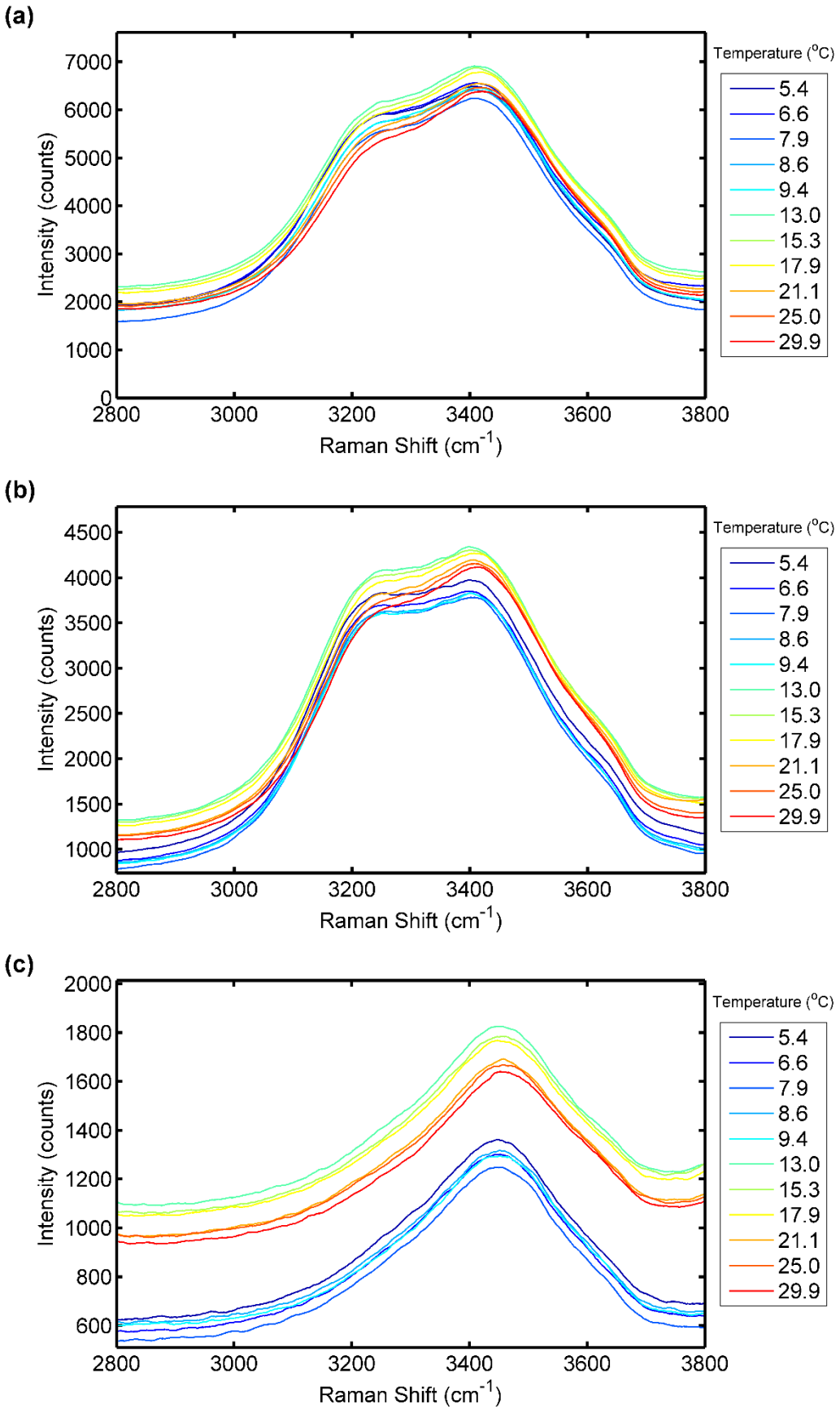

Figure 4.11 – Raman spectra and numerical analysis of the **Macquarie University Lake** water sample: (a) Unpolarised spectra. (b) Parallel polarised spectra. (c) Perpendicularly polarised spectra.

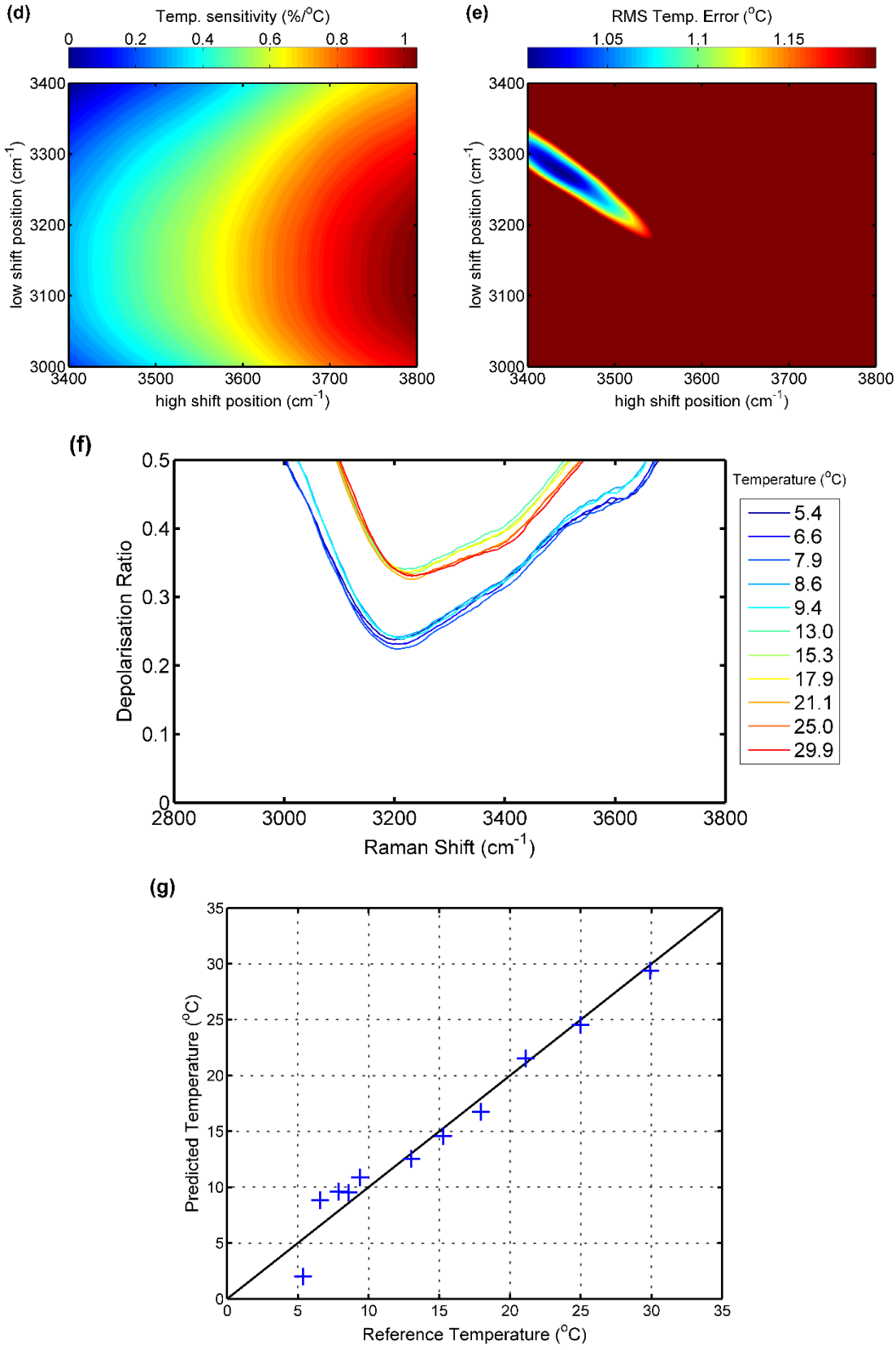

Figure 4.11 – Raman spectral analysis of the **Macquarie University Lake** water sample: (d) Temperature sensitivity for the two–colour ratio. (e) RMS temperature error for the two–colour ratio. (f) Depolarisation ratio. (g) Predicted vs. reference temperature for the two–colour method (RMSE: ±1.5 °C).

4.3 Origins and implications of baseline variation

The Raman spectra of the natural water samples analysed showed substantial baseline variation (compared with laboratory water) which we attribute to organic matter and suspended particulate content which can absorb or scatter excitation light, or fluoresce at wavelengths which overlap the Raman signal. As mentioned above, the severity of these effects varies greatly from sample to sample, and they are particularly strong in the samples from Rhodes and Macquarie University Lake (Figure 4.5 and Figure 4.11 respectively) which were also the most turbid samples. The effect of fluorescence peaks from CDOM or phytoplankton can potentially have a substantial negative impact on accurate assessment of Raman emission depending on intensity and spectral properties.

4.3.1 Fluorescence

Fluorescence emission was observed from all natural water samples examined using a fluorescence spectrometer (Horiba Fluorolog) and excitation at 405 nm. Emission peaks were evident, generally centred near 570-590 nm or 670-680 nm with widths of 25-30nm and 18-20nm respectively (FWHM).

To explore the extent to which fluorescence contributes to the baseline evident in the unpolarised spectra shown in Figure 4.2 to Figure 4.11, Rose Bay spectra (which exhibited the least baseline distortion) were subtracted from the spectra for other saltwater samples at each temperature level. Figure 4.12 shows difference spectra between the Clontarf and Rose Bay samples.

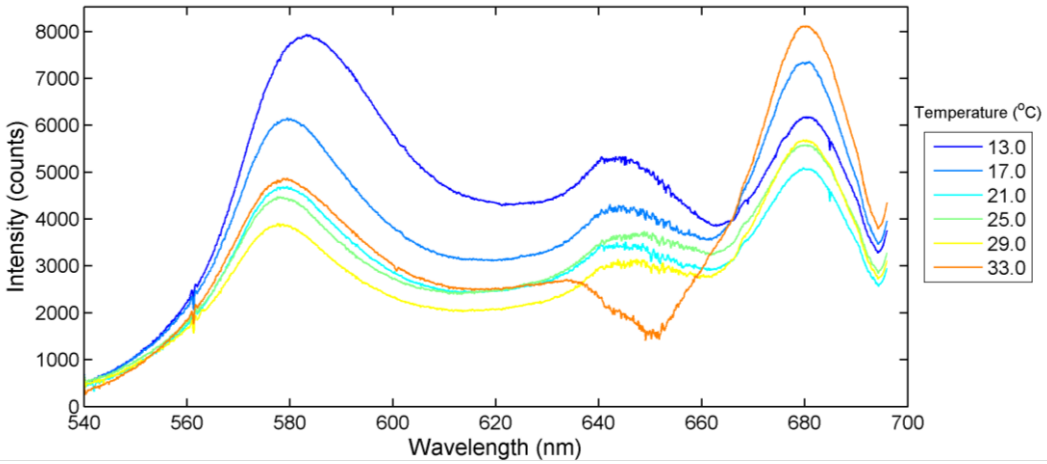

Figure 4.12 – Unpolarised Difference Raman spectra, with filtered Rose Bay sample spectra subtracted from Clontarf sample spectra.

Clear fluorescence peaks were evident at around 585 nm and 680 nm, while the region around 640nm is due to the differences in Raman emissions between the two samples. Table 4.1 lists the peaks observed in the difference spectra with Rose Bay spectra subtracted from spectra for each other seawater sample.

Sample Location	Peak Centres (nm)	Peak Widths (nm)
Woolwich	575, 680	24, 16
Clontarf	585, 680	28, 18
Sugarloaf Bay	572, 677	25, 16
Rhodes	576, 683	26, 18
North Head	681	18
Manly Beach	576,679	20, 17
Manly Dam	577, 683	17, 12
Macquarie University Lake	677	19

Table 4.1 – Approximate centre positions and approximate widths of peaks in difference spectra obtained when Rose Bay spectra were subtracted from spectra for each other seawater location. (Peak widths were measured as FWHM from the higher intensity background on either side of the peak).

The spectral features observed were analysed with comparison to literature sources. The peaks centred near 580 nm correspond with fluorescence from chromophoric (or coloured) dissolved organic matter (CDOM), sometimes referred to as “yellow matter” or “Gelbstoff” in literature [20, 117]. The peaks observed at ~680 nm are consistent with fluorescence from chlorophyll in various phytoplankton species and other photosynthetic organisms [22, 118-120].

Fluorescence has significant implications for Raman temperature and salinity sensing, depending on excitation wavelength and sensing system design. Both two–colour ratio and depolarisation ratio measurements may be negatively impacted by fluorescence which overlaps the OH stretching band. The fluorescence emissions observed here lie very close to the OH stretching band where 532 nm excitation is used for Raman excitation. Appropriate selection of the excitation wavelength is therefore important and future work should consider which excitation wavelength would minimise the impact of fluorescence on determining water temperature. James et al. have previously suggested a compensation method involving successive excitation with multiple laser wavelengths which are combined to produce a dataset corresponding to the baseline without the Raman band [85]. While this may prove effective, it would add greatly to the complexity of any measurement system.

4.3.2 Broad fluorescence and elastic scattering

A broad background increase in detected signal was observed in the Raman spectra of a majority of water samples. The average signal count in regions with minimal influence from water Raman peaks or other narrow spectral features roughly correlates with expectations of relative water quality. This background was reasonably uniform in intensity over the wavelength range examined (539-695 nm), with a weak, broad maximum near 2400 cm^{-1} (~610 nm). This background signal exhibited weak temperature dependence or temperature driven behaviour in almost all samples.

In order to better understand the origin of this behaviour, water samples were filtered (6μm Advantec No.1), with spectra taken directly before and after filtering. Figure 4.13 shows spectra acquired from a Rhodes water sample. This sample exhibited strong background relative to the samples analysed in Figure 4.2 to Figure 4.11, with a pedestal of over 5000 counts.

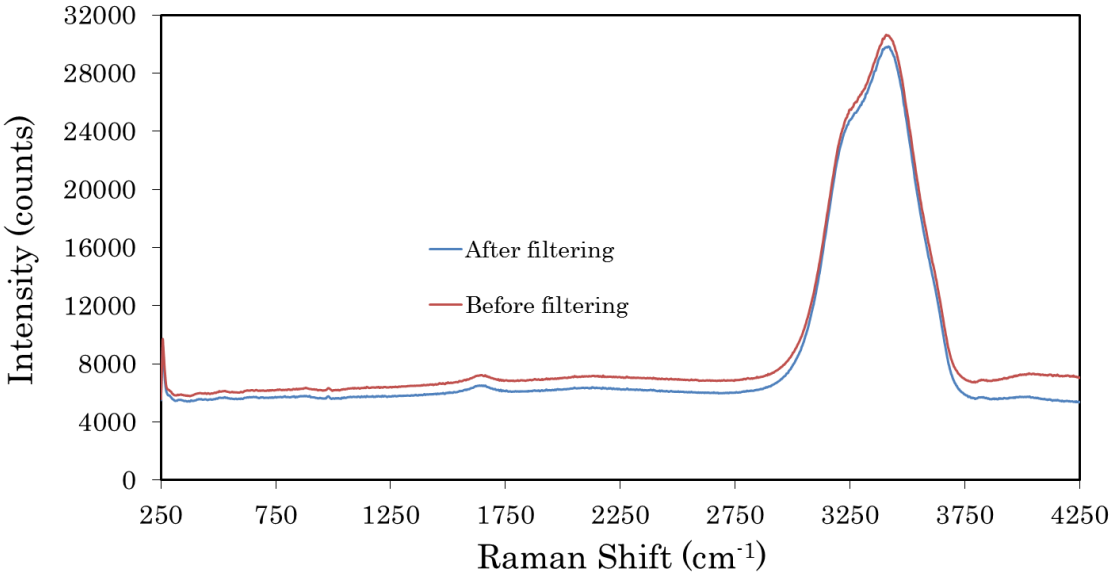

Figure 4.13 – Raman spectra before and after 6 μm filtering of a Rhodes water sample.

Filtering of natural water samples slightly reduced the baseline of the Raman signal. The reduction in the baseline was slight, but serves to illustrate the effect of removing larger particles and organic matter from the sample. Subtle fluorescence at 680 nm (~4150 cm^{-1}) was also removed by the filtration.

Stirring of water samples had a similar impact on the signal baseline. When magnetic stirring was applied (5 mm stir bar at 1 kHz), a background increase of 250 counts was evident even in a mains supply water sample.

Based on these observations, it seems likely that the background signal consists primarily of broadband fluorescence and elastic scattering from organic and inorganic particles suspended in the samples. This would explain the temperature behaviour observed, with convection effects increasing particulate circulation in sample cuvettes and hence affecting the rate of particles passing through the focal volume of the spectrometer during Raman signal acquisition.

4.3.3 Implications of baseline for temperature determination

Raman spectra acquired from clearer natural water samples, such as Rose Bay, can provide temperature measurement accuracy approaching that of laboratory or pure water as seen in sample RMSE maps (Figure 4.2e for Rose bay). However for more turbid samples such as Rhodes, baseline effects pose a significant problem with regards to temperature measurement.

The substantial background seen in some samples can have implications for the analysis required to determine temperature. How significant its impact depends on the precise behaviour. Relatively consistent (near uniform) baseline effects which are weak compared with the water Raman signal may not affect measurement accuracy to a great degree, while a sloping baseline can have disastrous consequences, particularly for the two–colour temperature measurement method.

A large baseline can also impact on the depolarisation ratio, with the weaker perpendicularly polarised signals being proportionally more affected. In anything but the clearest natural water samples, the depolarisation ratio was significantly degraded in terms of temperature measurement capability.

4.4 Assessment of temperature determination accuracy

Here we explore the accuracy of temperature determination in natural water samples, both with and without baseline correction. Averaged sample data (salt and fresh water separately) was evaluated to determine channel centre positions for best accuracy across multiple samples. This was followed by analysis of individual samples for the two–colour ratio and depolarisation ratio.

4.4.1 Baseline Correction

Several methods for baseline correction were assessed as a means of improving temperature measurement accuracy. These included linear subtraction and polynomial fitting schemes described in Section 2.5.2. It was determined that the simplest option which could be usefully implemented in a few–channel remote sensing system was a linear fit across the OH stretching band. This method can correct for broad baseline effects while only requiring one or two “guard band” detection channels. Linear baseline correction was applied to all water samples for both polarised and unpolarised spectra. Points on either side of the OH stretching band, at 2800 cm^{-1} and 3750 cm^{-1} were used, which are in the regions of minimum intensity.

To illustrate the effectiveness of this approach to baseline correction, maps of the root mean square error (RMSE) were calculated to show the effect of linear baseline correction on temperature determination accuracy of the samples (based on

the data shown in Figure 4.2e to Figure 4.11e). Figure 4.14 shows two–colour RMSE maps which are averages of the six saltwater sample maps before and after baseline correction. These maps use the same measurement parameters as the maps displayed in Section 4.2 (200 cm^{-1} channel widths).

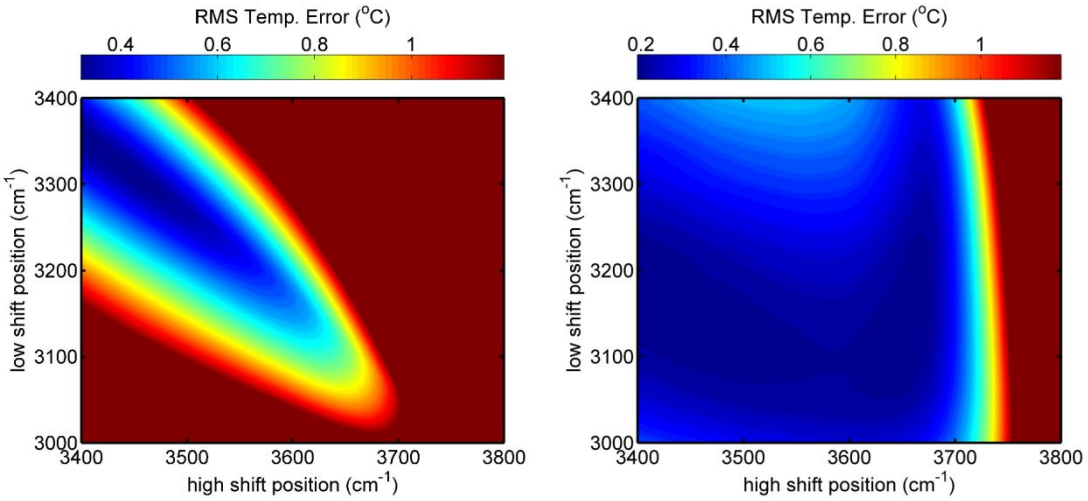

Figure 4.14 – Effect of linear baseline correction on two–colour RMS temperature error using 200 cm^{-1} channel widths with varying band centres, averaged over the six saltwater samples. Left: uncorrected. Right: baseline corrected.

Baseline correction was observed to significantly improve both the minimum temperature error and the constraints on band positioning. Figure 4.14(left) shows that RMS temperature accuracy of ~±0.3 °C can be achieved without baseline correction, however there is very little flexibility in positioning channels to obtain this accuracy. In contrast, Figure 4.14(right) illustrates how linear baseline correction enables temperature accuracy of ~±0.2 °C to be realised with considerably more flexibility in channel positioning.

The minimum averaged RMSE calculated was reduced from ±0.3 °C to ±0.2 °C when baseline correction was applied. With correction, the region with low RMSE expanded and shifted towards lower low shift band positions (3000-3300 cm^{-1}) and broader coverage in the high shift band position (3400-3700 cm^{-1}).

4.4.2 Two–Colour Method

Minimum two–colour RMS temperature error values were calculated both with and without baseline correction for all water samples. The laboratory water study in Chapter 3 found best two–colour results with band centres of 3240 cm^{-1} and 3450 cm^{-1} with 200 cm^{-1} channel widths. These values work well for clear, near pure

water, but provide increased temperature error when applied to samples with increased baselines due to organic or particulate matter content. In addition the behaviour of the saltwater and freshwater samples which had smaller regions of low temperature error differed from each other, and the selection of band centres was therefore separated for fresh and saltwater cases.

The averaged saltwater RMSE maps shown in Figure 4.14 indicate channel centre positions of 3322 cm^{-1} and 3438 cm^{-1} for best performance with no baseline correction, and 3150 cm^{-1} and 3432 cm^{-1} for baseline corrected spectra. Averaging the freshwater sample maps in the same way produced channel centre positions of 3276 cm^{-1} and 3410 cm^{-1} with no baseline correction, and 3204 cm^{-1} and 3400 cm^{-1} for baseline corrected spectra. These channel positions were then used to build predictive models for each water sample.

Figure 4.15 shows the minimum RMSE observed with the two colour method for each sample over the analysed temperature range, both with and without baseline correction. Consistent improvements in RMSE were seen when baseline correction was applied. As expected, less benefit was seen for samples with relatively low RMSE in the absence of baseline correction, while for samples with high RMSE significant improvement was obtained.

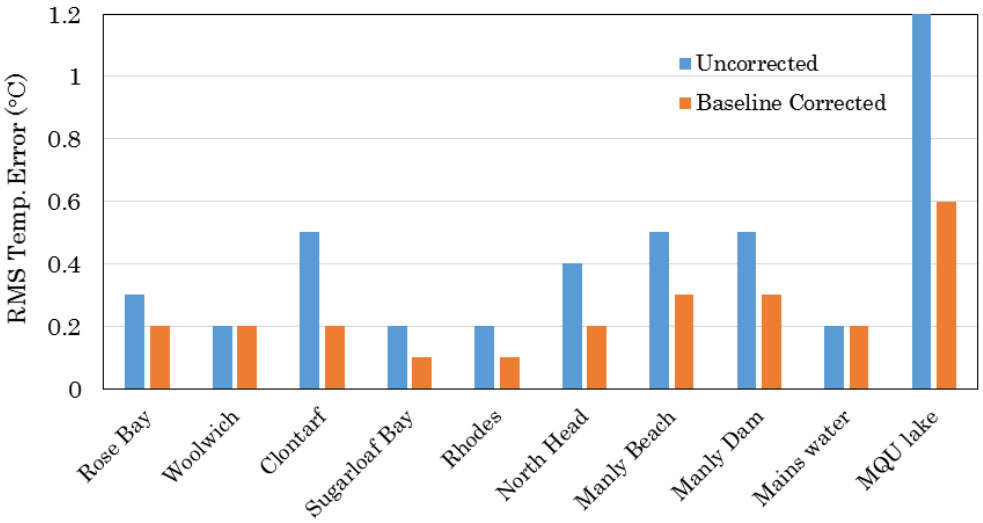

Figure 4.15 – RMS temperature error values representative of the two–colour method in natural water samples.

Figure 4.16 shows the relationship between two–colour predicted and reference (measured) temperature for water samples from Rose Bay and Clontarf, and the corresponding RMSE values may be found in Figure 4.15.

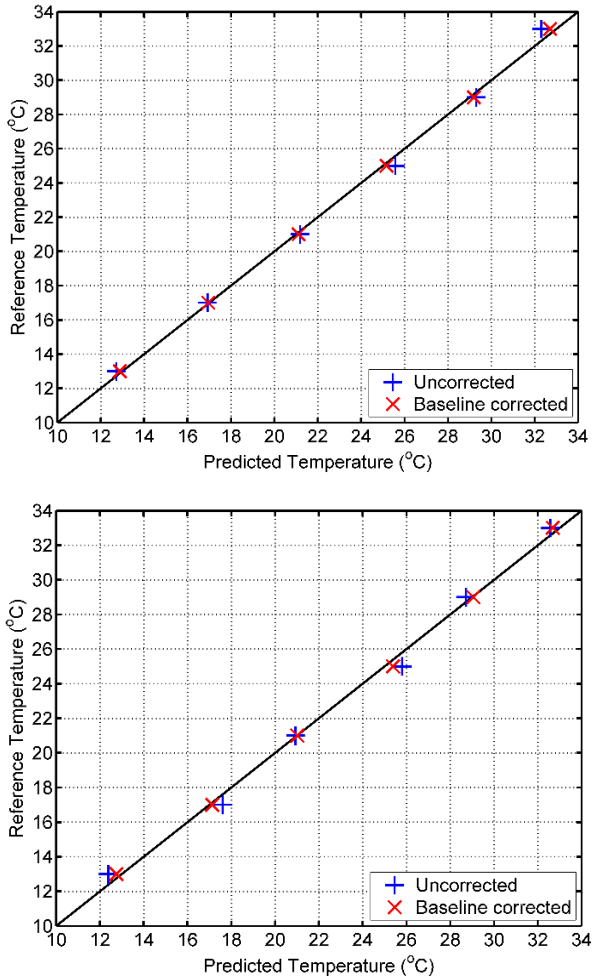

Figure 4.16 – Predicted vs. measured temperature with the two–colour method with baseline correction (3150 and 3432 cm^{-1}) and without baseline correction (3322 and 3438 cm^{-1}). (top) Rose Bay filtered sample. (bottom) Clontarf sample.

Both uncorrected and baseline corrected temperature values are shown, which were calculated for their respective optimised channel parameters from the averaged saltwater data in Figure 4.14. The Clontarf data showed a greater improvement with baseline correction as expected. The other samples examined showed similar behaviour to that seen here.

4.4.3 Depolarisation Ratio

The depolarisation ratio data for the natural water samples was analysed for best–case temperature determination accuracy with both uncorrected and baseline corrected spectra. A channel width of 100 cm^{-1} was used for all depolarisation ratio temperature analysis, which was found to significantly improve performance compared with the 200 cm^{-1} channel width employed in Chapter 3.

For uncorrected saltwater data, the minimum RMSE occurred at a channel centre position of 3450 cm^{-1}, as was the case for laboratory water. After baseline correction was applied, the saltwater minimum RMSE position was 3400 cm^{-1}. Analysis of freshwater samples without baseline correction found a minimum RMSE of ±2.3 °C at a channel centre position of 3100 cm^{-1}, though this region is impractical for use in remote sensing applications due to low Raman signal intensity in all polarisation states. When baseline correction was applied the minimum error occurred at 3418 cm^{-1}. This band position was also used for the uncorrected fresh water data displayed below.

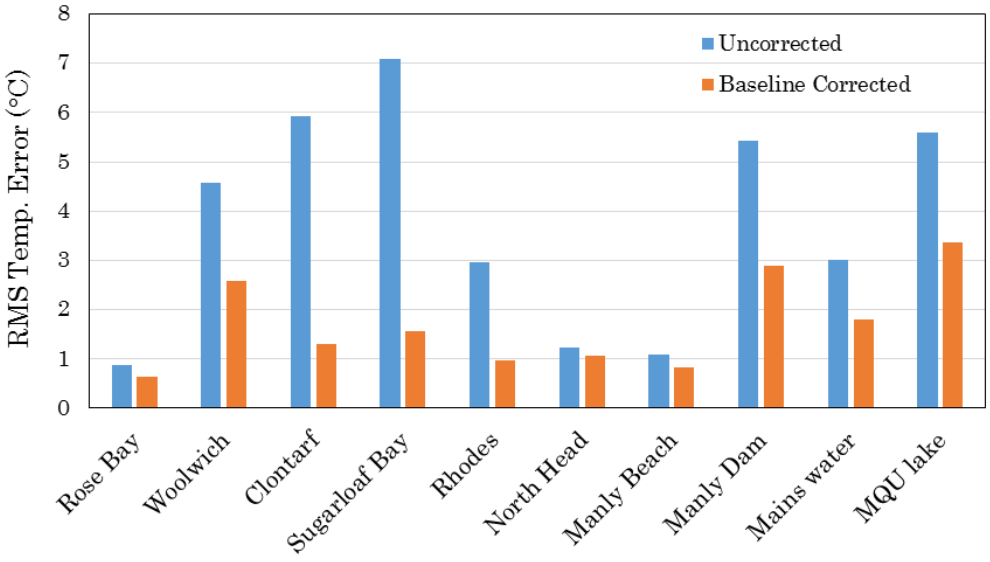

Figure 4.17 – RMS temperature error values for the depolarisation ratio method in natural water samples.

Figure 4.17 shows the RMS temperature error determined when using the depolarisation ratio method for each water sample examined with and without baseline correction applied.

In most cases baseline correction improved the depolarisation ratio temperature error. In some cases the improvement was substantial, such as Clontarf and Sugarloaf Bay which showed RMSE reductions of 4.7 °C and 5.8 °C respectively. The North Head sample required a single spectrum acquired at 33 °C to be removed in order to conduct a meaningful analysis, as it differed significantly from the other spectra.

Several samples produced RMSE values below ±1.0 °C, with the rest averaging roughly ±2.0 °C, which is not sufficient to provide useful temperature measurement capability for practical remote sensing applications. This is consistent

with the findings of Chapter 3, and may be due to the instrument limitations in acquiring polarised spectra (also discussed in Chapter 3).

4.4.4 Combination of parameters with multiple linear regression

Multiple linear regression (MLR) combinations of spectral parameters were calculated for all samples using the method described in Chapter 2, and applied to laboratory water in Chapter 3. The same issue observed in that case arose, with the depolarisation ratio behaviour being substantially more variable compared with the two–colour method. Because of this MLR values tended to track closely with the two–colour values, and hence provide no additional utility at this stage and have not been included here. Useful application of this method would require either improved depolarisation ratio accuracy, or the employment of other suitable temperature measurement parameters.

4.5 Site specificity of predictive models

The fitted equations which relate temperature–dependent spectral parameters to reference sample temperatures can be treated as a numerical model to predict temperature for some arbitrary water sample, given corresponding Raman spectra. Here we explore the extent to which a model based on data from one site can be used to predict the temperature of a sample from another location. Accordingly the temperature dependent predictive models generated for each of the water samples analysed here have been used to determine the temperature of samples from sites, other similar samples given their Raman spectra (with similar acquisition parameters).

This was performed for all combinations of saltwater samples examined in this chapter, and for both uncorrected and baseline corrected spectra. The intent here was to assess the range of temperature accuracy achievable with sample variability between samples. Table 4.2 shows the RMS temperature error for saltwater samples.

Test samples > / Model samples	Rose Bay		Woolwich		Clontarf		Sugarloaf		Rhodes		Manly Beach	
Rose Bay	0.3	0.2	2.7	2.9	1.2	3.4	1.8	1.7	4.3	2.8	0.8	0.4
Woolwich	2.3	2.4	0.2	0.2	3.2	0.8	3.3	1.6	6.6	0.2	2.6	2.2
Clontarf	1.0	3.1	3.2	0.8	0.5	0.2	1.1	2.3	3.4	1.0	0.8	2.9
Sugarloaf	1.5	1.2	2.6	1.3	1.0	2.2	0.2	0.1	3.5	1.1	1.2	1.0
Rhodes	4.4	2.2	7.3	0.3	3.5	1.0	4.1	1.3	0.1	0.1	4.1	2.0
Manly Beach	0.6	0.3	2.6	2.5	0.8	3.1	1.2	1.3	4.0	2.4	0.5	0.3

Table 4.2 – RMSE values (in °C) for temperature prediction of tested samples (columns) using models generated from the same set of water samples (rows). Left value: uncorrected, Right value: baseline corrected. Colour indicates relative temperature accuracy, with blue representing lower RMSE and red higher RMSE.

In cases where both the model and test water samples exhibit similar spectral properties, reasonable temperature determination accuracy may be achieved. The models based on Rose Bay and Manly beach samples in particular gave reasonable accuracy when one was used to determine temperature for the other, with baseline correction further improving accuracy. However this level of success changes as the samples become less alike. Very different samples produced highly inaccurate values compared with reference temperatures (RMSE greater than ±6 °C average for the Rhodes and Woolwich samples), and while baseline correction made large improvement in many of these cases, depending on the specific nature of the difference between the water sample spectra, these results highlight a challenge that needs to be addressed so that remote sensing of water temperature can be conducted over widespread areas. The lowest RMSE values were around ±0.2 °C to ±0.4 °C, which is broadly consistent with the corrected values observed for individual water samples in Figure 4.15. Average RMSE values of ±2.7 °C and ±1.7 °C were recorded for the uncorrected and baseline corrected data respectively.

4.6 Proposed design for multi–channel sensing system

The findings of this chapter have been applied to design a multi–channel Raman spectrometer that is suited to sensing temperature in natural waters where fluorescence and scattering add complexity to the case of “pure” laboratory water. Specifically it incorporates a pair of channels devoted to measuring the background

intensity at the edges of the OH stretching band for baseline correction of the Raman spectral channels. This instrument layout is shown in Figure 4.18.

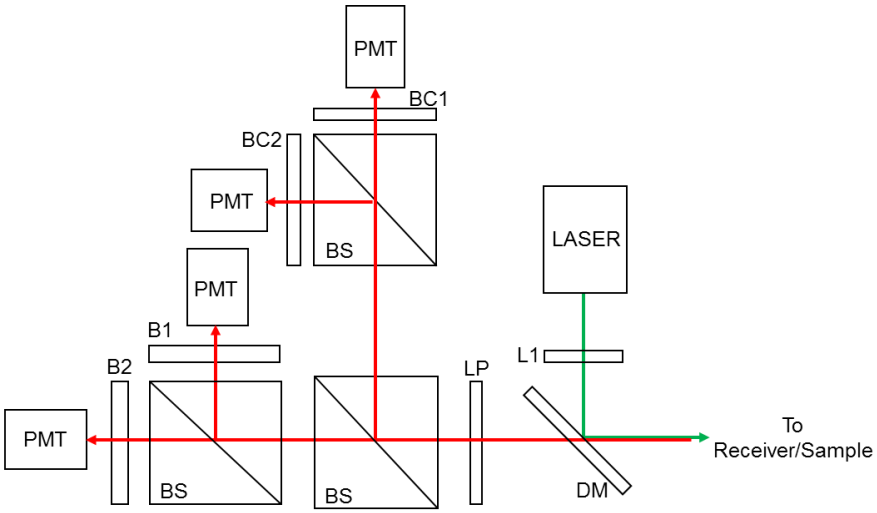

Figure 4.18 – Multi–channel Raman sensing configuration for two–colour temperature sensing with baseline correction.

The above design is one possibility for two–colour Raman sensing with baseline correction. The signal is divided into four portions with beamsplitters (BS). Each portion passes through a separate band–pass filter corresponding to the two–colour Raman channels (B1/2) and baseline correction channels (BC1/2). Each channel is then detected with a PMT. The proportion of the signal used for baseline correction could be adjusted by replacing the first 50:50 beamsplitter with a different ratio (e.g. 70:30) depending on the situation. Optimal efficiency would require band–stop dichroic mirrors or similar to minimise signal losses.

It is difficult to meaningfully predict the accuracy with which temperature may be determined using this arrangement due to the variability in water types it may be applied to. The incorporation of additional components to enable depolarisation ratio and linear combination methods are natural extensions to the apparatus in Figure 4.18 which could improve temperature determination accuracy.

4.7 Discussion and summary

In this chapter, polarised and unpolarised Raman spectra of water were presented as a function of temperature, for both fresh and seawater samples collected from Sydney Harbour and the surrounding environs. Similar Raman

spectral analysis to that detailed in Chapter 3 was carried out, and the optimal wavelengths for the temperature measurement in natural samples were determined and compared with laboratory water samples. Experimentation with natural fresh and salt–water samples achieved reasonable success in terms of temperature accuracy, which was highly dependent on water constituents and quality. The depolarisation ratio method was most adversely affected by water quality.

Water samples obtained from local estuaries and inner regions of Sydney Harbour showed significant variability. It remains to be seen whether reliable optical remote sensing of sub–surface water temperature can be performed in such areas. Based on observations made during this study, clean, clear ocean water should produce accuracy levels approaching those of filtered fresh water.

Significant baseline effects were evident with most natural salt water and fresh water samples studied. This was less of an issue for the two–colour method, but proved to be a major problem for depolarisation ratio measurements. These effects were attributed to fluorescence emission from organic material and scattering from suspended organic and inorganic matter. Linear baseline correction resulted in substantial improvements in temperature accuracy for both the two–colour method and the depolarisation ratio parameter. A practical approach to implementing such a correction would require the use of one or more spectral channels outside the Raman OH stretching band. It is also conceivable that the relative intensity of Raman features compared with fluorescence and elastic scattering may be improved by the move from the laboratory using continuous wave excitation, small collection volumes and long acquisition times, to pulsed lasers with large–area receivers and short acquisition times (microseconds to milliseconds). We postulate that the background will be less variable when the size of organic and inorganic matter suspended in the water is much smaller than the size of the collection volume.

It was found that there was significant difference in the optimal band positions for the various water samples compared with laboratory water for optimal temperature measurement. In the case of the "two–colour" method, both band centres tended towards slightly lower Raman shifts. This may have been influenced by the fluorescence at ~680 nm, relatively near to the long edge of the OH stretching band. In the case of the depolarisation method, the optimal wavenumber positions were relatively close to the optimal position found for laboratory water in Chapter 3.

Generating a temperature calibration model from Raman spectra of one or more samples for use in the measurement of temperature in other water samples

gave varied success. Where samples produced similar spectra, reasonably good temperature accuracy could be achieved, approaching that of self–fitting a sample in the best cases. Much poorer accuracy was achieved with widely varying samples. It seems likely that in any practical measurement scenario, particularly remote sensing applications, a variety of models would be needed. Model coefficients would need to be specified for different water types (for example based on Jerlov water types [5]). Alternatively for measurement from a surface vessel or fixed emplacement, samples of water could be periodically acquired for rapid temperature–stabilised calibration and a model generated while simultaneously acquiring more spectral data.

In general, the two–colour method has proven to be more accurate for laboratory based Raman temperature measurement compared with the depolarisation ratio. On the other hand, the major disadvantages inherent in the two–colour ratio mainly come into play with transmission through the water column or with various water constituents; namely differential attenuation due to absorption and more significant fluorescence from phytoplankton or dissolved organic matter (DOM). Further studies are needed to determine how significant these factors will be in Raman–based remote sensing of ocean temperature.

5 Temperature–Salinity Analysis

Past research has shown that, in addition to water temperature, salinity also has a significant impact on the Raman spectra of liquid water [47, 61, 121]. In the course of initial analysis of water Raman spectra, a brief study showed that salinity variation produced a somewhat similar response to temperature change.

Significant differences are to be expected between Raman spectra acquired from fresh and saline water due to the influence of various salt ions bonding into the water structure. The bonding affects OH bond vibrational transition frequencies, altering spectral shapes, and hence influencing temperature determination parameters described in previous chapters. Increased variability in spectra inevitably reduces temperature determination accuracy, and thus salinity would need to be taken into account in any practical remote sensing system intended for use in a variety of water types and conditions.

This chapter covers a series of experiments designed to explore simultaneous variation in water temperature and salinity. This was done to determine whether it is possible to decouple temperature and salinity to either: (1) improve the accuracy of temperature determination, or (2) determine temperature and salinity values simultaneously. The potential to develop optical sensing systems based on multiple channels for temperature and salinity acquisition is examined and the measurement capability assessed.

5.1 Experimental Methods

Several methods were tested to obtain water samples with known salinity values which accurately reflect the content of ocean water. Commercially available artificial salt mixtures were obtained (Sigma Aldrich, Instant Ocean) and attempts were made to produce solutions. It was found that the slightest hint of moisture in the air surrounding the powdered salt mixtures prior to dissolving in water led to the formation of insoluble by–products, most likely calcium carbonate ($CaCO_3$). This directly altered the balance of compounds dissolved in the water. As a result, both the Raman spectra observed and their response to changing sample salinity (i.e. concentration of the mixture) and temperature were slightly altered, defeating the purpose of using these mixtures in the first place. After multiple attempts failed to produce complete dissolution, this method was abandoned and it was decided to use diluted seawater as an alternative.

Seawater samples were obtained from the Macquarie University marine biology seawater facility, which stores filtered seawater collected from Sydney Harbour (see Section 2.3). These were diluted with Millipore water (18.2 MΩ at collection) to multiple salinity levels which were measured using a conductivity probe (Extech EC600). Each successive dilution and conductivity measurement was conducted directly prior to sample analysis. Conductivity values were converted to the Practical Salinity Scale using a simplified form of the equation defined for 25 °C [122, 123]. This scale is based on a ratio of measured conductivity against a potassium chloride reference sample at a specific temperature. The experiment was conducted over several days, and fresh water from the storage facility was obtained each day.

As in previous chapters, water Raman spectra were collected with a commercial Raman spectrometer (Enwave EZRaman–I) using a polarised 532 nm frequency doubled CW Nd:YAG laser for excitation. All measurements were collected using a 180° backscattering geometry. The spectrometer integration time was 30 seconds and each spectrum was an average of 3 acquisitions to improve consistency. The apparatus and procedure for temperature ramping was the same as that detailed in Section 3.1.

Each sample of different salinity was ramped through the temperature range investigated using a controlled cuvette holder (QNW QPod2e), with a waiting time

of several minutes allowed after reaching set point for the water sample to reach thermal equilibrium with the cuvette holder.

Unpolarised and linearly polarised spectra were recorded for 36 combinations of temperature and salinity, resulting in a set of 108 spectra. The depolarisation ratio was also calculated and analysed. Table 5.1 shows the temperature and salinity levels examined, and the measured conductivity values used for salinity calculation.

T (°C)	Salinity PSU	Conductivity (mS/cm)
13 ± 0.1	5.6 ± 0.3	10.0 ± 0.4
17 ± 0.1	10.0 ± 0.3	17.0 ± 0.4
21 ± 0.1	14.6 ± 1.3	24.1 ± 2
25 ± 0.1	19.9 ± 1.4	32.0 ± 2
29 ± 0.1	25.2 ± 1.5	39.6 ± 2
33 ± 0.1	32.4 ± 1.5	49.6 ± 2

Table 5.1 – Temperature, conductivity and calculated salinity levels.

The temperature and salinity ranges presented in Table 5.1 cover a significant portion of the natural water conditions encountered in estuarine and coastal waters. The salinity of the filtered seawater (32.4 PSU) was slightly lower than average ocean salinity (~35 PSU), but it was not possible to increase the salinity without losing some proportion of the dissolved salt content, which restricted the maximum salinity to that of the original seawater.

Spectral data were examined using multivariate analysis methods described in Chapter 2. The first step was to use Principal Component Analysis (PCA) to examine the variance of the spectral data. Partial Least Squares Regression (PLS–R) was then applied to correlate this variance with reference temperature and salinity values.

5.2 Examination of Raman Spectra

5.2.1 Unpolarised Raman Spectra

Figure 5.1 shows the effect of changing salinity on Raman spectra at a fixed temperature of 25 °C. As stated previously, the observed spectral changes bear some similarity to the response to temperature change. The baseline (as seen at the edges of the plot) rises slightly with increasing salinity. This baseline variation makes intuitive sense, considering the seawater will retain some level of dissolved and suspended organic matter in addition to the chemical constituents which form the saline content.

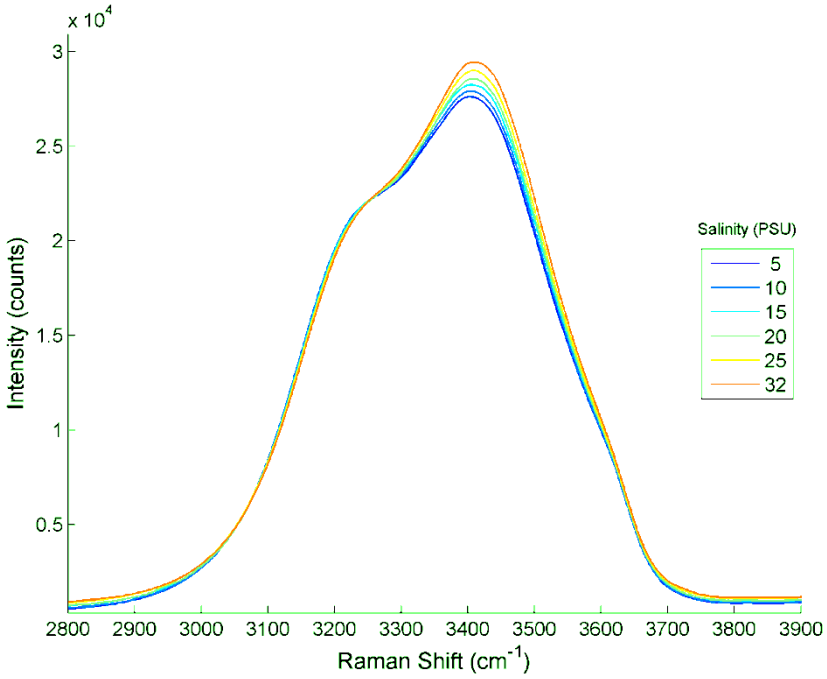

Figure 5.1 – Raman spectra with changing salinity and fixed temperature (25 °C).

Two isosbestic points occur, at ~3080 cm^{-1} and ~3250 cm^{-1}. The region between these points exhibit a reduction in intensity with increasing salinity, while above 3250 cm^{-1} intensity increases with increasing salinity. The maximum intensity variation with salinity is at ~3410 cm^{-1}, close to the peak maxima.

Figure 5.2 shows the spectral response to temperature change with fixed salinity (15 PSU). The temperature response is virtually identical to the pure water case (Chapter 3). The isosbestic point observed at 3410 cm^{-1} coincides very closely with the point of maximum intensity variance with salinity. Very slight baseline

variation with temperature was observed, though notably less compared to the variation with salinity.

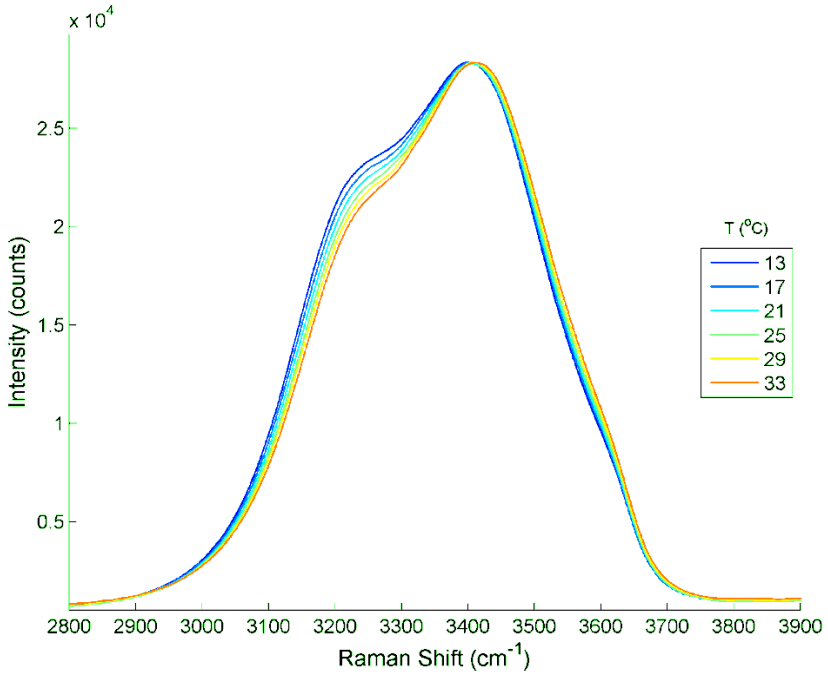

Figure 5.2 – Raman spectra with changing temperature and fixed salinity (15 PSU).

Inspection of the spectra presented in

Figure 5.1 and Figure 5.2 demonstrated regions in the unpolarised data which may be measured for acquisition of both parameters. The overlap between the short Raman shift bands for both salinity and temperature change (3050 – 3250 cm^{-1}) provides a region influenced by both properties. A second band centred at 3410 cm^{-1} gives information concerning salinity with minimal temperature influence, while a third band at the long Raman shift end at ~3550 cm^{-1} provides temperature information with limited salinity influence. It is therefore intuitively reasonable to expect that it may be possible to simultaneously extract information concerning both temperature and salinity from Raman spectra. Three parameters based on these spectral bands carry the information required to separate temperature and salinity effects for a reasonable degree of measurement accuracy.

5.2.2 Parallel Polarised Spectra

Figure 5.3 shows parallel polarised water Raman spectra with varying salinity and a fixed temperature of 25 °C. Generally similar salinity response is seen to the unpolarised case, though the positions of isosbestic points or “regions” are

shifted slightly. The isosbestic points occurred at ~3000 cm^{-1} and ~3290 cm^{-1}, shifted outward relative to the unpolarised positions. The slight baseline shift with salinity is still evident though reduced compared with unpolarised spectra, as expected based on the assertion that the baseline variation is a function of particle scattering.

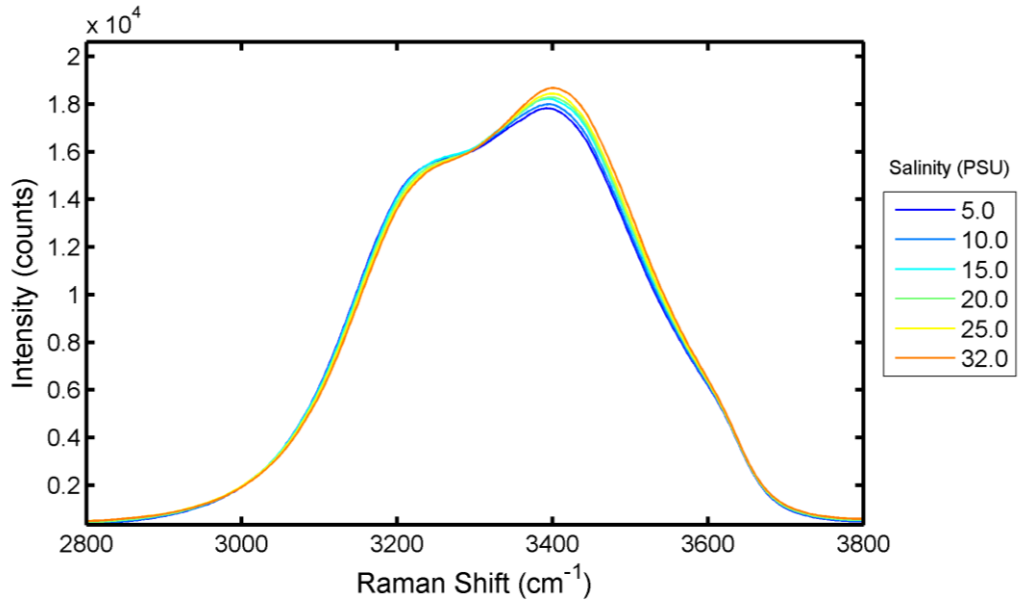

Figure 5.3 – Parallel polarised Raman spectra with varying salinity (25 °C).

Figure 5.4 shows the parallel polarised Raman spectra for six temperature levels and fixed salinity (15 PSU). As expected, the effect of temperature change is virtually identical to the pure water case (Chapter 3). The isosbestic point was located at ~3380 cm^{-1}.

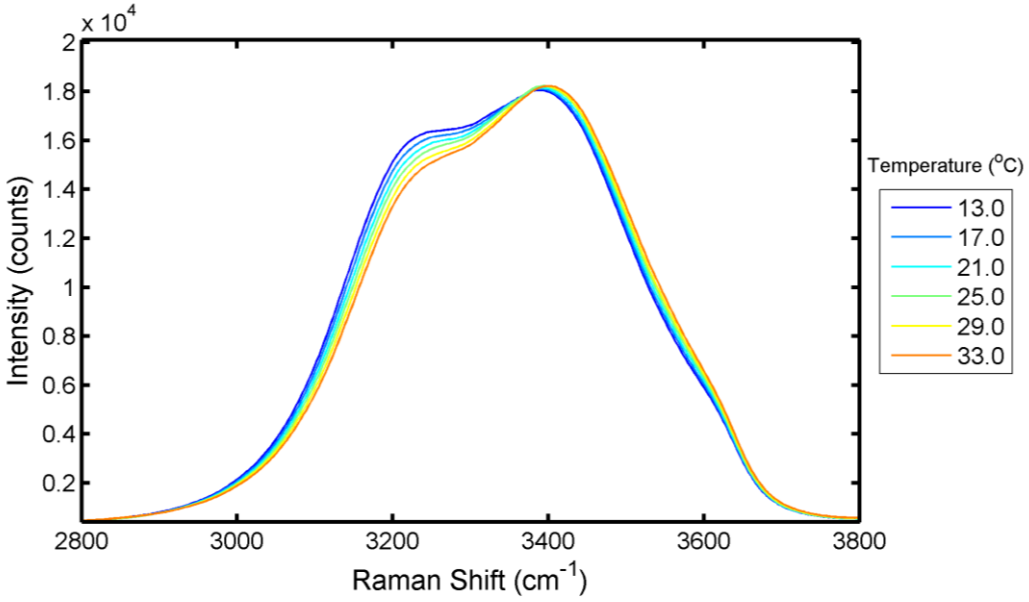

Figure 5.4 – Parallel polarised Raman spectra with varying temperature (15 PSU).

5.2.3 Perpendicular Polarised Spectra

The perpendicularly polarised spectral components are shown in Figure 5.5 and Figure 5.6 for varying salinity and temperature respectively. No isosbestic regions were evident with salinity change. The only effect of salinity appears to be an overall increase in intensity. The intensity at the peak exhibits slightly greater increase, while the rest of the spectrum appears to scale uniformly.

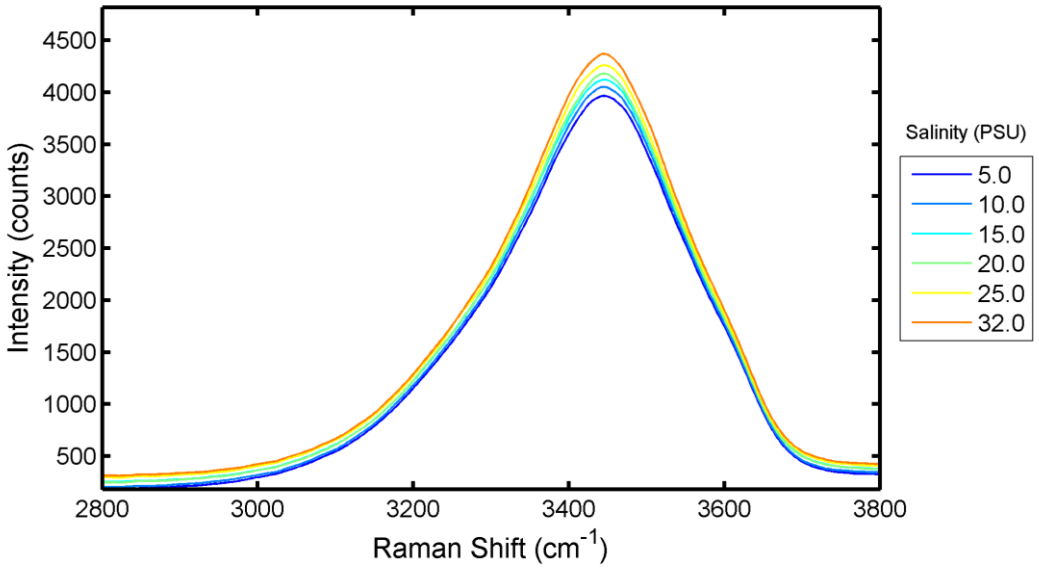

Figure 5.5 – Perpendicular Raman spectra with changing salinity and fixed temperature (25.0 °C).

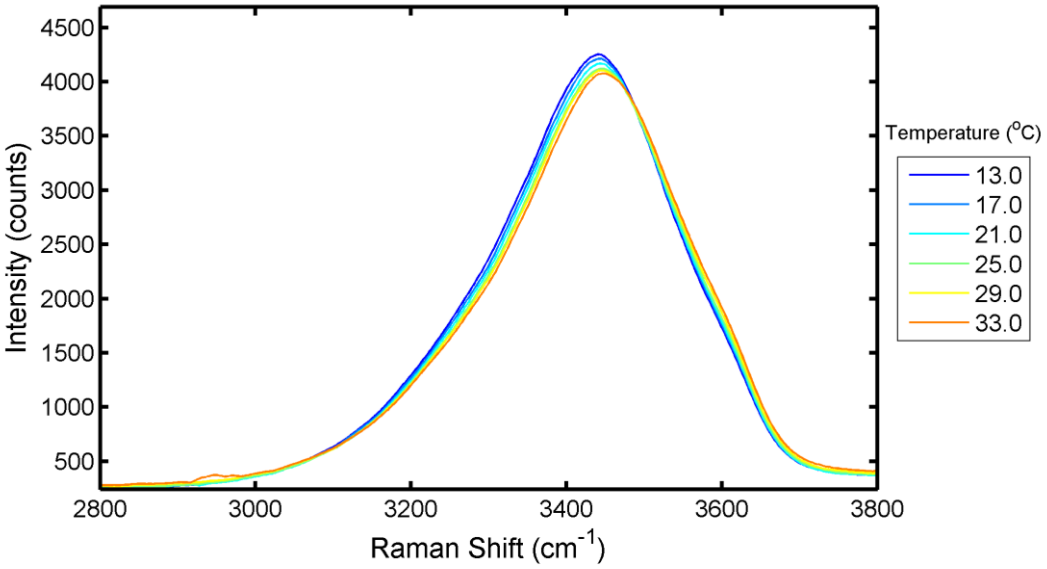

Figure 5.6 – Perpendicular Raman spectra with changing temperature and fixed salinity (15 PSU).

The temperature dependent spectra in Figure 5.6 again exhibit similar behaviour with temperature to the pure water case. The isosbestic point is at a slightly lower position of ~3490 cm^{-1}. The slight baseline variation with temperature

is more evident here due to the weak intensities compared with parallel polarised or unpolarised spectra.

5.2.4 Depolarisation Ratio

The depolarisation ratio was calculated from the polarised spectra shown above for both the cases of varying salinity and varying temperature. Figure 5.7 shows the effect of varying salinity on the depolarisation ratio.

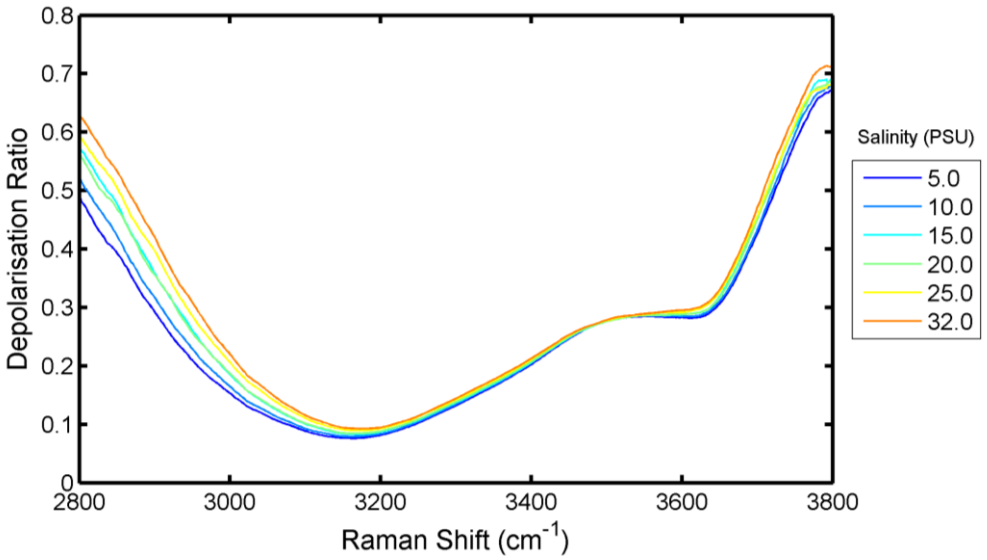

Figure 5.7 – Depolarisation ratio with varying salinity and fixed temperature (25 °C).

A region with minimal salinity dependence is evident at ~3500 cm^{-1}, however there is no crossing of the ratios, i.e. all ratio variation is in the same direction with varying salinity.

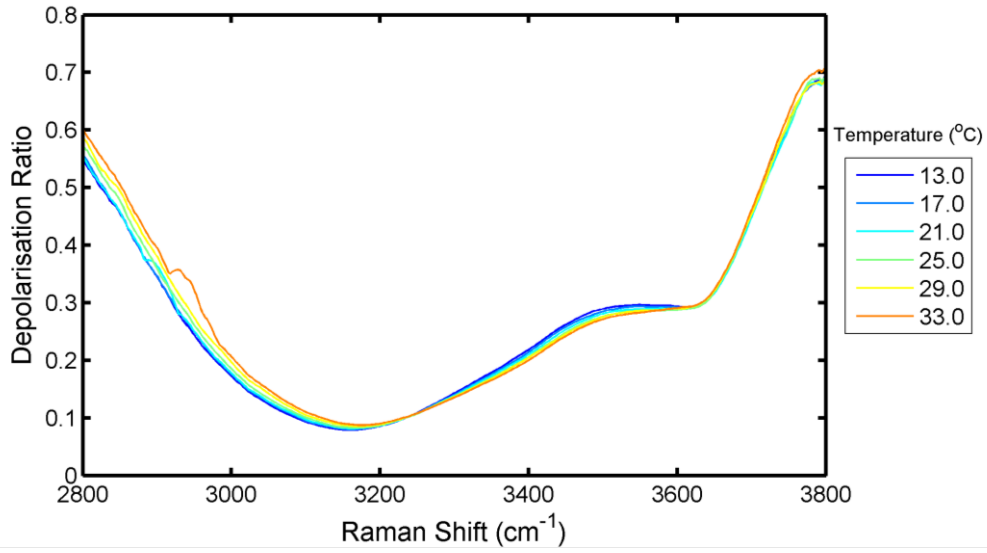

Figure 5.8 – Depolarisation ratio with varying temperature and fixed salinity (15 PSU).

The temperature variation data in Figure 5.8 in contrast, has a crossing point at 3230 cm^{-1}. The anomalous region in the 33 °C data at approximately 2950 cm^{-1} is due to the interaction of the Savitsky–Golay smoothing algorithm with a peak caused by cosmic ray interference with the spectrometer CCD during spectra acquisition. Its origin can be seen in the perpendicular polarised spectra in Figure 5.6. Aside from this, the depolarisation ratio temperature response is consistent with pure water behaviour.

5.3 Multivariate Analysis of Raman spectra

5.3.1 Multivariate Analysis – Unpolarised Spectra

Principal Component Analysis was applied to the complete set of 36 raw unpolarised Raman spectra.

The scores and loadings plots are shown in Figure 5.9. PCA was used as the first step in order to assess the spectral data variance without considering for the reference temperature and salinity data. The point labels in all following scores plots have the format “n−m” where n is the temperature (Celcius) and m is the salinity (PSU).

The scores plot (Figure 5.9a) shows the variation between spectra in terms of the first two principal components, Together the first two components account for 99% of the variation between the Raman spectra, with 66% of variation explained by PC1, and 33% explained by PC2. Clear separation of spectra was evident, with PC1 and PC2 each describing portions of the spectral response to both temperature and salinity change. Some structure corresponding to temperature and salinity was observed in the scores plot, with approximately linear spacing with temperature as indicated by the arrows in Figure 5.9a. The spread with salinity was much less regular, with inconsistent variation observed as salinity increased.

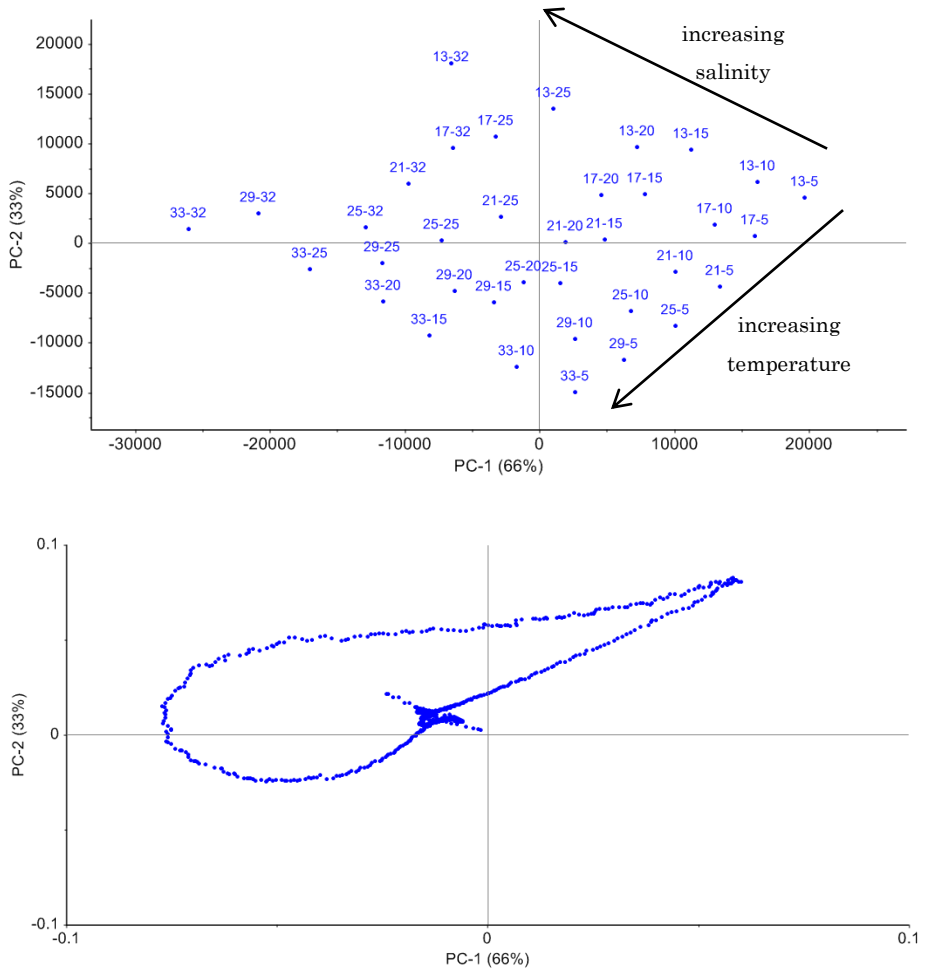

Figure 5.9 – PCA (a) scores and (b) loadings for full unpolarised Raman spectra (250-4200 cm^{-1}). (Numerical point labels in scores plots are "temperature–salinity").

The loadings plot (Figure 5.9b) shows points which correspond to the variance in intensity of the data set at each wavenumber position in terms of the first two principal components. The loadings data exhibits a looping curve of points which correspond to the OH stretching band (i.e. the regions where salinity and temperature influence are observed). The pointed section of this curve (upper–right) represents the response around 3180cm^{-1}, where both salinity and temperature affect the spectra in similar ways (decreasing intensity with increases in both temperature and salinity).

The cluster of points near the origin corresponds to the temperature and salinity insensitive regions and hence has minimal influence on the loadings. The offset of this cluster from the origin reflects the changing baseline.

PLS–R analysis was next conducted with the isolated H_20 stretching band (2800-3800 cm^{-1}), and the scores and loadings plots are shown in Figure 5.10. The partial least squares regression method produces similar output to principal

component analysis, but allows regression against the reference temperature and salinity values to generate a model for estimation of these parameters. Only variance in the spectra which is consistent with the changes in the reference parameter values is taken into account.

The correlation between the scores and the reference temperature and salinity values in Figure 5.10a was greatly improved compared with the full spectra analysis above. Reasonably consistent spacing between the spectra was evident with temperature change, while salinity showed more inconsistency. The first factor observes positive correlation between salinity and temperature, while the second factor observes negative correlation between these parameters. The percentage values associated with the factors (axis labels) indicate the calibration and validation variance explained by that factor. The second number on each axis is the validation variance, which is the value of most significance.

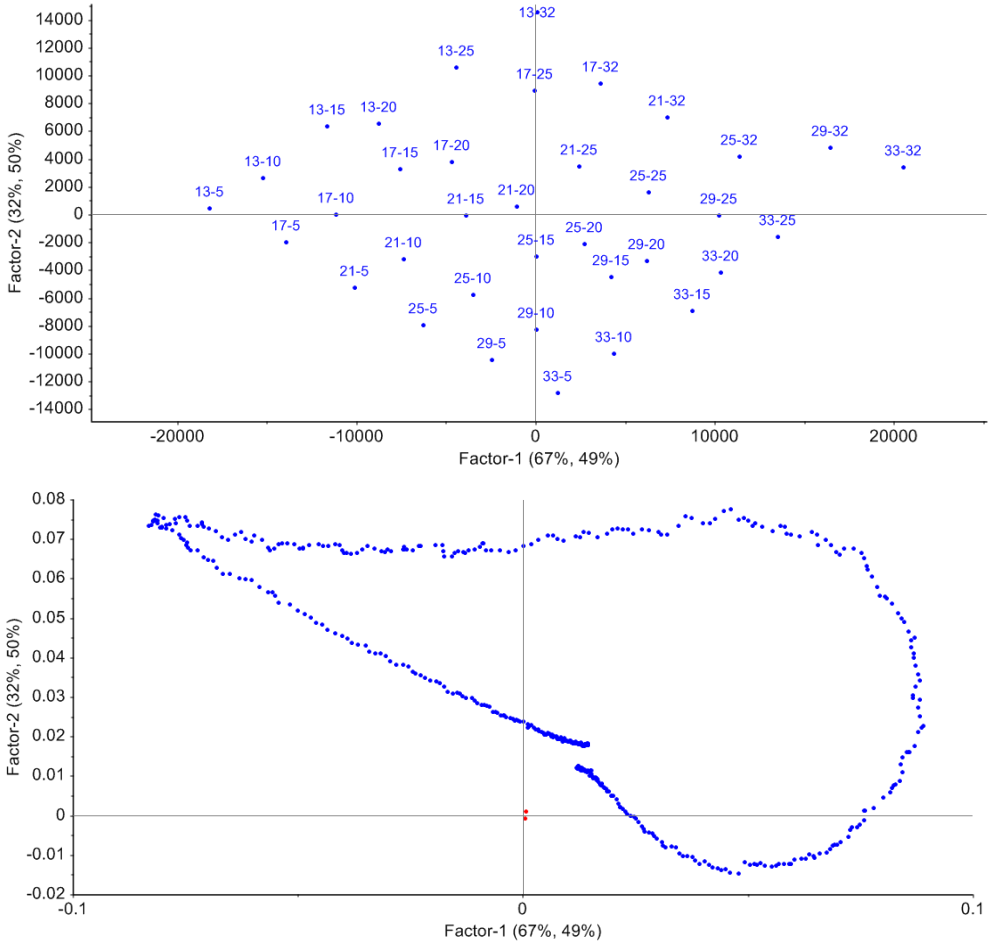

Figure 5.10 – PLS–R (a) scores and (b) loadings plots for the unpolarised OH stretching band (2800-3800 cm^{-1}).

Using two factors, this model produced validation RMSE values for temperature and salinity of ±0.6 °C and ±1.2 PSU respectively over the temperature and salinity ranges covered.

There are many regions in the spectra which provide relatively little information concerning either temperature or salinity. Further analysis was conducted in order to reduce the range of spectral data required while still retaining temperature and salinity information. The spectral regions which exhibit the greatest salinity and temperature influence were selected and another PLS–R model was produced, which is shown in Figure 5.11.

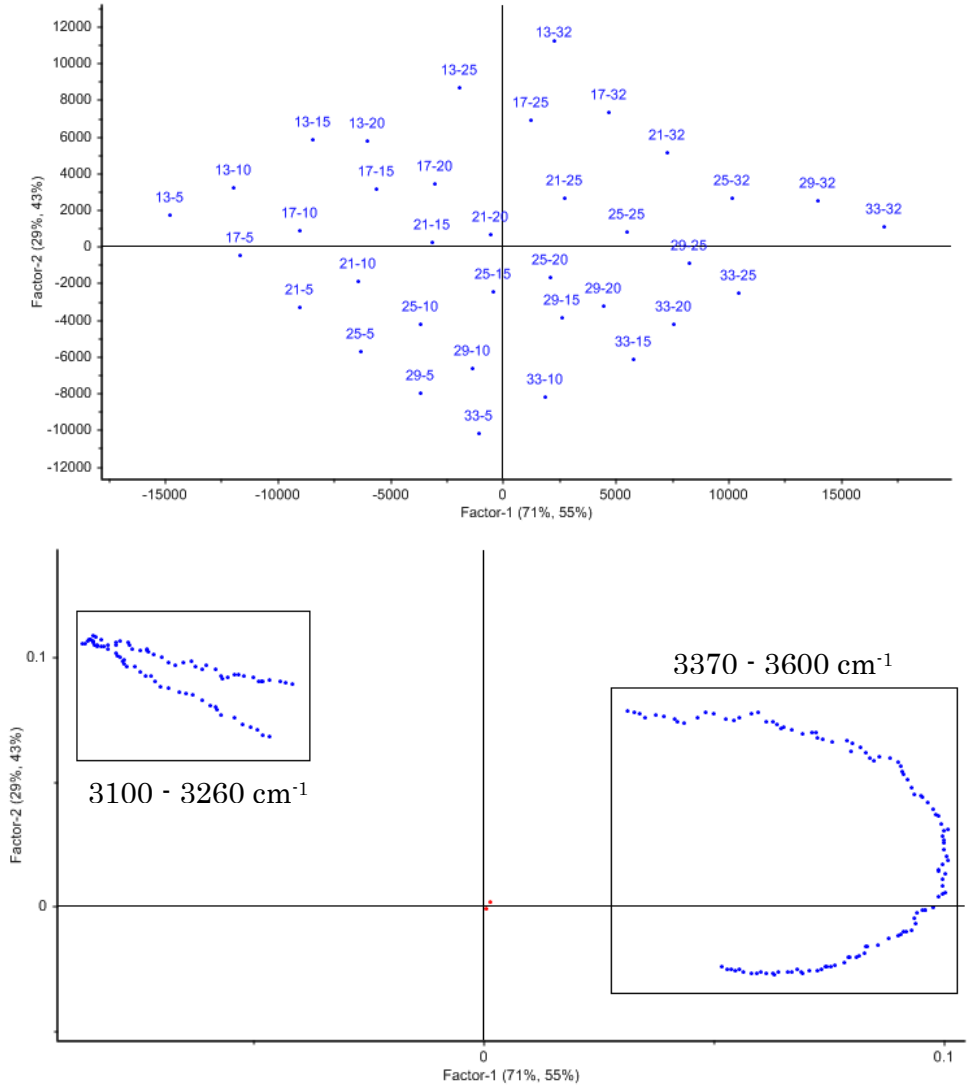

Figure 5.11 – PLS–R (a) scores and (b) loadings for portions of the unpolarised OH stretching band.

This model produced validation RMSE values for temperature and salinity of ±0.7 °C and ±1.1 PSU respectively when using two factors. This is reasonably close to the values for the model used to generate Figure 5.10, suggesting that this limited

set of data retains sufficient information to make reasonable measurements of both parameters.

On the basis of the results above, a set of three spectral bands were selected that could in principle be acquired using a three channel optical system. More spectral data points were removed from the set to produce the PLS–R model shown in Figure 5.12. The data was restricted to regions which are strongly influenced by temperature and salinity or exhibit influence from one parameter and very weak or no influence from the other.

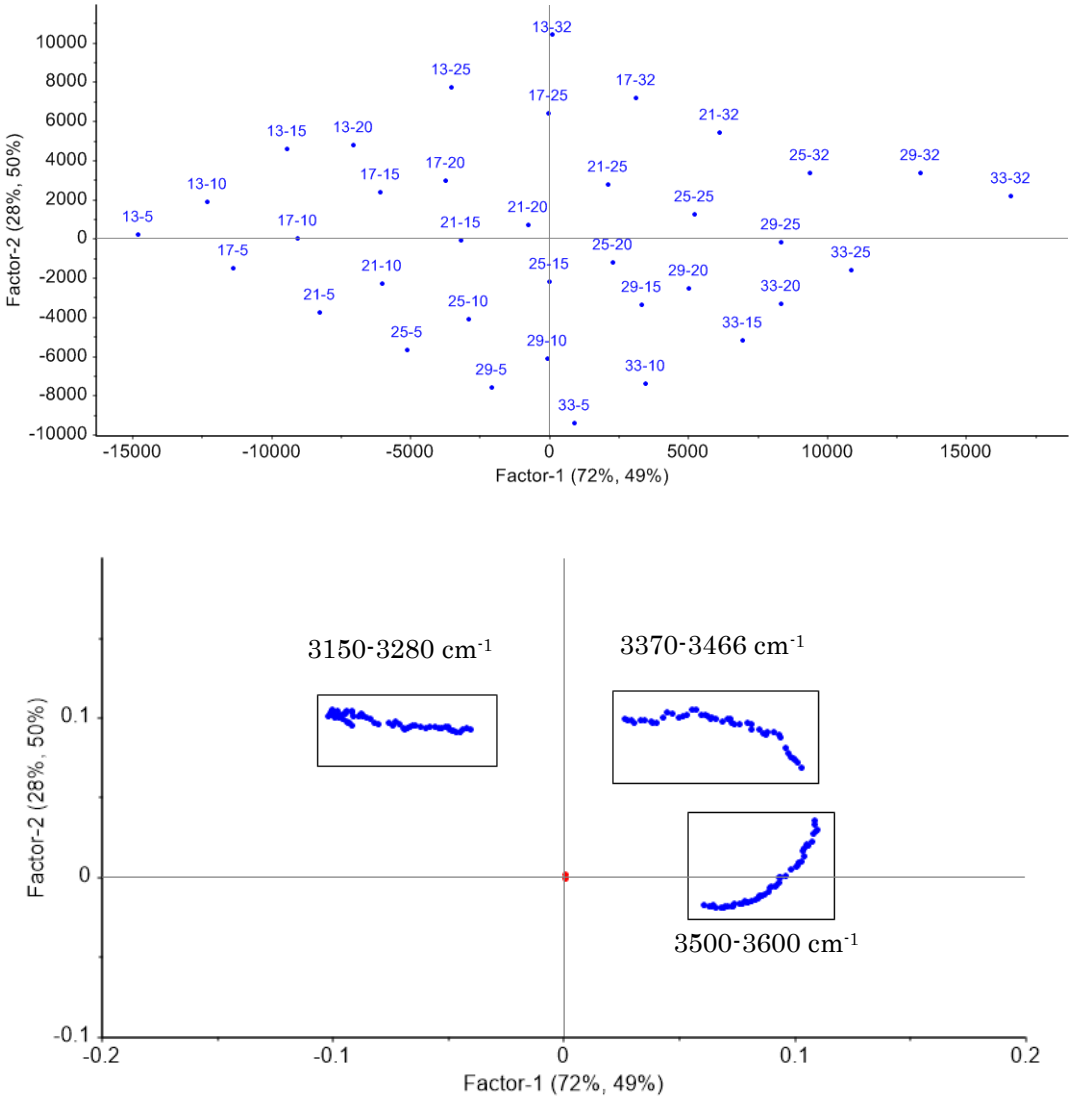

Figure 5.12 – PLS–R (a) scores and (b) loadings plots for three spectral regions from the unpolarised OH stretching band.

Similar loadings were observed to the previous model, indicating that the data removed was not critical. The RMSE values obtained were 0.7 °C for temperature and 1.3 PSU for salinity. For practical sensing, these spectral bands would be

acquired using integrated channels with wavelength–insensitive photodetectors. Figure 5.13 shows the same data, with each band summed to provide three data points representing these channels.

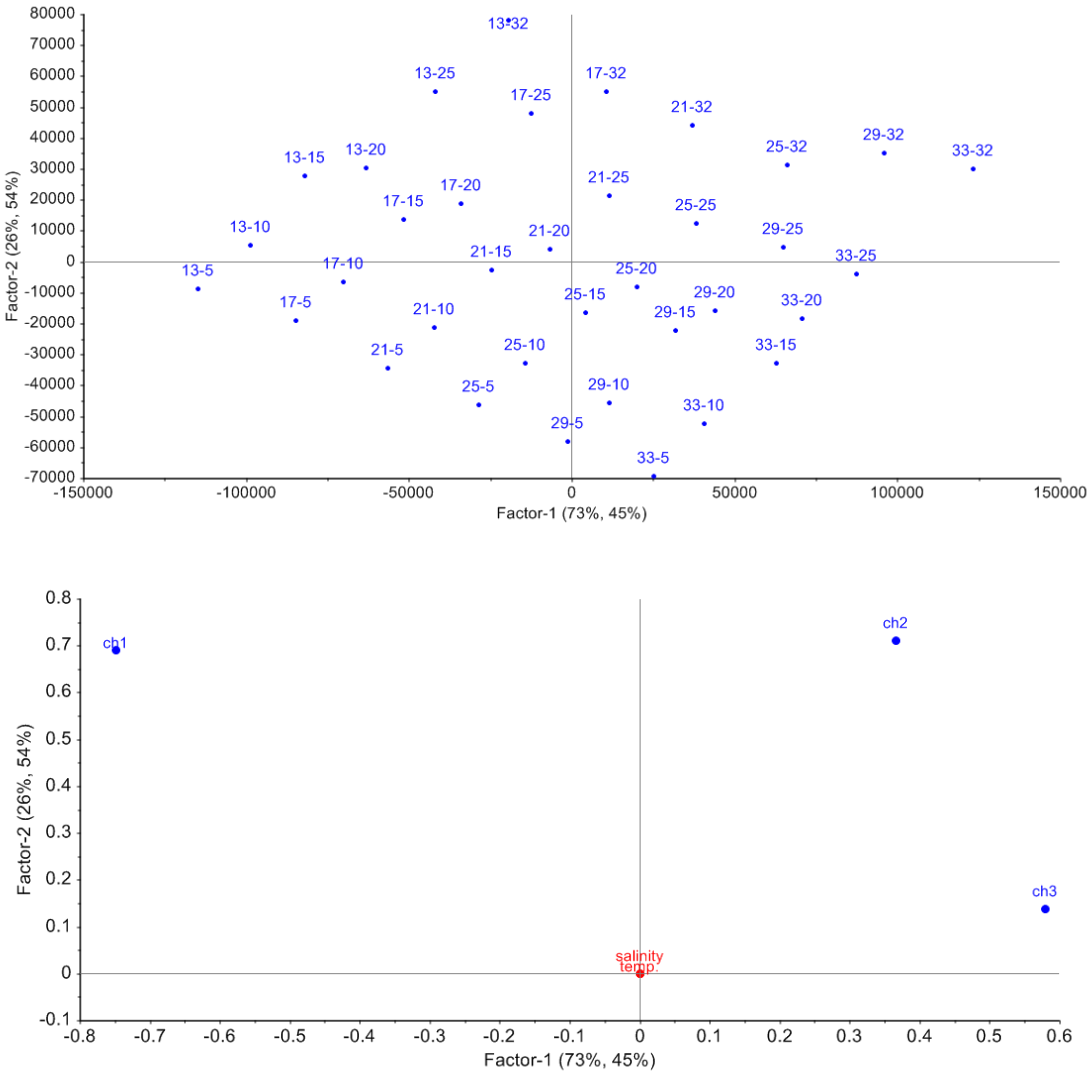

Figure 5.13 – PLS–R scores and loadings plots with 3 integrated spectral channels from unpolarised spectra.

As in the previous examples, the loadings plot retains virtually identical temperature and salinity information. Validation RMSE values were obtained for temperature and salinity of ±0.7 °C and ±1.4 PSU respectively with two factors.
A model of this kind should be capable of sufficient accuracy to acquire temperature and salinity information in the context of remote sensing. It should be noted that the error values produced here are for the entire temperature and salinity parameter space analysed. In the following analysis we consider whether improvement in performance can be derived from using constrained ranges of possible variation in temperature and salinity (e.g. through knowledge of local water conditions).

5.3.2 Multivariate Analysis – Parallel polarised spectra

Parallel polarised spectra were analysed in a similar manner to the unpolarised spectra above. This was done to assess whether simultaneous acquisition of temperature and salinity might be possible with sensing systems which utilise polarised signal detection. Figure 5.14 shows PCA plots for parallel polarised OH stretching band spectra. The 13 °C/25 PSU spectrum was removed due to severe distortion relative to the rest of the spectra set. Some structure is obvious in the scores plot, though the relationship with salinity was poor, far worse than was the case for unpolarised spectra. The behaviour with temperature was more consistent.

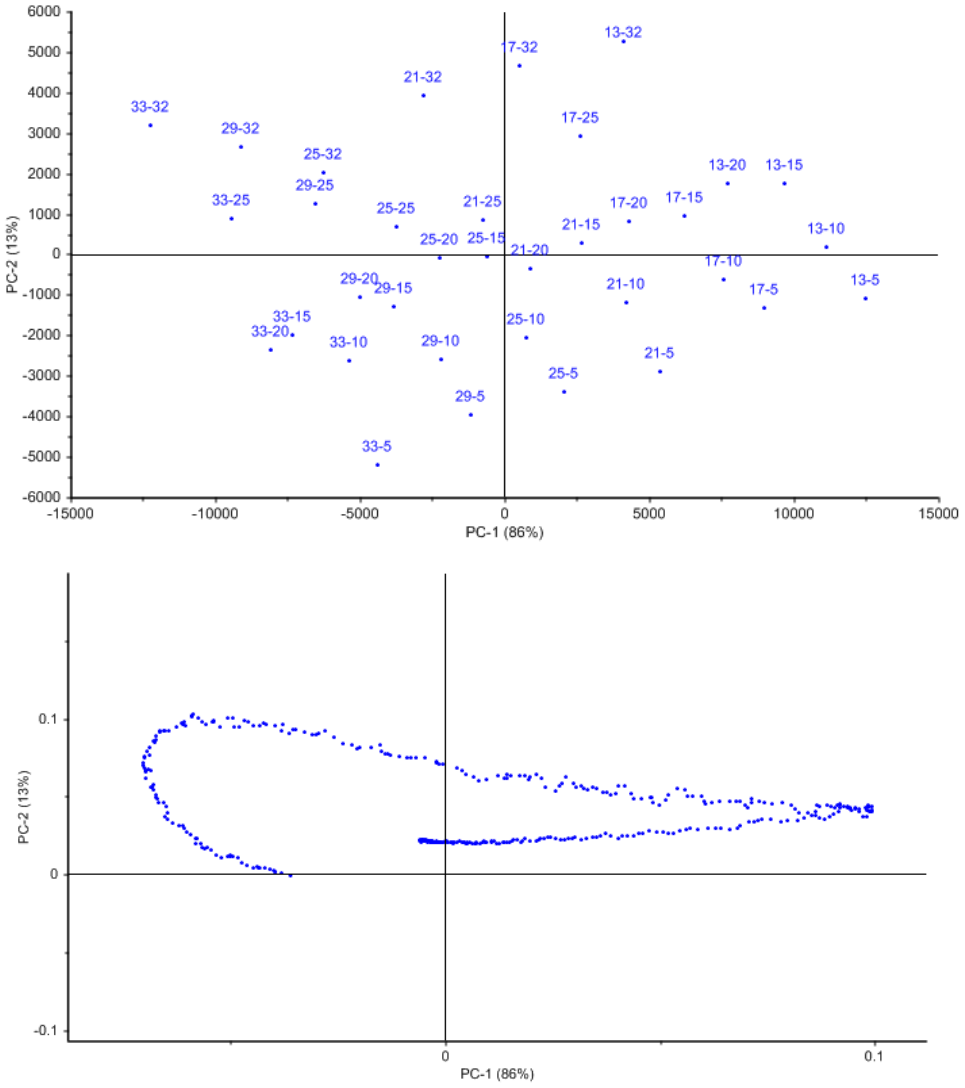

Figure 5.14 – PCA scores and loadings for parallel polarised Raman stretching band spectra (2800-3800 cm^{-1}).

Substantial correlation improvement is seen when the first derivative of spectra are analysed. Figure 5.15 shows the 1st derivative PLS–R scores and loadings for the stretching band with non–useful data removed.

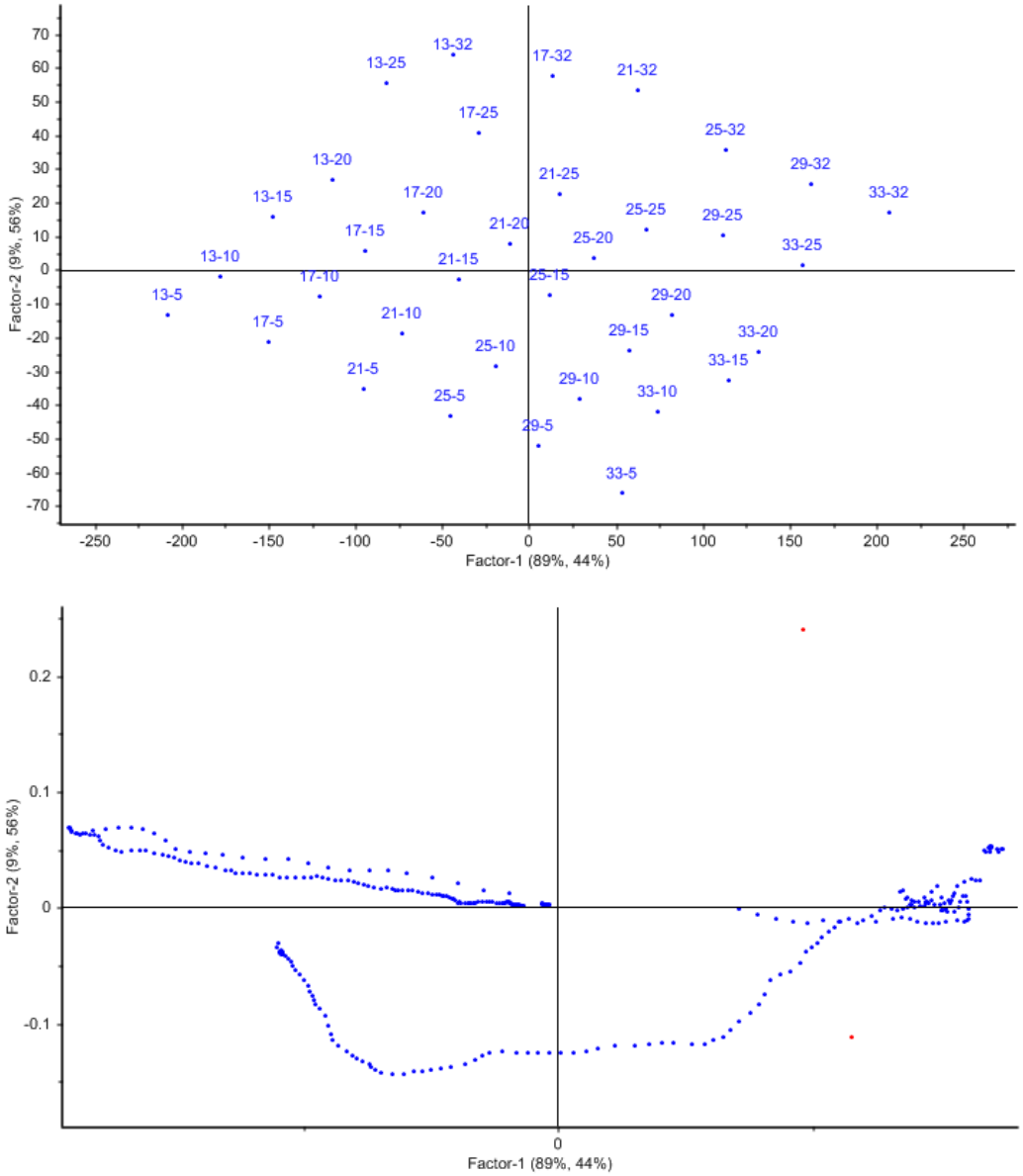

Figure 5.15 – PLS–R scores and loadings for 1st derivative parallel polarised Raman stretching band spectra (2800-3800 cm^{-1}).

The 1st derivative data produced RMSE values of ±0.5 °C and ±1.0 PSU for temperature and salinity respectively, indicating the data still contain the temperature and salinity information, albeit with more processing required than for the unpolarised case. This may be partially due to the lower signal intensity (~60% of the unpolarised peak intensity).

5.3.3 Multivariate Analysis – Perpendicular polarised spectra

PLS–R was used to analyse perpendicular polarised stretching band spectra in the same way as above, and RMSE values of ±0.7 °C and ±2.7 PSU were obtained. Significant improvement on these values was seen when the 1st derivative was taken prior to analysis, as shown in Figure 5.16 .

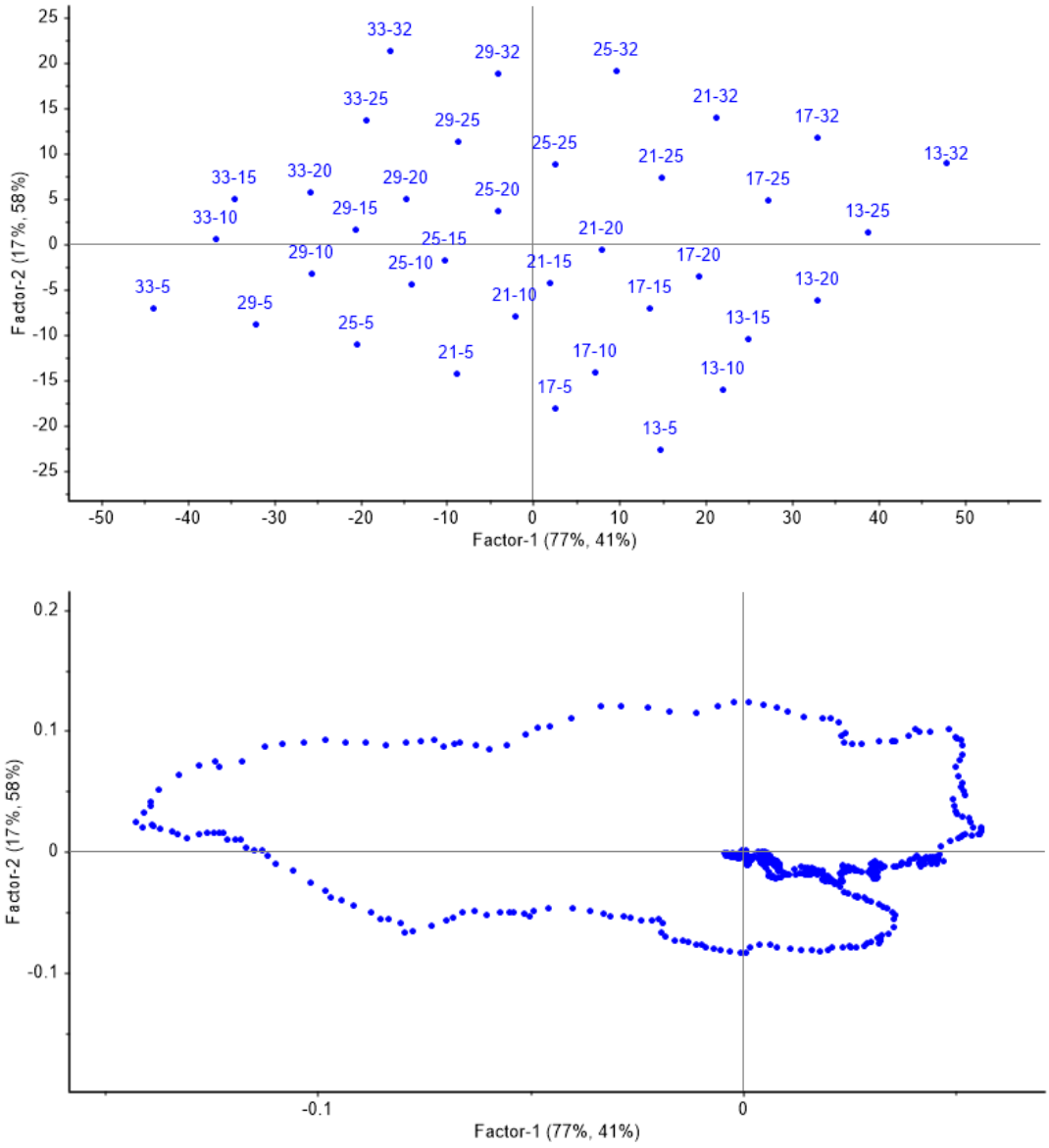

Figure 5.16 – PLS–R scores and loadings for 1st derivative perpendicular polarised spectra (2800-3800 cm⁻¹).

The 1st derivative of the perpendicular polarised spectra produced RMSE values of ±0.6 °C and ±1.1 PSU for temperature and salinity respectively. As in the parallel case, this indicates that the data still contain the temperature and salinity

information. This may not be the case when the available spectral information is limited (as in a narrow–band remote sensing system).

5.3.4 Multivariate Analysis – Depolarisation Ratio

PCA and PLS–R were used to examine the depolarisation ratio. Analysis using ratio values for the Raman shift range 2800-3800 cm^{-1} showed little correlation with the reference temperature and salinity data. When this range was reduced to 3100-3600 cm^{-1} some improvement was observed (Figure 5.17).

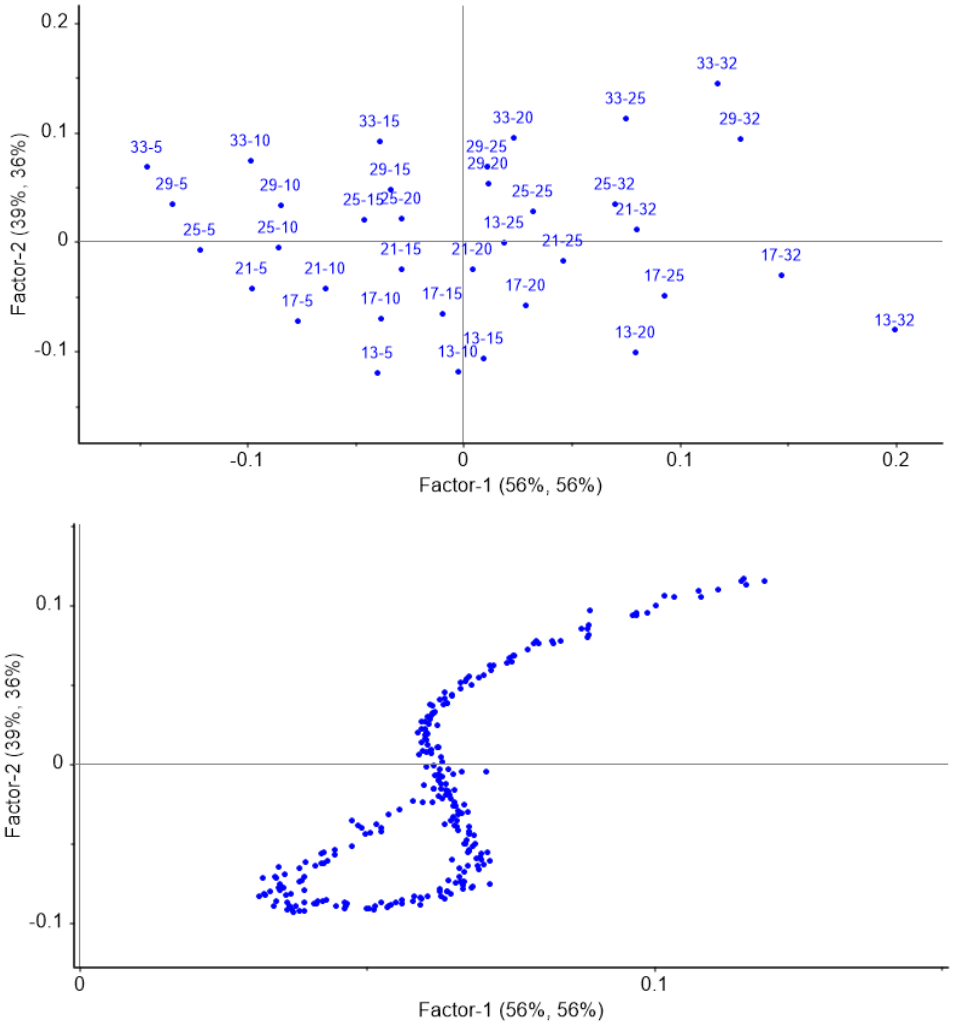

Figure 5.17 – PLS–R scores and loadings for the depolarisation ratio (3100-3600 cm^{-1}).

The PLS–R regression of this data produced RMSE values of ±2.0 °C and ±3.0 PSU for temperature and salinity respectively with two factors. These values are significantly higher than those found for the other multivariate spectral models examined here. The depolarisation ratio contains relatively little information concerning salinity change (see Figure 5.7), and so variance in the spectra which is

not related to temperature or salinity tends to distort both the salinity and temperature dependence. No further effort was made to study the depolarisation ratio for temperature and salinity determination.

5.4 Effect of parameter variation on measurement accuracy

The use of integrated spectral channels with unpolarised spectra to separate temperature and salinity inevitably means that cross–parameter interaction will occur, i.e. changes in salinity or temperature will result in additional uncertainty in measurement of the other parameter. The three channel unpolarised spectra scheme is considered from here onwards as the most viable option for remote sensing.

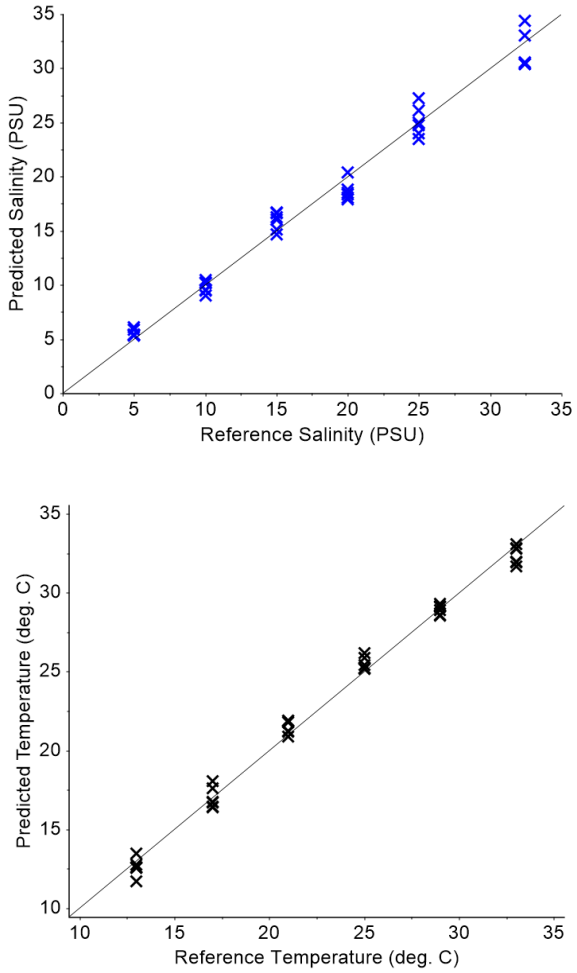

Figure 5.18 – Reference vs. Predicted (top) salinity (RMSE: 1.4) and (bottom) temperature (0.7) with the full range of unpolarised spectral data for the other parameter from three channels.

Figure 5.18 shows variation in unpolarised three channel (Figure 5.13) Raman determined temperature or salinity as the other parameter is varied. Up to two factors were used in the PLS–R models used to generate the data below.

The uncertainty in the plots shown in Figure 5.18 is caused by variation over the full range of the other parameter (temperature or salinity). The RMSE values for three spectral bands were ±0.7 °C for temperature and ±1.3 PSU for salinity, and ±0.6 °C and ±1.4 PSU respectively for integrated channels. The use of the entire data set under analysis here is not necessarily realistic in terms of the range of temperature and salinity values that occur naturally in an ocean water column. Reducing the range of variation in temperature and salinity to subsets of the full data set used above, (such as might be found in a geographically restricted area) may improve measurement accuracy. To assess the impact of the range of variation in temperature and salinity, models were built with ranges which might be observed in an ocean water column.

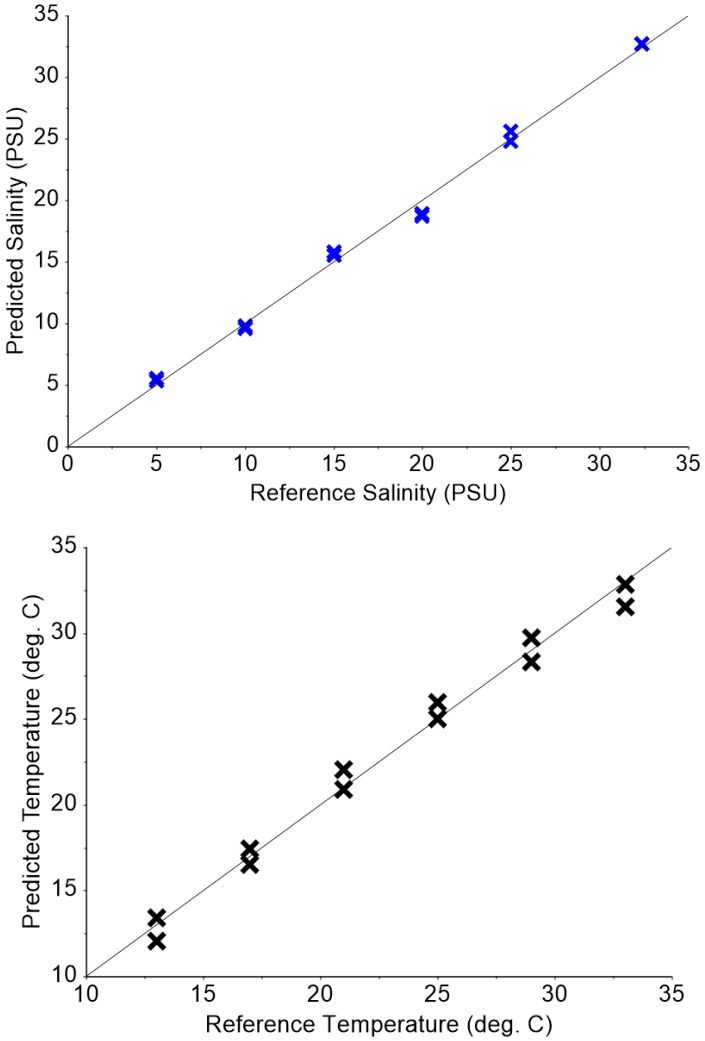

Figure 5.19 – Reference vs. Predicted (a) salinity (RMSE: ±0.6) and (b) temperature (RMSE: ±0.7 °C) with restricted range of variation for the other parameter (21-25 °C and 20-25 PSU respectively) from three channels.

Variations of roughly 4 °C and 5 PSU were determined to be reasonable ranges (for a geographically restricted study area) based on examination of water column data from several IMOS buoys along the Australian east coast [1].

Figure 5.19 shows plots with two successive levels of each parameter included, providing temperature-dependent data with salinity variation of 20-25 PSU, and salinity–dependent data with temperature variation of 21-25 °C. These temperature and salinity ranges were selected as being similar to natural levels which might be found in estuarine systems or coastal waterways. With the reduced parameter ranges, the RMSE values for three spectral bands were ±0.9 °C for temperature and ±0.6 PSU for salinity, and ±0.7 °C and ±0.6 PSU respectively for integrated channels. These values are similar to those for the full range of temperature and salinity covered in these experiments, with the exception of the RMSE value for 3 spectral bands with 20-25 PSU salinity (±0.9 °C), which was significantly higher than the average. A salinity range of 10-15 PSU for example, produced temperature RMSE values of 0.4 °C.

Table 5.2 summarises the temperature and salinity RMSE values acquired from PLS–R models using 3 bands of spectral data and for the same data integrated into single values representing channels.

Parameter	Salinity Coverage	RMSE	
		3 bands	3 integrated channels
Temperature (°C)	5-32 PSU	±0.7 °C	±0.6 °C
	20-25 PSU	±0.9 °C	±0.7 °C
	25 PSU	±0.6 °C	±0.6 °C

Parameter	Temp. Coverage	RMSE	
		3 bands	3 integrated channels
Salinity (PSU)	13-33 °C	±1.3 PSU	±1.4 PSU
	21-25 °C	±0.6 PSU	±0.6 PSU
	25 °C	±0.6 PSU	±0.6 PSU

Table 5.2 – Temperature and Salinity RMSE values comparing unpolarised spectral band data to integrated spectral channels over varying ranges of the other parameter.

Spectral data covering varying ranges of the "other parameter" (i.e. salinity in the case where temperature is being determined and temperature in the case where salinity is being determined) were used to observe the effect on RMSE values. The models described here suggest it should be feasible to determine both water temperature and salinity from water Raman scattered radiation with acceptable accuracy for many applications. When the "other parameter" is allowed to vary over a partial (realistic) range of ~4 °C or ~5 PSU, the RMSE values are similar to or lower than when the "other parameter" is allowed to vary over the full range examined (these ranges being ~20 °C and ~27 PSU). They also track fairly closely with RMSE values for isolated temperature or salinity change in saline water. This suggests that variations on this scale (~4 °C or ~5 PSU) should have minimal impact on measurement accuracy.

5.5 Proposed design of multi–channel sensing system

The findings of this chapter have been applied to design a multi–channel Raman spectrometer that is suited to sensing temperature and salinity. It incorporates three channels collecting Raman stretching band spectra for the separation and determination of temperature and salinity. The instrument layout is shown in Figure 5.20.

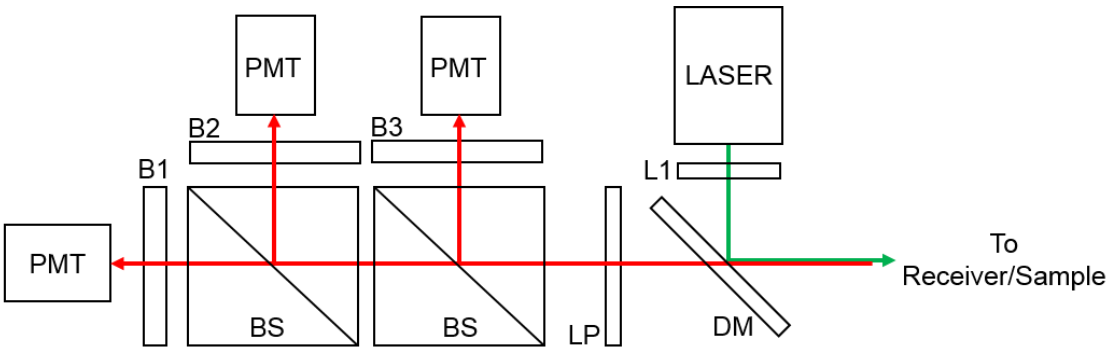

Figure 5.20 – Multi–channel Raman sensing configuration for three channel sensing of temperature and salinity.

The returning Raman signal (in red) is divided into three portions and passed through band–pass filters corresponding to spectral channels (such as those used in

Figure 5.13). The weakest channel would be directed to band–pass filter B3 for maximum signal intensity and optimal determination of temperature and salinity.

As in previous chapters, this spectrometer configuration can be extended in multiple ways. An additional channel could be added for monitoring of Rayleigh scattered return, which is useful for normalising detected Raman signals. Two out–of–band channels could be added for baseline correction as seen in Chapter 4.

5.6 Discussion and Summary

Unpolarised and polarised Raman spectra were measured for 36 combinations of temperature and salinity for saltwater collected from Sydney Harbour. Inspection of simple univariate plots, showing Raman spectra for different salinities (with fixed temperature) and different temperature (with fixed salinity) revealed different spectral regions having high salinity dependence/low temperature dependence and vice versa.

PCA and PLS–R offered a means by which the variance within the spectral data could be visualised. These tools were used to quantitatively explore which portions of the spectra contained the most "information" about temperature and salinity, leading to the identification of three spectral regions which correlate strongly with variation of one or both parameters. This exercise was conducted for unpolarised, parallel polarised and perpendicularly polarised spectra. Somewhat different spectral regions were found for each case, and more complex processing methods (e.g. taking derivatives) was required for temperature and salinity extraction from polarised spectra.

Based on the work in this chapter, it should be possible to determine both temperature and salinity from unpolarised spectra of water samples from this source with RMSE values of ±0.7 °C and ±1.3 PSU. For the case where three spectral regions are integrated to simulate channels, the predicted RMSE was found to be ±0.6 °C and ±1.4 PSU. A design for a multi–channel Raman spectrometer to acquire such channels has been proposed. The method involved bear similarity to the two–colour method for temperature determination, and could be considered a "three–colour" method.

On the basis of the multivariate analysis, the unpolarised spectra were used to build predictive models of temperature and salinity with the goal of determining

how much error would be introduced in one of these (e.g. temperature) by variation in the other. This is particularly relevant to the determination of water temperature in a column of seawater which will naturally have some salinity variation with depth. It was found that for water samples with salinity varying in a range of 5 PSU, temperature could be determined with RMSE values of ±0.4-0.7 °C.

6 Conclusions and Future Outlook

This thesis has addressed key aspects for the optical sensing of water temperature, with sensing of water salinity as a secondary goal. It has covered experimental investigations and numerical analysis of laser–induced Raman scattering in water, with a focus on the eventual goal of implementing rapid, depth–resolved measurement of water temperature and salinity in natural waters. The research has presented a new approach to analysis of Raman spectra for the purpose of temperature sensing incorporating multivariate methods. The analysis was more quantitative and detailed compared with previous studies which had comparable goals, most of which were based on spectral decomposition of the Raman OH stretching band.

Investigations using the two–colour ratio and depolarisation ratio have been conducted in the past, primarily with single point intensity values, little to no optimisation and often with some form of spectral decomposition required. The linear combination approach is a new development of this work which was intended to improve the robustness of temperature determination. Evaluation of the depolarisation ratio, and hence the linear combination, was hampered by experimental issues in collection of polarised Raman spectra.

Analytical tools were developed to optimise these temperature measurement methods. Two–colour ratio maps of temperature sensitivity and RMS temperature error were generated and used to identify optimal channel specifications. Depolarisation ratio sensitivity and RMSE plots were produced in the same way.

These tools provided the ability to predict the performance of simple multi–channel instruments and design optimal configurations for various methods. Designs for several multi–channel sensing instruments were presented which should be capable of acquiring the two–colour ratio, depolarisation ratio or both parameters simultaneously.

The effectiveness of Raman temperature sensing in natural waters was investigated. Past research has tended to use clean seawater for laboratory studies, or a limited range of water types in field studies. Similar analysis to that applied to laboratory water was used to assess a variety of natural fresh and saltwater samples. Linear baseline correction was applied to spectra and the effect on two–colour ratio and depolarisation ratio temperature accuracy examined. The site–specificity of water temperature models was examined, applying sample models to temperature measurement in each other sample both with and without baseline correction.

The effect of changes in salinity and temperature on water Raman spectra was explored. Multivariate analysis methods were used to separate and quantify these parameters. Past studies have investigated acquisition of temperature and salinity, but the use of multivariate methods is new to this work. The accuracy of temperature measurement with different ranges of salinity variation was analysed, and the potential to acquire both temperature and salinity simultaneously from Raman spectra was examined.

6.1 Research Outcomes

These studies have outlined requirements for different aspects of the sensing of water temperature and salinity with Raman spectroscopic methods. The analysis of laboratory water spectra in Chapter 3 provided detailed examination of the two–colour ratio and depolarisation ratio methods which allow temperature change to be quantified. The two–colour method was generally found to be more consistent and produced greater accuracy in temperature determination. The minimum two–colour RMS temperature error which might be achieved in ideal circumstances was determined to be ±0.1-0.2 °C which approached the limit of the reference temperature accuracy, while the lowest observed error for the depolarisation ratio (±0.5 °C) was limited by issues in the collection of polarised spectra.

These results were built on in Chapter 4 to extend this analysis to natural water samples. The two–colour method with natural water produced low temperature error for very clean or filtered water samples, or when baseline correction was applied for all but the worst samples analysed. The depolarisation ratio appeared more vulnerable to the constituents of water samples than anticipated, with baseline correction substantially improving accuracy, though this may again be influenced by the need to acquire linearly polarised spectra with separate spectrometer scans. The best–case RMS temperature error was ±0.1-0.2 °C using the two–colour method.

Site specificity of temperature models was relatively limited in range, i.e. samples needed to be similar to each other for reasonable temperature determination accuracy. Baseline correction improved performance to some extent. The best cases observed (with or without baseline correction) produced RMSE values of ±0.3 °C. From this study it is clear that baseline correction or compensation of some form is required for anything other than the clearest natural waters.

The temperature and salinity analysis in Chapter 5 showed that these physical properties have somewhat similar effects on the Raman OH stretching band. This makes the two parameters somewhat difficult to decouple, with a minimum of three integrated spectral channels required to achieve this. Multivariate analysis was used to identify optimal locations for these channels over the OH stretching band for maximum temperature and salinity correlation. The transition from spectral data corresponding to the three identified bands to integrated single values representing channels resulted in very little change in RMSE values, suggesting the channels were well placed for temperature and salinity determination. Small variations in either temperature or salinity were shown to have relatively low impact on RMSE over the full range of the other parameter. This indicates that compensation for salinity in temperature measurement is not strictly required for waters with relatively small salinity variations (up to 5 PSU) and the same holds for temperature compensation in salinity measurement.

During my PhD I carried out a number of studies which are not detailed in this thesis. First, a remote sensing system based on the two–colour method was constructed and tested in the late stages of this research project. Preliminary field experimentation was carried out, which included the trialling of several receiver designs, assessment of the impact of ambient light and direct sunlight on signal–to–noise ratios, and the acquisition of Raman signals with a pulsed 532 nm laser source

averaged over multiple pulses. A brief summary of the work leading up to and including the field work is provided in Appendix D.

Second, a pilot study was conducted into the sensing of temperature in the human eye during ophthalmic surgery, in collaboration with an industry partner during my PhD project. Raman spectra were collected from a range of animal ocular tissues for characterisation. Further development would be required to fully assess the potential this technique might hold for improving surgical procedures.

Third, I applied multivariate analysis to an interesting investigation of blue fluorescence in crystalline Raman materials, in a quest to understand the origin of this fluorescence. The journal paper stemming from that work is in Appendix A.

The results presented in this thesis clearly demonstrate the feasibility of using Raman spectroscopy for optical sensing of water temperature, with temperature errors well below 1 °C observed in a wide range of situations. Measurement accuracy achieved was equivalent or better when contrasted with past research in this area (see Table 1.3 and Table 1.4), particularly for pure fresh water and relatively clean salt water samples. The temperature accuracy obtained in these cases (~±0.1 °C) was roughly equivalent to the measurement accuracy of the hardware sensors which were used to acquire reference temperature data.

The measurement methods investigated here are well–suited to virtually any laboratory or industrial application which would benefit from non–contact, accurate measurement of water temperature. With the addition of LIDAR methods and depth resolution, we anticipate strong potential for many practical applications in the areas of hydrology, oceanography and climate science.

6.2 Future Outlook

The outcomes of this research enable us to identify areas where further work is needed to reach the goal of depth–resolved remote temperature sensing.

Laboratory validation of the multi–channel spectrometer configurations is required, particularly the depolarisation and linear combination designs. The simultaneous collection of spectral data should alleviate the issues with variability which adversely affected the temperature dependence of the depolarisation ratio, enabling practical comparison of the two–colour and depolarisation methods.

The need for baseline correction or compensation in natural waters, particularly those with high concentrations of organic matter and suspended particulates was made clear in Chapter 4. More sophisticated correction techniques (compared with the linear baseline methods employed here) may be required for these cases.

A scheme which would completely eliminate baseline effects with the two–colour method was conceived during the research project, and it bears future investigation. The use of two excitation laser sources with appropriate wavelength separation would allow their corresponding Raman stretching band emission to overlap in wavelength such that both sides of the stretching band could be acquired with a single band–pass filter and detector configuration. This would require alternating pulses from each source, or possibly a single pulsed laser source which can generate both wavelengths, such as a solid–state Raman laser. Such a technique would also minimise differential attenuation effects caused by passage through the water column in remote sensing schemes.

Further field experimentation will be conducted, including studies to optimise the receiver used for signal collection, characterisation of various multi–channel sensing configurations for *in situ* remote sensing use, and assessment of temperature determination accuracy at depth, also estimating the maximum practical depths at which spectral information and hence temperature can be acquired. The use of shorter excitation wavelengths, such as 473 nm will be studied to improve the retrieval of Raman signals from depth. As part of this study, a multi–channel spectrometer for simultaneous acquisition of temperature and salinity will be constructed, characterised in the laboratory, and tested in the field.

There is significant potential to realise useful instrumentation in this area. Ideally this work will lead to development of LIDAR systems to remotely acquire water temperature and/or salinity data. These could be compact enough to mount on an underwater glider, AUV (autonomous underwater vehicle) or aerial drone. Depending on the desired configuration, suitable low-power laser sources, detectors and data acquisition hardware are readily available.

The required temperature and salinity accuracy will depend on the specific application, and consultation with experts will be required in the future. Rapid remote sensing of sub-surface temperature and salinity is a unique capability which is not available with currently available commercial measurement systems.

Performance of such a system would vary considerably based on our current methods, with good results expected in relatively clear ocean waters and somewhat lower measurement capability in turbid coastal waters, both in terms of depth (or range) of light propagation in water, and temperature and salinity measurement accuracy.

Bibliography

1. T. Trull, E. Schulz et al., "The Australian Integrated Marine Observing System Southern Ocean Time Series facility" in OCEANS 2010 IEEE-Sydney, (2010).
2. D. Roemmich, O. Boebel et al.,"Argo: the global array of profiling floats (2001).
3. D. M. Carey and G. M. Korenowski,"Measurement of the Raman spectrum of liquid water", The Journal of chemical physics **108** (1998).
4. P. Ball,"Water: Water -- an enduring mystery", Nature **452** (7185), 291-292 (2008).
5. N. G. Jerlov, Optical oceanography. (Elsevier Pub. Co, Amsterdam, New York, 1968).
6. C. D. Mobley, Optical Properties of Water in *Handbook of Optics*, (McGraw-Hill, 1995), Vol. 1.
7. D. R. Lide, CRC Handbook of Chemistry and Physics, 2009–2010, 90th ed. (American Chemical Society, 2009).
8. Physical properties of sea water, 2.7.9 Kaye & Laby Online Version 1.0 (2005).
9. H. Sverdrup, M. Johnson et al., The Oceans: Their Physics, Chemistry, and General Biology. (Prentice-Hall, New York, 1942).
10. P. H. Bigg,"Density of water in SI units over the range 0-40°C", British Journal of Applied Physics **18** (4), 521 (1967).
11. S. V. Lishchuk, N. P. Malomuzh et al.,"Contribution of H-bond vibrations to heat capacity of water", Physics Letters A **375** (27), 2656-2660 (2011).
12. G. M. Hale and M. R. Querry,"Optical Constants of Water in the 200-nm to 200-μm Wavelength Region", Appl. Opt. **12**, 555-563 (1973).
13. M. Daimon and A. Masumura,"Measurement of the refractive index of distilled water from the near-infrared region to the ultraviolet region", Appl. Opt. **46**, 3811-3820 (2007).

14. A. H. Harvey, J. S. Gallagher et al.,"Revised Formulation for the Refractive Index of Water and Steam as a Function of Wavelength, Temperature and Density", Journal of Physical and Chemical Reference Data **27**, 761-774 (1998).
15. X. Quan and E. S. Fry,"Empirical equation for the index of refraction of seawater", Appl. Opt. **34**, 3477-3480 (1995).
16. H. Buiteveld, J. H. M. Hakvoort et al., "Optical properties of pure water", (1994).
17. R. C. Smith and K. S. Baker,"Optical properties of the clearest natural waters(200-800 nm)", Applied optics **20** (2), 177-184 (1981).
18. F. M. Sogandares and E. S. Fry,"Absorption spectrum (340–640 nm) of pure water. I. Photothermal measurements", Applied Optics **36** (33), 8699-8709 (1997).
19. A. C. Tam and C. K. N. Patel,"Optical absorptions of light and heavy water by laser optoacoustic spectroscopy", Applied Optics **18** (19), 3348-3358 (1979).
20. A. Bricaud, A. Morel et al.,"Absorption by dissolved organic matter of the sea (yellow substance) in the UV and visible domains", Limnol. Oceanogr **26** (1), 43-53 (1981).
21. R. M. Pope and E. S. Fry,"Absorption spectrum (380-700 nm) of pure water. II. Integrating cavity measurements", Applied optics **36** (33), 8710-8723 (1997).
22. M. Bazzani, B. Breschi et al., "Phytoplankton Monitoring by Laser Induced Fluorescence" in EARSeL ADVANCES IN REMOTE SENSING, (1992).
23. C. D. Mobley, Light and water: Radiative Transfer in Natural Waters. (Academic Press, 1994).
24. C. F. Bohren and D. R. Huffman, Absorption and Scattering of Light by Small Particles. (Wiley-Interscience, 1998).
25. R. Figgins,"Inelastic light scattering in liquids: Brillouin scattering", Contemporary Physics **12** (3), 283-297 (1971).
26. E. B. Wilson, J. C. Decius et al., Molecular Vibrations: The Theory of Infrared and Raman Vibrational Spectra. (Dover Publications, 1955).
27. G. D. Hickman, J. M. Harding et al.,"Aircraft laser sensing of sound velocity in water: Brillouin scattering", Remote sensing of environment **36** (3), 165-178 (1991).

28. E. S. Fry, Y. Emery et al.,"Accuracy limitations on Brillouin lidar measurements of temperature and sound speed in the ocean", Applied Optics **36** (27), 6887-6894 (1997).
29. K. Schorstein, A. Popescu et al.,"Remote Water Temperature Measurements Based on Brillouin Scattering with a Frequency Doubled Pulsed Yb:doped Fiber Amplifier", Sensors (Basel, Switzerland) **8** (9), 5820-5831 (2008).
30. C. V. Raman,"A New Radiation", Indian Journal of Physics **2**, 387-398 (1928).
31. J. R. Ferraro, K. Nakamoto et al., Introductory Raman Spectroscopy, 2nd ed. (Academic Press, 2003).
32. R. L. McCreery, Raman Spectroscopy for Chemical Analysis. (John Wiley & Sons, Inc., Hoboken, NJ, USA, 2005).
33. S. P. d. S. Porto,"Angular dependence and depolarization ratio of the Raman effect", JOSA **56** (11), 1585-1586 (1966).
34. G. Placzek,"Rayleigh scattering and the Raman Effect (transl.)", Handbuch der Radiologie **6** (1934).
35. L. A. Woodward and D. A. Long,"Relative intensities in the Raman spectra of some Group IV tetrahalides", Transactions of the Faraday Society **45** (1949).
36. R. B. Slusher and V. E. Derr,"Temperature dependence and cross sections of some Stokes and anti-Stokes Raman lines in ice lh", Applied optics **14** (9), 2116-2120 (1975).
37. S. Sugihara, M. Kishino et al.,"Contribution of Raman scattering to upward irradiance in the sea", Journal of the Oceanographical Society of Japan **40** (6), 397-404 (1984).
38. J. S. Bartlett, K. J. Voss et al.,"Raman scattering by pure water and seawater", Applied optics **37**, 3324-3332 (1998).
39. G. W. Faris and R. A. Copeland,"Wavelength dependence of the Raman cross section for liquid water", Applied optics **36** (12), 2686-2688 (1997).
40. B. R. Marshall and R. C. Smith,"Raman scattering and in-water ocean optical properties", Applied Optics **29** (1), 71-84 (1990).
41. C. Hu and K. J. Voss,"In situ measurements of Raman scattering in clear ocean water", Appl. Opt. **36**, 6962-6967 (1997).
42. V. Haltrin, Absorption and scattering of light in natural waters in *Light Scattering Reviews*, (Springer Berlin Heidelberg, 2006), pp. 445-486.
43. H. Hamaguchi and T. L. Gustafson,"Ultrafast Time-Resolved Spontaneous and Coherent Raman Spectroscopy: The Structure and Dynamics of

Photogenerated Transient Species", Annual Review of Physical Chemistry **45** (1), 593-622 (1994).

44. E. V. Efremov, F. Ariese et al.,"Achievements in resonance Raman spectroscopy: Review of a technique with a distinct analytical chemistry potential", Analytica Chimica Acta **606** (2), 119-134 (2008).
45. S. Schlücker,"Surface-Enhanced Raman Spectroscopy: Concepts and Chemical Applications", Angewandte Chemie International Edition **53** (19), 4756-4795 (2014).
46. C. L. Evans and X. S. Xie,"Coherent Anti-Stokes Raman Scattering Microscopy: Chemical Imaging for Biology and Medicine", Annual Review of Analytical Chemistry **1** (1), 883-909 (2008).
47. G. E. Walrafen,"Raman Spectral Studies of the Effects of Electrolytes on Water", The Journal of Chemical Physics **36**, 1035-1042 (1962).
48. Z. Wang, A. Pakoulev et al.,"Vibrational Substructure in the OH Stretching Transition of Water and HOD", The Journal of Physical Chemistry A **108** (42), 9054-9063 (2004).
49. D. E. Hare and C. M. Sorensen,"Raman spectroscopic study of dilute HOD in liquid HO in the temperature range- 31.5 to 160° C", The Journal of chemical physics **93** (1990).
50. S. A. Rice, M. S. Bergren et al.,"A theoretical analysis of the hydroxyl stretching spectra of ice Ih, liquid water, and amorphous solid water", The Journal of Physical Chemistry **87** (21), 4295-4308 (1983).
51. G. Avila, J. M. Fernández et al.,"The Raman spectra and cross-sections of H2O, D2O, and HDO in the OH/OD stretching regions", Journal of Molecular Spectroscopy **228** (1), 38-65 (2004).
52. P. Cieplak, P. Kollman et al.,"A new water potential including polarization: Application to gas-phase, liquid, and crystal properties of water", The Journal of chemical physics **92** (1990).
53. G. d'Arrigo, G. Maisano et al.,"Raman scattering and structure of normal and supercooled water", The Journal of Chemical Physics **75** (1981).
54. T. Hasegawa and Y. Tanimura,"A Polarizable Water Model for Intramolecular and Intermolecular Vibrational Spectroscopies", The Journal of Physical Chemistry B **115** (18), 5545-5553 (2011).

55. M. Paolantoni, N. F. Lago et al.,"Tetrahedral Ordering in Water: Raman Profiles and Their Temperature Dependence", The Journal of Physical Chemistry A **113** (52), 15100-15105 (2009).

56. J. D. Smith, C. D. Cappa et al.,"Unified description of temperature-dependent hydrogen-bond rearrangements in liquid water", Proceedings of the National Academy of Sciences of the United States of America **102** (40), 14171-14174 (2005).

57. Y. Tominaga, A. Fujiwara et al.,"Dynamical structure of water by Raman spectroscopy", Fluid Phase Equilib. **144**, 323-330 (1998).

58. Y. Zubavicus and M. Grunze,"New Insights into the Structure of Water with Ultrafast Probes", Science **304**, 974-976 (2004).

59. G. E. Walrafen,"Raman spectral studies of the effects of temperature on water and electrolyte solutions", The Journal of Chemical Physics **44** (1966).

60. G. E. Walrafen,"Raman spectral studies of the effects of temperature on water structure", J. Chem. Phys. **47** (1967).

61. G. E. Walrafen,"Raman Spectral Studies of the Effects of Solutes and Pressure on Water Structure", The Journal of Chemical Physics **55**, 768-792 (1971).

62. G. E. Walrafen, M. R. Fisher et al.,"Temperature dependence of the low and high frequency Raman scattering from liquid water", The Journal of Chemical Physics **85** (1986).

63. G. E. Walrafen, M. S. Hokmabadi et al.,"Raman isosbestic points from liquid water", J. Chem. Phys. **85** (1986).

64. G. E. Walrafen, M. S. Hokmabadi et al.,"Collision-induced Raman scattering from water and aqueous solutions", The Journal of Physical Chemistry **93** (8), 2909-2917 (1989).

65. W. B. Monosmith and G. E. Walrafen,"Temperature dependence of the Raman OH-stretching overtone from liquid water", The Journal of Chemical Physics **81**, 669-674 (1984).

66. K. Cunningham and P. A. Lyons,"Depolarization ratio studies on liquid water", J. Chem. Phys. **59**, 2132-2139 (1973).

67. J. R. Scherer, M. K. Go et al.,"Raman spectra and structure of water from -10 to 90 deg", The Journal of Physical Chemistry **78** (13), 1304-1313 (1974).

68. Q. Hu, H. Guo et al.,"Raman spectroscopic investigation on aqueous NaCl solutions at temperatures from 273 to 573K: Effect of NaCl on water structure", Journal of Molecular Liquids **199**, 83-87 (2014).

69. K. Furić, I. Ciglenečki et al.,"Raman spectroscopic study of sodium chloride water solutions", Journal of Molecular Structure **550–551** (0), 225-234 (2000).

70. C. I. Ratcliffe and D. E. Irish,"Vibrational spectral studies of solutions at elevated temperatures and pressures. 5. Raman studies of liquid water up to 300. degree. C", The Journal of Physical Chemistry **86** (25), 4897-4905 (1982).

71. D. N. Whiteman, G. E. Walrafen et al.,"Measurement of an isosbestic point in the Raman spectrum of liquid water by use of a backscattering geometry", Applied Optics **38** (12), 2614-2615 (1999).

72. M. Becucci, S. Cavalieri et al.,"Raman spectroscopy for water temperature sensing", Applied Optics (38), 928-93122–93425 (1999).

73. G. Cecchi and V. Raimondi, "Remote Raman spectra for the monitoring of water column temperature" in Quantitative Remote Sensing for Science and Applications, IGARSS '95., (1995).

74. D. A. Leonard, B. Caputo et al.,"Remote sensing of subsurface water temperature by Raman scattering", Applied Optics **18** (11), 1732-1745 (1979).

75. D. A. Leonard, B. Caputo et al.,"Experimental remote sensing of subsurface temperature in natural ocean water", Geophysical Research Letters **4** (7), 279-281 (1977).

76. M. Baumgartner and R. J. Bakker,"Raman spectroscopy of pure H2O and NaCl-H2O containing synthetic fluid inclusions in quartz—a study of polarization effects", Mineralogy and Petrology **95**, 1-15 (2009).

77. B. Breschi, G. Cecchi et al., "Measurement of Water Column Temperature by Raman Scattering", (1992).

78. C. S. Lin,"Tunable laser induced scattering from coastal water", Geoscience and Remote Sensing, IEEE Transactions on **37** (5), 2461-2468 (1999).

79. V. Raimondi and G. Cecchi,"Lidar Field Experiments for Monitoring Sea Water Column Temperature", EARSeL Advances in Remote Sensing **3**, 84-89 (1995).

80. D. Risović and K. Furić,"Comparison of Raman spectroscopic methods for the determination of supercooled and liquid water temperature", Journal of Raman Spectroscopy **36** (8), 771-776 (2005).

81. M. Bradley,"Curve fitting in Raman and IR spectroscopy: basic theory of line shapes and applications", Thermo Fisher Scientific, Madison, USA, Application Note **50733** (2007).
82. T. Sundius,"Computer fitting of Voigt profiles to Raman lines", Journal of Raman Spectroscopy **1** (5), 471-488 (1973).
83. Z. Liu, J. Zhang et al., "Remote sensing of subsurface water temperature using Raman lidar", (1992).
84. C. H. Chang and L. A. Young, "Remote measurement of ocean temperature from depolarization in Raman scattering" in The use of Lasers for Hydrographic Studies, (1975).
85. J. E. James, C. S. Lin et al.,"Simulation of Laser-Induced Light Emissions from Water and Extraction of Raman Signal", Journal of Atmospheric and Oceanic Technology **16** (3), 394-401 (1999).
86. C. H. Chang and L. A. Young, DTIC Document, 1972.
87. R. L. Schwiesow, "Raman scattering studies of pollutant systems" in Joint Conference on Sensing of Environmental Pollutants, (1971).
88. C. H. Chang, L. A. Young et al., US Patent No. 3,986,775 1976 1976.
89. D. J. Collins, J. A. Bell et al., "Recent progress in the measurement of temperature and salinity by optical scattering" in Ocean Optics VII, (1984).
90. C. S. Lin,"Tunable laser induced scattering from coastal water", Geoscience and Remote Sensing, IEEE Transactions on **37**, 2461-2468 (1999).
91. C. S. Lin,"Characteristics of laser-induced inelastic-scattering signals from coastal waters", Remote Sensing of Environment **77** (1), 104-111 (2001).
92. M. Becucci, S. Cavalieri et al.,"Accuracy of remote sensing of water temperature by Raman spectroscopy", Applied optics **38** (1999).
93. S. A. Burikov, I. V. Churina et al.,"New approaches to determination of temperature and salinity of seawater by laser Raman spectroscopy", EARSeL eProceedings **3** (2004).
94. S. A. Burikov, T. A. Dolenko et al.,"The effect of hydration of ions of inorganic salts on the shape of the Raman stretching band of water", Optics and Spectroscopy **98**, 235-239 (2005).
95. T. Dolenko, S. Burikov et al.,"Remote determination of temperature and salinity in presence of dissolved organic matter in natural waters using laser spectroscopy", EARSeL eProceedings **10** (2), 159-165 (2011).

96. T. A. Dolenko, I. V. Churina et al.,"Valence band of liquid water Raman scattering: some peculiarities and applications in the diagnostics of water media", Journal of Raman Spectroscopy **31**, 863-870 (2000).

97. S. V. Patsayeva,"Remote Measurement of Sea Water Temperature, Salinity and Thickness of Oil Film Using Water Raman Scattering", INTERNATIONAL ARCHIVES OF PHOTOGRAMMETRY AND REMOTE SENSING **29** (1993).

98. A. F. Bunkin, V. K. Klinkov et al.,"Remote sensing of seawater and drifting ice in Svalbard fjords by compact Raman lidar", Applied Optics **51** (22), 5477-5485 (2012).

99. S. M. Pershin, A. F. Bunkin et al.,"Evolution of the spectral component of ice in the OH band of water at temperatures from 13 to 99°C", Quantum Electronics **40** (12), 1146 (2010).

100. D. A. Leonard and B. Caputo,"Raman Remote Sensing Of The Ocean Mixed-Layer Depth", OPTICE **22** (3), 223288-223288- (1983).

101. Y. Pan, R. E. Faw et al.,"Laser-Raman remote temperature sensing in liquids", Experiments in fluids **2** (2), 81-88 (1984).

102. K. L. Davis, K. L. K. Liu et al.,"Spatially resolved temperature measurements in electrophoresis capillaries by Raman thermometry", Analytical chemistry **65** (3), 293-298 (1993).

103. A. Ewinger, G. Rinke et al.,"In situ measurement of the temperature of water in microchannels using laser Raman spectroscopy", Chemical Engineering Journal **223** (0), 129-134 (2013).

104. R. Kuriyama and Y. Sato,"Non-intrusive measurement of microscale temperature distribution by spontaneous Raman imaging", Microfluidics and Nanofluidics **14** (6), 1031-1037 (2013).

105. S. H. Kim, J. Noh et al.,"Micro-Raman thermometry for measuring the temperature distribution inside the microchannel of a polymerase chain reaction chip", Journal of Micromechanics and Microengineering **16** (3), 526 (2006).

106. R. Kuriyama and Y. Sato,"Two-wavelength Raman imaging for non-intrusive monitoring of transient temperature in microfluidic devices", Measurement Science and Technology **25** (9), 095203 (2014).

107. N. J. C. Bauer, M. Motamedi et al.,"Remote temperature monitoring in ocular tissue using confocal Raman spectroscopy", BIOMEDO **10** (3), 031109-0311095 (2005).

108. V. Pikov and P. H. Siegel,"Thermal Monitoring: Raman Spectrometer System for Remote Measurement of Cellular Temperature on a Microscopic Scale", Engineering in Medicine and Biology Magazine, IEEE **29** (1), 63-71 (2010).

109. H. T. Beier, G. D. Noojin et al.,"Localized thermal mapping using coherent anti-Stokes Raman spectroscopy", BIOMEDO **17** (8), 0805011-0805013 (2012).

110. J. Mukerjee, DSTO, 2001.

111. InPhotonics, *Technical Note #13* (1999).

112. A. Savitzky and M. J. E. Golay,"Smoothing and Differentiation of Data by Simplified Least Squares Procedures", Analytical Chemistry **36**, 1627-1639 (1964).

113. P. H. Eilers and H. F. Boelens,"Baseline correction with asymmetric least squares smoothing", Leiden University Medical Centre Report (2005).

114. K. H. Esbensen, D. Guyot et al., Multivariate Data Analysis: In Practice : an Introduction to Multivariate Data Analysis and Experimental Design. (CAMO, 2002).

115. S. Engelen, M. Hubert et al., Robust PCR and Robust PLSR: a comparative study in *Theory and applications of recent robust methods*, (Springer, 2004), pp. 105-117.

116. S. Wold, M. Sjöström et al.,"PLS-regression: a basic tool of chemometrics", Chemometrics and intelligent laboratory systems **58** (2), 109-130 (2001).

117. R. F. Chen and J. L. Bada,"The fluorescence of dissolved organic matter in seawater", Marine Chemistry **37** (3), 191-221 (1992).

118. A. Morel and S. Maritorena,"Bio-optical properties of oceanic waters: A reappraisal", Journal of Geophysical Research: Oceans (1978–2012) **106** (C4), 7163-7180 (2001).

119. H. R. Gordon, K. J. Voss et al.,"Angular Distribution of Fluorescence from Phytoplankton", Limnology and Oceanography **38** (7), 1582-1586 (1993).

120. S. W. Wright, S. W. Jeffrey and R. F. C. Mantoura, Phytoplankton pigments in oceanography : guidelines to modern methods. (UNESCO Publishing, Paris, 2005).

121. P. Terpstra, D. Combes et al.,"Effect of salts on dynamics of water: A Raman spectroscopy study", The Journal of chemical physics **92** (1990).

122. E. Lewis,"The practical salinity scale 1978 and its antecedents", Oceanic Engineering, IEEE Journal of **5** (1), 3-8 (1980).

123. L. Schemel,"Simplified conversions between specific conductance and salinity units for use with data from monitoring stations", IEP Newsletter **14** (1), 17-18 (2001).

124. R. A. Leathers, T. V. Downes et al., Naval Research Laboratory, 2004.

125. D. N. Whiteman,"Examination of the traditional Raman lidar technique. I. Evaluating the temperature-dependent lidar equations", Applied optics **42** (15), 2571-2592 (2003).

126. U. Wandinger and A. Ansmann,"Experimental Determination of the Lidar Overlap Profile with Raman Lidar", Applied Optics **41** (3), 511-514 (2002).

Appendices

The following appendices detail work and additional information related to the thesis content.

- Appendix A – A list of relevant publications is presented, followed by copies of refereed manuscripts.
- Appendix B – Tabulated data for charts shown in Chapter 4.
- Appendix C – Program code for analysis of Raman spectra and remote sensing simulations written in Matlab.
- Appendix D – Brief summary of the remote sensing experimental and numerical simulation work conducted towards the end of the research project.
- Appendix E – Equipment details for remote sensing experimentation.
- Appendix F – Example data showing the effect of the smoothing used in the thesis on raw unpolarised Raman spectra.

Appendix A

Refereed Publications

- C. P. Artlett and H. M. Pask, "Raman spectral analysis for remote measurement of water temperature", Proc. SPIE 8532, Remote Sensing of the Ocean, Sea Ice, Coastal Waters, and Large Water Regions 2012, 85320C (October 2012); doi:10.1117/12.974569; http://dx.doi.org/10.1117/12.974569

- J. J. Neto, C. Artlett et al., "Investigation of blue emission from Raman–active crystals: Its origin and impact on laser performance", Opt. Mater. Express **4** (5), 889-902 (2014); http://dx.doi.org/10.1364/OME.4.000889

Conference presentations

- C. Artlett and H. Pask, "Optical Remote Sensing of water temperature in natural water samples", Light, Energy and the Environment, Canberra, (2014).

- C. P. Artlett and H. M. Pask, "Remote Sensing of water temperature and salinity using Raman spectroscopy: From principles to field trials" 21st Australian Institute of Physics Congress, Canberra, (2014).

- C. Artlett and H. Pask, "Raman analysis of the temperature and salinity of seawater for active remote sensing" 10th Australian Conference on Vibrational Spectroscopy, Adelaide, (2014).

- C. Artlett and H. Pask, "Experimental Remote Sensing Of Water Temperature With Raman Spectroscopic Methods", 20th Australian Institute of Physics Congress, Sydney, (2012).

- C. Artlett and H. Pask, "Optical Remote Sensing of Water Temperature by Raman Spectroscopy Techniques" in Proceedings of the International Quantum Electronics Conference and Conference on Lasers and Electro–Optics Pacific Rim 2011, Sydney, (2011).

- C. Artlett and H. Pask, "Remote sensing of ocean temperature using Raman spectroscopy", 19th Australian Institute of Physics Congress, Melbourne, (2010).

Raman Spectral Analysis for Remote Measurement of Water Temperature

C. P. Artlett* and H. M. Pask
MQ Photonics Research Centre, Department of Physics and Astronomy
Macquarie University NSW 2109 Australia

ABSTRACT

We present a detailed investigation on the temperature-dependence of polarized and unpolarised Raman spectra for various laboratory water, fresh and saltwater samples. We have identified the spectral parameters which are most sensitive to water temperature, and compared these between the water samples from different locations. We have then applied linear regression methods and multiple linear regression methods to investigate the accuracy with which water temperature can be estimated from Raman spectral data.

keywords: Raman spectroscopy, water temperature, temperature measurement, optical remote sensing

1. INTRODUCTION

Measurement of the physical and chemical properties of bodies of water is of importance in fields including oceanography, climate change research and marine engineering. In particular, parameters such as temperature and salinity cannot be profiled rapidly in three dimensions with the direct measurement methods currently available. A practical technique for rapid, sub-surface, depth-resolved temperature measurement would complement the currently available technologies.

Active optical remote sensing has the potential to fulfill these criteria. Optical techniques are well suited to sensing of water properties to depths in the tens of metres due to the low absorption of water for blue-green wavelengths [1, 2]. The measurement of water Raman scattering in particular has the potential to acquire water temperature and salinity data simultaneously. Multiple groups have conducted work in this area in the past[3-8], though in general such studies have been limited purely to laboratory investigations, measurements at a single depth near the water surface, or approximate temperature readings over the accessible portion of the water column. Of particular note are studies by Chang et al.[9], and Leonard et al[6]. Using a 460 nm dye laser for excitation, Chang et al [10] reported temperature sensitivities of the measurands to be approximately 1-1.7% per °C, and predicted that it would be feasible to measure water temperature to depths of 10-100 m from an airborne platform. Leonard et al [11] investigated practical considerations for airborne remote sensing, such as surface waves, ambient light, fluorescence etc. However the potential of this of this early work has not, to our knowledge, been realised in practice. It is also noteworthy that these studies date back to the seventies, and that there have since been major advances in detectors, hydrologic modelling of underwater light fields and LIDAR methods.

The Raman scattered emission of water exhibits a spectral response to temperature change[12, 13]. This temperature dependence is observed in a weak, broad emission band from 2900 – 3900 cm^{-1}, which consists of overlapping vibrational transitions resulting from symmetric and antisymmetric stretching vibrations of both free and lattice bonded OH groups[14]. As water temperature increases the intensities of these transitions are altered around isoskedastic points in the spectra. Typical polarised and unpolarised Raman spectra for water at three temperatures are shown in Figure 1. The spectra for Raman-scattered light polarised parallel and perpendicular to the polarisation of the excitation laser are significantly different; the spectrum with parallel polarisation is dominated by two peaks at approximately 3250 cm^{-1} and 3400 cm^{-1}, while the perpendicular polarisation has one dominant peak at around 3460 cm^{-1}. There are two main techniques that have been used for analysing water Raman scattering to deduce temperature, and these are known as the "two-colour" technique and the "depolarisation" technique. In the former, Raman-scattered light is analysed to determine the ratio of amplitudes corresponding to the two main peaks.

*christopher.artlett@mq.edu.au; phone 61 2 9850-8929; mq.edu.au/groups/mqphotonics/

Remote Sensing of the Ocean, Sea Ice, Coastal Waters, and Large Water Regions 2012, edited by Charles R. Bostater Jr., Stelios P. Mertikas, Xavier Neyt, Caroline Nichol, Dave C. Cowley, Jean-Paul Bruyant, Proc. of SPIE Vol. 8532, 85320C

Most commonly, spectra are recorded to which a series of Gaussian or Voigt line-shapes are fitted, consistent with a "mixture" model of water [6], and these are then analysed to estimate water temperature. For the latter technique, the Raman signal is separated according to polarisation and the ratio of emission intensity for orthogonal polarisation states is measured. In both of these techniques a ratio is measured which varies proportionally with water temperature.

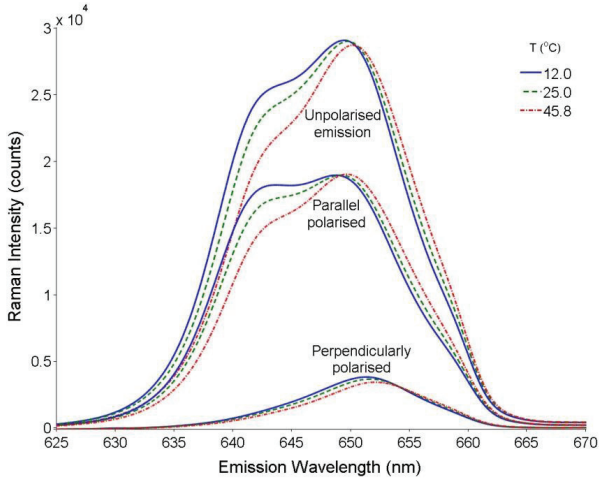

Figure 1. Polarised and unpolarised Raman OH stretching band for several water temperatures (Excitation laser wavelength: 532 nm).

In this work, we report a detailed characterisation of temperature-dependence of the Raman spectrum of water. In Part 1 of this paper, we use a "standard" (reverse-osmosis) water sample and analyse the spectral features of polarised and unpolarised Raman spectra, in order to identify those features most sensitive to changes in temperature, and therefore most optimal for Raman temperature measurement. The analysis is then extended to a variety of water samples from different locations around Sydney, both fresh and salt water. In Part 2 of this paper, we present multiple linear regression models, based on the optimum parameters identified in part 1. These models predict water temperature to an accuracy of 0.3 °C in the case of the "standard" water sample. We present models for a saltwater sample, and discuss the issues that presently limit the temperature accuracy.

2. TEMPERATURE SENSITIVITY OF RAMAN SPECTRAL FEATURES

2.1 Experimental Methods

Unpolarised and linearly polarised Raman spectra were recorded for various water samples at temperatures ranging from 10 to 50 °C. Multiple spectra were collected with acquisition times ranging from 6-30 seconds (though these times were consistent for each water sample) and averaged to improve consistency. Reverse-osmosis (RO) filtered water (Boss WaterMax RO) as used for most of the analysis. In addition test water samples were collected from multiple locations around Sydney (both fresh and salt water). Samples from natural water sources were probed within several hours of their collection. Reverse osmosis purified water was used as a reference sample, against which water samples from other locations could be compared.

The experimental arrangement is shown in Fig. 2. A custom-built aluminium cell was used to contain water samples during the acquisition of Raman spectra. This cell had a volume of approximately 1 ml and a BK7 window with broadband visible AR coating to couple the excitation laser (532 nm) and Raman signal (620-670 nm). A single-stage Peltier element and a 10 kΩ feedback thermistor with ±0.2 °C accuracy (GE MC65F103B) were connected to a

TEC Controller (Newport 350B) to provide active cell temperature control. Internal cell temperature was calibrated using a ±0.1 °C temperature probe (Digitron 2024T), so that the water temperature was known to an accuracy of ±0.3 °C.

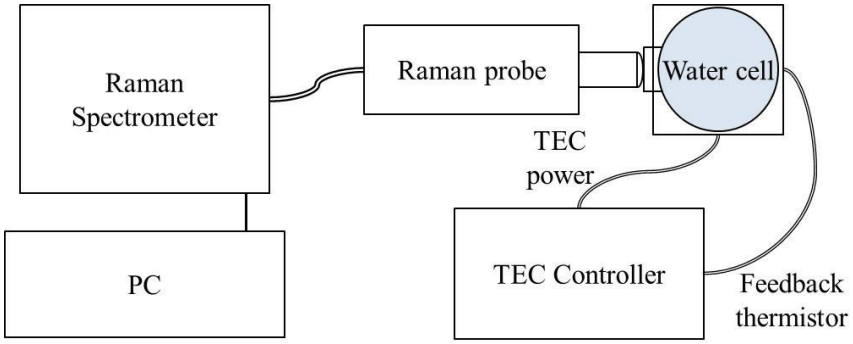

Figure 2. Experimental setup for collection of water Raman spectra.

Raman spectra were collected over a frequency span of 250 to 4400 cm^{-1} with a dispersive Raman spectrometer (Enwave EZRaman-I) using a 180 backscattering geometry. The optical resolution of the spectrometer is approximately 10 cm^{-1}. Wavelength calibration of the spectrometer was carried out using an acetonitrile (CH_3CN) reference sample. The excitation source was a frequency-doubled, linearly polarised, CW Nd:YAG laser (30mW at 532 nm) which is integrated into the spectrometer probe. Data processing and analysis were conducted using Matlab (R2011b, The Mathworks). A Savitsky-Golay smoothing filter was applied to spectra (2^{nd} order, 50 cm^{-1} window) [15].

The Raman spectral response of water to temperature change was investigated in terms of variation in signal intensity, intensity ratios from unpolarised spectra, and depolarisation ratios. Unpolarised intensity ratios were calculated from integrated intensities of narrow spectral bands, and exhibited a linear relationship with temperature. Spectral bands were identified which produced significant intensity ratio sensitivity to temperature.

This sensitivity was quantified as a percentage ratio change per degree Celsius. Depolarisation ratios were also calculated for the entire OH band and analysed to identify the spectral region of maximum temperature sensitivity.

2.2 Analysis of Raman Spectra using the "standard" water sample

2.2.1 Two-colour method (Unpolarised intensity ratio)

Unpolarised water Raman spectra (Figure 3a) were first analysed to find those wavelengths for which the Raman signal was most sensitive to temperature. These wavelengths, indicated by the pair of vertical lines labelled "A", were found to be 3182 cm^{-1} and 3542 cm^{-1}. As described in the introduction, the two-colour method is based on a ratio of Raman signal intensities at two wavelengths, one on either side of the isosbestic point which exhibits a linear response to temperature change.

The unpolarised spectra were next studied to determine the pair of wavelengths for which this ratio exhibited the greatest sensitivity to temperature (Figure 3b). These were found to be 3122 cm^{-1} and 3588 cm^{-1} and are indicated by the pair of vertical lines labelled "B" in figure 3a. The pairs of lines labelled "C" and "D" are included to provide points of comparison which have dissimilar signal intensities.

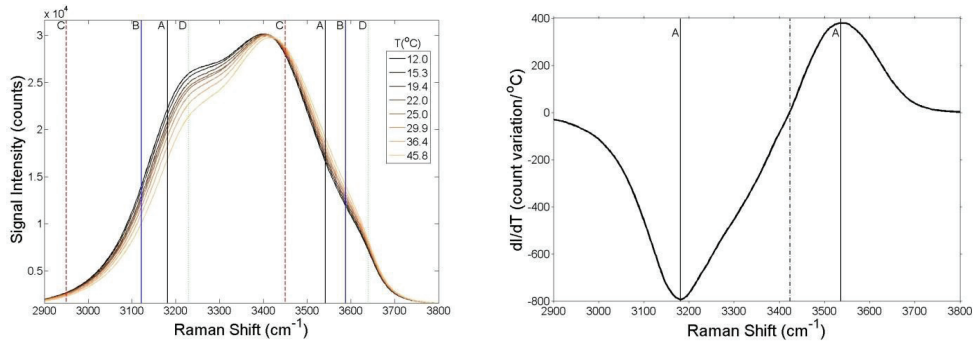

Figure 3. (a) Unpolarised water Raman spectra, with wavenumber combinations for intensity ratio calculation marked. (b) Temperature sensitivity as a function of Raman shift (dashed line marks the isosbestic point).

Intuitively the spectral regions with maximum temperature sensitivity might be expected to produce the ratio with the maximum variation. However, low intensity values in the denominator of the ratio will result in larger ratio values, and vice versa for the numerator. To account for this we scale the two-colour intensity ratios by the mean value of these ratios, obtained over the range of temperatures investigated, as shown below:

$$\text{Mean-scaled intensity ratio} = \frac{dR}{dT}\frac{1}{Mean(R)} \tag{1}$$

where R represents the set of unpolarised intensity ratio values, and T is the set of corresponding temperature values. The mean-scaled intensity ratios for the pairs of wavelengths (A-D) indicated in Figure 3a, are plotted in Figure 4 as a function of temperature, and the slope of each line gives the mean-scaled two-colour intensity ratio temperature sensitivity.

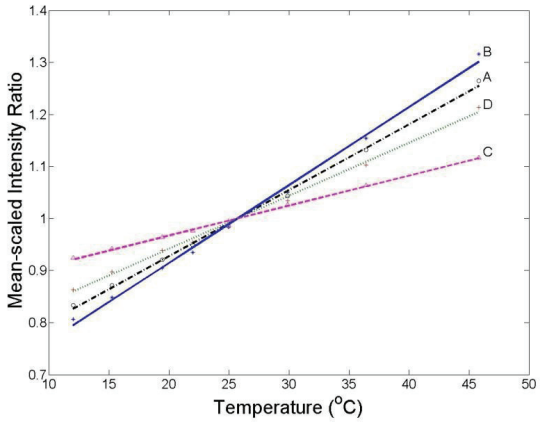

Figure 4. Mean-scaled unpolarised intensity ratios against sample temperature.

The highest mean-scaled temperature sensitivity occurs for the B spectral ratio and is 1.5 % per °C, significantly higher than the temperature sensitivities of 1.3, 1.0 and 0.6 % per °C found for wavelength pairs A, D and C respectively.

Differential absorption between the wavelength channels has previously been noted as a shortcoming of the two-colour method[6], and Lin and James have proposed the use of wavelengths other than 532 nm to avoid this problem[5, 16]. Clearly there will also be a trade-off between maximum temperature sensitivity and signal intensity, depending on the signal to noise ratio in a practical system. To this point we have analysed the temperature sensitivity for individual wavelengths and next we consider the effects of increasing the widths of the wavelength channels on temperature sensitivity and signal intensity. These are shown in Figures 5(a) and (b) respectively.

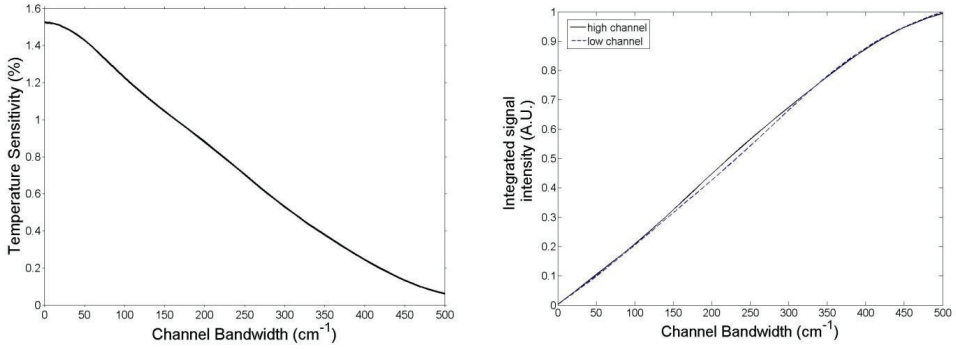

Figure 5. (a) Effect of channel bandwidth (channels matched) on the temperature sensitivity of the "B" unpolarised intensity ratio. (b) Integrated channel intensity vs. channel bandwidth at 25 °C for the "B" ratio.

Increasing the channel bandwidth reduces the measured temperature sensitivity quite significantly, while the detected signal intensity increases rapidly. Both channels required for the unpolarised ratio parameter exhibit similar signal strength-bandwidth behaviour. An optimal point for practical sensing will lie within the range examined here.

2.2.2 Depolarisation method

As described in the introduction, the ratio of signal intensities having orthogonal polarisation states (parallel and perpendicular to that of the excitation laser) exhibits temperature dependence. The depolarisation ratio for wavelengths across the stretching band is shown in Figure 6a and the temperature sensitivity of the ratio is plotted in Figure 6b.

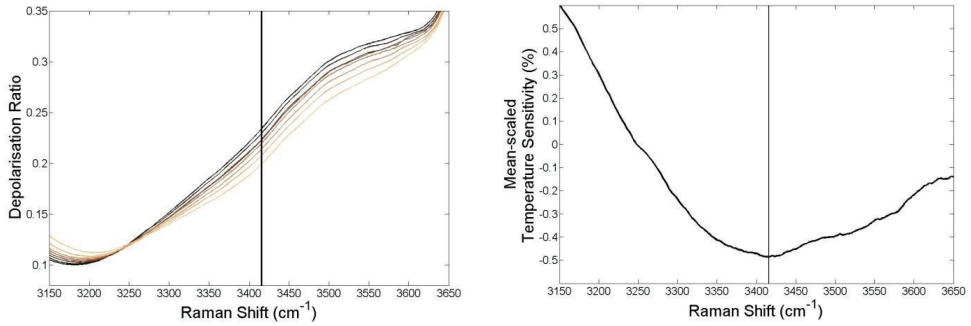

Figure 6. (a) Depolarisation ratio as a function of Raman shift, (b) Mean-scaled temperature sensitivity of the depolarisation ratio as a function of Raman shift.

Maximum temperature sensitivity was observed at a Raman shift of 3416 cm^{-1}. The linear depolarisation ratio is somewhat less sensitive to temperature relative to the unpolarised intensity ratio (approximately 0.5 % per °C mean-scaled temperature sensitivity). The impact of channel bandwidth on measurement performance is examined in Figure 7.

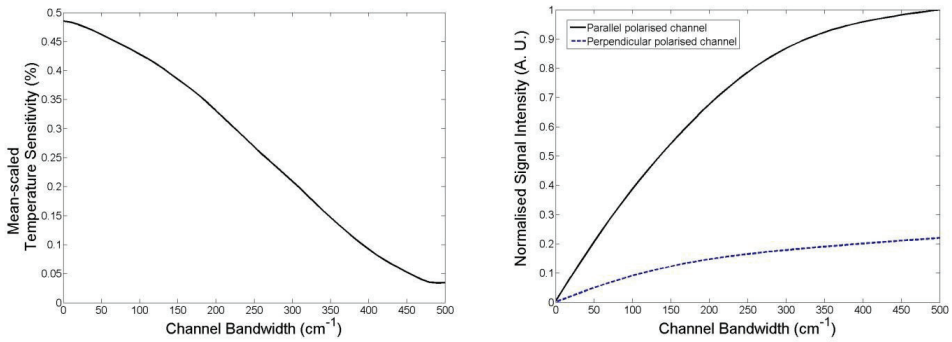

Figure 7. (a) Effect of channel bandwidth on the mean-scaled temperature sensitivity of the depolarisation ratio. (b) Integrated channel intensity vs. channel bandwidth at 25 °C (polarisation states are relative to the laser polarisation).

The depolarisation ratio parameter exhibits somewhat similar channel bandwidth behaviour to the unpolarised intensity ratio. Detected intensity of the perpendicularly polarized channel may be an issue, as a weak signal will be more vulnerable to the impact of fluorescence, ambient light etc.

2.3 Analysis of fresh and saltwater samples

We measured polarised and unpolarised Raman spectra as a function of water temperature for tap water, de-ionised water, and freshwater samples from Manly Dam, as well as various sea water samples from around Sydney Harbour (Woolwich, Sugarloaf Bay, Rhodes, Clontarf) and several kilometres offshore. Similar analysis to that detailed above was carried out, and the optimal wavelengths for the natural samples were compared to the standard sample.

It was found that there was relatively little difference in the optimal parameters for the various water samples. In the case of the "two-colour" method, the optimal wavelengths were within 40 cm^{-1} of the optimal wavelengths for the "standard". In the case of the depolarisation method, the optimal wavelength was also within 40 cm^{-1} of the optimal wavelength for the "standard". The temperature sensitivity was observed to decrease somewhat, according to the (qualitatively assessed) purity of the water sample. While the maximum temperature sensitivity for the "standard" water sample was ~1.14 % per °C, that for Sugarloaf Bay was 1.08 % per °C, and that for Clontarf was as low as 0.82 % per °C (At the "A" wavenumber pairs for all water samples). These are preliminary findings, which will be evaluated more fully in the future.

3. DEVELOPING PREDICTIVE MODELS FOR WATER TEMPERATURE BASED ON RAMAN SPECTRA

3.1 Experimental methods

The same Raman spectral data from the "standard" water was next calibrated to the cell reference temperature, producing a linear equation which can then be applied to estimate the temperature of other water samples. By using the equation with its original calibration data, an estimate of the uncertainty in temperature values can be obtained.

This was first done for the two-colour and depolarisation ratios independently, and then a linear combination of these two parameters was created using MLR. Specifically the MLR variant known as "robust regression" was selected in order to iteratively re-weight the data, reducing the impact of isolated or non-linear changes in either spectral parameter on the calibration model.

The regression equation takes the form:

$$\textbf{Temperature} = a_0 + a_1 * \textit{Two-colour ratio} + a_2 * \textit{Depol. Ratio}$$

where a_0,a_1 and a_2 are the coefficients generated by the MLR procedure. The individual parameter equations have the standard linear form:

$$\textbf{Temperature} = b_0 + b_1 * \textit{Two-colour Ratio}$$

$$\textbf{Temperature} = c_0 + c_1 * \textit{Depol. Ratio}$$

The relative performance of these three parameters was assessed. A saltwater sample was then analysed in the same way.

3.2 MLR model for "standard" water sample

Figure 8 demonstrates the relationships developed between spectral parameters and the reference thermocouple temperatures measured in the water cell. The spectral data and reference temperature values are used to produce linear fit equations, which are then applied to obtain temperature estimates based on the Raman spectra, which will from here on be referred to as "Raman temperature(s)" for clarity. Channel bandwidths of 200 cm^{-1} (~8 nm) were used in calculating spectral parameters in order to simulate calibration of a practical temperature sensing system.

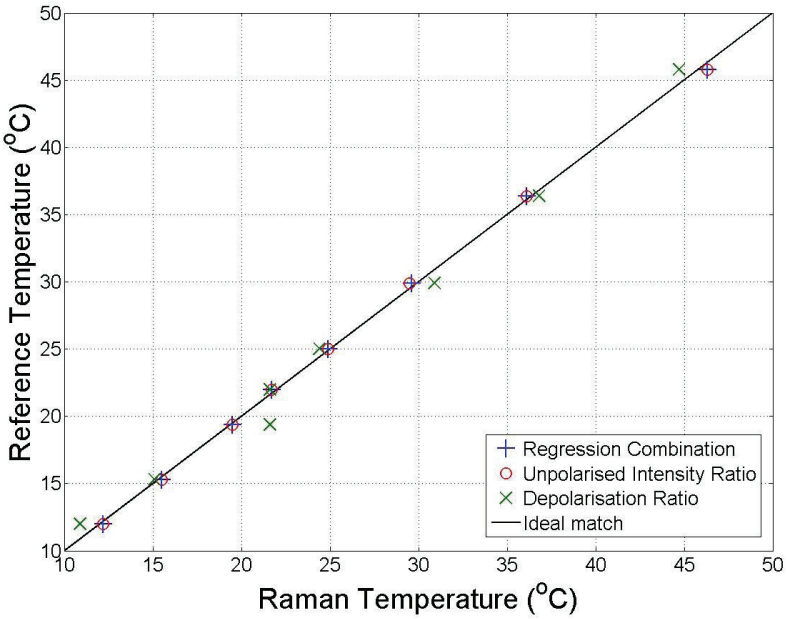

Figure 8. Raman vs. reference temperature calibration for RO filtered water for individual spectral parameters and the regression combination.

The two-colour ratio parameter in Figure 8 exhibits an RMS (root mean square) temperature error of ±0.3 °C, which is approximately the precision limit of the cell thermocouple employed in this study. In general the unpolarised ratio parameter produced very consistent results with minimal processing applied to spectra (Savitsky-Golay smoothing).

However, temperature measurement based on the depolarisation ratio exhibits significantly more variability, with an RMS temperature error of ±1 °C. The weaker temperature dependence of the depolarization ratio relative to the

unpolarised ratio may be partially responsible for this. Variability here may also be due to the inability of the spectrometer used to record orthogonal linearly polarised spectra simultaneously. Each set of polarised spectra was recorded from a separate spectrometer scan, with an appropriate filter inserted to select the desired polarisation. On the other hand, the unpolarised intensity ratio was calculated from a single spectrum. Experiments are planned which will determine whether this is the case and if so, eliminate it as a concern. Because of the depolarisation ratio inconsistency, regression models tend to produce similar measurement error behaviour to the unpolarised ratio data.

3.3 MLR model for natural water samples

Experimentation with natural fresh and salt-water samples has achieved varying success in terms of temperature accuracy. Significant differences are to be expected between salt and fresh water spectra due to the influence of ions bonding into the water lattice structure. The bonding of various salt ions with water affects OH bond vibrational transition frequencies, altering spectral line shape, and hence influencing the temperature dependent parameters defined above. Increased variability in spectra negatively affects the observed temperature sensitivity, and salinity will need to be taken into account in any practical remote sensing system.

Temperature accuracy is highly dependent on the similarity of calibration water samples to test samples, as well as water constituents and quality. The depolarisation ratio in particular seems to be very sensitive to any change in water quality. Figure 9 shows a spectral vs. reference temperature plot for an ocean water sample collected from several kilometres offshore from Sydney.

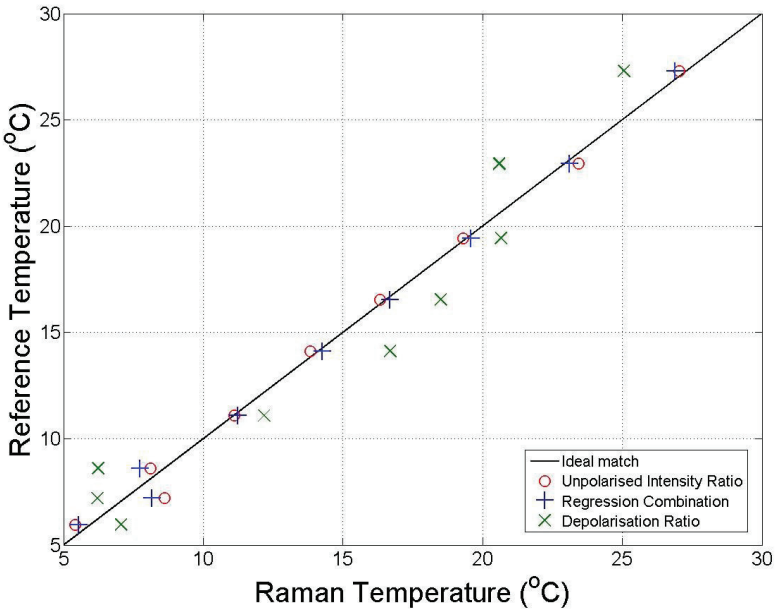

Figure 9. Raman vs. reference temperature calibration for an ocean water sample for individual spectral parameters and the regression combination.

The unpolarised ratio parameter in Figure 9 showed an RMS temperature error of ±0.6 °C, the regression-based combination ±0.5 °C, and the depolarization ratio ±1.9 °C. Useful temperature accuracy was achieved with the unpolarised intensity ratio (< 1 °C), and the regression combination mirrored this, effectively discounting the influence of the depolarization ratio data.

As with the fresh water example, much more substantial variation was observed in the depolarization ratio. Water samples obtained from local estuaries and inner regions of Sydney Harbour produced even more substantial variability depending on tidal and weather conditions. It remains to be seen whether useful optical remote sensing of water temperature can be performed in such areas. Based on observations made during this study, clean water in the open ocean should produce accuracy levels approaching those of purified fresh water.

Significant baseline fluctuations were evident with most salt water and natural freshwater samples studied. This was not an issue for the unpolarised ratio, but proved to be a major concern for depolarization ratio measurements. This is likely due to weak fluorescence emission from organic material and scattering from suspended particulate matter. Here we note that the models discussed to date did not include any baseline correction. When we did investigate additional processing of polarised spectra, including several types of baseline correction and normalization, baseline correction made substantial improvements in temperature accuracy with the depolarization parameter for some water samples; however this type of processing is not generally applicable to a sensing system using a few relatively narrow spectral channels. One potentially viable option would be the use of one or two spectral channels outside the Raman OH stretching band emission peak to enable a crude background subtraction.

In general, the unpolarised intensity ratio has proven to be substantially more accurate for laboratory based Raman temperature measurement compared with the depolarization ratio. On the other hand, the major disadvantages inherent in the two-colour ratio mainly come into play with transmission through the water column or with various water constituents; namely differential attenuation due to absorption and fluorescence from organisms such as phytoplankton or dissolved organic matter (DOM). Further studies are planned which will determine how significant these factors will be in Raman-based remote sensing of ocean temperature.

4. CONCLUSION

Temperature measurement of water can be achieved through spectroscopic analysis of Raman emission. Measurement accuracy is highly dependent on water quality, spectral acquisition conditions and the spectra processing techniques which are employed. By employing a regression combination of multiple spectral parameters, the reliability of temperature measurement can be improved.

References

[1] R. M. Pope, and E. S. Fry, “Absorption spectrum (380-700 nm) of pure water. II. Integrating cavity measurements,” Appl. Opt., 36(33), 8710-8723 (1997).

[2] R. C. Smith, and K. S. Baker, “Optical properties of the clearest natural waters (200-800 nm),” Appl. Opt., 20(2), 177-184 (1981).

[3] B. Breschi, G. Cecchi, L. Pantani *et al.*, "Measurement of Water Column Temperature by Raman Scattering." EARSeL ADVANCES IN REMOTE SENSING Vol. 1, 131-134.

[4] S. Burikov, I. Churina, S. Dolenko *et al.*, “New approaches to determination of temperature and salinity of seawater by laser Raman spectroscopy,” EARSeL eProceedings, 3(3), 298 (2004).

[5] J. E. James, C. S. Lin, and W. P. Hooper, “Simulation of Laser-Induced Light Emissions from Water and Extraction of Raman Signal,” J. Atmos. Oceanic Technol., 16(3), 394-401 (1999).

[6] D. Leonard, B. Caputo, and F. Hoge, “Remote sensing of subsurface water temperature by Raman scattering,” Appl. Opt., 18(11), 1732-1745 (1979).

[7] M. Becucci, S. Cavalieri, R. Eramo *et al.*, “Accuracy of remote sensing of water temperature by Raman spectroscopy,” Applied optics, 38(6/20), (1999).

[8] G. Cecchi, and V. Raimondi, "Remote Raman spectra for the monitoring of water column temperature." 3, 1741-1743.

[9] C. H. Chang, and L. A. Young, “Seawater temperature measurement from Raman spectra,” Technical Report, Avco Everett Research Laboratory, 960, (1972).

[10] C. H. Chang, and L. A. Young, [Seawater temperature measurement from Raman Spectra] Avco Everett Research Laboratory, (1972).

[11] D. A. Leonard, B. Caputo, and F. E. Hoge, "Remote sensing of subsurface water temperature by Raman scattering," Appl. Opt., 18(11), 1732-1745 (1979).
[12] G. Walrafen, "Raman spectral studies of the effects of temperature on water structure," J. Chem. Phys., 47, 114 (1967).
[13] G. Walrafen, M. Hokmabadi, and W. Yang, "Raman isosbestic points from liquid water," J. Chem. Phys., 85, 6964 (1986).
[14] Y. Tominaga, A. Fujiwara, and Y. Amo, "Dynamical structure of water by Raman spectroscopy," Fluid Phase Equilib., 144(1-2), 323-330 (1998).
[15] A. Savitzky, and M. J. E. Golay, "Smoothing and Differentiation of Data by Simplified Least Squares Procedures," Analytical Chemistry, 36(8), 1627-1639 (1964).
[16] C. Lin, "Tunable laser induced scattering from coastal water," Geoscience and Remote Sensing, IEEE Transactions on, 37(5), 2461-2468 (1999).

Investigation of blue emission from Raman-active crystals: Its origin and impact on laser performance

Jonas Jakutis Neto,[1, 2, *] Christopher Artlett,[1] Andrew Lee,[1] Jipeng Lin,[1] David Spence,[1] James Piper,[1] Niklaus Ursus Wetter[2] and Helen Pask[1]

[1]*MQ Photonics Research Centre, Department of Physics, Macquarie University, Sydney, NSW 2109, Australia*
[2]*Instituto de Pesquisas Energéticas e Nucleares, CNEN/SP, Universidade de São Paulo, CEP 05508-000, São Paulo/SP, Brazil*
[*]*jonasjakutis@usp.br*

Abstract: The origin and consequences to laser performance of blue emission observed in some Raman crystals has been studied in detail, leading us to attribute the origin of the phenomenon to fluorescence from $Tm^{3+}(^1G_4)$ impurity ions which are excited via sequential upconversion. For the specific case of a Nd:YLF/KGW Raman laser, we show that the blue fluorescence has modest but significant impacts on laser performance and thermal loading. If the blue fluorescence was eliminated, then laser efficiency could be increased by 15% and thermal loading in the KGW crystal reduced by 17%.

OCIS codes: (140.3550) Lasers, Raman; (140.3580) Lasers, solid-state; (140.5680) Rare earth and transition metal solid-state lasers.

References and links

1. A. S. Grabtchikov, A. N. Kuzmin, V. A. Lisinetskii, G. I. Ryabtsev, V. A. Orlovich, and A. A. Demidovich, "Stimulated Raman scattering in Nd:KGW laser with diode pumping," J. Alloy. Comp. **300–301**(0), 300–302 (2000).
2. H. M. Pask, "Continuous-wave, all-solid-state, intracavity Raman laser," Opt. Lett. **30**(18), 2454–2456 (2005).
3. L. Fan, Y. X. Fan, Y. Q. Li, H. Zhang, Q. Wang, J. Wang, and H. T. Wang, "High-efficiency continuous-wave Raman conversion with a $BaWO_4$ Raman crystal," Opt. Lett. **34**(11), 1687–1689 (2009).
4. A. J. Lee, H. M. Pask, J. A. Piper, H. J. Zhang, and J. Y. Wang, "An intracavity, frequency-doubled $BaWO_4$ Raman laser generating multi-watt continuous-wave, yellow emission," Opt. Express **18**(6), 5984–5992 (2010).
5. Y. M. Duan, H. Y. Zhu, G. Zhang, C. H. Huang, Y. Wei, C. Y. Tu, Z. J. Zhu, F. G. Yang, and Z. Y. You, "Efficient 559.6 nm light produced by sum-frequency generation of diode-end-pumped Nd:YAG/$SrWO_4$ Raman laser," Laser Phys. Lett. **7**(7), 491–494 (2010).
6. Y. Duan, F. Yang, H. Zhu, Z. Zhu, C. Huang, Z. You, Y. Wei, G. Zhang, and C. Tu, "Continuous-wave 560 nm light generated by intracavity $SrWO_4$ Raman and KTP sum-frequency mixing," Opt. Commun. **283**(24), 5135–5138 (2010).
7. H. Y. Zhu, Y. M. Duan, G. Zhang, C. H. Huang, Y. Wei, W. D. Chen, Y. D. Huang, and N. Ye, "Yellow-light generation of 5.7 W by intracavity doubling self-Raman laser of YVO_4/Nd:YVO_4 composite," Opt. Lett. **34**(18), 2763–2765 (2009).
8. W. Baoshan, T. Huiming, P. Jiying, M. Jieguang, and G. Lanlan, "Low threshold, diode end-pumped Nd^{3+}:$GdVO_4$ self-Raman laser," Opt. Mater. **29**(12), 1817–1820 (2007).
9. H. Yu, Z. Li, A. J. Lee, J. Li, H. Zhang, J. Wang, H. M. Pask, J. A. Piper, and M. Jiang, "A continuous wave $SrMoO_4$ Raman laser," Opt. Lett. **36**(4), 579–581 (2011).
10. M. T. Chang, W. Z. Zhuang, K. W. Su, Y. T. Yu, and Y. F. Chen, "Efficient continuous-wave self-Raman Yb:KGW laser with a shift of 89 cm^{-1}," Opt. Express **21**(21), 24590–24598 (2013).
11. A. J. Lee, H. M. Pask, D. J. Spence, and J. A. Piper, "Efficient 5.3 W CW laser at 559 nm by intracavity frequency summation of fundamental and first-Stokes wavelengths in a self-Raman Nd:$GdVO_4$ laser," Opt. Lett. **35**(5), 682–684 (2010).
12. D. J. Spence, X. Li, A. J. Lee, and H. M. Pask, "Modeling of wavelength-selectable visible Raman lasers," Opt. Commun. **285**(18), 3849–3854 (2012).
13. G. M. Bonner, H. M. Pask, A. J. Lee, A. J. Kemp, J. Wang, H. Zhang, and T. Omatsu, "Measurement of thermal lensing in a CW $BaWO_4$ intracavity Raman laser," Opt. Express **20**(9), 9810–9818 (2012).

#203411 - $15.00 USD Received 24 Dec 2013; revised 22 Mar 2014; accepted 27 Mar 2014; published 1 Apr 2014

14. H. Zhu, Y. Duan, G. Zhang, Y. Zhang, and F. Yang, "Laser induced blue luminescence phenomenon," Jpn. J. Appl. Phys. **50** (Copyright (C) 2011 The Japan Society of Applied Physics), 090203 (2011).
15. I. A. Khodasevich, A. A. Kornienko, E. B. Dunina, and A. S. Grabtchikov, "On the influence of dopant ions on blue emission in KGW crystal excited by infrared laser radiation," J. Appl. Spectrosc. **79**(1), 38–45 (2012).
16. I. A. Khodasevich, A. A. Kornienko, E. B. Dunina, and A. S. Grabtchikov, "Transformation of optical properties of crystal media (KGW, YVO_4) exposed to quasi-continuous laser radiation in the range of the transmission band of the medium," Opt. Spectrosc. **115**(3), 325–334 (2013).
17. Y. F. Chen, "Efficient 1521-nm Nd:$GdVO_4$ Raman laser," Opt. Lett. **29**(22), 2632–2634 (2004).
18. N. Zong, Q. J. Cui, Q. L. Ma, X. F. Zhang, Y. F. Lu, C. M. Li, D. F. Cui, Z. Y. Xu, H. J. Zhang, and J. Y. Wang, "High average power 1.5 microm eye-safe Raman shifting in $BaWO_4$ crystals," Appl. Opt. **48**(1), 7–10 (2009).
19. Y. T. Chang, K. W. Su, H. L. Chang, and Y. F. Chen, "Compact efficient Q-switched eye-safe laser at 1525 nm with a double-end diffusion-bonded Nd:YVO_4 crystal as a self-Raman medium," Opt. Express **17**(6), 4330–4335 (2009).
20. R. Lisiecki, W. Ryba-Romanowski, and T. Lukasiewicz, "Blue up-conversion with excitation into Tm ions at 808 nm in YVO_4 crystals co-doped with thulium and ytterbium," Appl. Phys. B **81**(1), 43–47 (2005).
21. F. Güell, X. Mateos, J. Gavaldà, R. Solé, M. Aguiló, D. Amp, F. Díaz, M. Galan, and J. Massons, "Optical characterization of Tm^{3+}-doped $KGd(WO_4)_2$ single crystals," Opt. Mater. **25**(1), 71–77 (2004).
22. F. Güell, X. Mateos, J. Gavaldà, R. Solé, M. Aguiló, D. Amp, F. Díaz, and J. Massons, "Blue luminescence in Tm^{3+}-doped $KGd(WO_4)_2$ single crystals," J. Lumin. **106**(2), 109–114 (2004).
23. Y. Yang, B. Yao, B. Chen, C. Wang, G. Ren, and X. Wang, "Judd–Ofelt analysis of spectroscopic properties of Tm^{3+}, Ho^{3+} doped $GdVO_4$ crystals," Opt. Mater. **29**(9), 1159–1165 (2007).
24. F. S. Ermeneux, C. Goutaudier, R. Moncorgé, M. T. Cohen-Adad, M. Bettinelli, and E. Cavalli, "Growth and fluorescence properties of Tm^{3+} doped YVO_4 and Y_2O_3 single crystals," Opt. Mater. **8**(1–2), 83–90 (1997).
25. K. H. Esbensen, D. Guyot, and F. Westad, *Multivariate Data Analysis: In Practice* (Camo, 2000).
26. A. A. Kaminskii, *Laser Crystals: Their Physics and Properties* (Springer-Verlag, 1981).
27. R. Paschotta, N. Moore, W. A. Clarkson, A. C. Tropper, D. C. Hanna, and G. Maze, "230 mW of blue light from a thulium-doped upconversion fiber laser," IEEE J. Sel. Top. Quantum Electron. **3**(4), 1100–1102 (1997).
28. X. Li, H. M. Pask, A. J. Lee, Y. Huo, J. A. Piper, and D. J. Spence, "Miniature wavelength-selectable Raman laser: new insights for optimizing performance," Opt. Express **19**(25), 25623–25631 (2011).
29. P. Dekker, H. M. Pask, D. J. Spence, and J. A. Piper, "Continuous-wave, intracavity doubled, self-Raman laser operation in Nd:$GdVO_4$ at 586.5 nm," Opt. Express **15**(11), 7038–7046 (2007).
30. T. Omatsu, M. Okida, A. Lee, and H. M. Pask, "Thermal lensing in a diode-end-pumped continuous-wave self-Raman Nd-doped $GdVO_4$ laser," J. Appl. Phys. B **108**(1), 73–79 (2012).

Introduction

Crystalline Raman lasers offer a practical and efficient approach to laser frequency conversion. They have been extensively studied around the world, using a diverse range of Raman active media, configurations, and temporal regimes that include continuous wave (CW), nanosecond pulse and ultrafast pulse. An unusual phenomenon has been observed in many of these lasers, a blue luminescence, and this has become a subject of speculation as to its origin and effect on Raman laser performance. Above the threshold for the stimulated Raman scattering (SRS), such luminescence is strong, clearly visible and bright in a well-lit room. It is isotropic and emanates from the resonator mode volume. Several groups have reported the effect in their Raman lasers, showing the presence of the phenomenon in many different crystals, KGW [1, 2], $BaWO_4$ [3, 4], $SrWO_4$ [5, 6], YVO_4 [7], $GdVO_4$ [8], $LuVO_4$ and $SrMoO_4$ [9], all based in Neodymium lasers. It was also reported in a Yb:KGW laser [10]. Some authors tried to explain the origin of the emission, either by upconversion in Nd^{3+} ions [1, 8], or by upconversion in Tm^{3+} impurity ions [2]. However, the focus of these works was the Raman laser itself, and the blue luminescence was a secondary issue, discussed only briefly.

Raman lasers have now reached a high level of development with simple CW intracavity Raman lasers reaching overall efficiencies of up to 13% [3] in the infrared (IR) and 21% in the visible [11]. It has been shown that minimizing resonator losses [12] and managing the effects of thermal loading [13] are critical to achieving such high performance. A better understanding of the origins of the observed blue luminescence is necessary, so that the potential effects on Raman laser performance, either as an extra loss, or as an extra source of thermal load, can be determined.

#203411 - $15.00 USD Received 24 Dec 2013; revised 22 Mar 2014; accepted 27 Mar 2014; published 1 Apr 2014

Recently, three published articles have specifically discussed the blue luminescence [14–16]. Zhu *et al.* [14] characterized the emission in three crystals, YVO_4, $GdVO_4$ and $SrWO_4$, with fundamental oscillations at 1063 nm, 1064 nm, 1079 nm and 1342 nm. The strongest blue emissions were found in $SrWO_4$ crystals, when the fundamental was in the 1 μm range, but no luminescence was observed for the 1342 nm fundamental. They concluded that the luminescence occurred with only fundamental oscillation at around 1 μm, and in the presence or absence of the SRS process. However, they did not explain the origin of the emission. In [15], Khodasevich *et al.* made a deeper analysis of the phenomenon, comparing the experimental blue emission spectrum from a KGW crystal with calculated lineshapes for Nd:KGW and Tm:YLF crystals. They found more similarities with the Neodymium emission band around 475 nm than with the Thulium band, but concluded there was not enough evidence to state that Nd^{3+} is responsible for the blue emission. They did not however compare to spectra from Tm:KGW, and ultimately concluded that neither Nd^{3+} nor Tm^{3+} impurities were the origin of the emission and that an alternative explanation was needed. Subsequently Khodasevich *et al.* [16], proposed that the blue emission is originated from a transformation, or change of the optical properties of the crystals that results from exposure to intense light for relatively long periods of time.

In this paper, we present a comprehensive spectroscopic study of the blue emission from Raman lasers that goes well beyond the scope of previous studies. We have investigated the spectra, power dependence and lifetimes for the blue emission from several Raman-active crystals, and measured the concentration of impurity ions such as Tm^{3+} in these crystals. Our measurements, which are more extensive but largely consistent with other studies in the literature, show that the blue emission most probably emanates from Tm^{3+} ions which are present as impurities in the crystals we investigated. A three-step upconversion process is proposed for exciting the $Tm^{3+}(^1G_4)$ from which the blue emission emanates. In the second part of the paper we consider the implication of this upconversion process for laser operation, particularly with regard to laser efficiency and thermal loading of the Raman crystal. We find that the upconversion process leading to blue emission results in a modest but significant decrease in laser efficiency and increases in thermal loading.

Part 1: Spectroscopic investigation of the blue emission

1.1 The occurrence of blue luminescence in Raman-active crystals

As noted in the introduction, blue emission has been observed in numerous Raman-active crystals. There are other Raman-active crystals which do not exhibit blue emission. Based on our extensive studies of using a large number of Raman-active crystals over many years, in which the excitation laser for SRS has been a Nd laser operating around 1μm, we can list the crystals in which we have observed blue emission as: $BaWO_4$, $SrMoO_4$, $KGd(WO_4)_2$ (KGW), Nd:KGW, YVO_4, Nd:YVO_4, Nd:$GdVO_4$, and $LuVO_4$. Those Raman-active crystals in which we have observed an absence of blue emission include: $Ba(NO_3)_2$, $LiIO_3$, diamond, KTP and $LiNbO_3$. We have found no reports in the literature of blue emission from Raman lasers pumped at 1.3 μm and generating first Stokes emission around 1.5 μm [17–19], in contrast to the case of Raman lasers based on the 1.06 μm transition where reports of blue fluorescence are prolific. Figure 1(a) is a photograph showing strong blue light emanating isotropically from the region of a KGW crystal which overlaps the resonator modes. Below the threshold for SRS, the blue emission is weak but visible. In [14], the research was focused on the blue emission excited by the fundamental wavelength around 1 μm only, while this work, like [16], focuses on the much stronger blue emission that occurs in the presence of SRS process. Figure 1(b) shows the blue emission as a function of diode pump power, together with a much weaker red emission that typically accompanies the blue emission, also reported in [10]. It is clear that their intensities are considerably higher when above the threshold for SRS, in this case around 4 W. The same observation was made in [16]. In this work we also observed the

#203411 - $15.00 USD Received 24 Dec 2013; revised 22 Mar 2014; accepted 27 Mar 2014; published 1 Apr 2014

blue emission for an acousto-optic Q-switched laser, and found it to be much weaker than for the CW case. This was consistent with the low duty cycle (<0.1%) of the Q-switched laser. Finally, we note that for Raman lasers with separate laser gain and Raman crystals, any blue emission in the laser crystal was much weaker than in the Raman crystal, indeed in most cases it was not observable by eye.

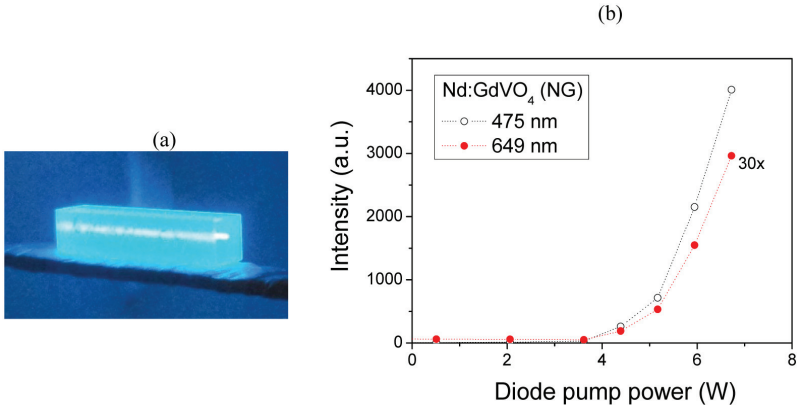

Fig. 1. (a) Picture of the blue emission in a 25mm long KGW crystal and (b) curve showing the intensity of the blue and red (30x) luminescence as a function of diode pump power for a Nd:$GdVO_4$ crystal from Northrop Grumman (NG)

1.2 The spectral properties and lifetime of the blue luminescence

We investigated several Raman-active crystalline media from which blue emission has been previously reported. Specifically we studied KGW (EKSMA), $BaWO_4$ (State Key Laboratory of Crystal Materials, Shandong University, China), 0.3% Nd:$GdVO_4$ (from Castech and Northrop Grumman), YVO_4 (Castech) and 0.5% Nd:YVO_4 (FEE). In each case, a portion of the blue emission exiting the crystal face was coupled into a fiber with a 200 μm diameter by means of two spherical lenses, and was analysed using an spectrometer (Ocean Optics HR4000) which had a resolution of 0.1 nm. The Raman laser cavity for the self-Raman cases comprised a flat mirror (M1) as the pump mirror, with high reflectivity (HR) at 1064 nm and 1177 nm (R>99.9%) and a plane-concave mirror (M2) with radius of curvature (ROC) of 200 mm as the output coupler, either with HR coatings at both 1064 nm and 1177 nm (R>99.9%) or with 0.4% transmission at 1177 nm to couple out the 1st Stokes. The laser cavity was typically 50 mm long, providing a resonator mode in the laser crystal of around 340 μm in diameter that was well matched to the diode pump beam. Nd:$GdVO_4$ and Nd:YVO_4 were investigated using a self-Raman configuration (i.e. these crystals perform the dual functions of generating the fundamental and SRS). For the other crystals, a separate Raman crystal was used as depicted in Fig. 2. The cavity elements and length were changed to maintain similar beam parameters in the laser crystal. A 30 W fiber-coupled diode laser emitting at 880 nm was used to pump the Nd doped crystals.

#203411 - $15.00 USD Received 24 Dec 2013; revised 22 Mar 2014; accepted 27 Mar 2014; published 1 Apr 2014

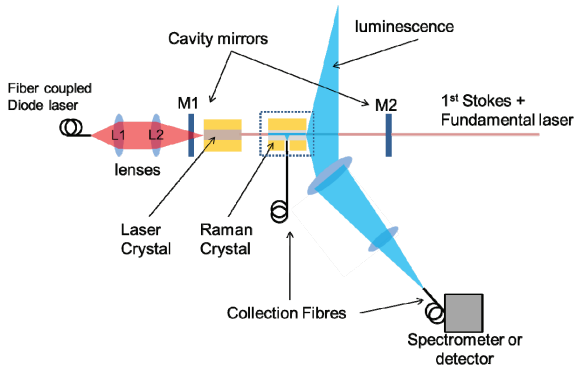

Fig. 2. Setup used for spectral measurements of blue emission. The Raman crystal was omitted for a self-Raman configuration.

Figure 3 shows blue emission spectra for the various crystals, recorded for a diode pump power of 15 W. Note the arbitrary units in all plots – there is no correspondence in the relative intensity of the signals from different crystals. It is possible to see strong similarities between the spectra for all the four crystals, despite the fact that two are vanadates and two are tungstates, and that two are intentionally doped with Nd^{3+} and two are undoped. There are even stronger similarities between tungstate based hosts and between vanadate based hosts. In addition, the high spectral resolution reveals substructure in the emission that can be compared to high resolution spectra found in the literature. We found that our blue spectra from Nd:YVO_4 was quite similar to that reported in [20] for YVO_4 doped with 1at.% Tm^{3+} and 8at.% Yb^{3+}, while that for KGW was almost identical to that reported in [21] for Tm:KGW. Specifically, we found our spectra for KGW had an overall width of 7 nm and peaks at 474 nm, 476 nm and 480 nm which closely matched those reported in [21] for Tm:KGW.

Qualitative observations were made about the intensity of the blue emission in different crystals for the same amount of diode pump power. Blue emission was weakest for $BaWO_4$ and strongest for KGW. In the case of the vanadates, the blue emission from one Nd:$GdVO_4$ crystal (supplied by Northrop Grumman) was several times stronger than the other crystals.

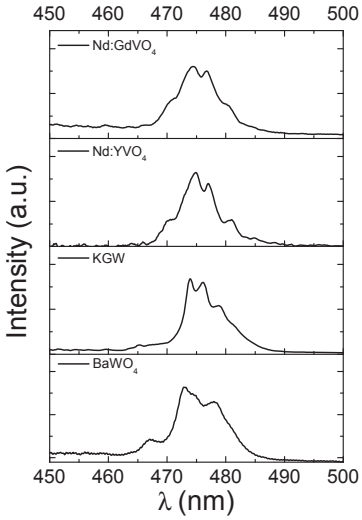

Fig. 3. Spectra of the blue emission for KGW, Nd:$GdVO_4$, $BaWO_4$, Nd:YVO_4

#203411 - $15.00 USD Received 24 Dec 2013; revised 22 Mar 2014; accepted 27 Mar 2014; published 1 Apr 2014

In order to measure the decay time of the blue emission, four Q-switched Raman lasers were built using different Raman active crystals. The lasers were similar to those described above, but with the addition of an acousto-optic Q-switch in the cavity (NEOS model 33027-25-2-1). A Nd:YAG crystal was used as the laser active medium in the case where separate Raman crystals (YVO_4, KGW and $BaWO_4$) were used. For Nd:$GdVO_4$ a self-Raman laser was built since there was no undoped $GdVO_4$ crystal available. Using a 50 mm lens to collect the blue emission from the Raman crystal and a 75 mm lens to image it into a photomultiplier tube (Hamamatsu R456), and filters to select only blue emission at 475nm, it was possible to measure luminescence decay times.

The decay curves for the Nd:$GdVO_4$, YVO_4, KGW and $BaWO_4$ are shown in Fig. 4. An exponential fit was used to extract decay times for each of them, which were then compared to lifetime values found in the literature for the same hosts doped with Tm^{3+}. These are summarised in Table 1. No data was available for Tm:$BaWO_4$. For KGW, we compared our measured decay time to lifetime values for a 0.1 at% Tm:KGW crystal [22]; the low Tm^{3+} concentration is good for comparing to our measurements, where any impurity Tm^{3+} concentration will be very low. For the vanadate crystals we compared to radiative lifetimes calculated for Tm^{3+} in $GdVO_4$ [23] and YVO_4 [24]; these represent an upper limit to the luminescence lifetime because they don't consider any parallel processes that may shorten the lifetime. It was found that the measured decay times were between 11% and 16% shorter than lifetimes taken from the literature, and given this level of agreement, it is safe to say that the measured decay time for the blue emission is consistent with the origin of that decay coming from the $^1G_4$ level of Tm^{3+} impurities. Finally, we note that Khodasevich *et al.* [16] measured the fall time (from 90% to 10%) of the blue emission in a Nd:KGW crystal, considering the intensity decay and found a value of 500 µs (which corresponds to 228 µs using the 1/e decay approximation). While experimental details in [16] are scant, their lifetime using the 1/e decay approximation is close to the literature value of 127 µs for Tm:KGW [22] and is consistent with a non-instantaneous processes like upconversion.

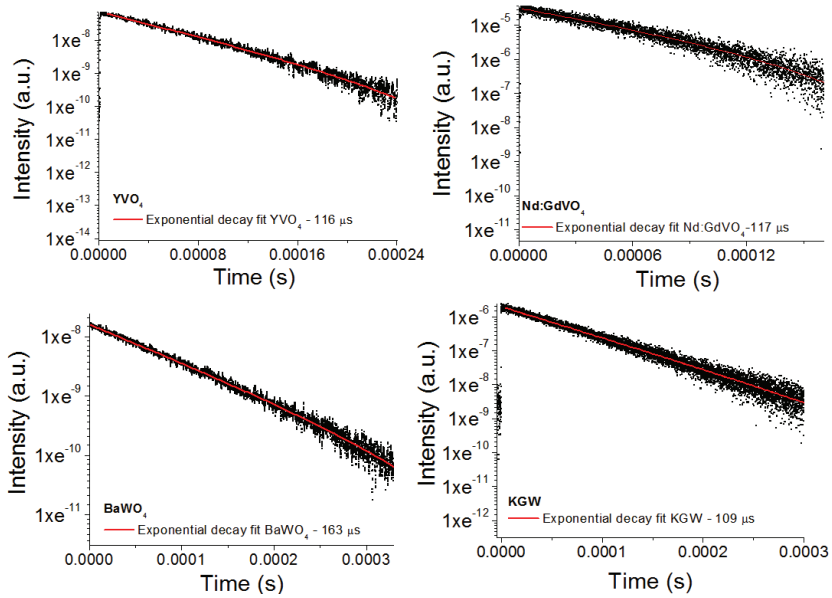

Fig. 4. Decay curves of the blue emission in Nd:$GdVO_4$, YVO_4, KGW and $BaWO_4$.

#203411 - $15.00 USD Received 24 Dec 2013; revised 22 Mar 2014; accepted 27 Mar 2014; published 1 Apr 2014

Table 1. Experimental blue luminescence lifetime and $Tm^{3+}(^1G_4)$ lifetimes from the literature for KGW, $BaWO_4$, $GdVO_4$ and YVO_4.

	Luminescence decay time – this work (μs)	$Tm^{3+}(^1G_4)$ lifetime – literature (μs)
KGW	109 ± 2	127 (0.1 at%) fluorescence lifetime [22]
$BaWO_4$	163 ± 2	-
Nd:$GdVO_4$	117 ± 2	140 radiative lifetime [23]
YVO_4	116 ± 2	131 radiative lifetime [24]

1.3 Analysis of visible emission

The blue band at 475 nm is by far the strongest emission from the Raman crystals when SRS is taking place, but it is not the only visible emission. The richest spectrum was found to come from Nd:$GdVO_4$. Figure 5(a) shows the spectrum of visible emission between 450 nm and 700 nm, measured for Nd:$GdVO_4$ above the threshold for SRS, and the luminescence excited from Nd:$GdVO_4$ (the resonator was blocked for this measurement). It is clear from the spectra in Fig. 5(a) that emissions around 525 nm, 550 nm and 600 nm are present above and below the SRS threshold, while the blue emission (475 nm) and the red emission around 650 nm only become strong above the SRS threshold. This suggests that the blue and red emissions do not arise from standard Nd^{3+} fluorescence. In the case of KGW, far weaker blue luminescence (by at least an order of magnitude) was observed below SRS threshold, and this was also noted in [16].

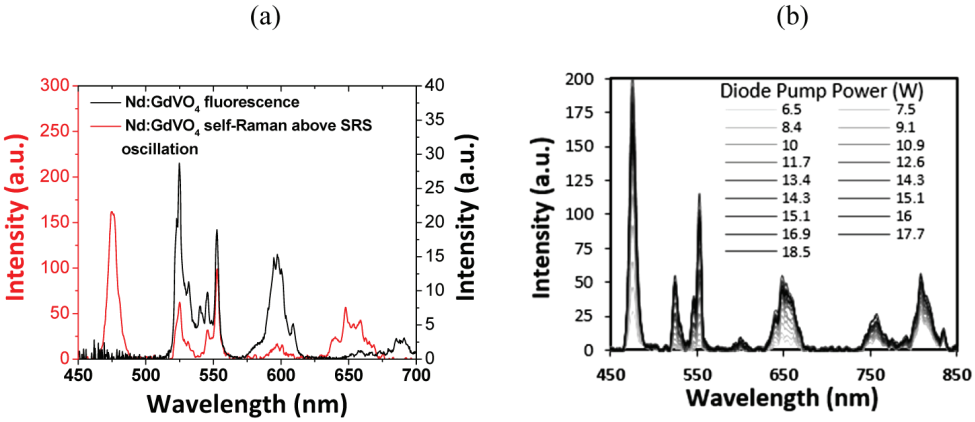

Fig. 5. (a) Emission spectra from Nd:$GdVO_4$ crystal above the SRS threshold, and fluorescence only (resonator blocked). (b) Emission spectra as a function of diode pump power.

Emission spectra were also collected for various diode pump powers above the SRS threshold. These spectra are shown in Fig. 5(b). The powers measured after the output coupler at diode (880 nm), fundamental (1063 nm) and Stokes (1173 nm) wavelengths were also collected. It was not possible to find clear (uni-variate) correspondences between variables (e.g. peak luminescence intensities and infrared powers). For this reason, we chose to adopt a multivariate approach to analyzing this data. The data was imported into The Unscrambler 10.2 (Camo Software), a statistical analysis program primarily designed for spectroscopic analysis, and the spectra were pre-processed using 5 point Savitsky-Golay smoothing and to remove the baseline. All data were mean centred and scaled to account for both the relatively low intensity luminescence and the high intensity laser output.

#203411 - $15.00 USD Received 24 Dec 2013; revised 22 Mar 2014; accepted 27 Mar 2014; published 1 Apr 2014

The Unscrambler performs eigenvector decomposition of the data set to reduce dimensionality, generating new orthogonal variables (principal components) which correspond to maximum variability in the data set [25]. The first two variables generated in this case are the principal components (PC1 and PC2) shown in Fig. 6, and together they account for 99% of the variance in the data.

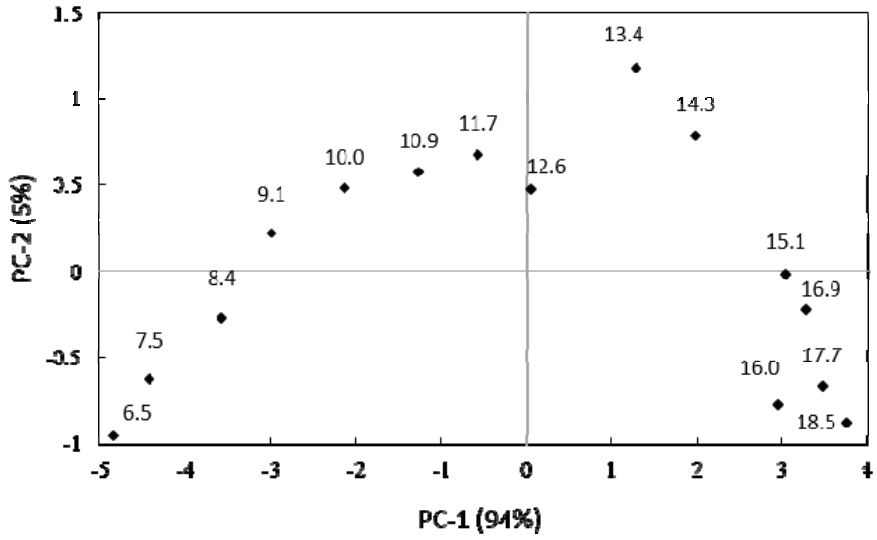

Fig. 6. PCA scores plot. Point labels correspond to diode pump power (W). PC-1 explains 94% of data variance, PC-2 explains 5%.

Principal component 1 (PC1) primarily represents the increase of light emission with pump power (the factor producing the greatest variability in the data set). Different behaviours are observed for the 6.5-12.6 W power range and the 13.4-18.5 W power range (this latter range corresponds to a roll-off in laser output). Component 2 (PC2) increases with increasing diode pump power and then declines as the pump power increases further. Figure 7 shows the loadings plot corresponding to Fig. 6. The loadings represent the correlation between the scores and the principal components. The emissions at 475 nm and 648 nm cluster together and are well separated from the green emissions (525 nm, 546 nm and 553 nm). This indicates strong correlation between the red and blue emissions, which is consistent with these lines emanating from the same upper energy level. The clustering of the green lines is also consistent with the suggestion by Khodasevich that they arise from Er^{3+} impurities [16].

#203411 - $15.00 USD Received 24 Dec 2013; revised 22 Mar 2014; accepted 27 Mar 2014; published 1 Apr 2014

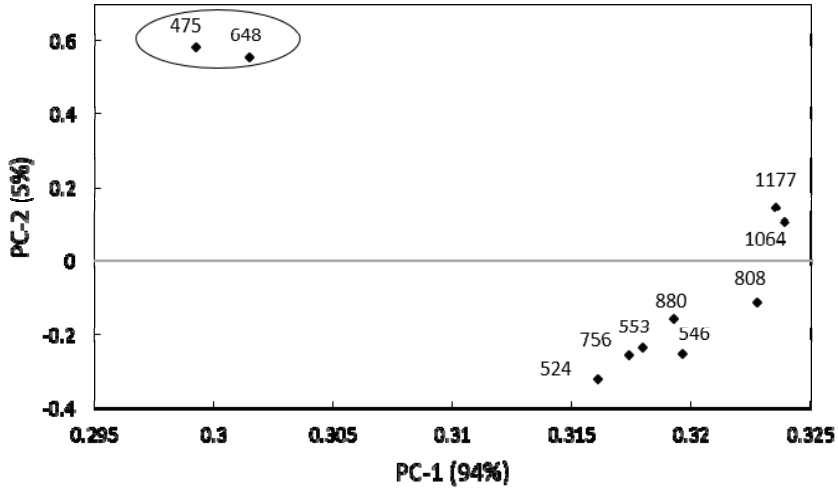

Fig. 7. PCA loadings plot. Point labels correspond to peak wavelengths (nm).

1.4 Measurement of impurity ion concentrations in Raman-active crystals

Inductively-coupled plasma mass spectrometry is a well-known method to quantify the elements contained in a specific material. In the 7500 ICP-MS (Agilent), used for this work, a laser is used to ablate material from crystal samples. The ablated material goes to the plasma torch of the ICP-MS where it is ionized and quantified by a mass spectrometer.

We have measured the concentration of trace elements in several Raman-active crystals investigated here to verify the presence of Tm^{3+} in two different Nd:$GdVO_4$ crystals from Northrop Grumman (NG) and Castech, and Tm^{3+} and Nd^{3+} in undoped KGW and $BaWO_4$ crystals. We also measured the concentration of Tm ions in $LiIO_3$ and $LiNbO_3$, two crystals in which we observed an absence of blue emission, and found the Tm concentration to be below the minimum detectable limit, ie <0.0069ppm for $LiNbO_3$ (HC Photonics) and <0.0071ppm for $LiIO_3$. The concentrations averaged for the two locations measured are shown in Table 2. The quoted uncertainties relate to the difference found in the two measurements.

Table 2. Concentration of Nd^{3+} and Tm^{3+} found in the in the Raman crystals studied.

Concentration in ppm weight ± 10%				
	Nd:$GdVO_4$ (Castech)	**Nd:$GdVO_4$ (NG)**	**KGW**	**$BaWO_4$**
Tm^{3+}	0.069	0.279	0.090	0.0085
Nd^{3+}	1759.48	1417.42	0.343	0.035

In order to cross-check the measured concentration values, we have calculated the expected ppm values using the stoichiometric distribution for each crystal, and setting one of the main host elements to calibrate the others (e.g. V for the $GdVO_4$, W for the KGW and Ba for the $BaWO_4$). We then checked the ppm concentration of the other main contents, and they were well matched to the calculated ones, with only a small error (5%).

As noted above, at similar pump levels, the blue emission in the Nd:$GdVO_4$ crystal from NG was markedly stronger than for the crystal from Castech. This corresponds well with the measured Tm^{3+} concentration being four times higher for the NG crystal. Similarly, blue emission from KGW was much stronger than for $BaWO_4$, and this corresponds to a much higher Tm^{3+} concentration in the KGW. While the concentrations found are small, it is possible to have an intense blue emission if the excitation rates of Tm^{3+} are high.

#203411 - $15.00 USD Received 24 Dec 2013; revised 22 Mar 2014; accepted 27 Mar 2014; published 1 Apr 2014

Part 2: Proposed origin of the blue emission

Based on the spectroscopic investigation detailed above, we consider it most likely that the blue luminescence originates from the $^1G_4$ to $^3H_6$ transition in Tm^{3+}, which is present as an impurity in the crystals we have studied. A large body of evidence supports this conclusion. Firstly there are the spectral similarities between the blue emission from various crystals, and by their Tm^{3+}-doped counterparts, and the similarities between measured lifetimes and those reported in the literature. Second the similar behaviours of the blue and red emission that are apparent from spectra taken above and below threshold, and also indicated by multi-variate analysis of the visible and near-IR emission spectra, are consistent with both blue and red transitions emanating from the same Tm^{3+}($^1G_4$) level. Finally, the ICP-MS measurements prove the presence of Tm^{3+} impurities in all the hosts studied here, with higher Tm^{3+} concentrations determined in crystals with higher levels of blue luminescence.

We can now proceed to propose the sequential absorption mechanism that raises the Tm^{3+} ions to the $^1G_4$ level, which then emits in the blue. It involves three steps, as shown in Fig. 8. First, a Tm^{3+} ion in the ground state ($^3H_6$) is excited to $^3H_5$ by the absorption of a 1st Stokes photon, which decays rapidly and non-radiatively to populate the $^3F_4$ level. Next, the absorption of another 1st Stokes photon or a fundamental photon populates the $^3F_3$ or $^3F_2$ levels respectively, which rapidly decay non-radiative decay to populate the $^3H_4$ level. Finally, another Stokes photon is absorbed, thus populating the $^1G_4$ level.

Table 3 lists the fundamental and first Stokes photon energies, and the energy separation of the levels involved, as sourced from the Stark levels given in [26] for Tm:YVO_4 at 300K. It can be seen that the Stokes photon energy is well-matched to the transitions labeled S1, S2, S3, while the fundamental photon energy is well-matched to the transition labeled F1. Two multiphonon transitions are denoted by H1 and H2. We speculate that the absorption steps could be assisted to some extent by the phonon field built up by the SRS process, as this could explain the typical lack of blue fluorescence in non-Raman-active laser crystals. It is also worth noting that this same 3-step sequential upconversion scheme has been used for efficient excitation of blue Tm-doped upconversion fibre lasers. For example in [27], 1.6 W of pump power at 1123 nm gave rise to 230 mW blue laser output at 481 nm, and the optimum pump wavelength was identified as 1140 nm, for that Tm:ZBLAN host.

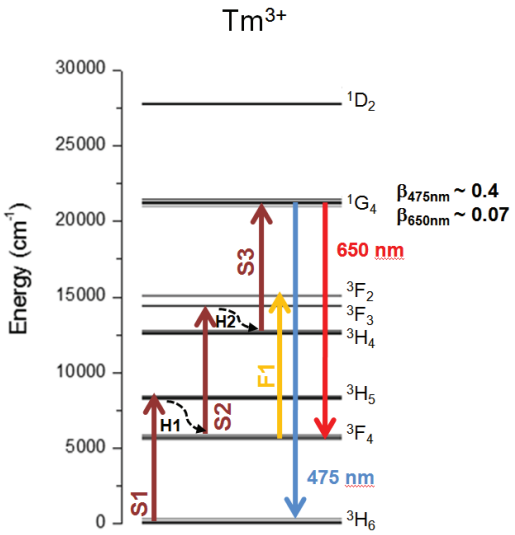

Fig. 8. Energy level diagram for Tm:YVO_4 showing blue upconversion steps [26].

#203411 - $15.00 USD Received 24 Dec 2013; revised 22 Mar 2014; accepted 27 Mar 2014; published 1 Apr 2014

Table 3. Transitions, photon and phonon energies for the Tm:YVO_4 system.

	Energy (cm^{-1})								
	1st Stokes supported transitions			Fundamental supported transition	Multiphonon supported transitions		1064 nm	1176 nm	Highest phonon energy
	S1	S2	S3	F1	H1	H2			
Min	7872	8532	8164	9128	2325	1637	9398	8503	890
Max	8491	8925	8936	9597	2941	1952			

Part 3: The implications of blue fluorescence for Raman laser performance

3.1 Power measurement of blue emission

To determine if the excitation processes resulting in blue emission have any significant impact on the operation of Raman lasers, it is necessary to make an accurate absolute measurement of the power emitted on the observed blue band. For this, we used an integrating sphere (Labsphere) in the setup displayed in Fig. 9. The Raman laser we constructed for this purpose used a Nd:YLF crystal as the active medium and KGW as the Raman active medium. The Stokes wavelength in this case was 1163 nm. This combination of crystals was chosen because the KGW (oriented for the 901 cm^{-1} shift) exhibited strong blue emission, and the Nd:YLF was used because its weak thermal lens enabled a long cavity to be made which would accommodate the integrating sphere, which had a diameter of 9.5 cm. The laser was similar to that described in section 1.2, however the longer cavity length resulted in a resonator mode less well matched to the pump mode, and as a consequence, the laser did not operate so efficiently as for shorter cavities. However this was not considered important in this case, given the complexity of the measurement. Measurement of the blue emission power was made for the case where the absorbed pump power was 15 W, the Stokes power was 470 mW, and the residual fundamental power was 850 mW.

The integrating sphere was positioned carefully in the laser resonator, and the 25 mm long KGW crystal was inserted into the sphere on a metal platform wrapped in white teflon tape to minimize absorption and the blue power incident on the silicon detector at the exit port of the sphere was measured. A photopic filter was placed in front of the detector, in order to exclude any infrared emission. Considerable attention was paid to calibrating the collection efficiency of the arrangement, which was accomplished with the aid of a green laser pointer of known output power. We measured a total blue emission power of P_{blue} = 19 mW ± 2.8 mW.

#203411 - $15.00 USD Received 24 Dec 2013; revised 22 Mar 2014; accepted 27 Mar 2014; published 1 Apr 2014

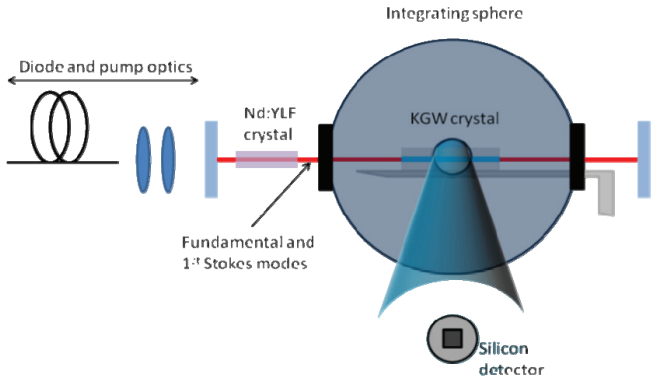

Fig. 9. Laser cavity with the integrating sphere used to measure the blue emission power.

3.2 Implications of blue emission for laser efficiency

Intracavity Raman lasers are characterized by relatively low gain, and to achieve good performance it is absolutely critical to minimize resonator losses. The mirror reflectivities used here are very high, so that the resonator losses are typically dominated by bulk crystal losses associated with scattering and absorption [28]. Therefore it is reasonable to question whether the blue emission presents a significant loss to the intracavity Stokes optical field.

Here we consider the worst case scenario, which is the use of three Stokes photons to reach the $Tm^{3+}(^1G_4)$ level. We also recognize that not every Tm^{3+} ion in the $^1G_4$ level will decay by emitting a blue photon and so, the branching ratio (β) of the $^1G_4$ level and the quantum efficiency (η_{qe}), have to be taken in account. The branching ratio value (0.4) is found in the literature [24], while the quantum efficiency is calculated from the ratio of the measured fluorescence lifetime (τ_f) to the radiative lifetime (τ_r). In this case we used the fluorescence lifetime found in the literature for a low Tm^{3+} doping concentration (0.1at%), which is expected to be close to the radiative lifetime. Based on the lifetime values described in the previous section, the quantum efficiency is calculated to be 0.86.

For a measured blue power P_{blue}, we find the number of blue photons emitted is $N_{blue} = P_{blue}/h\nu_{blue}$. The number of Tm^{3+} ($^1G_4$) ions excited to generate P_{blue} can be calculated by

$$N_{Tm(1G4)} = \frac{N_{blue}}{\eta_{qe} \cdot \beta} \tag{1}$$

Now we assume that three Stokes photons were consumed for each $^1G_4$ level that was excited, and find the power extracted from the Stokes field is given by

$$P_{Stokes} = 3 \cdot h\nu_S \cdot N_{Tm(1G4)} \tag{2}$$

where h is the Planck constant, ν_s is the Stokes frequency. For the measured value of P_{blue} of 19 mW, we find that 68 mW of Stokes power are extracted from the intracavity Stokes field.

Based on the coupling mirror transmission of 0.2% and the measured output power the intracavity Stokes field is estimated to be approximately 230 W. The 68 mW represents a loss of about 0.029% for the Stokes field. For the case where only two Stokes photons and one fundamental photon are involved in the process, this loss will be somewhat lower.

If we were able to prevent the processes leading to blue emission and the associated 0.029% loss (by using a KGW crystal with zero Tm^{3+} impurity) we would in principle be able to increase the output coupling by an equivalent 0.029% while maintaining the same intracavity optical powers, and so extract an additional 68 mW of Stokes output power, increasing the Stokes output power by 15% to 538 mW.

#203411 - $15.00 USD Received 24 Dec 2013; revised 22 Mar 2014; accepted 27 Mar 2014; published 1 Apr 2014

The extent to which the efficiency of other Raman lasers may be impacted by the processes leading to blue fluorescence depend on the power of the blue emission and the output coupling for the Stokes field. However it is reasonable to conclude that crystals containing high levels of Tm^{3+} impurity will experience commensurately higher losses. We note in this context that the geometric constraints of the integrating sphere made it impractical to measure the absolute power of blue emission for the self-Raman laser crystals.

3.3 Implications of blue emission for thermal loading of Raman-active crystals

It has been noted on several occasions [29, 30] that the thermal lensing in CW intracavity Raman lasers is somewhat stronger than anticipated on the basis of estimated thermal loads due to pump heating and Raman heating. In [30], the thermal lens in an intracavity Nd:$GdVO_4$ Raman laser was measured interferometrically, and the slope of the thermal lens power was found to approximately double above the threshold for SRS; it was suggested that this might be linked to the strong blue emission observed in that system. Here we consider the possibility that the excitation processes leading to blue emission might be contributing to the thermal load in a Raman-active crystal, based on the measured blue power of 19 mW from KGW.

In order to find the thermal power added due to the blue fluorescence, we first consider the three sequential absorption steps for excitation of the $Tm^{3+}(^1G4)$ level. As shown in Fig. 8, the energy of 3 Stokes photons exceeds the energy level of Tm ($^1G_4$), the difference being the energy of the two nonradiative decays labelled H1 and H2 in Fig. 8. This gives a first contribution to the thermal load associated with the blue fluorescence.

$$P_{heat\ blue\,1} = \left(3 \cdot h\nu_S - h\nu_{blue}\right) \cdot N_{Tm(1G4)} = 12.44\ \text{mW} \tag{3}$$

where $N_{Tm(1G4)}$ is from Eq. (2).

Now we consider the various decay channels for $Tm^{3+}(^1G_4)$ ions. Those that decay radiatively to the ground state by emitting a blue photon contribute no thermal load. Those 14% that decay nonradiatively are assumed to contribute fully to the thermal load, and so

$$P_{heat\ blue\,2} = P_{Stokes} \cdot \left(1 - \eta_{qe}\right) = 9.47\ \text{mW} \tag{4}$$

For the other 60% of Tm-$^1G_4$ ions that decay radiatively eg at 650 nm or 800 nm to levels other than the ground state, we estimate that ~1/3 of the energy is deposited as heat.

$$P_{heat\ blue\,3} = \frac{P_{blue} \cdot \dfrac{0.6}{0.4}}{3} = 9.5\ \text{mW} \tag{5}$$

where P_{blue} is the blue power measured with the integrating sphere setup.

Summing the different contributions we find that the total heat deposited in the KGW Raman crystal by the processes leading to the blue emission is $P_{heat\ blue}$~31 mW. The main uncertainty in this estimate is whether all the blue photons emitted from $Tm^{3+}(^1G_4)$ are detected, ie that there is no reabsorption of the blue emission. Given the low Tm^{3+} and Nd^{3+} concentrations, at least in KGW, this is a reasonable assumption.

Next we consider the Raman heating, so that the two heat loads can be compared. For every Stokes photon generated, a small amount of heat ($h\nu_f - h\nu_s$) is deposited in the Raman crystal. To determine the Stokes power generated we must consider the Stokes output power plus the Stokes photons lost as a result of passive cavity losses and blue generation. Thus the Raman heating in the Raman crystal is given by

$$P_{heat\ Raman} = \frac{\left(h\nu_f - h\nu_s\right) \cdot P_{Stokes}^{out} \cdot \left(T_{oc} + L_{passive} + L_{blue}\right)}{T_{oc}} \tag{6}$$

#203411 - $15.00 USD Received 24 Dec 2013; revised 22 Mar 2014; accepted 27 Mar 2014; published 1 Apr 2014

In the present example, where the passive round trip cavity losses are estimated to be ~0.5%, we then estimate that the generated Stokes power is 3.65 times higher than the Stokes output power of 470 mW, ie it is 1.72 W. From Eq. (6), the thermal load associated with Raman heating can be calculated to be ~178 mW, and the total heat load ($P_{heat\ Raman} + P_{heat\ blue}$) is 209 mW.

If we were able to prevent the blue emission in this particular laser, for example by using a KGW crystal with no Tm^{3+} impurity ions, and we increased the output coupling by 0.029% to maintain the same intracavity Stokes field, then the total heat load would be reduced by 17%, to the Raman heating component only (178 mW). This is a 17% reduction in heat load, and would be accompanied by the 15% increase in output power discussed in the previous section. Lowering the pump power to keep the Stokes output power at 470 mW would result in a total heat load of 151 mW, 25% less than for the same laser at the same output power. We can also see that in the event that the round trip losses were in fact lower than the estimated 0.5%, then the additional thermal load due to the blue fluorescence would become even more significant. We note that these estimates of the thermal load are very dependent on the round trip loss values, which are notoriously difficult to measure.

The analysis above suggests that for the KGW Raman laser considered here, the blue fluorescence leads to an additional thermal load of 17%. The extent to which blue fluorescence might impact thermal loading of other Raman lasers will depend on the power of the blue emission, and the total cavity losses for the Stokes field. For the case of self-Raman lasers such as in [30], we anticipate the resonator round trip losses would be lower than those estimated here, however heating associated with the quantum defect between the diode pump and fundamental pump photon energies will dominate Raman heating. For 15 W absorbed diode pump power, pump heating would amount to around 3.7 W. Thus it appears quite unlikely, that the thermal loading associated with blue fluorescence (31 mW in the case of the KGW Raman laser) would make a substantial contribution to the overall thermal load in a self-Raman laser.

Conclusion

The phenomenon of blue emission from a variety of Raman-active crystals has been investigated in detail. Various spectroscopic methods were used to measure the spectral characteristics of the blue emission, its lifetime, and power-dependence, while ICPMS was used to determine the concentration of Tm^{3+} ions. This investigation leads us to attribute the origin of the phenomenon to fluorescence from Tm^{3+} ($^1G_4$) impurity ions which are excited via sequential upconversion.

For the specific case of a Nd:YLF/KGW Raman laser, in which the KGW crystal contained Tm^{3+} impurity ions at 0.09 ppm, we measured the blue fluorescence power to be around 19 mW. Loss to the first-Stokes optical field associated with the proposed excitation mechanism was estimated to be 68 mW or 0.029%. We further found that if the processes leading to blue fluorescence could be eliminated, the laser efficiency could be increased by 15% and thermal loading in the KGW crystal reduced by 17%.

We conclude generally that high levels of Tm^{3+} impurity in tungstate and vanadate Raman crystals will result in significantly inferior Raman laser performance; conversely crystals with low levels of Tm^{3+} impurity will give best performance.

Acknowledgments

Jonas Jakutis Neto gratefully acknowledges the award of a CAPES scholarship (Proc nº 5381/09-6) and IMQRS scholar from Macquarie University. We gratefully acknowledge our colleagues Prof. Jiyang Wang and Huaijin Zhang from the State Key Laboratory of Crystal Materials, Shandong University, China who provided the Barium tungstate crystal used for this work.

#203411 - $15.00 USD Received 24 Dec 2013; revised 22 Mar 2014; accepted 27 Mar 2014; published 1 Apr 2014

Appendix B

Additional data

Tables B.1 and B.2 show two–colour and depolarisation method temperature RMSE values with and without baseline correction corresponding to the column charts shown in Figure 4.15 and Figure 4.17 in Chapter 4.

Sample ID	RMS Temperature Error (°C)	
	uncorrected	baseline corrected
Rose Bay	±0.3	±0.2
Woolwich	±0.2	±0.2
Clontarf	±0.5	±0.2
Sugarloaf Bay	±0.2	±0.1
Rhodes	±0.2	±0.1
North Head	±0.4	±0.2
Manly Beach	±0.5	±0.3
Manly Dam	±0.5	±0.3
Mains water	±0.2	±0.2
MQU lake	±1.2	±0.6

Table B.1 – Two-colour RMSE errors for natural water samples with and without baseline correction.

Sample ID	RMS Temperature Error (°C)	
	uncorrected	baseline corrected
Rose Bay	±0.9	±0.6
Woolwich	±4.7	±2.5
Clontarf	±5.9	±1.2
Sugarloaf Bay	±7.1	±1.3
Rhodes	±3.0	±1.0
North Head	±1.2	±1.1
Manly Beach	±1.1	±0.7
Manly Dam	±5.4	±2.5
Mains water	±3.0	±1.6
MQU lake	±5.6	±2.8

Table B.2 – Depolarisation ratio RMSE errors for natural water samples with and without baseline correction.

Appendix C

Matlab program code

The following are scripts and functions for the analysis of water Raman spectra which were written by the author during the course of this project. Code relating to data analysis is shown in full, while sections for figure generation or data display are removed for clarity.

- Water_spectral_analysis
- RMSE_map
- Plot_temp
- Depol_rmse
- Lidar3d_v1

Water_spectral_analysis

This script analyses the temperature-dependent behaviour of water Raman spectra. A data file with unpolarised and polarised spectra is imported, and figures and values are generated.

```
%file import
filename= uigetfile({'*.xls';'*.xlsx';'*.csv'},'Select a data
file','MultiSelect','on');
if ~iscell(filename)
    idx=1;
else
    idx=numel(filename);
end

%image save directory selection
savedir=uigetdir('C:\','Choose save directory');

%spectrometer calibration data
calfile='enwave intensity cal.txt';
caldata=importdata(calfile);
tic
%step through multiple data files if selected.
for fileindex=1:idx;
    if iscell(filename)
        unpoldata = xlsread(filename{fileindex}, 'Sheet1');
        poldata = xlsread(filename{fileindex}, 'Sheet2');
        [~,storename,~]=fileparts(filename{fileindex});
        t=unpoldata(1,2:end);
        unpoldata(1,:)=[];
        unpoldata(:,1)=[];
        poldata(:,1)=[];
        poldata(1,:)=[];
    else
        unpoldata = xlsread(filename, 'Sheet1');
        poldata = xlsread(filename, 'Sheet2');
        [~,storename,~]=fileparts(filename);
        t=unpoldata(1,2:end);
        unpoldata(1,:)=[];
        unpoldata(:,1)=[];
        poldata(:,1)=[];
        poldata(1,:)=[];
    end

%instrument calibration of spectral data
unpoldata=bsxfun(@times,unpoldata,caldata);
poldata=bsxfun(@times,poldata,caldata);

%option for linear baseline correction
% unpoldata=baseline_tilt(unpoldata);
% poldata=baseline_tilt(poldata);

depoldata=zeros(size(unpoldata));
unpoldata=smoother(unpoldata); %Applies Savitsky-Golay smoothing to
spectra.
poldata=smoother(poldata);
wavenumber=250:2:4428;
```

```
band1_low=3000;
band1_high=3400;
band2_low=3400;
band2_high=3800;

a = (band1_low-250)/2;
ar = a-1;
b = (band1_high-250)/2;
c = (band2_low-250)/2;
cr = c-1;
d = (band2_high-250)/2;

%initialising variables
p = zeros(b-a+1,d-c+1);
parallel_p=p;
p1 = p;
p2 = p;
perc = p;
perc1 = p;
parallel_perc=p;
ps = zeros(b-a+1,1);
q = ps;

w=200;   %default channel width in cm-1.
w1=200;  %low wavenumber channel width.
w2=200;  %high wavenumber channel width.
depol_w=100;
xdepol=((2*1275)+250):2:((2*1775)+250);
phigh=zeros(b-a+1,1);
R=zeros(b-a+1,d-c+1);
Rm=R;
pmax=zeros(b-a+1,1);
p5=p2;

t_out=cell(length(t),1);
for i=1:length(t)
t_out{i}=sprintf('%.1f',t(i));
end

disp(['sample id: ' storename])

%generate depolarisation ratio from polarised spectra.
for index = 1:numel(t)
    depoldata(:,index) = poldata(:,2*index)./poldata(:,2*index-1);
end

%Unpolarised Raman spectral analysis
for k=c:d
    for j=a:b
        p(j-ar,k-cr) = mean(diff(sum(unpoldata(round(k-
w2/2):round(k+w2/2),:),1)./sum(unpoldata(round(j-
w1/2):round(j+w1/2),:),1),1,2)./diff(t));

        parallel_p(j-ar,k-cr) = mean(diff(sum(poldata(round(k-
w2/2):round(k+w2/2),1:2:end),1)./sum(poldata(round(j-
w1/2):round(j+w1/2),1:2:end),1),1,2)./diff(t));
    end
end
[val,max_short]=max(p);
[~,max_long]=max(val);
```

```
if w>0
    for k=c:d
        for j=a:b
            perc(j-ar,k-cr) = p(j-ar,k-cr)/mean(sum(unpoldata(round(k-
            w2/2):round(k+w2/2),:))/sum(unpoldata(round(j-
            w1/2):round(j+w1/2),:)));

            parallel_perc(j-ar,k-cr) = parallel_p(j-ar,k-
            cr)/mean(sum(poldata(round(k-
            w2/2):round(k+w2/2),1:2:end))/sum(poldata(round(j-
            w1/2):round(j+w1/2),1:2:end)));
        end
    end
else
    for k=c:d
        for j=a:b
            perc(j-ar,k-cr) = p(j-ar,k-
cr)/(mean(unpoldata(k,:)/unpoldata(j,:)));
            parallel_perc(j-ar,k-cr) = parallel_p(j-ar,k-
cr)/(mean(poldata(k,1:2:end)/poldata(j,1:2:end)));
        end
    end
end

r=mean(diff(unpoldata(1275:1825,:),1,2)./repmat(diff(t,1,2),551,1),2);

%Depolarisation ratio analysis
depolratio=zeros(301,301);
depolratio1=zeros(301,301,size(t,1));
polratio=zeros(size(t,1),1);

z=(a*2)+250:2:(d*2)+250; %Depol coverage of OH stretching band.
pr = zeros(d-a+1,1);


for j=a:d
    pr(j-ar) = mean(diff(unpoldata(j,:),1,2)./diff(t));
    for k=a:d
        for i=1:size(t)
            polratio(i)=poldata(j,2*i)./poldata(k,2*i-1);
        end
        depolratio(j-ar,k-ar)=mean(gradient(polratio,t));
        depolratio1(j-ar,k-ar,:)=polratio;
    end
end

depol=mean(diff(depoldata(1275:1775,:),1,2)./
repmat(diff(t,1,2),501,1),2);

[~,mindex] = min(pr(:));
[~,maxdex] = max(pr(:));
[depmin,position]=min(depol);

[percmax,poscol]=max(perc);
[~,posrow]=max(percmax);

[rmax,rmaxcol]=max(r);
[~,rmaxrow]=max(rmax);
```

```
[rmin,rmincol]=min(r);
[~,rminrow]=min(rmin);
%***
[mapdata,rmap]=rmse_map(unpoldata,w,t);

 [val,poscol]=min(mapdata);
[~,posrow]=min(val);

low=round((3120-3000)/2);
high=round((3586-3400)/2);
temp_out(rmap,depoldata,low,high,t)

end
toc
```

Rmse_map

This function calculates the RMS temperature error for all possible two–colour ratio channel positions (in the range 3000-3800 cm^{-1}) and outputs a 2D array of these values and a 3D array of the ratio values at each temperature investigated is produced.

```
function [rmse_val,ratio_map]=rmse_map(unpol,w,temp)
a=1375;
ar=a-1;
b=1575;
c=1575;
cr=c-1;
d=1775;
ratio_map=zeros(b-a+1,d-c+1,length(temp));
rmse_val=zeros(b-a+1,d-c+1);

for k=c:d
    for j=a:b
        if w>0
            ratio_map(j-ar,k-cr,:)          =          sum(unpol(int16(k-
            w/2):int16(k+w/2),:))./sum(unpol(int16(j-
            w/2):int16(j+w/2),:));
        else
            ratio_map(j-ar,k-cr,:) = unpol(k,:)./unpol(j,:);
        end
        r=squeeze(ratio_map(j-ar,k-cr,:))';
        fitcheck=corrcoef(r,temp);
        if fitcheck(1,2) >=0.5
            p=polyfit(r,temp,1);
            temp_out=p(1)*r+p(2);
            rmse_val(j-ar,k-cr)=sqrt(sum((temp_out-
            temp).^2)./numel(temp_out));
        else
            rmse_val(j-ar,k-cr)=2;
        end
    end
end
end % function end
```

Temp_out

This function calculates the two-colour ratio, depolarisation ratio and linear combination for spectra of a specific water sample, and outputs a combined predicted vs. reference plot and the RMSE for each method.

```
function temp_out=temp_out(rmap,depoldata,low,high,t)
savedir=uigetdir('C:\');

low=round((3386-3000)/2);
high=round((3478-3400)/2);
if low==0
    low=1;
end
if high==0
    high=1;
end
if numel(low)&&numel(high)>=2
    p=zeros(2,numel(low));
    temp_out=zeros(numel(t),numel(low));
    r=temp_out;

    for i=1:numel(low)
        r(:,i)=squeeze(rmap(low(i),high(i),:));
        p(:,i)=polyfit(r(:,i),t,1);
        temp_out(:,i)=p(1,i)*r(:,i)+p(2,i);
    end
else
    r1=squeeze(rmap(low,high,:));
    p=polyfit(r1',t,1);
    temp_out=p(1)*r1+p(2);
    depol_temp_out=depol_line(depoldata,100,t);
    %100cm-1 is the channel width used for the depol ratio in ch4.
    c=regress(t',[ones(numel(t),1) temp_out depol_temp_out']);

    disp('two-colour')
    disp(sqrt(sum((temp_out'-t).^2)./numel(temp_out')))
    disp('depol')
    disp(sqrt(sum((depol_temp_out-t).^2)./numel(depol_temp_out)))
    disp('MLR')
    disp(sqrt(sum(((c(1)+c(2)*temp_out+c(3)*depol_temp_out')'-
     t).^2)./numel(c(1)+c(2)*temp_out+c(3)*depol_temp_out')))
end
end %function end
```

Depol_rmse

This function generates depolarisation ratio values for all channel positions (centre positions in the range 2800-3800 cm^{-1} with 2cm^{-1} steps), and returns both the ratio and RMSE values.

```
function [depol_temp_out,rmse_depol] = depol_rmse(depoldata,w,t)
    a=1275;
    d=1775;
    ar=a-1;
    depolrange=zeros(d-a+1,numel(t));
    temp_out=depolrange;
    rmse_depol=zeros(d-a+1,1);

    for j=a:d
        depolrange(j-ar,:)=squeeze(sum(depoldata(j-w/2:j+w/2,:),1));
        p_depol=polyfit(depolrange(j-ar,:),t,1);
        temp_out(j-ar,:)=p_depol(1).*depolrange(j-ar,:)+p_depol(2);
        rmse_depol(j-ar)=sqrt(sum((temp_out(j-ar,:)-t).^2)./numel(t));
    end
    depol_temp_out=squeeze(temp_out(((3450-250)/2)-1274,:));
    %3418 for freshwater optimised with baseline correction
    %3428cm-1 0.8 deg C minimum for 200cm-1 bandwidth (RO).
    %3560cm-1 for min temp with 2cm-1 band intensities (RO).
    %3450 for max variation in intensity.
end
```

Lidar3d_v1

This code runs a three–dimensional Raman remote sensing simulation, which was constructed with heavy modification from a simple one–dimensional Raman simulation. The 1-D simulation was developed based on irradiance calculation code published by Leathers et al. [124].

```
function [ramanoutput]=lidar3d_v1(NP)
%Initialise variables
abgreen=0.05;
abred=0.34;
%attenuation coefficients from:
% R. Smith and K. Baker, "Optical properties of the clearest natural
waters (200-800 nm)," Appl. Opt. 20, 177-184 (1981)
% Pope and Fry, "Absorption spectrum (380-700nm) of pure water. II.
Integrating cavity measurements", 1997.

% NP=1e8;                %# of photon packets to trace
n=1.34;                  %refractive index of water.
ns=20;                   %# of scatter events to track.
mucrit=sqrt(1-1/n^2);    %critical angle
w0=0.8;                  %single scattering albedo
tracker=zeros(NP,ns);
beamradius=0.01;
cell_length=5;
cell_radius=0.1;

disp('Starting calculation:')
tic
[L,cdf] = raman_cdf;
[pulse_time_scale,total_out] = pulse_cdf;

for i=1:NP %photon loop
    r=beamradius*sqrt(-log(1-rand));
    s_azimuth=2*pi*rand;
    p=[r*sin(s_azimuth);r*cos(s_azimuth);0]; %set random initial
                                              %position within beam.
    mu=[0;0;1]; %set initial photon direction
    strack=0;
    w=1; %initialise packet weight
    %     wlog=0; % plot summed w's for binned TOF values.
    lambda=532; %laser wavelength
    countlambda=0;
    counttime=0;
    last_scatter=0;
    scattercount=0;
    weightcount=0;

    if abs(mu(3))==1;
        ra=((n-1)/(n+1))^2; %reflection normal to surface
    else
        tinc = acos(mu(3)); %angle of incidence
        trefr = asin(n*sqrt(1-mu(3)^2)); % angle into water
        ra = ((sin(tinc-trefr)/sin(tinc+trefr))^2+(tan(tinc-
        trefr)/tan(tinc+trefr))^2)/2;
```

```
        mu(3) = cos(trefr); % new direction
    end
    w = w*(1-ra);

    for j=1:ns %number of scattering events
        w=w*w0;

        % Beers Law path length
        if lambda==532
            s=-log(rand)/abgreen; %pathlength
        elseif lambda>532
            s=-log(rand)/abred;
        end

        p_old=p;
        p=p+mu*s;
        strack=strack+s;

        if p(3)>cell_length %boundary condition: tube cell length in
                             metres.
            break
        end

        if sqrt(p(1)^2+p(2)^2)>cell_radius %boundary condition: tube
                                            diameter
            break
        end

        p_interface=[p_old(3)*(mu(1)/mu(3))+p_old(1);
        %Locate X-Y position at which packet strikes water-air
        interface.
        p_old(3)*(mu(2)/mu(3))+p_old(2); 0];

    if p_old(3)>0&&p(3)<0&&sqrt(p_interface(1)^2+p_interface(2)^2)<
       cell_radius
            countlambda=lambda;
            [~, timeindex]=min(abs(total_out-rand));%photon initiation
                                                    timing
            %log total packet travel time.
            counttime=(strack+norm(p_interface-p_old)-
                      s)*(n/3E8)+pulse_time_scale(timeindex(1))+2E-9;

            last_scatter=p_old(3); %record z position of last scatter
                                   event prior to detection.
            weightcount=w;
            mu(3)=-mu(3); %change to positive value
            p(3)=0;
            w=w*w0;
            continue %new transit of packet required before next
                      scatter event
    end

        if lambda==532;
            q=rand;
            if rand<=0.0574 %Bartlett et al. absolute Raman
                            coefficient value: 2.7E-4 m-1  *using 0.05
                            as a test value.
                mus=1.3*q^3-2*q^2-1.3*q+1; %Raman scattering
                [~, b]=min(abs(cdf-rand));
```

```
                lambda=L(b);
            else
                mus=1.9*q^3-2.9*q^2-q+1; %Rayleigh scattering - green
            end
        elseif rand<=0.999
            q=rand;
            mus=1.9*q^3-2.9*q^2-q+1; %Rayleigh scattering - red
        else
            break %second Stokes rejection
        end

        %Update direction cosines for post-scatter unit vector
        azimuthal=2*pi*rand;

        if (mu(3)^2)<0.999
                  translate=[mu(1)*mu(3)/sqrt(1-mu(3)^2) -
                  mu(2)/sqrt(1-mu(3)^2) mu(1); mu(2)*mu(3)/sqrt(1-
                  mu(3)^2) mu(1)/sqrt(1-mu(3)^2) mu(2); -sqrt(1-
                  mu(3)^2) 0 mu(3)];

                  update=[sqrt(1-mus^2)*cos(azimuthal); sqrt(1-
                  mus^2)*sin(azimuthal); mus];
                  mu=translate*update;
        elseif (abs(mu(3))-1)<0.001
            if mu(3)>0
       mu=[sqrt(1-mus^2)*cos(azimuthal); sqrt(1-mus^2)*cos(azimuthal);
           mus];
            else
       mu=-[sqrt(1-mus^2)*cos(azimuthal); sqrt(1-
           mus^2)*cos(azimuthal); mus];
            end
        end
        w=w*w0;
        if w<0.0001
            if rand<0.1
                w=w*10;
            else
                break
            end
        end

        scattercount=scattercount+1;
    end % scattering loop

    tracker(i,1)=countlambda;     %packet wavelength
    tracker(i,2)=counttime;       %packet arrival time
    tracker(i,3)=last_scatter;    %location of last scatter prior to
                                  detection
    tracker(i,4)=scattercount;    %number of scatter events undergone.
    tracker(i,5)=weightcount;     %packet weight

    if mod(i*100/NP,10)==0 %Display 10% time intervals
        disp([num2str(i*100/NP),'% completed.'])
    end

end %photon loop
toc;
disp([num2str(toc/60),' minutes.'])

bin=0:1E-10:6E-8;
```

```
[n1,bin1] = histc(tracker(tracker(:,1)==532,2),bin);
[n2,bin2] = histc(tracker(tracker(:,1)>532,2),bin);

rayleighweightarray=tracker(tracker(:,1)==532,5);
rayleighweightarray(bin1==0)=[];
bin1(bin1==0)=[];
rayleighweightsums=accumarray(bin1,rayleighweightarray);

ramanweightarray=tracker(tracker(:,1)>532,5);
ramanweightarray(bin2==0)=[];
bin2(bin2==0)=[];
ramanweightsums=accumarray(bin2,ramanweightarray);

figure;
hold on

line(bin,n1,'Color','g');
line(bin,n2,'Color','r');
line(bin(1:numel(rayleighweightsums)),rayleighweightsums,'Color','g');
line(bin(1:numel(ramanweightsums)),ramanweightsums,'Color','r');

hold off
time=bin(1:numel(ramanweightsums));
rayleighoutput=rayleighweightsums;
ramanoutput=ramanweightsums;
end %main function

%**************************
%generate laser pulse photon timing cdf.
function [pulse_time_scale,total_out] = pulse_cdf
      pulse_time_scale=-2E-9:1E-10:2E-9;
      pulse=0.007581*exp(-(((pulse_time_scale-
      mean(pulse_time_scale))./std(pulse_time_scale)-
      0.009147)./0.8672).^2);
      total_out=cumsum(pulse);
      total_out=total_out/max(total_out);
end
%**************************

%**************************
%generate Raman scattering wavelength emission cdf.
function [L,cdf] = raman_cdf
    L1=round((1/((1E7/532)-2800))*1E7);
    L2=round((1/((1E7/532)-3900))*1E7);
    L = L1:0.1:L2;                          %wavelength range
investigated.
    Aj = [2000 17500 22000 3000 4000];      %gaussian component
amplitudes
    Kj = [3060 3230 3425 3535 3612];        %gaussian component centre
positions
    dK = [112 90 90 75 50];                 %gaussian component fwhm.
    fRL = zeros(4,length(L));
    for j = 1:4                             %peak number (left to right).
        fRL(j,:) = Aj(j)*exp(-((10^7*((1/532)-(1/L(:)))-
Kj(j)).^2)/(2*dK(j)^2));
    end
    fR = (sum(fRL));
    fRw = fR./(sum(fR));
    cdf=cumsum(fRw);
```

```
end
%**************************

%**************************
%calculate photon packet distance to boundary.
function F = lsolve(x)
        if dot(mu,mu)~=0
            orth1=[mu(3) mu(3) -mu(1)-mu(2)];
            orth2=[-mu(2)-mu(3) mu(1) mu(1)];
        end
    F=[orth1(1)*(x(1)-p(1))+orth1(2)*(x(2)-p(2))+orth1(3)*(x(3)-p(3));
       orth2(1)*(x(1)-p(1))+orth2(2)*(x(2)-p(2))+orth2(3)*(x(3)-p(3));
       x(1)^2+x(2)^2-radius^2];
        end
%**************************
```

Appendix D

Summary of remote sensing experimentation

Remote sensing experimentation and development was conducted alongside the later Raman spectroscopic studies presented in this thesis. The aim here was to explore the practicalities of implementing the methods developed in the thesis. Initial goals included: the retrieval of Raman signals from a depth of several metres, detection of Raman signals in the presence of ambient light, and assessment of the potential depth resolution possible using LIDAR methods.

Temporal and spatial ranging measurements were made with both laser pulses and water Raman scattered returns. This was primarily for characterisation of a variety of detectors, including Geiger–mode APD arrays, photodiodes and photomultipliers.

Sensing spectrometer configurations were developed (as shown in the experimental thesis chapters), initially for two–colour measurement, and later for the depolarisation ratio and the linear combination approach.

Tube cells were designed and constructed for laboratory measurement of Raman signals over long, continuous paths in water. These cells were used for ranged Raman signal measurement and characterisation of the spectrometer configurations. Laboratory studies of remote temperature sensing were conducted.

Simulations of remote sensing Raman returns were developed for comparison with laboratory and field experiments. Both stochastic and analytic solutions were investigated. Preliminary field trials of a two–colour instrument were carried out on Sydney Harbour. The following sections briefly describe: laboratory remote temperature sensing experiments, simulation of remote sensing return signals, and remote sensing field trials.

Laboratory remote temperature sensing

A 5 metre long horizontal tube cell was built for remote sensing experiments. The cell was constructed from 100 mm diameter PVC piping in three sections. T–junctions were used to provide access ports at two locations along the cell, and the

ends were sealed with 100 mm diameter, anti–reflection coated glass windows (Francis Lord Optics). Only the exterior facets of the windows were coated. The volume of the cell is ~37 L. A schematic and an image of the cell are shown below.

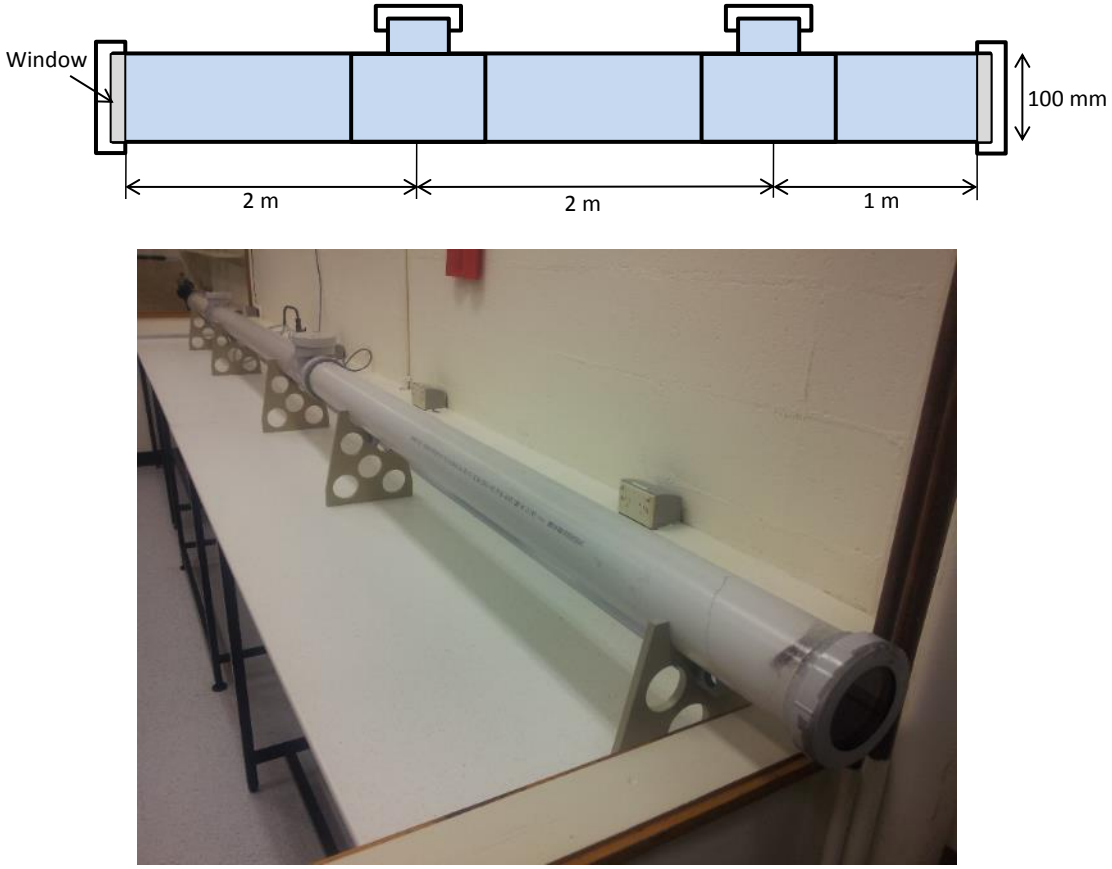

Figure D.1 – Schematic and image of the 5 metre tube cell.

The interior walls and ports of the cell were painted black to reduce reflection of scattered light. Windows were used in both ends of the cell to facilitate beam alignment and ranged testing. The far window from the sensing apparatus was covered with black cloth, or beam dumped in order to minimise back reflection of laser light. This cell was primarily built to provide a 5 metre water 'depth' for laboratory sensing experimentation, and was also used to quantify the performance of various pieces of equipment, including lasers, detectors, and optical filters.

Creating a sustained temperature gradient in the 5 metre cell proved difficult. As an alternative, a 1 metre length tubular cell (with glass windows) was constructed for temperature experiments. This cell was filled with mains supply water at 50 °C and placed into the experimental setup shown below.

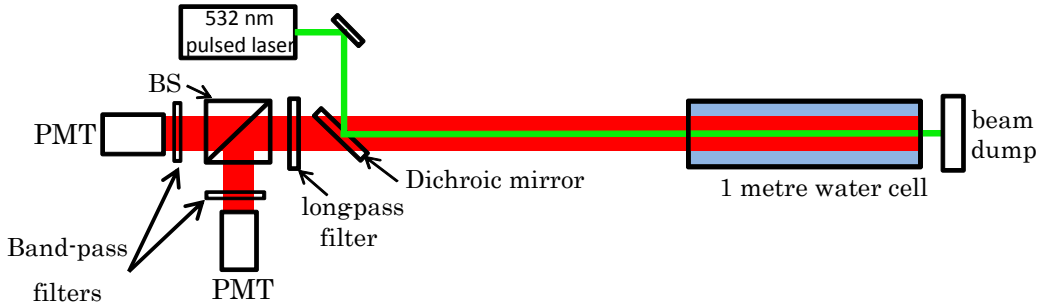

Figure D.2 – Experimental arrangement for laboratory remote temperature sensing.

Pulses from the 532 nm Nd:YAG laser (25 μJ, 1 ns) were directed into the water cell and the Raman scattered light was collected using band–pass filters to select two–colour ratio channels within the OH stretching band. Measurements were made every few degrees as the water temperature dropped from 50 °C to 30 °C. PMT signals were acquired with an oscilloscope (Tektronix DPO4104B) as the cell cooled. The oscilloscope was triggered at the laser pulse repetition rate using a pick–off reflection from the laser detected with a high–speed photodiode. Detected signals were averaged over 512 laser pulses (~128 ms) to improve consistency. The water temperature was monitored with the handheld Digitron probe described in Section 2.4.

Photomultiplier signals were integrated over a 5 ns segment in the centre of the Raman return, and two–colour ratio values were calculated for each measurement point. Figure D.3 shows the relationship between reference temperature and the two–colour ratio.

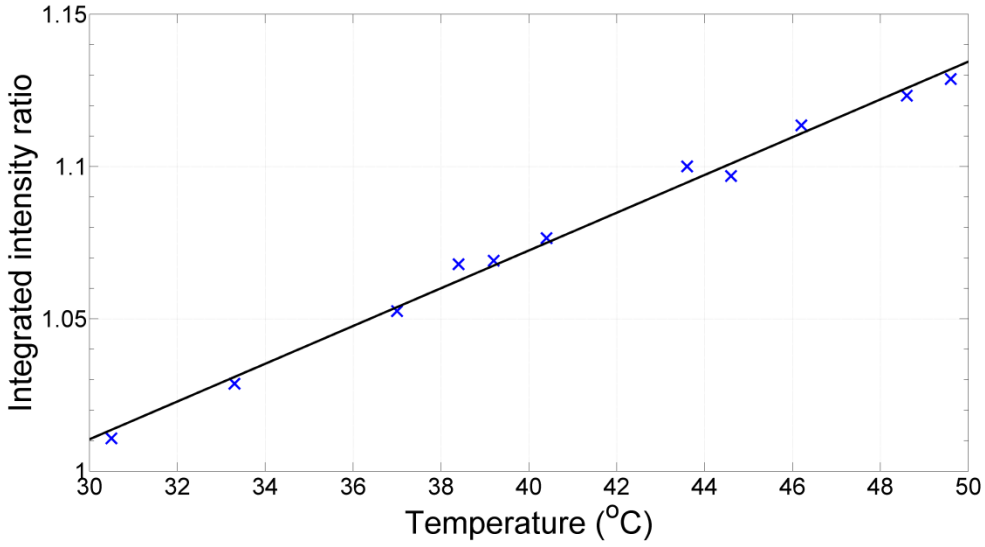

Figure D.3 –Temperature dependence of the two–colour ratio.

The ratio showed strong temperature dependence with low variability. A regression fit was calculated and the predicted vs reference temperature relationship was plotted, and is shown in Figure D.4.

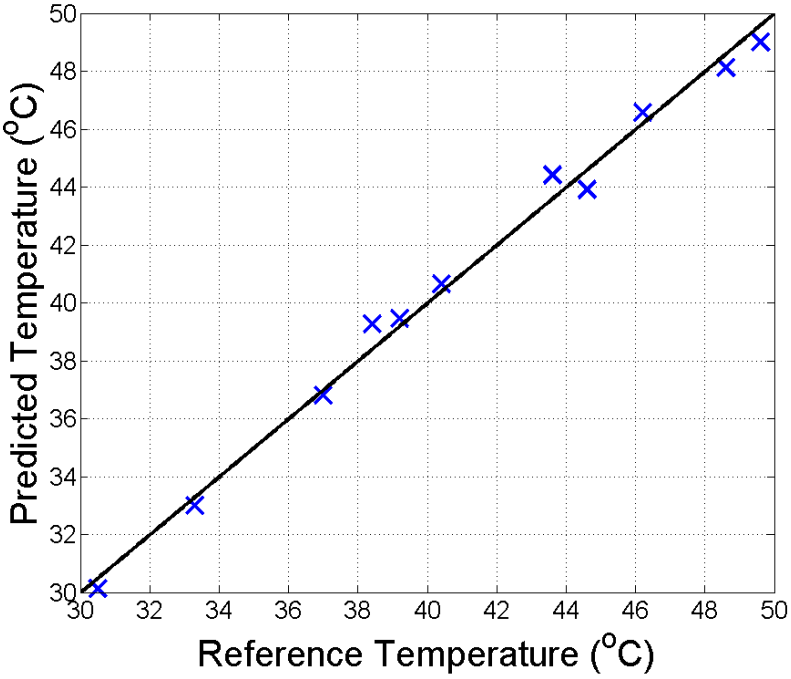

Figure D.4 – Predicted vs.reference temperature for the 1 metre cell.

The RMS temperature error was ±0.7 °C. This was higher than anticipated based on spectroscopic studies, but improved signal collection efficiency and photomultiplier configuration may improve this performance.

Modelling of Remote Sensing Retrieval

Simulations of laser–induced water Raman scattering were constructed in order to provide comparison with ranged sensing experiments. Stochastic simulations using Monte Carlo methods and analytic models for simple cases were developed and compared with experimental data.

Monte Carlo Simulation

The term "Monte Carlo" refers to algorithms which rely on repeated random sampling of variables in order to build a data set which converges to provide some desired information. These methods have huge application in scientific fields in particular, enabling complex problems to be explored. The main drawback of such

methods is their inefficiency, i.e. relatively long calculation times are required for sufficient iterations to reach the required accuracy.

A three–dimensional Monte Carlo routine was developed which simulates photon packets within a laser pulse propagating into a water column, and accumulates returning scattered photons. The simulation was written in Matlab, a language well suited to this type of calculation. It incorporates water absorption, multiple–scattering, and can include boundary conditions designed to mimic the tube cells used in laboratory experimentation. Outputs from the simulation can include temporal or spatial Raman and Rayleigh signals, 1st stokes Raman scattering event locations, and the correlation between scattering locations and detection time. Program code for this simulation can be found in Appendix C. The simulation was developed from a simplistic one–dimensional radiative transfer model, which itself was originally based on code and knowledge from Leathers et al. [124]. Figure D.5 shows the output of Raman return simulations of a 532 nm laser pulse propagating into water filled one metre and five metre tube cells described above.

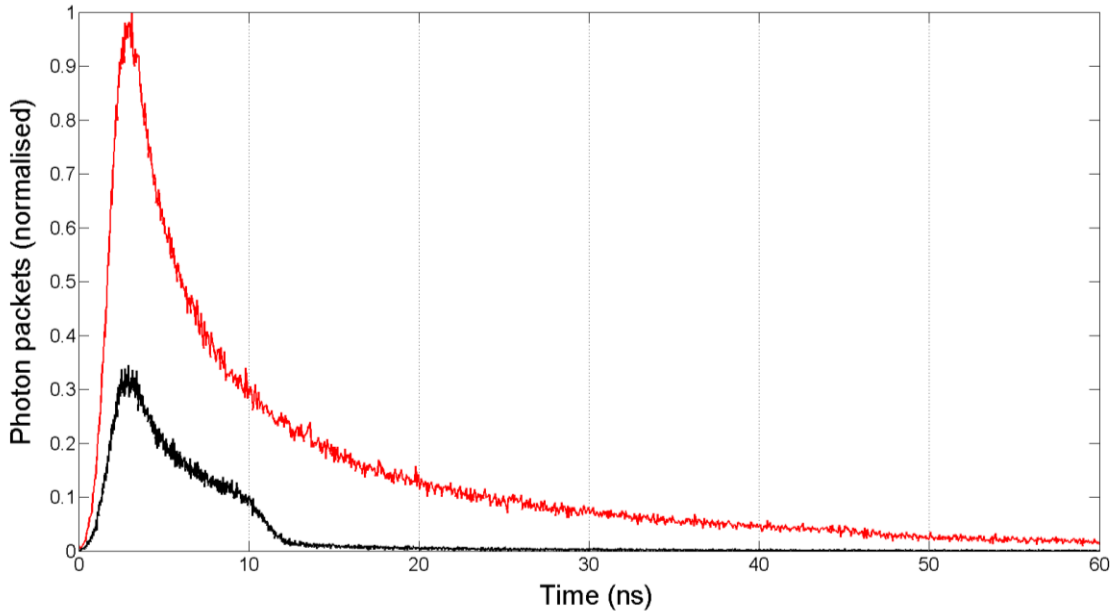

Figure D.5 – Time–series output of the Monte Carlo remote sensing simulation.
Red: 5 metre water cell; Black: 1 metre water cell.

When scaled for intensity these results correspond fairly well to experimental data considering the added response of the optical system, which the simulation does not take into account. The other parameters acquired from the simulation allow additional information to be collected; for example, depth resolution can be assessed

based on the spatial distribution of Raman scattering events which result in return of packets within a set time window.

Analytic model

An analytic expression for laser–induced Raman scattering in water was developed for comparison with Monte Carlo simulations and experimental data. This was conducted in Microsoft Excel as the simplest option available. It was based on the radiative transfer equation with modifications to include Raman scattering behaviour [125, 126]. Only single scattering was considered and each scattering event was assumed to be independent (no transfer of energy to other scatterers).

Remote sensing field trials

Preliminary field experiments were conducted in Middle Harbour (Sydney). A flat–bottomed 5 metre vessel supplied by the Sydney Institute of Marine Science (SIMS) was outfitted for remote sensing of water Raman scattering. A PC–based oscilloscope (Picotech) and laptop PC were used to acquire detector signals and record time series data. Electrical components were powered with a pair of 12V marine batteries.

The two–colour method sensing spectrometer (from the laboratory study above) and a 1 ns pulsed, 532 nm laser were coupled to several different receiver configurations, including a simple turning mirror for both laser pulses and return Raman signals, fibre coupling the spectrometer to a vertically mounted Schmidt–Cassegrain telescope, or mounting the spectrometer directly onto the telescope. These last two options completely separated the excitation and signal collection optical paths. All these approaches gave rise to clear Raman signals, with the most satisfactory configuration being the 2-channel prototype mounted on top of the telescope. The telescope and turning mirror were mounted on a pivoting aluminium arm which extended ~ 1 metre over the side of the vessel, and could be rotated in–board and secured for travel. Figure D.6 shows the vessel being prepared for launch, and the sensing system configured with a shroud to block ambient light and direct sunlight. The shroud proved unnecessary for the system configurations used due to the high intensity of Raman return signals. Raman signals were retrieved from depths of 4-6m.

Figure D.6 – (top) Research punt used for experimentation; (bottom) the sensing system ready for acquisition.

Ongoing work is aimed at improving collection efficiency so as to extend this depth to 20m, which is challenging given the large dynamic range of the return signal. Figure D.7 shows typical Raman channel signals retrieved during the field trials.

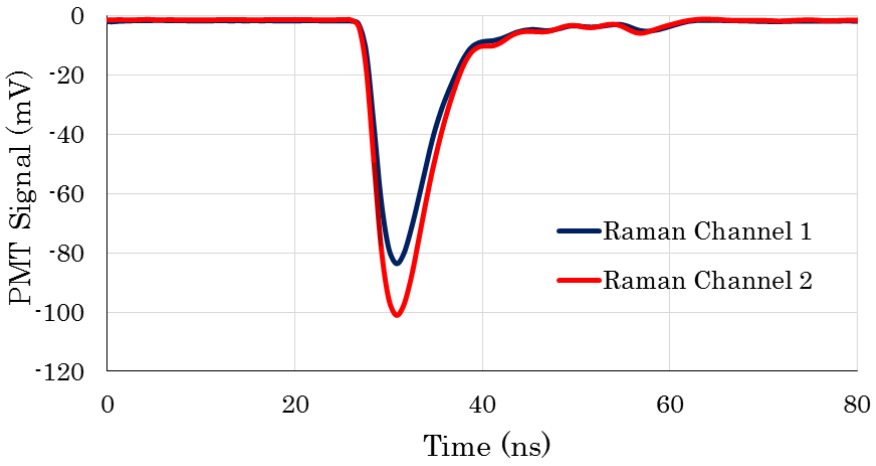

Figure D.7 – PMT signal response to returning Raman scattered radiation.

The difference in channel intensity was clearly evident. The zero position of the time axis corresponds to the trigger time from the laser pulse detected with a high–speed, fibre coupled photodiode. Only a minimal attempt was made to acquire quantitative temperature information, as these preliminary trials were focused on the acquisition of Raman signals and to developing familiarity with operating the hardware in the field.

Appendix E

Equipment used for remote sensing experimentation

This appendix describes the optics, lasers, detectors and data acquisition hardware used for ranged remote sensing experimentation.

Laser/Rayleigh light rejection

In order to study water Raman scattering with different excitation wavelengths, a combination of optical filters was needed for each source which could adequately reject laser and Rayleigh scattered light while allowing transmission of the Raman signal. These included:

- A laser line filter to eliminate residual pump light and clean up any weakly lasing emission lines.
- A 45° dichroic beamsplitter to allow transmission of Raman signals while reflecting a significant portion of the laser radiation. This also allowed co–linear excitation.
- A long pass filter with appropriate cut–off wavelength to further reject laser light.

These sets of filters were also used with an Ocean Optics QE65000 Raman spectrometer for characterisation of band–pass filters response and measurement of water Raman signal comparisons with remote detection methods. The QE65000 spectrometer has no built–in rejection of laser light or Rayleigh scattering, instead relying entirely on an external filter module appropriate to the excitation source. Because of this the unit can be connected to multiple visible laser sources and filter sets, making it very flexible in terms of its capabilities. Figure E.1 shows the basic filter configuration used in Raman experiments with the QE65000 spectrometer.

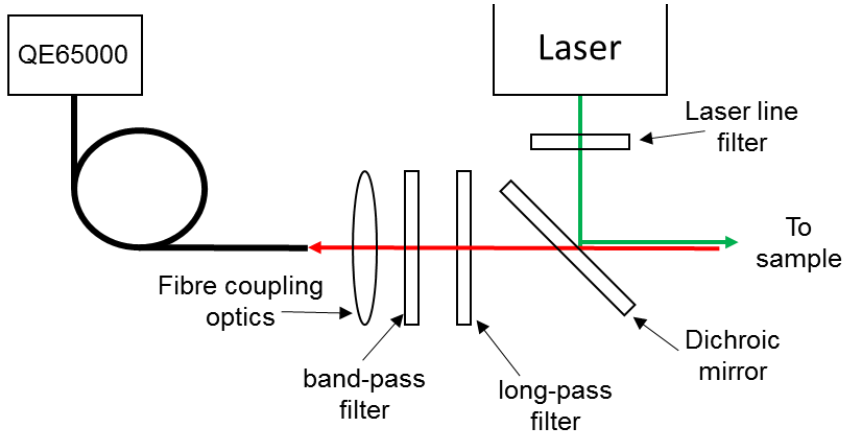

Figure E.1 – Filter configuration for laser light rejection and Raman signal collection with a fibre–coupled spectrometer.

In situations with optical noise outside the Raman band, a broad band–pass filter was added to improve signal to noise ratio in the spectral region of interest.

Optical Filters

A variety of multi–layer coated optical filters were used in various aspects of this work. Band–pass filters were used to select segments of the water Raman band for detection. Long–pass filters and dichroic mirrors were employed for laser light and Rayleigh scattering rejection. Transmission spectra for the filter sets used for 473 nm and 532 nm excitation are shown in Figures E.2 and E.3 respectively.

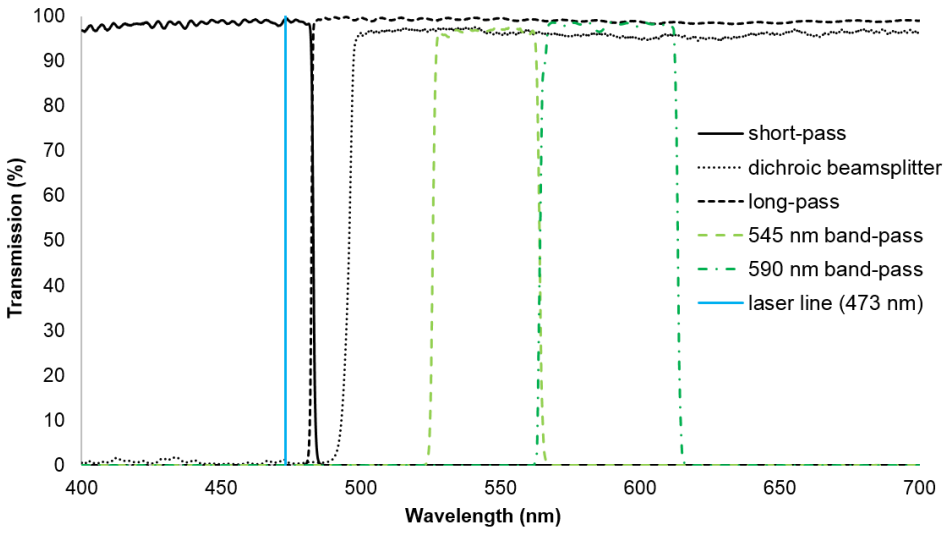

Figure E.2 – Filter spectra for 473 nm excitation.

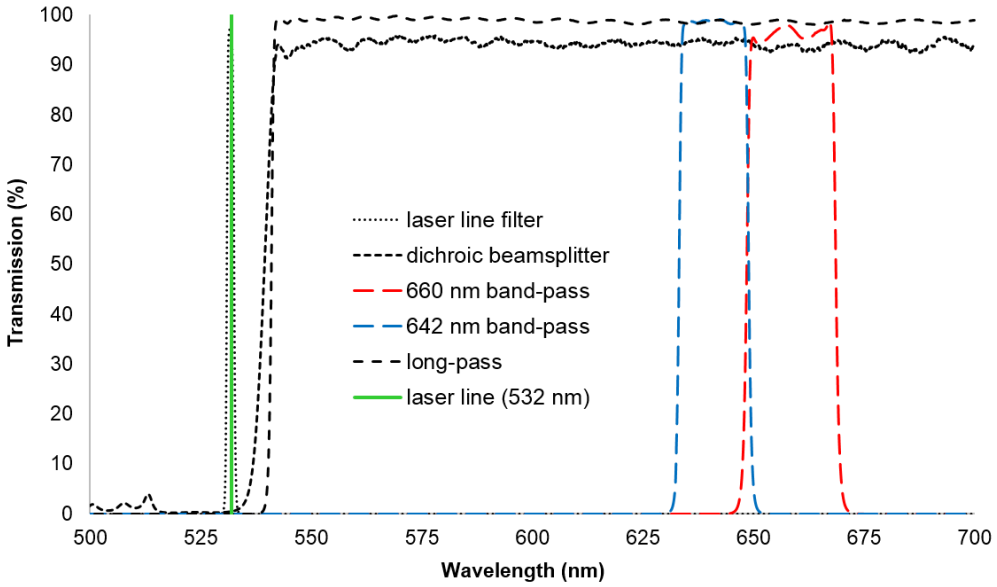

Figure E.3 – Filter spectra for 532 nm excitation.

The band–pass filters used for 473 nm excitation were considerably broader than those used with 532 nm light. This was due to the limited availability of suitable filters in this wavelength range.

Excitation Wavelength	**473 nm**	**532 nm**
Laser line filters	Semrock FF01-492/SP	Semrock LL01-532
Dichroic mirror	Semrock Di02-R488	Semrock FF538-FDi01
Long pass filters	Semrock BLP01-473R	Semrock BLP01-532R
Band–pass filters	Semrock FF01-571/72 Chroma ET545/40m Chroma ET590/50m	Thorlabs FB650-40 Semrock FF01-642/10 Semrock FF01-660/13

Table E.1 – Filters selected for remote sensing spectrometers.

Laser Sources

A green laser source was used for water Raman scattering experiments (aside from those conducted with the Enwave Raman spectrometer) and remote sensing studies. This was a frequency–doubled Nd:YAG microchip laser (Innolight μ-Flare-532) which was linearly polarised (horizontal) and emitting at 532 nm. Basic specifications are shown in Table E.2.

Manufacturer	Innolight
Emission wavelength	532 nm
Average power	115 mW
Pulse duration	0.9 ns
Pulse repetition rate	4.5 kHz
Pulse energy	25.5 μJ

Table E.2 – Green laser source specifications.

This laser is passively Q–switched using an intra–cavity Cr4+:YAG crystal, a material which acts as a saturable absorber in the wavelength range 850-1250nm. The crystal is highly absorbing until a threshold intensity is reached within the cavity, when it becomes partially transmitting, producing a short, high intensity laser pulse from the entire excited population of neodymium ions in the laser mode volume. These pulses are then frequency doubled from the fundamental wavelength to the desired 532 nm output. The laser is classified as a class 3B source, and hence required appropriate laser safety goggles to be worn during its operation. A pulse profile for the laser is shown in Figure E.4.

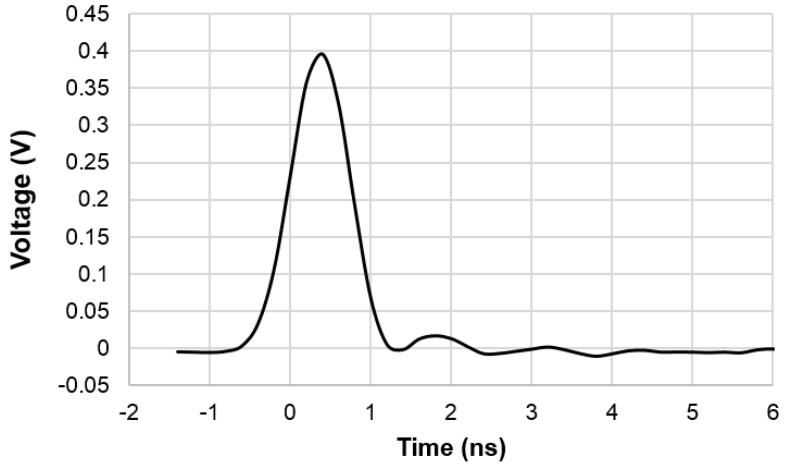

Figure E.4 – Pulse profile for the Innolight 532 nm laser.

The pulse duration was approximately 900 ps full width half maximum (FWHM). This duration provided appropriate temporal (and hence ranged) signal resolution for Raman ranging experimentation.

A laser emitting at 473 nm was also acquired for future remote sensing studies (Alphalas PULSELAS-P-473-6-SP). This is a Nd:YAG based laser, operating on a three–level transition and emitting a fundamental wavelength of 946 nm, which

was then frequency–doubled to give 473 nm output. Table E.3 shows basic manufacturer specifications.

Manufacturer	Alphalas
Emission wavelength	473 nm
Average power	25 mW
Pulse duration	~1.5 ns
Pulse repetition rate	5 kHz
Pulse energy	5 μJ

Table E.3 – Blue laser source specifications.

A pulse profile for this laser is shown in Figure E.5. The pulse duration was approximately 1.3 ns (FWHM).

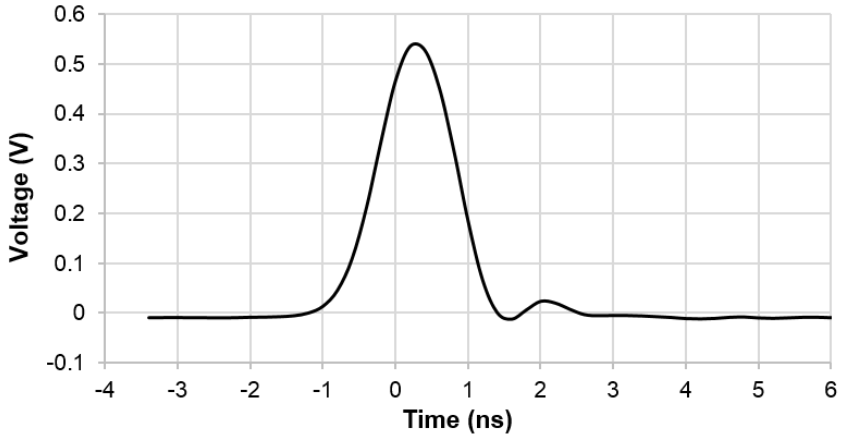

Figure E.5 – Pulse profile for the Alphalas 473 nm laser.

This is slightly longer in duration than the 532 nm laser, but still sufficient to enable good ranging of Raman signal returns. This laser had particularly poor beam collimation in the horizontal direction, with divergence measured to be ~30 mrad. Optics were added in front of the aperture which dramatically improved this performance.

Detectors

Optical detectors were employed for multiple purposes in this work. These ranged from pulse timing and triggering to remote sensing signal acquisition. Silicon photodiode arrays were characterised as a potential detector option for rapid sensing of Raman signals (SensL SPMMini). The detector surface consists of a 3x3 mm^2 grid of 20 μm avalanche photodiodes operated in Geiger mode, providing a gain of ~10^5.

Further amplification was provided by a trans–impedance amplifier, giving a total gain of ~2.6x10^6. The rise time was approximately 20 ns when taking the amplifier into account, which substantially limits ranged signal resolution. For this reason, these detectors were deemed inadequate for Raman signal acquisition.

Photomultiplier modules were used for rapid acquisition of laser–induced water Raman scattering (Hamamatsu H10721-20). These devices have a rise time of 0.57 ns and adjustable gain ranging from 10^3 – 10^7. The photocathode is an extended range multi–alkali type with a spectral response from 230 – 920 nm and maximum sensitivity at ~630 nm.

Figure E.6 – Hamamatsu H10721-20 PMT module.

These modules require a bias voltage of 5.5 V with a maximum current draw of ~2.7 mA. The voltage conversion circuitry necessary to produce the high dynode voltages for electron multiplication is incorporated. The package dimensions are 50x22x22 mm, substantially smaller than the majority of self–contained PMT modules. The combination of relatively fast rise times, compactness, ease of use and high sensitivity made these detectors ideal for acquiring Raman signals.

A fibre–coupled silicon photodiode (Thorlabs DET02AFC) was used for laser pulse characterisation and oscilloscope triggering for timed signal acquisition in ranged sensing experiments with 532 nm excitation (the 473 nm laser source incorporated a photodiode for triggering). This photodiode is reverse–biased with a spectral range of 400-1100 nm, a rise time of 50 ps, fall time of 250 ps, and a bandwidth of 1.2 GHz. This detector was selected as an ideal choice to providing a triggering signal for PMT Raman signal acquisition, as well as for laser pulse duration measurement.

Data Acquisition

Temporal data observation and acquisition was provided by a digital oscilloscope (Tektronix DPO4104B). This scope has a bandwidth of 1 GHz, a sample rate of 5 GS/s and a 20 MS record length. Other similar oscilloscopes were used at various stages, including Tektronix TDS 794 and TDS 3054 units.

A PC-based oscilloscope unit was used where portable measurement was required (Picotech Picoscope 6404C). This unit has a 500 MHz bandwidth, 5 GS/s sample rate and a 1 GS record length.

Appendix F

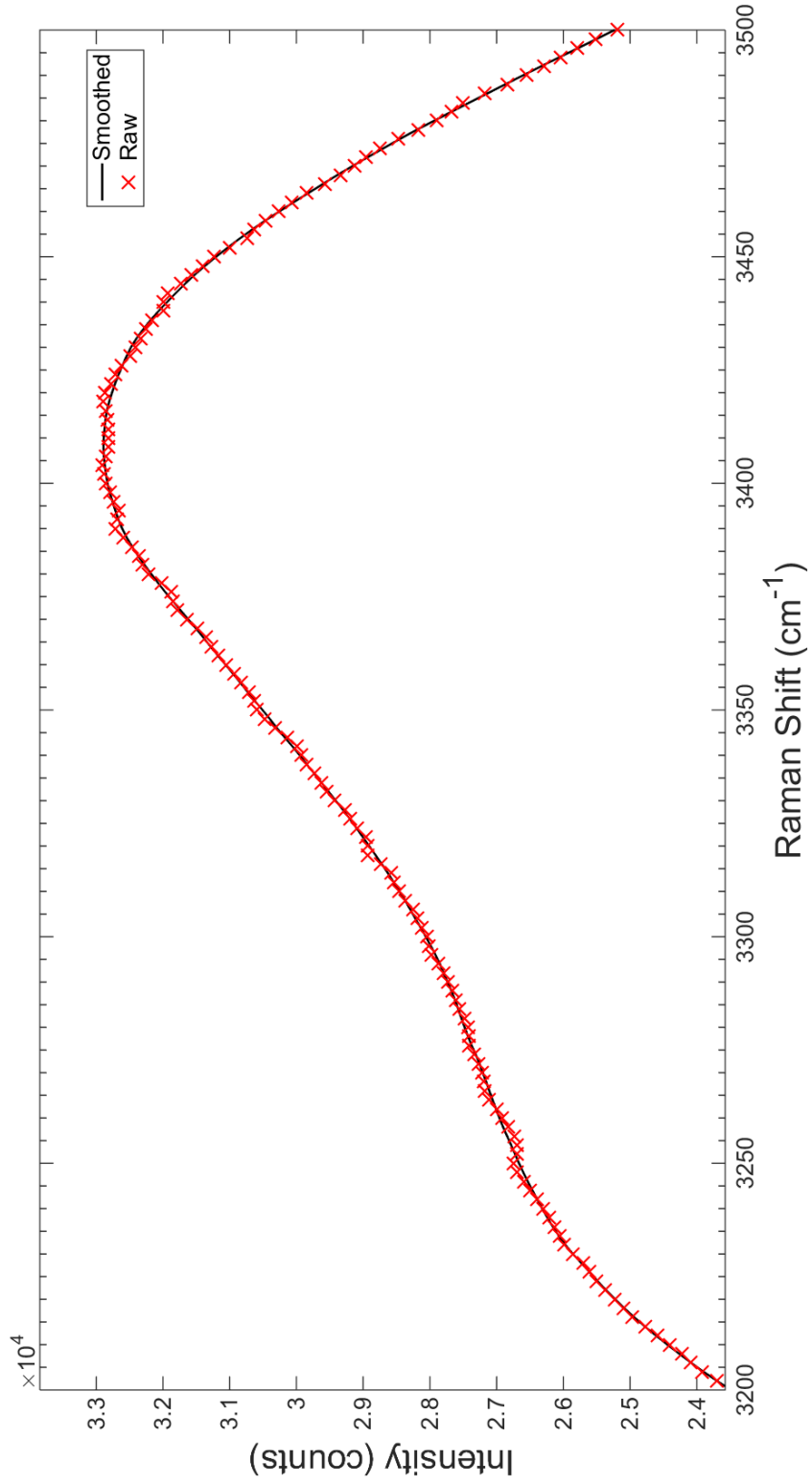

Figure F.1 — Comparison between smoothed and raw Raman spectra showing a subsection of the unpolarised OH stretching band for a reverse osmosis water sample.